Near Infrared Spectroscopy Systems for Tissue Oximetry

Petersen, Søren Dahl

Publication date:
2014

Document Version
Publisher's PDF, also known as Version of record

Near Infrared Spectroscopy Systems for Tissue Oximetry

Søren Dahl Petersen
PhD Thesis September 2014

DTU Nanotech
Department of Micro- and Nanotechnology

DTU Nanotech
Department of Micro- and Nanotechnology

Ph.D. Thesis

Near Infrared Spectroscopy Systems for Tissue Oximetry

Søren Dahl Petersen

September 2014

DTU Nanotech - Department of Micro and Nanotechnology
Technical University of Denmark

Supervisor: Professor Erik Vilain Thomsen
Co-supervisor: Professor Dr. Med. Gorm Greisen
Collaboration Partners: University Hospital of Copenhagen
Funded by: The Danish Council for Independent Research (DFF)

Preface

This thesis is submitted as a partial fulfilment of the requirements to obtain the Ph.D. degree at the Technical University of Denmark (DTU). The work has been carried out at the Department of Micro and Nanotechnology (DTU Nanotech). The project lasted from the 15th June 2011 to the 19th September 2014. This period also included a total of 14 weeks of parental leave. The project work has been supervised by Professor Erik Vilain Thomsen and co-supervised by Professor Dr. Med. Gorm Greisen from the University Hospital of Copenhagen. The project was funded by the Danish counsel of independent research (DFF).

Søren Dahl Petersen
19th of September, 2014
DTU Nanotech
Technical University of Denmark
Kongens Lyngby
Denmark

Abstract

We present flexible silicon device platforms, which combine polyimide with polydimethylsiloxane in order to add flexibility and biocompatibility to the silicon devices. The device platforms are intended as tissue oximeters, using near infrared spectroscopy, but could potentially also be used for other medical applications. The tissue oximeters are realised by incorporation of pn-diodes into the silicon in order to form arrays of infrared detectors. These arrays can then be used for spatially resolved spectroscopy measurements, with the targeted end user being prematurely born infant children.

Monte Carlo simulations have been performed on a model of a neonatal head and they show only weak changing signals as function of changes in cerebral oxygenation. A mechanical and electrical analysis of the device platforms, both by analytical expressions and numerical simulation, indicated that the proposed designs were feasible.

A number of different devices were fabricated including devices with detectors formed as arrays (1D) and as matrices (2D). The mechanical testing of the devices showed that they could be bent to more than 90° over their full lengths and strained with 3 % without damage to the electrical interconnects. Furthermore, the devices could be repeatedly bent more than 10,000 times with no indication of fatigue. IV-measurements indicated fairly low reverse bias current densities in the order of 12-30 nA/cm^2 depending on the detector size and shape. By depositing a 30 nm thick layer of aluminium oxide, as passivation on the detectors, the reverse bias current could be reduced by 30 % for small devices. Quantum efficiencies of 80-85 % were measured for the best detectors. By using black silicon nanostructures, the reflectance from the detector surfaces could be reduced for all angles of incidence. Thus, also minimising the drop in quantum efficiency for light incident at 38° from normal to only 5.2 % compared to a drop of 9.1 % for devices without the black silicon nanostructures. In conclusion both the flexible device platforms and infrared detectors were found to work.

Dansk Resumé

Vi præsenterer fleksible silicium sensor platforme, der kombinerer polyimid med polydimethylsiloxan for at tilføje fleksibilitet og biokompatibilitet til silicium sensorerne. Sensor platformene er tiltænkt brug i vævsoximetri ved hjælp af nær infrarød spektroskopi, men kan potentielt også benyttes til andre medicinal sensor. Vævsoximeterne realiseres ved inkorporering af pn-dioder i siliciummet for at danne rækker af infrarøde detektorer. Disse rækker kan derefter anvendes til rumligt opløst spektroskopi målinger, hvor slutbrugeren skal være for tidligt fødte spædbørn.

Monte Carlo simuleringer er blevet udført på en model af et spædbarns hoved og de viser kun svage signalændringer som funktion af ændringer i cerebral iltning. En mekanisk og elektrisk analyse af sensor platformene, både ved analytiske udtryk og numerisk simulering, viste at de foreslåede design var gennemførlige.

En række forskellige sensorer blev fremstillet, herunder sensorer med detektorer, der er formet som rækker (1D) og som matricer (2D). Mekaniske test af sensor platformene viste, at de kan bøjes til mere end 90°, i deres fulde længder og strækkes med 3 % uden at beskadige de elektriske forbindelsesledninger. Desuden kunne de bøjes mere end 10,000 gange uden angivelse af slitage. IV målinger viste forholdsvis lave mørkestrømtætheder i størrelsesordenen 12-30 nA/cm^2 afhængig af detektorernes størrelse og form. Ved at deponere et 30 nm tykt lag af aluminiumoxid, som passivering på detektorerne, kan mørkestrømtætheden reduceres med 30 % for små detektorer. Kvanteeffektiviteter på 80-85 % blev målt for de bedste detektorer. Ved at bruge sort silicium nanostrukturer, kunne reflektansen fra detektorenes overflade reduceres for alle indfaldsvinkler. Dermed vil reduktionen i kvanteeffektivitet blive minimeret, ved et lysindfald på 38° fra normal, til kun 5,2 % i forhold til en reduktion på 9,1 % for sensorer uden sorte silicium nanostrukturer. Som konklusion fungerede både de fleksible sensor platforme og de infrarøde detektorer.

Acknowledgements

First and foremost I would like to thank my supervisor Professor Erik Vilain Thomsen for his supervision and guidance during this project. Eriks extensive knowledge of silicon micro technology and his profound overview has been very helpful. I would also like to thank the entire MEMS-AppliedSensors group at DTU Nanotech for help and assistance especially my office mate Postdoc Anders Lei. For the collaboration concerning black silicon nanostructures I would like to acknowledge Ph.D. student Rasmus Schmidt Davidsen from DTU Nanotech.

I would like to acknowledge the collaboration with the University Hospital of Copenhagen represented by my co-supervisor Professor Dr. Med. Gorm Greisen and Ph.D. student Simon Hyttel-Sørensen. As potential end users their knowledge of neonatal medicine has been essential for my work.

During this project I have co-supervised a number of excellent students who were carrying out their project work in the MEMS-AppliedSensors group. Their hard work has contributed to the achieved results of this project. They include: bachelor student Mathias Engholm and master students Anders Thyssen, Joachim Dahl Thomsen and Lucia Alcalá.

I would also like to acknowledge DTU Danchip and its staff for providing the process means for this project by keeping the cleanroom up and running and for being open to assistance and questions.

I would like to thank Camilla Dahl and Anders Thavlov for proofreading of this thesis. Finally, Thanks to my wife Marie Louise Skjerning and my two children Valdemar and Leonora for creating a loving atmosphere at home.

Contents

List of Abbreviations

1D - One-dimensional
2D - Two-dimensional
ALD - Atomic layer deposition
BGA - Blood gas analyser
BHF - Buffered hydrofluoric acid
BSG - Borosilicate glass
CMUT - Capacitive micromachined ultrasonic transducers
CSF - Cerebrospinal fluid
DI - Deionised
DRIE - Deep reactive ion etching
FEM - Finite element method
Hb - De-oxygenated haemoglobin
HbO - Oxygenated haemoglobin
HMDS - Hexamethyldisilazane
IC - Integrated circuit
ICP - Inductive coupled plasma
IQE - Internal quantum efficiency
LED - Light emitting diode
LPCVD - Low pressure chemical vapour deposition
MEMS - Micro electromechanical systems
NIRS - Near infrared spectroscopy
PDMS - Polydimethylsiloxane
PECVD - Plasma enhanced chemical vapour deposition
RIE - Reactive ion etching
SEM - Scanning electron microscope
SERS - Surface enhanced Raman spectroscopy
SIMS - Secondary ion mass spectroscopy
SRS - Spatially resolved spectroscopy

StO_2 - Tissue oxygenation
TEOS - Tetraethyl orthosilicate
TOI - Tissue oximetry index
TRS - Time resolved spectroscopy
UV - Ultra violet
ZIF - Zero insertion force

Chapter 1

Introduction

According to the 2012 report, from the World Health Organisation, 15 million children are born prematurely every year [1]. When neonates are born prematurely they can easily suffer from complications when recovering in their incubators [2, 3]. It is therefore essential to their survival that their vital signs are monitored. One of the most important vital parameter to monitor is the oxygen saturation in the cerebral tissue [4–7]. This is due to the fact that the prematurely born neonates have difficulties in regulating the oxygen saturation in their bodies and therefore they often receive oxygen from an artificial supply through a nasal cannula. However, this oxygenation has to be monitored since a too low concentration can lead to brain damage and a too high concentration can cause blindness as well as other disabilities [8–10]. Being able to precisely monitor and regulate the cerebral oxygenation are very crucial for the future medical treatment of neonates.

A typical method used for analysing the cerebral oxygenation is by drawing blood samples and investigating the parameters using a blood gas analyser (BGA). However, this method is invasive and can be stressful for the neonates, due to the inflicted pain, as well as removing relatively large volumes of blood, which can result in the need for blood transfusions [11]. Furthermore, BGA is not an on-line method for cerebral oxygenation measurement and a certain delay is therefore expected between sampling and result.

During the past few years, hospitals have started using different sensor systems that utilise near infrared spectroscopy (NIRS) in order to measure the cerebral oxygen saturation non-invasively [12–14]. Many studies have been conducted and they show the feasibility of NIRS sensor systems, when used for tissue oximetry monitoring, but also the limitations of the systems developed so far [15–18]. Today, we are left with three decades of research within tissue oximetry systems as well as with some commercial systems that have recently entered the marked. However, in order to ensure better medical treatment of prematurely born neonates sensor

systems, which offer higher precision in determining the cerebral oxygen saturation must be invented.

In this project we have used our knowledge of silicon micro fabrication as well as our access to the DTU Danchip cleanroom facilities in order to design, fabricate and characterise tissue oximetry devices made from a silicon platform with integrated biocompatibility and flexibility. The oximetry devices contain multiple detectors, which should increase their ability to precisely measure even small changes in cerebral oxygenation for prematurely born infants.

1.1 Oximetry and Neonatology

The ability to determine the oxygen saturation of blood, using only light, is an extremely valuable medical diagnostics method since it is both non-invasive and on-line. This diagnostics method has therefore been researched during the past century. The first successful attempt, at determine the oxygen saturation of blood using only light, was performed by K. Matthes in 1935. He measured through the earlobe using red and green light and was able to determine the oxygen saturation from these two measurements. The modern pulse oximetry diagnostics method was developed in 1972 by T. Aoyagi and M. Kishi [19, 20] and it is now utilising red and near infrared light, as described in the next section. Pulse oximetry can determine both the arterial blood saturation and the heart rate. This method was an immediate success and was commercialised within a few years. Today it is used worldwide to monitor patients who are admitted at hospitals.

Tissue oximetry later arose as a more specific type of oximetry since it was aiming at determine the regional oxygenation of a specific part of the body rather than the arterial oxygenation. This method has the advantage that it can determine if critical tissue, e.g. cerebral tissue, has low oxygen saturation even though the general arterial saturation of the body is normal. This can be useful for certain modalities, e.g. internal haemorrhage or thrombus and also during surgery and as mentioned for monitoring of cerebral oxygenation in neonates.

1.1.1 Pulse and Tissue Oximetry

Pulse and tissue oximetry are both relying on two distinct optical properties of tissue. Firstly, the reason that light can be used to probe the tissue is due to low light absorption for a specific wavelength range. In popular terms this wavelength range is called the "tissue window" and is generally spanning wavelengths from red light to the first half of the near infrared spectrum, corresponding to approximately 650-1000 nm, as can be seen from Figure 1.1. In this "tissue window" both lipids,

protein and water exhibits low absorption whereas melanin and haemoglobin exhibits strong absorption.

The haemoglobin absorption is the second tissue property, which enables pulse and tissue oximetry. It is due to the two facts that haemoglobin exhibits different absorption spectra depending on whether it is oxygenated (HbO) or deoxygenated (Hb) and because both oxygenated and de-oxygenated haemoglobin have absorption spectra, which changes greatly within the "tissue window", as can be seen from Figure 1.2.

Pulse oximetry is typically realised by measuring through body extremities e.g. a finger tip or an earlobe. In this case the major part of the oximetry signal will come from arterial blood with a minor contribution from venues and capillary blood. By measuring with light of two different wavelengths both the heart rate and arterial oxygenation can be determined using Beer-Lamberts law of absorption. A pulse oximeter can therefore function using only two light sources and one photo detector.

Another possible setup for a pulse oximeter is to measure the diffuse reflected light. The diffuse reflected light is light that has been injected into the tissue, diffused around due to the strong scattering properties of the tissue and then finally will return through the skin. This is useful when measurement on thin tissue samples is not possible and a common method is to measure on the sternum [23]. Figure 1.3a shows a typical finger clip pulse oximeter used at hospitals and Figure 1.3b shows

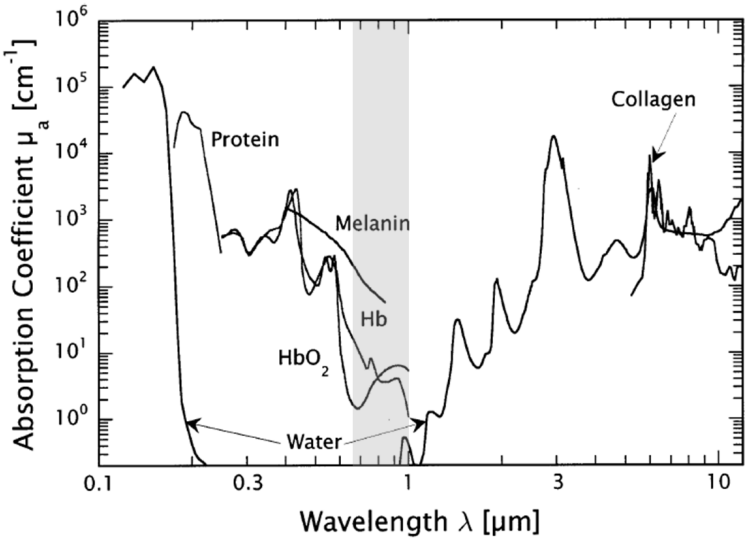

Figure 1.1: Absorption coefficient for different tissue components plotted from the ultra-violet to the infrared region. The tissue window spans from 650 nm to 1000 nm and is marked with gray. The plot is from [21].

an experimental sternal pulse oximeter.

When performing tissue oximetry measurements the typical targets will be cerebral or muscular tissue, where the measurement is performed externally, or viscus tissue, where the measurement is performed internally, e.g. during surgery. In all cases these tissue types will differ from body extremities by mainly containing capillary blood instead of arterial blood. The signal from optical probing will there-

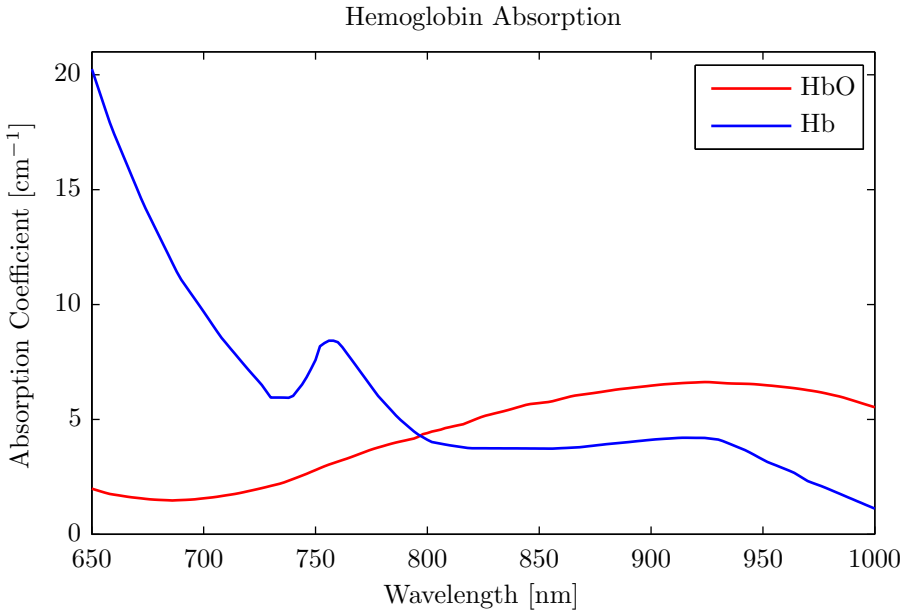

Figure 1.2: The absorption coefficient for oxygenated and deoxygenated haemoglobin. For wavelengths shorter than 800 nm the absorption is highest for the deoxygenated haemoglobin and for wavelength larger than 800 nm the absorption is highest for oxygenated haemoglobin. The two types of haemoglobin exhibits an isobestic point at approximately 800 nm. [22].

(a) *Trancemittance type finger clip pulse oximeter*

(b) *Reflectance type sternal pulse oximeter [24]*

Figure 1.3: Two different types of pulse oximeters. In (a) a finger clip type is shown. This type is the most widely used design and functions by measuring the light that is transmitted through the finger. A reflection type, so called "e-patch", is shown in (b). It functions by measuring the light that is diffuse reflected.

fore be different and as a result alternative methods have to be used in order to determine the Hb and HbO concentrations.

The most used measurement method for tissue oximetry is a specific type of NIRS called spatially resolved spectroscopy (SRS). Here, the intensity of the diffuse reflected light is measured as a function of distance from the light source, which again utilises light of different wavelengths, as can be seen in Figure 1.4a. A picture of a commercial tissue oximeter, from Nonin Medical Inc., can be seen in Figure 1.4b [25]. The objective of the SRS measurement is to determine the relative tissue oxygenation index (TOI), which is given by:

$$TOI = \frac{C_{HbO}}{C_{HbO} + C_{Hb}} \tag{1.1}$$

where C_{HbO} is the concentration of oxygenated haemoglobin and C_{Hb} is the concentration of deoxygenated haemoglobin in the tissue. A detailed description of light and tissue interaction for SRS tissue oximetry is presented in Chapter 2.

1.1.2 Neonatal Oximetry

Oximetry is today widely used in neonatal medicine. Previously, electrocardiography was the only available method for monitoring, but today pulse oximetry is typically used because of its ability to monitor both the heart rate and the peripheral oxygenation. For prematurely born infants this is often done by measurement through a foot or a hand, as can be seen from Figure 1.5a. Tissue oximetry is still mostly used for research purposes, but over the past few years, commercial systems have become available and this has sparked renewed interest in using this method

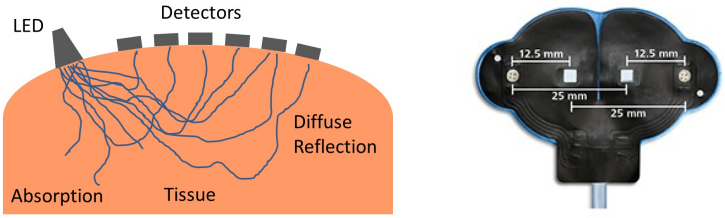

(a) *The principle behind SRS*

(b) *A commercial tissue oximeter*

Figure 1.4: The working principle of SRS used for tissue oximeters is shown in (a). Light from a light emitting diode (LED) is injected into the tissue where it undergoes scattering and absorption. The diffuse reflected light is measured as a function of distance to the light source using a number of detectors. A commercial tissue oximeter, from Nonin Medical Inc. is shown in (b). It consists of two light sources (with four different LEDs) and two detectors, which are integrated into a medical silicone patch [25].

for monitoring of neonates. The main focus will be to monitor the cerebral oxygenation, which is typically done by measuring on the forehead or temple of the neonate, as can be seen from Figure 1.5b.

Because NIRS tissue oximetry is both non-invasive and on-line it is the focus of studies that seek to expand the diagnostic tools for neonatal monitoring. One such project, of which this Ph.D. project is collaborating with, is the SafeBoosC study. SafeBoosC is an acronym for: "Safeguarding the brain of our smallest children" and the name of a clinical feasibility study regarding NIRS monitoring of prematurely born infants [26]. In this study, which is conducted on 166 preterm infants in 12 European countries, the cerebral oxygenation is monitored and if possible stabilised during the first 72 hours of the infants life. In Denmark, the study is performed at the University Hospital of Copenhagen. The goal of the study is to investigate, if NIRS can be used for non-invasive tissue oximetry monitoring, and if this is the case whether or not any reduction in complications for the neonates can be observed.

(a) *A neonatal pulse oximeter*

(b) *Neonatal tissue oximetry*

Figure 1.5: Pulse oximetry is today widely used in neonatal medicine as can be seen in (a) [27]. Cerebral tissue oximetry is still mostly used for research purposes. The measurements are typically performed on the forehead of the neonate (b) [25].

1.2 Tissue Oximetry Systems

NIRS systems for tissue oximetry have been a research topic for at least the past three decades culminating with the introduction of commercial systems during the past few years. Many different solutions have been proposed, but many of the solutions also appear to be similar.

Most of the commercial available devices work on similar principles by utilising SRS with two measurement distances and light with three or four different wavelengths. Furthermore, the sensor devices are made from discrete components that are integrated into a one time use silicon medical patch, as was shown in Figure 1.4b. This includes devices from Nonin, CAS medical systems, ViOptix and Covi-

dien. This indicates that the companies behind these devices are focused on using a simple detector design and then compensating for this with advanced algorithms for calculation of the TOI. The advantage of a simple sensor design, consisting of discrete components, is a low manufacturing cost. The disadvantage is that there will be a greater chance for error when using only two measurement distances, since one or both detectors might be disturbed during measurement. This disturbance could be caused by incorrect placement of the detector or invisible defects in the skin and skull. The tissue oxygen saturation (StO_2) measuring range and accuracy of some commercial devices are listed in Table 1.1.

The NIRS tissue oximetry devices, which have been presented in literature are more diverse regarding working principle and design, when compared to the commercial systems. Some utilises the SRS measuring principle while others instead uses time resolved spectroscopy (TRS) or frequency resolved spectroscopy. Some utilises many detectors for SRS measurements and others only two. Some of the device concepts, which were identified during the literature study for this project, are present below.

A number of NIRS tissue oximetry devices that are being developed at research institutions actually resemble the commercial available systems. One such system is the OxyPrem detector, which is in development at the Biomedical Optics Research Laboratory at the University Hospital of Zurich in Switzerland [28]. The OxyPrem sensor is shown in Figure 1.6a. It consists, like the commercial sensors, of two detectors, but instead it has four light sources that are equally spaced to the detectors with distances of 15 mm and 25 mm. The advantage of this more complex design is that multiple light sources help to reduce the chance that the signal is disturbed by artefacts in the skin or covered with hair. This self-calibrating method is described in [29].

Another NIRS sensor that resembles the commercial systems is the NIRO 300 [30], which can be seen in Figure 1.6b. The device consists of two patches; one containing the light source and one containing the detectors. The light source and the detectors can then be placed on the subject with a distance that can be varied depending on the subject or measurement type. The detector patch contains three 8 mm $\times$ 2 mm detectors, which have a separation of 1 mm, i.e a pitch of

Manufacture	Device name	StO_2 range	StO_2 accuracy	Refrsh rate
CAS medical systems	Fore-sight Elite^{TM}	0-99 %	$\pm$3.1 %	2 s
Nonin	Equanox^{TM}7600	0-100 %	$\pm$4.1 %	1.5 s
ViOptix	T.Ox^{TM}	0-100 %	$\pm$5.9 %	4 s

Table 1.1: Three commercial tissue oximetry devices and their performance parameters.

3 mm. One major conclusion from the article is that the extra detector improves the measurement precision when comparing to a similar device with only two detectors.

A tissue oximetry system, which uses a different principle, when compared to the commercial systems, was presented in [31]. This device is shaped like a helmet that can be placed on the head of the neonate, as can be seen from Figure 1.6c. The helmet has several light sources and detectors embedded and they are used to measure the light, which is transmitted through the head using TRS rather than SRS. This device has the advantage that it can measure on a large volume of cerebral tissue. However, TRS requires very fast light sources and detectors, which are both

(a) *The OxyPrem sensor [28]*

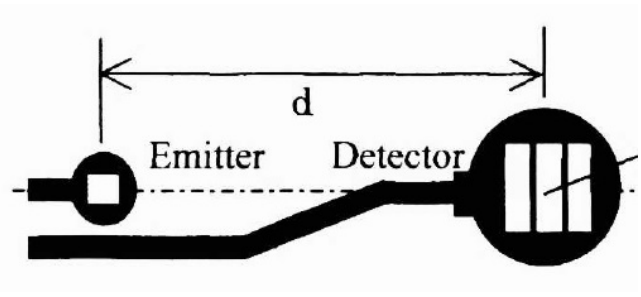

(b) *The NIRO 300 sensor [30]*

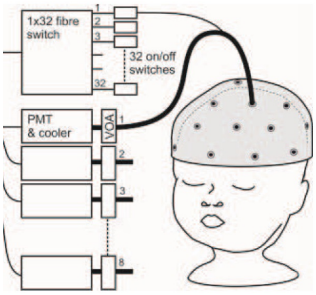

(c) *TRS helmet sensor [31]*

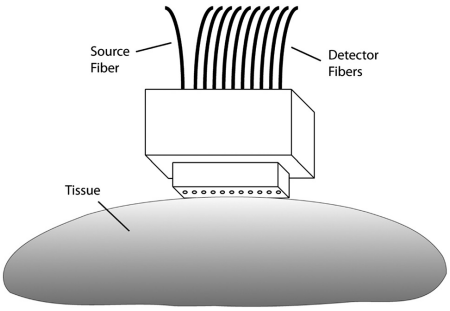

(d) *Fiber bundle sensor [32]*

Figure 1.6: Different NIRS sensors, which have been presented in literature. Some sensors share similarities with the commercial available devices and others work using principles and designs that are not similar to the commercial systems. The OxyPrem sensor shown in (a) utilises the standard two detectors but four light sources. This enables more precise measurements and self-calibration. The Niro 300 sensor shown in (b) uses three detectors, which improves the precision of the measurements. An experimental system designed as a helmet is shown in (c). This system uses TSR instead of SRS by measuring the light that is transmitted through the head rather than measuring on the diffuse reflected light. A fiber bundle sensor is shown in (d). This device uses up to 20 points of measurements for SRS. The sensor is designed to distinguish between healthy tissue and cancer tissue and the system proves that using many measurement points will improve SRS measurements.

very costly and not feasible for all device designs.

Finally, a device using many detectors for SRS is presented in [32]. The device is made up of 20 optical fibers, which are connected to a handle piece that spaces the fibers with 1 mm distance. This design enables very precise measurements of the diffuse reflected light as function of distance to the light source. The purpose of the sensor is not to make tissue oximetry measurements, but to measure the optical difference between healthy tissue and cancer tissue, which is proven to be feasible. This requires very precise determination of the absorption and scattering properties of the tissue, indicating that even better NIRS tissue oximetry devices could be made by using sensors with multiple detectors.

In conclusion, adding multiple light sources to the devices and using multiple detectors for the SRS measurements will improve the performance of the devices. These are therefore two important design parameters to consider when choosing a device design, which can improve neonatal tissue oximetry.

1.3 Flexible Silicon Devices

As mentioned in the previous section a number of design solutions, for NIRS tissue oximeters, have been presented both commercially and in literature. The vast majority are devices that consist of discrete components, which are integrated into a silicone medical patch or other similar structures. However, a number of medical devices, which have been presented in literature, are fabricated as silicon devices with the flexible medical patch structure fully integrated into the silicon itself. This has proven to be feasible for silicon devices that are designed for both internal and external body use as well as for other non-medical devices. The advantage is that very specific or complicated devices, i.e. micro electromechanical systems (MEMS), can be mass produced using traditional integrated circuit techniques and then have flexibility and biocompatibility added to these devices during the fabrication. Typically, this is achieved by combining the silicon with materials such as polyimides or Polydimethylsiloxane (PDMS). Many polyimides are compatible with standard integrated circuit (IC) processes and can therefore be readily used in cleanrooms. However, they are often not completely biocompatible and are translucent or opaque to visible and near infrared light. The different types of PDMS are typically transparent to visible and near infrared light and extremely biocompatible types exist. However, the process of casting PDMS is in general not considered compatible with IC cleanroom processes. Some of the published solutions for adding flexibility to silicon devices are presented below.

In [33] a MEMS shear stress sensor, that utilises PI to add flexibility to silicon, is presented. The device is made of wet etched silicon islands, which are connected

by a 17 μm thick layer of PI that sandwiches an aluminium metallisation. The device performs excellent when being bent around curved surfaces and does not loose electrical conductivity through the metallisation. The entire fabrication process for this device is compatible with standard IC processes. Although, using only 17 μm of PI creates a flexible platform that has to be handled carefully.

Another MEMS device with integrated flexibility is a capacitive micromachined ultrasonic transducer (CMUT), which utilises PDMS for flexibility [34]. The flexibility is achieved by etching of trenches in the device using deep reactive ion etching (DRIE) then filling the trenches with PDMS outside the cleanroom facility and finally continue the IC processing when the PDMS has cured. The final device is a 2D array of 16 $\times$ 16 CMUTs that is flexible enough to follow the curvature of different body parts, as seen in Figure 1.7b.

When designing flexible silicon devices for medical use it is not enough to ensure that the devices are biocompatible and that the structure can endure being bent multiple times. The individual elements on the devices will have to be connected with electrical interconnects. Electrical interconnect manufactured by IC processing will typically have en thickness of only a few hundred nanometre to a few micrometre. They will therefore be very fragile and could break if being bent around sharp corners or strained longitudinally. Furthermore, the fragile electrical interconnects will have to be encapsulated in order to protect them from the outside environment. A number of different solutions to the above mentioned problems have been presented in literature.

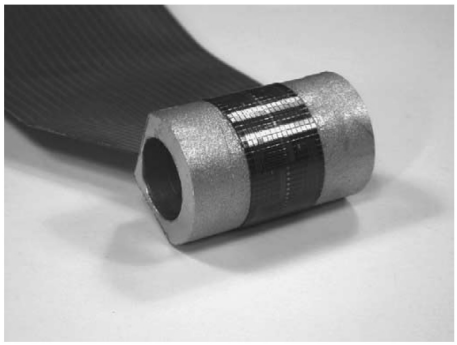

(a) *Flexible sensor made from polyimide [33]*

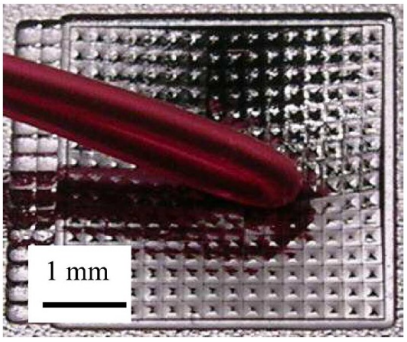

(b) *CMUT array achieving flexibility from PDMS [34]*

Figure 1.7: Two different approaches for adding flexibility to silicon devices. In (a) polyimide is used together with silicon to create a flexible shear stress sensor. This sensor can be curved around objects with a small radius of curvature. In (b) PDMS is used to form flexible joints between individual elements of a CMUT device. This enables the device to follow the curvatures of body parts.

Some research results have been presented where flexible electrical interconnects were fabricated using PDMS as the flexible platform. In [35] so called micro cracked gold is formed on PDMS substrates. This is done by evaporation thin layers of gold onto the PDMS substrates using a special technique. These layers will, due to the micro cracks, maintain electrical conductivity even when the PDMS substrate is longitudinally strained. The micro cracked gold can also be repeatedly strained and released without any wear to the gold thin film. However, the gold thin film suffers from being fragile due to the fact that it is freely exposed to the environment and its relatively small thickness of typically only 20-30 nm. The small thickness of the gold layer also means that any electrical interconnects will have a very high sheet resistance when compared to conventional IC metallisation.

A second approach using PDMS is presented in [36]. Here the PDMS itself is made conducting by adding carbon or silver particles in order to form electrical interconnects. The conductivity of the conductive PDMS can be controlled by changing the concentration of the carbon or silver particles from 10^{-2} S/m to 10^{5} S/m. The conductive PDMS will function as encapsulated conductors and thus be protected from the outside environment. However, the large sheet resistance becomes an issue again even for PDMS with a high silver particle concentration. Moreover, fabrication of un-cured PDMS is not possible in the DTU Danchip cleanroom facilities and this approach would therefore not be feasible for this project.

Both approaches with the micro cracked gold and the PDMS with silver particles also suffer from a high relative resistance change as function of strain. These results are not useful for many MEMS device applications where the electrical interconnects should maintain a constant resistance, even when being bent, so that the impedance of the device is constant.

Another possible solution is to have a spring like structure in the flexible areas between the rigid silicon areas. Such structures have been tested in [37] and found to be very durable and could be both bent and strained longitudinally. However, the fabrication process for making these types of flexible electrical interconnects is very complicated and a NIRS oximetry device functioning by the SRS principle should only be bendable and not stretchable, since this would change the relative distance between the detectors.

1.4 Project Description

The above presented NIRS devices and flexible silicon processes have been used to analyse how we can use our knowledge of silicon micro fabrication to develop tissue oximetry devices with improved performance. We have chosen the following design parameters for our devices:

- The fabrication of the devices should be done at the facilities we have available at DTU Nanotech (workshops and laboratories) and DTU Danchip (cleanroom facilities).
- The devices will be fabricated on wafer scale with the biocompatibility and flexibility integrated into the devices. The devices will, therefore, need electrical interconnects that can withstand being bent.
- The devices will consist of multiple detectors, which will aim at improving the spatial resolution on SRS measurements. Moreover, the detectors should be optimised for tissue oximetry.

These design parameters have been the basis for our work during this project, when developing NIRS tissue oximetry sensors for prematurely born infants. In general the project work has been split up into two parts:

1. **Flexible silicon device platforms** - Design, fabricate, optimise and test different silicon platforms with integrated biocompatibility and flexibility. The platforms should be bendable in order to follow the curvature of a neonatal head without degradation of the electrical interconnects. Moreover, the platforms should be large enough to function as SRS tissue oximeters with multiple detectors, but could in principle also be used for other medical devices where flexibility is needed e.g. CMUTs.
2. **High quality infrared detectors** - Fabricate, optimise and characterise infrared detectors for NIRS tissue oximetry. The infrared detectors should be integrated into the flexible silicon platforms in order to fabricate the final devices using a single process recipe. Test devices for optimisation of the infrared detectors have also be fabricated.

Our solution has been to develop a flexible silicon device platform, which consists of both polyimide and PDMS, as can be seen in Figure 1.8a. The PDMS will act both as a flexible backbone of the device and be the biocompatible contact surface. The polyimide will encapsulate the fragile electrical interconnects and ensure that the interconnects are not subjected to longitudinal strain when the device is being bent. The complete analysis of this design is given in Chapter 3. Figure 1.8b and 1.8c show two flexible silicon platforms that were developed during this project using the combination of silicon, polyimide and PDMS. The first is a one-dimensional (1D) linear array of silicon structures with flexible joints in between the silicon. This device was used as a prototype for evaluation of the fabrication process for structural tests and for tests of the electrical interconnects. The second

platform is a two-dimensional (2D) matrix of silicon structures, which again have flexible joints in between the silicon. It was used to optimise the fabrication process for the matrix platform and test the structural integrity of fabricated devices.

These flexible silicon device platforms have then been used to fabricate SRS tissue oximetry sensors, by incorporating infrared detectors into the silicon structures. The infrared detectors are designed as back-side pn-junction photo diodes, as shown in Figure 1.9a. The complete detector analysis is presented in Chapter 4. Two devices, which were developed during this project can be seen in Figure 1.9b and 1.9c. The 2D device consists of 36, 2 mm × 2 mm, silicon pn-junction back side photo diodes with flexible joints between the individual diodes. Electrical interconnects have been routed to nine of the diodes. The 1D device consists of eight pn-junction back side diodes, which for this device are 10 mm × 2 mm. The device has an LED bonded to the back side. The LED can emit infrared light, of 735 nm, 805 nm and 850 nm, through an etched hole in the device. An investigation where black silicon nanostructures and coatings of Al_2O_3 were used to improve the detectors performance, was also carried out.

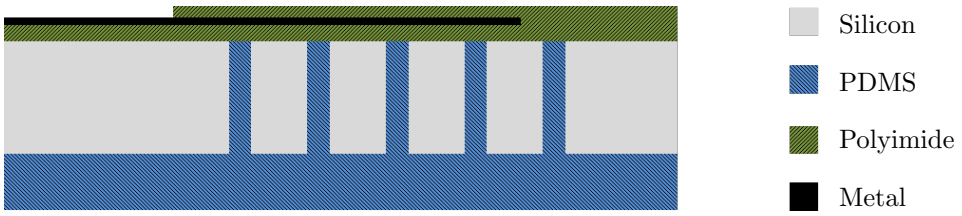

(a) *Cross section of the flexible platform*

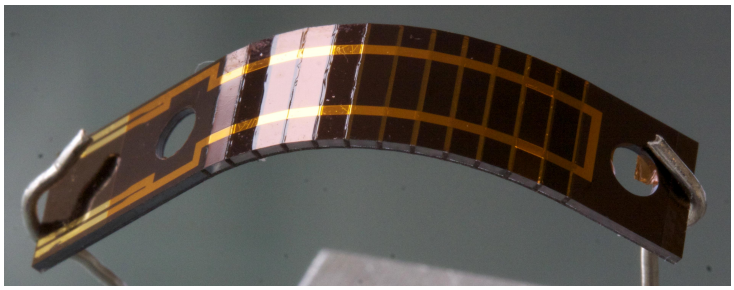

(b) *1D linear array*

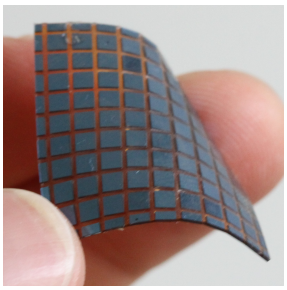

(c) *2D square matrix*

Figure 1.8: The flexible silicon device platforms. The concept behind the platforms is described by the schematic cross section drawing in (a). It shows how silicon is combined with PDMS and polyimide in order to form flexible joints between the silicon structures as well as a biocompatible contact surface. Furthermore the polyimide will act as encapsulation material for the fragile metallisation. A 1D and a 2D platform, which were developed during this project, are shown in (b) and (c) respectively. Both platforms are fabricated using the concept shown in (a).

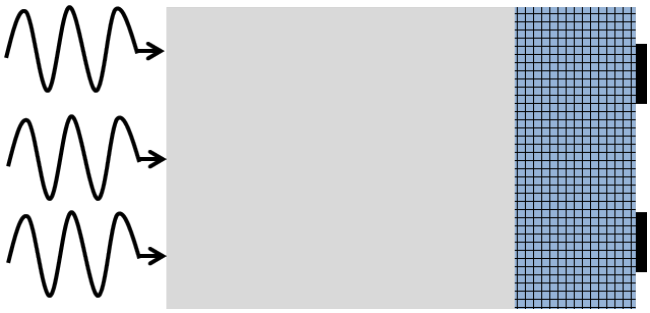

(a) *Back side photo diode*

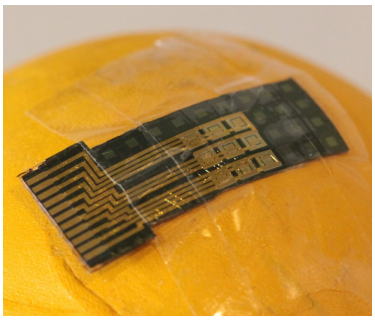

(b) *2D infrared sensor device*

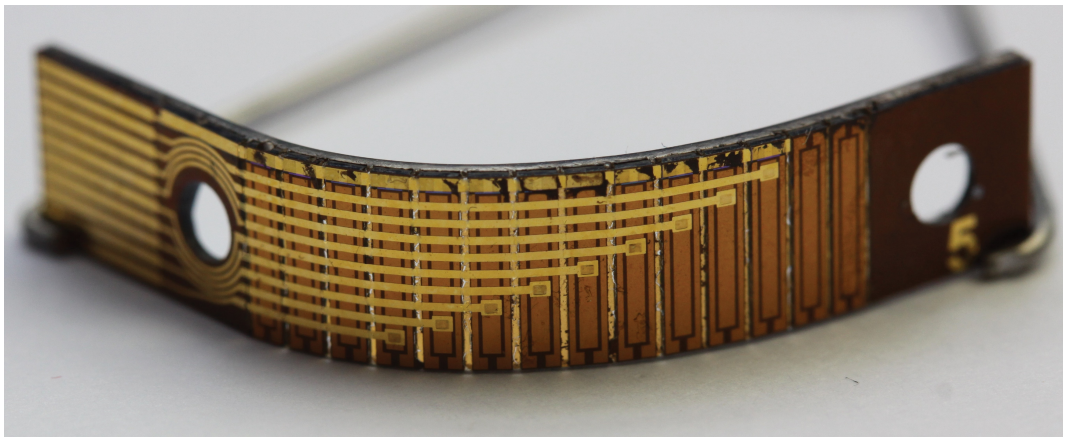

(c) *1D infrared sensor device*

Figure 1.9: The concept of a back side photo diode is shown in (a). The light enters the silicon (grey) from the opposite side of the pn-junction. The light is then absorbed in the bulk of the silicon and the generated carriers will have to diffuse to the depletion region (crossed blue) in order to contribute to the photo current. All the metallisation (black) is located on the opposite side of the light incident surface. A 2D infrared sensor prototype is shown in (b). It consists of 36 silicon elements with flexible joints between the elements. Electrical interconnects have been routed to nine of the elements. A 1D tissue oximeter device is shown in (c). It consists of 14 silicon structures with flexible joints in between. Electrical interconnects have been made to 9 of the detectors.

1.5 Outline of Thesis

The remainder of the thesis is organised as follows:

- **Chapter 2 Tissue Optics and Oximetry** - This chapter presents our analysis and modelling of the interaction between light and tissue. Monte Carlo simulation is used to model how the changing cerebral oxygenation effects infrared light.

- **Chapter 3 Design of Flexible Silicon Platforms** - This chapter presents the platform design as well as analytical and finite element models of how the flexible platforms would behave when being bent.
- **Chapter 4 Design of Infrared Detectors** - Here, the analysis of how the infrared detectors behave and should be fabricated for optimal results is given. Both analytical models and numerical simulations are used.
- **Chapter 5 Device Design and Fabrication** - The description of the many different devices and the finalised process recipe are presented. Each step in the process recipe is laid out in detail.
- **Chapter 6 Process Development** - This chapter describes the work that have been done in the cleanroom facility and laboratories in order to develop and optimise the fabrication process steps. The presented results have been used to finalise the process recipe listed in the previous chapter.
- **Chapter 7 Test and Characterisation of Devices** - In this chapter the results from the mechanical and electrical testing are presented. The mechanical tests includes bending and stretching while the electrical characterisation includes I-V analysis and quantum efficiency measurements. The results are discussed and compared to other results from literature.
- **Chapter 8 Conclusion and Outlook** - The conclusions for everything that has been achieved doing this Ph.D. project are presented together with an outlook.

Parts of the performed research have been presented at conferences and published in scientific Journals. The publications are included in Appendix A. A patent, with application number: PA 2014 70546, has also been filed

Chapter 2

Tissue Optics and Oximetry

Tissue is a very complex medium for light propagation. Thus, an understanding of how the near infrared light will interact with tissue is needed before one can use oximetry to determine the different haemoglobin concentrations. As mentioned the mechanism behind oximetry is the fact that HbO and Hb absorb light differently for different wavelengths. However, both absorption and scattering will occur from all the different layers of tissue. This chapter will introduce the basic concepts behind light and tissue interaction and use an analytical model to describe how the diffuse reflected light will behave as a function of distance from the light source. Finally, Monte Carlo simulations are performed on a layered model of a neonatal head.

2.1 Light and Tissue Interaction

When describing how light and tissue will interact one can use a number of different approaches. However, due to the complexity of tissue a number of assumptions and simplifications must be used. Tissue is not a homogeneous medium but consists of many different components i.e. cells, fluids and fiber structures, which have different absorption and scattering properties [38]. Also, the tissue composition will be different at the various body parts of a human. One model would be to assume that the tissue consists of a random distribution of scatterers and absorbers. Such a medium is called a turbid medium. Light entering a slap of tissue can then undergo four different events: be absorbed by the medium, be diffuse transmitted through the medium and escape from the backside, be diffuse reflected by the medium and escape from the incident side and finally pass through the medium unaffected, as can be seen in Figure 2.1. A simplified model, which can be used when dealing with thick specimens of tissue, would be to consider the tissue as semi infinite. In this case the problem reduces to light being either absorbed or diffuse reflected.

The most important equations governing the absorbing and scattering prop-

erties are given in [39]. The absorption and scattering of the medium are described by the total attenuation coefficient, μ_t, given by:

$$\mu_t = \mu_a + \mu_s \tag{2.1}$$

where μ_a is the absorption coefficient and μ_s is the scattering coefficient of the medium. The total attenuation coefficient will be the total number of light interactions per length. Two other important quantities of a turbid media are the albedo Λ, given by:

$$\Lambda = \frac{\mu_s}{\mu_t} = \frac{\mu_s}{\mu_s + \mu_a} \tag{2.2}$$

and the reduced scattering coefficient μ_s', given by:

$$\mu_s' = (1 - g)\mu_s \tag{2.3}$$

where g is the scattering anisotropy factor. For most types of tissue $\mu_s \gg \mu_a$, which means that $\Lambda \approx 1$, also most types of tissue are strongly forward scatterers with $g \approx 0.9$.

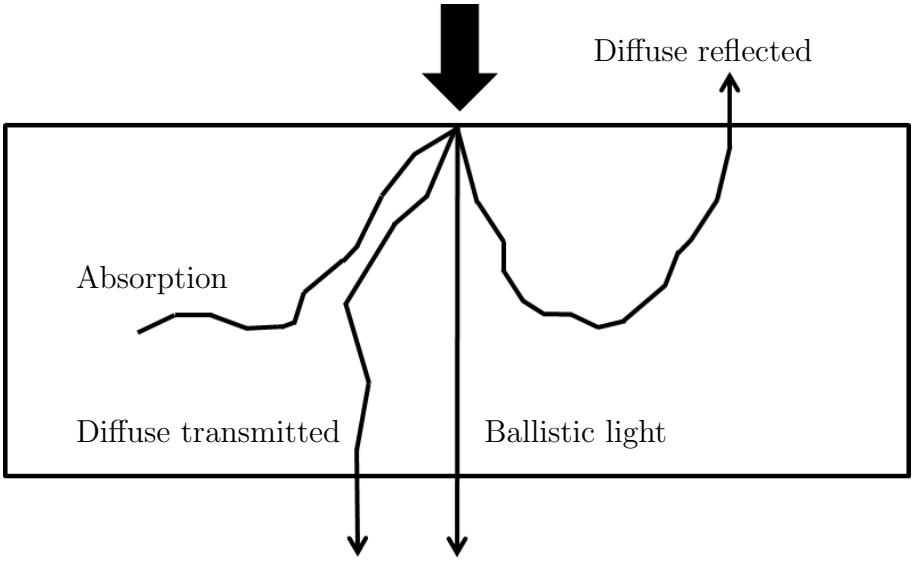

Figure 2.1: Light entering a slap of tissue can undergo several interaction events. The light can be absorbed by the tissue, it can scatter and pass through the opposite interface and it can scatter and pass through the incident interface. Finally, there can be a ballistic component, which passes through the tissue unaffected.

2.2 Modeling Light Propagation in Tissue

The propagation of light in a medium can be described by the use of Maxwell's equations and this will yield the complete description of wave propagation. However, this method is for most problems, especially problems including tissue, too complex to be of practical importance. Instead transport theory, which models the transport of energy in a random media, is a more straight forward approach. The transport theory yields the radiative transport equation [40], which is based on the conservation of energy:

$$\frac{1}{c}\frac{\partial L(\mathbf{r},\mathbf{s},t)}{\partial t} = -\mathbf{s}\cdot\nabla L(\mathbf{r},\mathbf{s},t) - \mu_t L(\mathbf{r},\mathbf{s},t) + \mu_s \int_{4\pi} L(\mathbf{r},\mathbf{s},t)P(\mathbf{s}',\mathbf{s})d\Omega' + S(\mathbf{r},\mathbf{s},t) \tag{2.4}$$

where c is the speed of light, $L(\mathbf{r},\mathbf{s},t)$ is the time dependent radiance in the position $\mathbf{r}$ in the direction of the unit vector $\mathbf{s}$, $P(\mathbf{s}',\mathbf{s})$ is a phase function describing the scattering of the flux which comes from a direction $\mathbf{s}'$ and scatters into solid angle $d\Omega$ in the direction $\mathbf{s}$. Finally, $S(\mathbf{r},\mathbf{s},t)$ is a source in the position $\mathbf{r}$ in the direction of the unit vector $\mathbf{s}$. The radiative transport equation is basically describing the change in energy, due to: a loss from divergence, a loss from extinction, an increase from scattering into the volume and an increase from sources located in the volume, all together governed by conservation of energy.

Although Equation 2.4 is much easier to handle than Maxwell's equations it is still complex and no analytical solutions are available so numerical methods are used. However, when light propagation is dominated by multiple scattering, as is the case when the medium is tissue and have an albedo close to 1, the diffusion approximation to the radiative transfer equation can be used. Here the radiance inside the diffusive medium is assumed to be almost isotropic and the diffusive radiance is approximated by the first two terms of a series expansion in spherical harmonics [40]:

$$L(\mathbf{r},\mathbf{s},t) = \frac{1}{4\pi}\Phi(\mathbf{r},t) + \frac{3}{4\pi}\mathbf{J}(\mathbf{r},t)\cdot\mathbf{s} \tag{2.5}$$

where $\Phi(\mathbf{r},t)$ is the fluence rate and $\mathbf{J}(\mathbf{r},t)$ is the current density, here defined as the net energy flow per unit area per unit time. Substituting Equation 2.5 into Equation 2.4, multiplying by $\mathbf{s}$ and integrating over the full solid angle yields:

$$\frac{\partial \mathbf{J}(\mathbf{r},t)}{c\partial t} + (\mu_a + \mu_s')\mathbf{J}(\mathbf{r},t) + \frac{1}{3}\nabla\Phi(\mathbf{r},t) = S(\mathbf{r},t) \tag{2.6}$$

Assuming that changes in the current density are small within the transport mean free time, the current density can be defined using Fick's law:

$$\mathbf{J}(\mathbf{r},t) = -D\nabla\Phi(\mathbf{r},t) \tag{2.7}$$

where D is the diffusion coefficient given by:

$$D = \frac{1}{3(\mu_a + \mu_s')} \tag{2.8}$$

Finally, the time-dependent diffusion equation can now be obtained, as a differential equation containing only $\Phi(\mathbf{r},t)$, by substituting Equation 2.7 into Equation 2.6:

$$\frac{\partial\Phi(\mathbf{r},t)}{c\partial t} + \mu_a\Phi(\mathbf{r},t) - D\nabla^2\Phi(\mathbf{r},t) = S(\mathbf{r},t) \tag{2.9}$$

In cases where continuous wave light is used one can neglect the time dependence of the diffusion equation and it reduces to:

$$-D\nabla^2\Phi(\mathbf{r}) + \mu_a\Phi(\mathbf{r}) = S(\mathbf{r}) \tag{2.10}$$

2.3 Spatially Resolved Spectroscopy

In spatially resolved spectroscopy the light attenuation is measured as a function of the distance to the light source. For a highly scattering medium, such as tissue, it will typically rely on measuring the diffuse reflected light, which is scattered multiple times and then returns back through the incident surface. In the case where the tissue is relative thick the amount of light, which will escape through the back side of the tissue, as either ballistic light or diffuse transmitted light, is negligible. In this case the incident light will either be absorbed by the tissue or diffuse reflected. The goal when using spatial resolved spectroscopy is of course to be able to link the measurements of light attenuation to optical properties of the tissue, which can then be used to derive values of the concentration of Hb and HbO in order to calculate the TOI from Equation 1.1. A number of different methods can be used to derive the TOI from a series of attenuation measurements.

In [41] a neural network was used to determine μ_a and μ_s' from spatially resolved measurements. Here, the measurements, for a given wavelength and a certain tissue oxygenation, will be a unique "fingerprint", which can then be identified. The neural network method performed faster than a traditional least square fit method, but the algorithm behind the neural network requires a lot of known data in order to return fast and precise estimations of the tissue optical properties.

In [42] a Sugeno fuzzy inference system was used to extract μ_a and μ_s' from diffuse reflectance profiles. This method increased the accuracy of both parameters but required a large number of detection spots, i.e. 46 individual spots, for measuring

the diffuse reflected light. Again, this will not be feasible for oximetry measurements where the measurement and data processing should be fast.

A simpler method is presented in [43] where an expression for the diffuse reflectance is derived from Equation 2.9. The derivation is done under the assumption that an infinitely narrow beam of photons, called a pencil beam, is perpendicularly incident on a boundary of a semi-infinite geometry, which can be seen in Figure 2.2. At the depth $z = z_0$ the light is assumed to be scattered isotropically. The distance a photon travels before it has lost its original direction is the inverse of the reduced scattering coefficient, so $z_0 = {\mu'_s}^{-1}$. For simplicity it is also assumed that there is no mismatch in the refractive index between the media on both sides of the boundary, which means that no Fresnel reflection will occur. Using these assumptions an expression for the reflectance R as a function of distance r can be derived from Equation 2.10, for the case where $r^2 \gg z_0^2$:

$$R(r) = \frac{e^{-\mu_{\text{eff}} r}}{2\pi\mu'_s r^2}\left(\mu_{\text{eff}} + \frac{1}{r}\right) \tag{2.11}$$

where:

$$\mu_{\text{eff}} = \sqrt{3\mu_a(\mu_a + \mu'_s)} \tag{2.12}$$

is the effective attenuation coefficient. A typical value of the reduced scattering coefficient, for tissue, would be $\mu'_s = 20$ cm^{-1}. In this case $z_0^2 = 0.25$ mm so $r \gg 0.5$ mm for the approximation to be valid. For the large values of r, which has already been assumed, Equation 2.11 can be simplified further by assuming that $1/r \ll \mu_{\text{eff}}$:

$$R(r) = \frac{\mu_{\text{eff}}}{2\pi\mu'_s r^2} e^{-\mu_{\text{eff}} r} \tag{2.13}$$

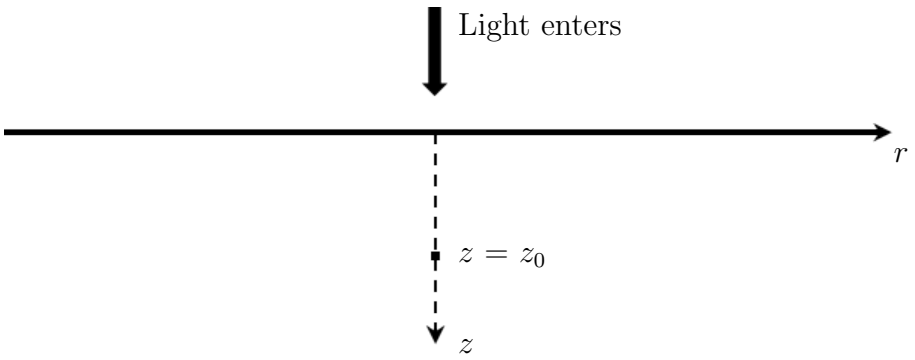

Figure 2.2: The semi-infinite geometry used for the derivation of an expression for the diffuse reflected light. The light enters at the air/tissue boundary in the point $r = 0$, $z = 0$. The light is assumed to scatter isotropically at a depth $z = z_0$.

Equation 2.13 provides an analytical expression of the diffuse reflectance and although it has been derived through a number of assumptions and simplifications it can be used to describe how the signal from a SRS sensor will behave. In Figure 2.3 the normalised diffuse reflectance is plotted for three different values of μ_a using Equation 2.13. For all three plots $g = 0.9$ and $\mu_s = 100$ cm^{-1}.

Now that an expression for the diffuse reflectance has been found it can be used to derive a method for extracting the TOI from diffuse reflection measurements performed using multiple distances and multiple wavelengths. This has been done in [30] where the attenuation $A(r)$ is defined as:

$$A(r) = -\log R(r) = -\log\left(\frac{\mu_{\text{eff}}}{2\pi\mu_s' r^2} e^{-\mu_{\text{eff}} r}\right) = -\frac{1}{\ln(10)}\left(\ln\left(\frac{\mu_{\text{eff}}}{2\pi\mu_s' r^2}\right) - \mu_{\text{eff}} r\right) \tag{2.14}$$

Differentiation of $A(r)$ with respect to r gives:

$$\frac{dA(r)}{dr} = -\frac{1}{\ln(10)}\frac{d}{dr}\left(\ln\left(\frac{\mu_{\text{eff}}}{2\pi\mu_s'}\right) + \ln\left(\frac{1}{r^2}\right) - \mu_{\text{eff}} r\right) = \frac{1}{\ln(10)}\left(\frac{2}{r} + \mu_{\text{eff}}\right) \tag{2.15}$$

A further simplification is to assume that $\mu_a + \mu_s' \approx \mu_s'$ in Equation 2.12, which then reduces the effective extinction coefficient to: $\mu_{\text{eff}} = \sqrt{3\mu_a\mu_s'}$. Furthermore, the

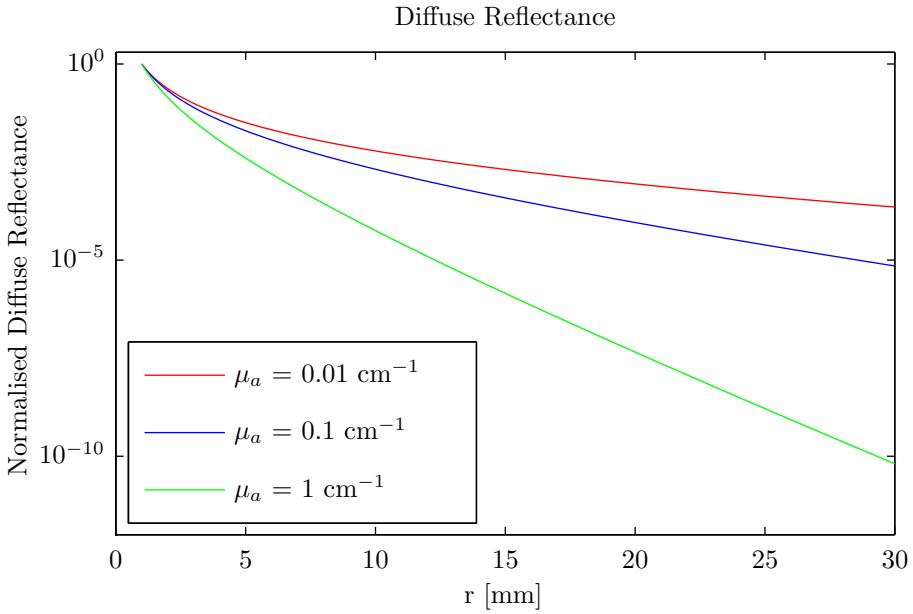

Figure 2.3: Plot of the diffuse reflectance $R(r)$ as a function of distance r from the light source. The plot shows $R(r)$ for three different values of μ_a. In all cases $g = 0.9$ and $\mu_s = 100$ cm^{-1}. The diffuse reflectance is normalised at 1 mm.

reduced scattering coefficient for most types of tissue exhibits almost no wavelength dependence in the near infrared spectrum. In [44] actual measurements performed on an adult human head showed almost no variation in reduced scattering coefficient in the wavelength interval of 700-900 nm. If μ_s' is approximated with a constant k only the absorption coefficient will be wavelength dependent $\mu_a(\lambda)$. Equation 2.15 can then be written as:

$$\frac{dA(r)}{dr} = \frac{1}{\ln(10)}\left(\sqrt{3\mu_a(\lambda)k} + \frac{2}{r}\right) \tag{2.16}$$

By measuring the attenuation $A(r)$ using several wavelengths $\mu_a(\lambda)k$ can be calculated for these different wavelengths. For a device consisting of several photo detectors this could be done by calculating the attenuation using i.e. the calibrated photo current of the detectors. The more photo detectors that are used the better the spatial resolution of the attenuation will be. What is left now is to link the absorption coefficients to the concentration of the hemoglobin components. This is done by using the known molar extinction coefficients for Hb and HbO and linking the relative concentration to the absorption coefficient:

$$\begin{bmatrix} k\mu_a(\lambda_1) \\ k\mu_a(\lambda_2) \\ \cdots \\ k\mu_a(\lambda_n) \end{bmatrix} \begin{bmatrix} \epsilon_{i,j} \end{bmatrix} = \begin{bmatrix} kC_{Hb} \\ kC_{HbO} \end{bmatrix} \tag{2.17}$$

where $\epsilon_{i,j}$ is the extinction coefficient for the i'th absorber (Hb or HbO) at the j'th wavelength. Finally, when kC_{Hb} and kC_{HbO} are calculated they can be used to determine the TOI from equation 1.1:

$$TOI = \frac{kC_{HbO}}{kC_{HbO} + kC_{Hb}} = \frac{C_{HbO}}{C_{HbO} + C_{Hb}} \tag{2.18}$$

2.4 Monte Carlo Simulations

Another approach to investigate how light and tissue will interact is to use numerical simulation by the Monte Carlo method. Here, the trajectory of a photon is modelled as a persistent random walk with the direction of each step depending on that of the previous step. If a sufficient number of photons are simulated one can estimate physical quantities such as diffuse reflectance and absorption. A clear advantage offered by Monte Carlo simulation is that results from more complex layered tissue models can more easily be achieved.

The so called MCML model, presented in [45], offers very good results when simulating light interaction with multi-layered tissue and it is freely available to

the public. A template file, containing the information about the tissue model, is compiled by the program and the results are returned to an output file. The model works by a pencil beam being perpendicularly incident on the multi-layered medium, which is defined in the input file. A schematic drawing of the tissue model is shown in Figure 2.4. Each layer is defined by: a thickness d, a refractive index n, the absorption coefficient μ_a, the scattering coefficient μ_s and the scattering anisotropy g. The layers are divided into a number of grid elements in the z and r direction.

A first approach of the MCML model is to investigate how the simulated diffuse reflectance would fit to the calculated diffuse reflectance, from Equation 2.13, for a simple one layered medium. The normalised diffuse reflectance is simulated and plotted against the analytical model and the results can be seen in Figure 2.5. The two models are seen to be consistent with each other.

Since the strength of the MCML model is to simulate the behaviour of multi layered structures it has been used to evaluate how light interacts with a model of a neonatal head. The head is modelled as a four layered structure consisting of: the skin, the skull, the cerebrospinal fluid (CSF) and finally cerebral tissue, which in reality is made up of two different layers: the gray matter and the white matter. Values for the optical parameters of the different tissue types have been found in [46–50] and can be seen in Table 2.1. The thickness of the cerebral tissue layer has been chosen to represent the case of a semi-infinite medium where the diffuse transmittance is zero, so the calculated values are the absorbance and diffuse

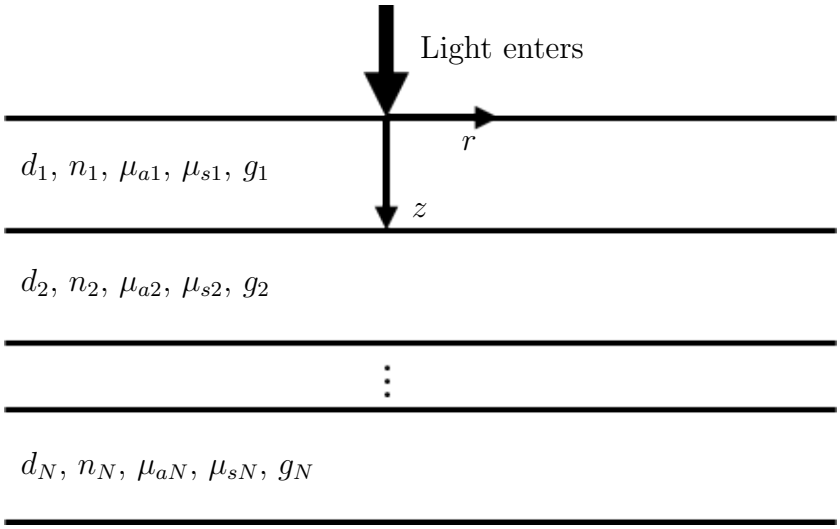

Figure 2.4: A schematic drawing of the MCML Monte Carlo tissue model. Light, in the form of a pencil beam, enters at $r = 0$, $z = 0$. The different layers in the medium are defined by a thickness d, a refractive index n, an absorption coefficient μ_a, a scattering coefficient μ_s and the scattering anisotropy g.

reflectance. Also, the MCML model calculates the specular reflectance, which is the reflectance occurring at the interface of the first layer. The photon absorption, using this tissue model, can be seen in Figure 2.6.

Some obvious weaknesses of this Monte Carlo model include that many of the tissue parameters, such as n, μ_a and μ_s, are wavelength dependent. In the case of the refractive indices and the scattering coefficients, the wavelength dependence is less significant for the spectrum of light used in NIRS. However, the absorption coefficient of the cerebral tissue will have a strong wavelength dependence due to the haemoglobin being present. The values listed in Table 2.1 are from measurements performed using light with a wavelength of 670-780 nm. To get accurate results from the model, one must enter the values of n, μ_a and μ_s for a given wavelength λ_1 and then perform the calculations. Hereafter, tissue parameters for wavelengths $\lambda_2, \lambda_3, ..., \lambda_N$ can be entered and the model solved. The cerebral tissue absorption coefficients, for a given wavelength, can also be altered to fit different levels of cerebral tissue oxygenation. The model is based on a number of flat and straight layers but in reality the head of a neonate is a curved structure, which could resemble an ellipse having a circumference of 23 to 37 cm for neonates of a gestational age of 24 to 46 weeks [51]. The CSF layer will also be entangled in the grey matter and white matter layers and therefore vary in thickness across the entire circumference of the head.

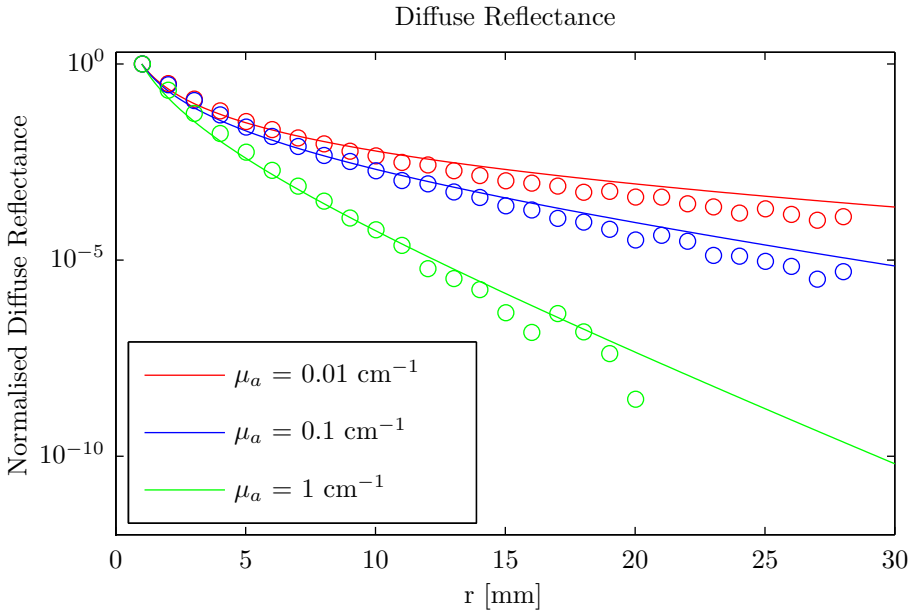

Figure 2.5: Plot of the diffuse reflectance $R(r)$ as a function of distance r from Equation 2.11 and the results from the MCML simulations. The plot shows $R(r)$ for three different values of μ_a. In all cases $g = 0.9$ and $\mu_s = 100$ cm^{-1}.

The results of running the MCML algorithm using the tissue parameters from Table 2.1 can be seen in Table 2.2. It is notable that the strong scattering properties of tissue causes 60 % of the incident photons to be diffuse reflected. In order to calculate how the diffuse reflectance will behave as a function of cerebral tissue oxygenation, a model for the absorption coefficient of the cerebral tissue must be created, for the four layered model presented earlier. In order to define this model a number of assumptions are made:

- It is assumed that only the absorption coefficient of the cerebral tissue will vary as function of wavelength and oxygenation. All other absorption coefficients are assumed constant.
- All scattering coefficients are assumed constant.
- The cerebral tissue is divided into two parts: 90 % which are cerebral matter that is unaffected by oxygenation and 10 % which are the blood present in the cerebral tissue.
- The absorption coefficient of the blood is equal to the absorption coefficient for haemoglobin weighted by the ratio of Hb and HbO

The cerebral tissue absorption coefficient $\mu_{a,MC}(\lambda, \%Hb, \%HbO)$, for the Monte Carlo simulations, can now be calculated using the following equation:

$$\mu_{a,MC}(\lambda, \%Hb, \%HbO) = 90\% \times \mu_{a,c} + 10\% \times (\%Hb \times \mu_{a,Hb}(\lambda) + \%HbO \times \mu_{a,HbO}(\lambda)) \tag{2.19}$$

where λ is the wavelength of the light, $\%Hb$ is the percentage of Hb, $\%HbO$ is the percentage of HbO, $\mu_{a,c}$ is the absorption coefficient of the cerebral matter

Tissue type	$\boldsymbol{d}$ **[mm]**	$\boldsymbol{n}$	$\boldsymbol{\mu_a}$ **[cm^{-1}]**	$\boldsymbol{\mu_s}$ **[cm^{-1}]**	$\boldsymbol{g}$
Skin	2.0	1.39	0.18	200	0.90
Skull	2.0	1.37	0.16	200	0.92
Cerebrospinal fluid	1.0	1.33	0.04	2.50	0.05
Cerebral tissue	55	1.36	0.50	100	0.86

Table 2.1: Tissue parameters for the four different layers used in the Monte Carlo model. The parameters are: thickness d in mm, refractive index n, absorption coefficient μ_a in cm^{-1}, scattering coefficient μ_s in cm^{-1} and scattering anisotropy g. The parameters are valid in the wavelength interval of 670-780 nm and for normal levels of cerebral tissue oxygenation.

that is unaffected by oxygenation, $\mu_{a,Hb}(\lambda)$ is the absorption coefficient for Hb at a specific wavelength and $\mu_{a,HbO}(\lambda)$ is the absorption coefficient for HbO at a specific wavelength. The coefficients have been entered into the Monte Carlo simulations and the resulting diffuse reflectance has been calculated for wavelengths of 700 nm, 800 nm and 900 nm, as well as for tissue oxygenations of 75 %, 80 %, 85 %, 90 %, 95 % and 100 %. The results from this simulation can be seen in Figure 2.7.

The results from the Monte Carlo simulations, performed on the presented model, show two distinct properties. First of all the diffuse reflectance will be high and account for approximately 60 % of the photons. This indicates that large

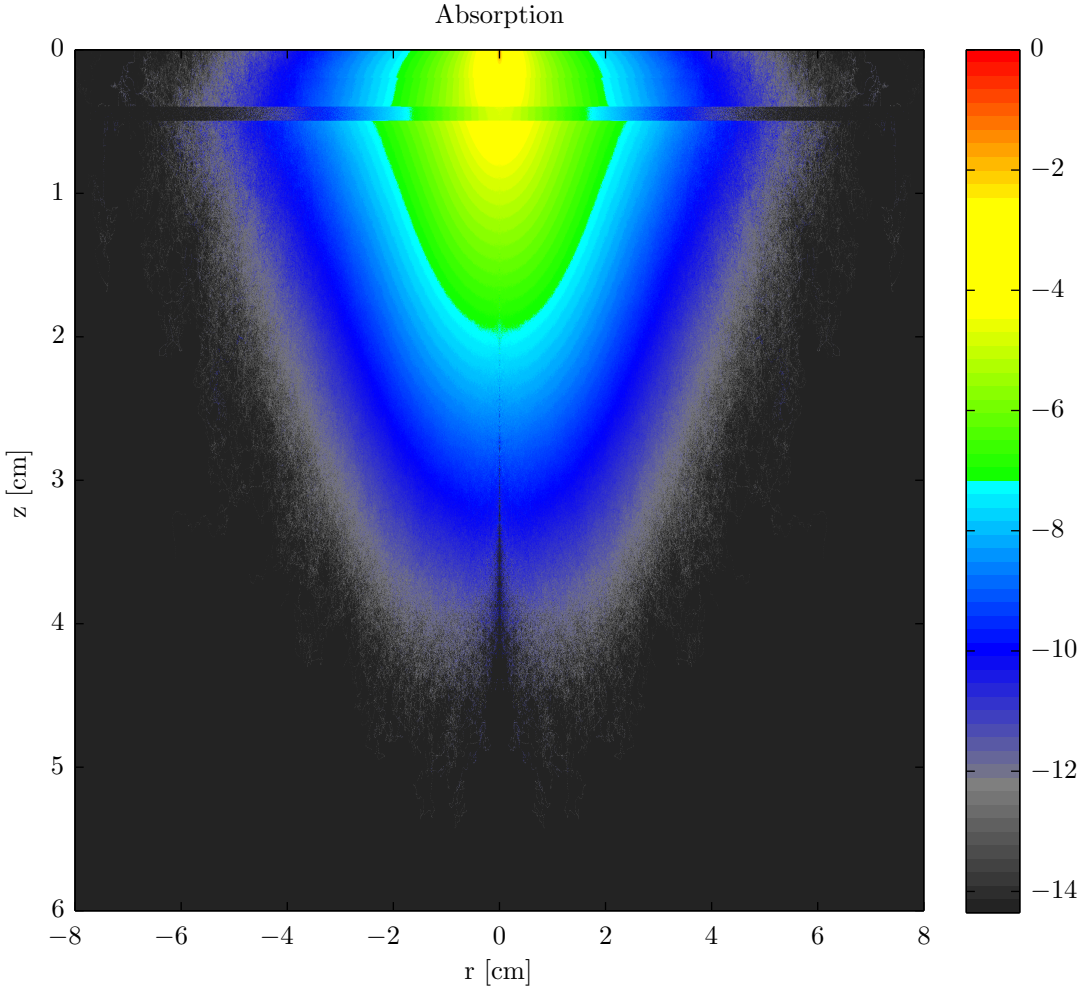

Figure 2.6: The absorption, for a Monte Carlo simulation using 10,000,000 photons, plotted as function of z and r. The calculations are done using the values listed in Table 2.1. The absorption can be seen to happen at depths of up to 5 cm, and lateral distances of up to 6 cm from the point of incidence. The colour scale shows the logarithm to the normalised absorption.

detection signals can be achieved even by using low power light sources. However, the same model shows that the change in diffuse reflectance will be very small even for relative large changes in cerebral tissue oxygenation. In order to detect these small changes in signal, high performing detectors must be used.

A tissue oximetry sensor that works using the spatially resolved spectroscopy principle will measure part of the diffuse reflected light as function of distance from the light source for a given wavelength. The Monte Carlo model can be used to predict how the signal will depend on source detector spacing by calculating how the diffuse reflectance will depend on distance to the light source. Simulations, using 700 nm light, have been performed for a cerebral tissue oxygenation of 75 % and 100 %. The result can be seen in Figure 2.8. The plots for the two different tissue

Specular reflectance	Diffuse reflectance	Absorbance	Diffuse transmittance
2.66 %	60.71 %	36.62 %	0.00 %

Table 2.2: The results when running the Monte Carlo model using the tissue parameters listed in 2.1. It can be seen that a major part of the photons will be diffuse reflected.

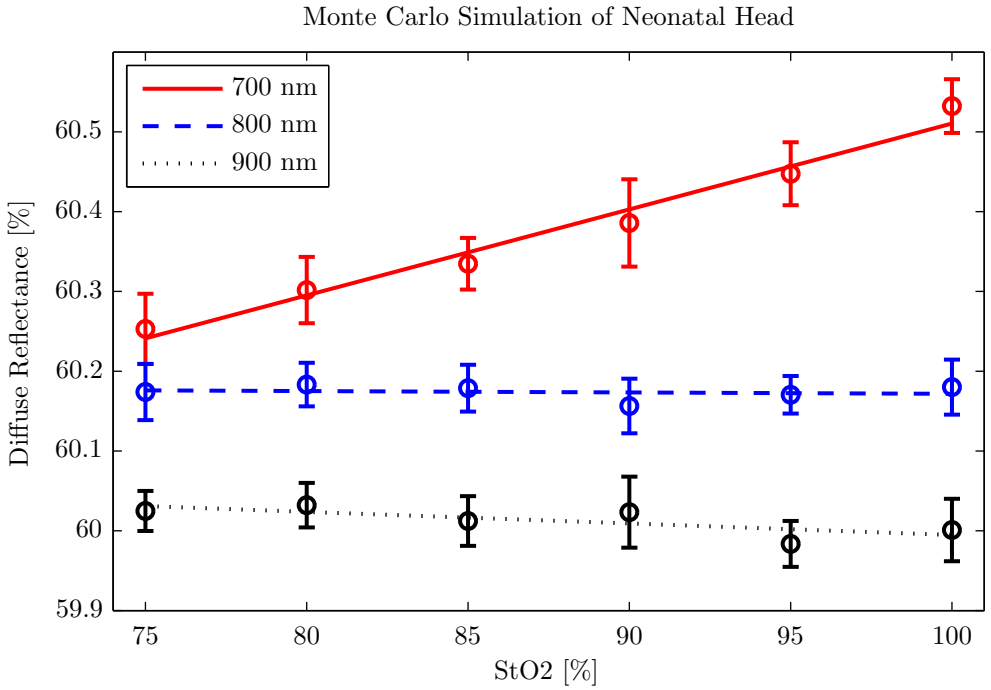

Figure 2.7: Monte Carlo simulation performed on the model of a neonatal head, here showing the diffuse reflectance as function of cerebral tissue oxygenation. The diffuse reflectance is plotted for light with a wavelength of: 700 nm, 800 nm and 900 nm and a cerebral tissue oxybenation between 75-100 %.

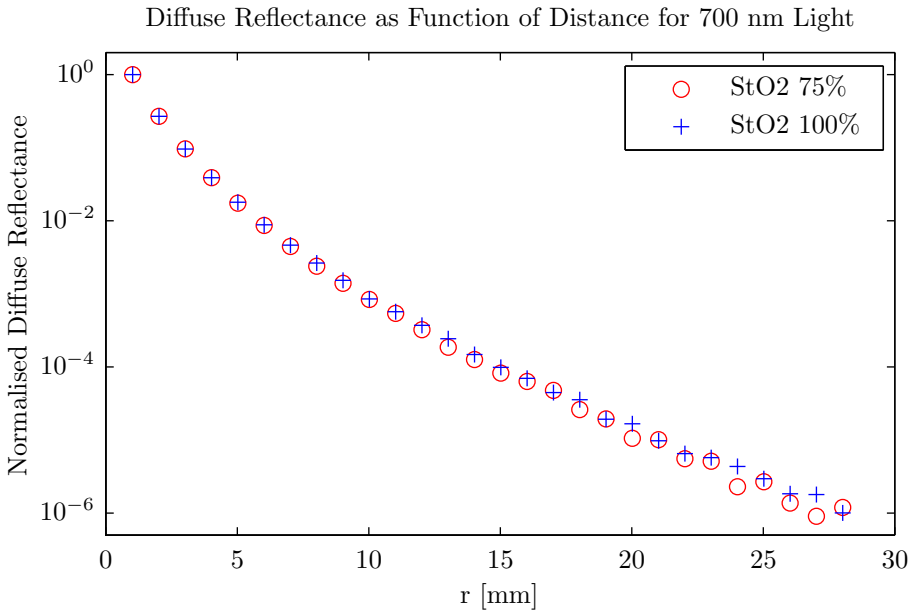

Figure 2.8: Normalised diffuse reflection plotted as function of the distance to the pencil beam. The simulation has been done using 700 nm light and a cerebral tissue oxygenation of 75 % and 100 %. The diffuse reflectance can be seen to be very semilar for the two oxygenation levels.

oxygenations can be seen to have very similar values for distances up to 10 mm. At further distances they become distinguishable, which emphasises a device design that uses multiple detectors with a large total device span.

2.5 Summary

The basic properties for light and tissue interaction were explained. Then the diffusion approximation to the radiative transfer equation was used to describe how the light would be diffuse reflected and how SRS can be used to determine the tissue oxygenation. The diffuse reflected light will be scattered isotropic after moving just a few millimetre through the tissue.

Monte Carlo simulations were performed on a model of a neonatal head. They showed that approximately 60 % of the injected light would be diffuse reflected but also that the changes in the diffuse reflected light will only be weakly dependent on the cerebral oxygenation.

Chapter 3

Design of Flexible Silicon Platforms

Silicon is an excellent material for light detection and serves as the base material for many MEMS devices. However, silicon, being both stiff and brittle, is not a flexible material when considering typical thicknesses of wafers used in the semiconductor industry. An oximetry sensor working by the spatially resolved spectroscopy method presented in Chapter 2 should be able to confine to the head of a neonate. An oximetry devices fabricated in silicon would therefore have to be made flexible enough to fulfil this design requirement.

The curvatures that are inflicted upon an oximetry sensor used on a neonate are not extreme and could in many cases be almost non-existing. However, an oximetry device should be able to be bent to an angle of 90° over the entire length of the device, i.e. a few centimetres, without any damage or wear to the electrical interconnects. This Chapter presents an analysis of how a flexible device platform can be integrated into silicon and thereby be used in the fabrication of a tissue oximetry sensor or of other devices where flexibility is a requirement.

3.1 Flexible Silicon Device Platforms

As described in Chapter 1 many different methods can be used to add flexibility to the otherwise stiff and brittle crystalline silicon used in silicon wafers. Which method that should be chosen depends on the design parameters and functionality of the final device. The oximetry devices developed in this project are all functioning by using the spatially resolved spectroscopy method. The simplest way of realising this method is to fabricate a single array of detectors, which can then detect the diffuse reflected light at different distances from the light source. If such a device is relatively narrow compared to its length it will basically just be bend in one

dimension if it is placed at a curved surface of a body part e.g. the head of an infant child or the forearm of a test subject. If the device instead has a square shape it would, for most cases, have to confine to a double curved surface when placed in contact with the skin. The advantage of a square shape would be that one could either implement a number of small detectors to this design, which can act as pixels in the oximetry measurement, or implement circular sensors, which would lead to a large signal as a maximum of light would be collected by each detector. The three different designs can be seen in Figure 3.1.

The flexibility of these devices can be achieved by making the devices either completely flexible or piecewise flexible. Since the oximetry devices utilises infrared light an amount of bulk silicon is needed in order to create detectors of high quality. The complete analysis of this problem is presented in Chapter 4 and it shows that thinning the silicon down to below 100 μm and combining this thin silicon with e.g.

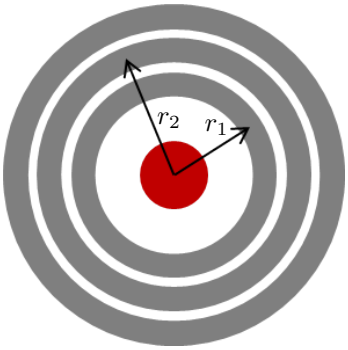

(a) *Annular device*

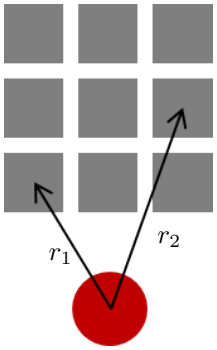

(b) *Square array device*

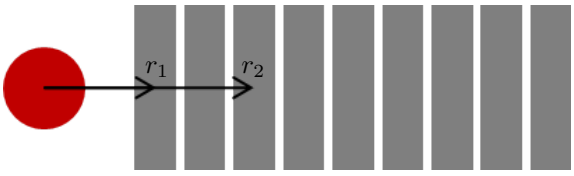

(c) *Linear array device*

Figure 3.1: Three different realisations of a flexible platform for a spatially resolved spectroscopy oximeter. Each of the devices have a number of photo detectors with different distances to the light source. In (a) a device with annular shaped detectors is shown. Such a device will have the largest sensitivity but each detector will also take up a large amount of space. Adding flexibility to this device will be difficult. In (b) a square array device is shown. This type of device will have many detectors per unit area but will also be complicated to fabricate. Finally, a linear array is shown in (c). This is a far more simple device which can have many detectors for a given device length. However, the device can only bend in one dimension.

a polymer substrate would not be a feasible solution. Instead, a piecewise flexible structure is chosen where parts of the device consist of rigid silicon detectors and other parts of flexible joints.

As previously described any bending of a flexible device containing electrical interconnects will strain the fragile interconnects. Also, the fragile interconnects will need to be protected from the outside environment. The solution of having micro cracked gold interconnects on PDMS will therefore not be feasible, because the electrodes are not encapsulated. Forming electrodes in conductive PDMS is also a promising solution but the processing of PDMS is not possible at the Danchip cleanroom facilities. Since the devices need to be in contact with the skin the solution we have chosen is to combine both PDMS and polyimide with silicon. The PDMS will make up the flexible backbone of the device and also serve as a contact surface to the skin. PDMS is both biocompatible and optical transparent for the wavelengths of interest. The silicon will serve as the individual detectors for the spatially resolved spectroscopy oximeter. Finally, the polyimide will be used to encapsulate the fragile electrical interconnects and at the same time help to reduce the strain in these interconnects when the device is bend. This is done by ensuring that the neutral axis of the system lies very close to the electrical interconnects. A schematic drawing showing the cross section of a piecewise flexible platform and a thinned down flexible platform can be seen in Figure 3.2.

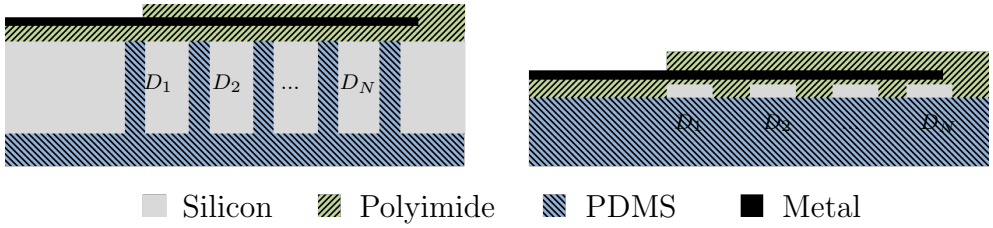

Figure 3.2: A schematic drawing showing the cross section of a piecewise flexible device (left) and a device where the silicon has been thinned down and transferred to a flexible substrate (right). The devices are made from silicon, polyimide, PDMS and metal and can contain a number of individual silicon photo detectors D_1 to D_N.

3.2 Analytical Analysis of a Flexible Silicon Device Platform

In order to investigate how strain will be distributed in the flexible joints of the linear array shown in Figure 3.1c, when it is bend in one direction, both analytical and numerical approaches can be used. The following sections will present a number

of analytical approximations as to how the placement of the neutral axis can be calculated. The models will also be used to investigate how large the strain will be in the flexible joints when the device is bend.

3.2.1 Bending of a Beam

Beam mechanics can be used as an approximation as to how the stress and strain will behave in the flexible joints of the sensor system. If a flexible joint is approximated with a homogeneous beam of material the stress and strain in the joint can be described as function of the radius of curvature [52]. The longitudinal strain ϵ_x is given by:

$$\epsilon_x = \frac{z}{r} \tag{3.1}$$

where z is the distance from the center line of the beam and r is the radius of curvature. At $z = 0$ there will be no longitudinal strain and this line is therefore called the neutral axis. The longitudinal stress in the beam, σ_x, will be linked to the strain by Hook's law:

$$\sigma_x = \epsilon_x E = \frac{zE}{r} \tag{3.2}$$

where E is Young's modulus. Again, there will also be no longitudinal stress at the neutral axis when the beam is bend. By placing the electrical interconnects at the neutral axis of a flexible joint any longitudinal strain or stress can be avoided in these interconnects.

3.2.2 Bending of a Composite Beam

The neutral axis will not in all cases be placed at the center line of a beam. In order to investigate how the placement of the neutral axis will depend on the materials that make up the flexible joints on the device, further knowledge from structural mechanics can be used. If the flexible joints are now approximated with a composite beam complete analytical solutions can be found. In this project the joints will be made of PDMS and polyimide, with the very thin metal conductors placed in the polyimide. The metal conductors will typically have a thickness of a few hundred of nanometres, whereas the PDMS and polyimide layers will have a combined thickness in the same order of the silicon wafer, i.e. a few hundred of micrometers. The metal conductors can therefore be omitted in the analytical analysis of the neutral axis. Therefore, the problem reduces to a composite beam consisting of only two materials. The problem is defined in Figure 3.3. Here a beam is made up of two different materials with thicknesses H_1 and H_2 and Young's moduli E_1 and E_2. The

distances from the edges of the two materials to the neutral axis are denoted d_1 and d_2 respectively. The placement of the neutral axis can be calculated for such a structure, which has been done in [53]. The result is two equations defining d_1 and d_2:

$$d_1 = \frac{1}{2}\frac{E_1H_1^2 + E_2H_2^2 + 2E_2H_1H_2}{E_1H_1 + E_2H_2} \tag{3.3}$$

$$d_2 = \frac{1}{2}\frac{E_1H_1^2 + E_2H_2^2 + 2E_1H_1H_2}{E_1H_1 + E_2H_2} \tag{3.4}$$

The distance from the interface of the two materials to the neutral axis, d_{NA}, can be found by subtracting d_1 from H_1:

$$d_{NA} = H_1 - d_1 = \frac{1}{2}\frac{E_1H_1^2 - E_2H_2^2}{E_1H_1 + E_2H_2} \tag{3.5}$$

Equation 3.5 can now be used to plot the position of the neutral axis as a function of the thickness of the polyimide for the PDMS/polyimide beam using Young's moduli of: $E_{\text{PDMS}} = 1$ MPa and $E_{\text{Polyimide}} = 2.2$ GPa. The results can be seen in Figure 3.4 for three different thicknesses of PDMS, i.e. 300 μm, 400 μm and 500 μm. In all cases the neutral axis will be positioned at the interface for polyimide thicknesses of 5-10 μm. Thicker layers of polyimide will draw the neutral axis into the polyimide and for thicknesses larger than 20 μm the neutral axis will be very close to the center line of the polyimide.

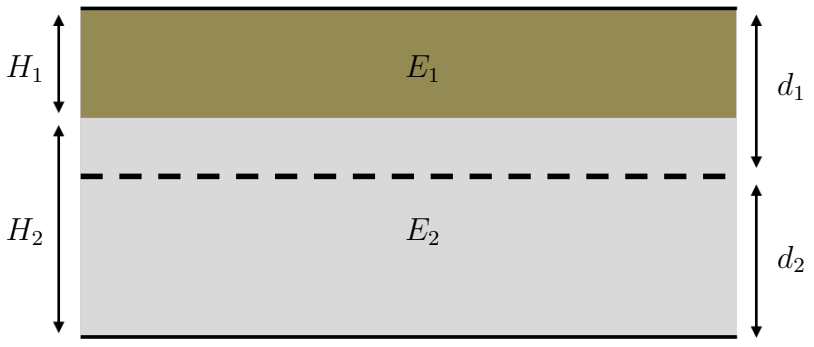

Figure 3.3: A Schematic drawing of a composite beam made up of two different materials. The thicknesses of the materials are H_1 and H_2 and the Young's moduli are E_1 and E_2. The distances from the edges of the two materials to the neutral axis (dashed line) are d_1 and d_2.

3.2.3 Bending of a Piecewise Flexible Structure

Although the electrical interconnects can be placed at the neutral axis so strain is avoided, the other parts of the joints will still experience longitudinal strain when the device is bend. Furthermore, it is likely that there will be an offset in the placement of the electrical interconnects with respect to the neutral axis, which means that they will experience strain when the joints are bend. An analysis of the strain in the different materials of the joints is presented here. The joints in the devices will ensure that they will be flexible but the devices will also consist of non-flexible silicon areas. When a device is confined to a curved surface it will therefore only bend at the joints. This will make the devices a piecewise flexible system. In order to investigate the level of strain that will be present in the polyimide and PDMS a model for a piecewise flexible structure must be defined. The structure of length L is assumed to be made up of N segments. Each segment consists of a rigid silicon part of length A and a flexible joint of length B, as can be seen in Figure 3.5. If the structure is bend it will span over an angle θ given by:

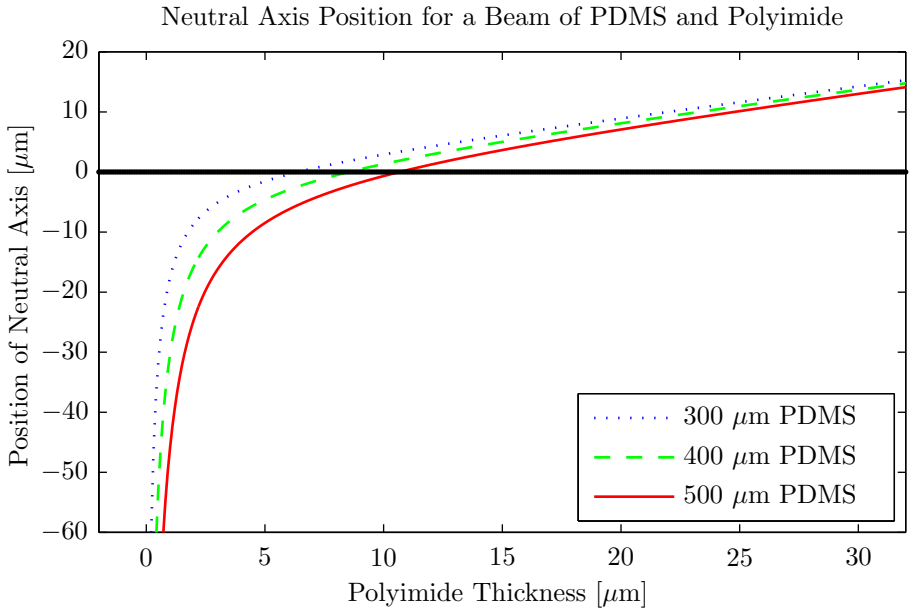

Figure 3.4: The position of the neutral axis as a function of polyimide thickness for three different thicknesses of PDMS. Negative values will place the neutral axis in the PDMS and positive values will place it in the polyimide. In all cases the neutral axis will be positioned close to the interface for polyimide thicknesses of 5-10 μm. Thicker layers of polyimide will draw the neutral axis into the polyimide and for thicknesses larger than 20 μm the neutral axis will be very close to the center line of the polyimide.

$$\theta = \frac{L}{R} = \frac{N(A+B)}{R} \tag{3.6}$$

Assuming that the structure is bend uniformly in the N sections each joint will span an angle, ϕ, of:

$$\phi = \frac{\theta}{N} \tag{3.7}$$

The radius of curvature for a joint, r, is given by:

$$r = \frac{B}{\phi} = \frac{BN}{\theta} = \frac{RB}{A+B} \tag{3.8}$$

By inserting this value of the radius of curvature into Equation 3.1 the strain in the flexible joints can be defined:

$$\epsilon = \frac{z}{r} = \frac{z(A+B)}{RB} = \frac{z}{R}\left(1 + \frac{A}{B}\right) \tag{3.9}$$

Equation 3.9 will of course not make sense for all values of R. Due to the piecewise flexibility of the structure the length of the silicon parts A will define how small a radius of curvature the structure can be conformed to while still making the model valid. We will therefore only consider the model valid for devices where $A \leq 5$ mm and $R \geq A/B$.

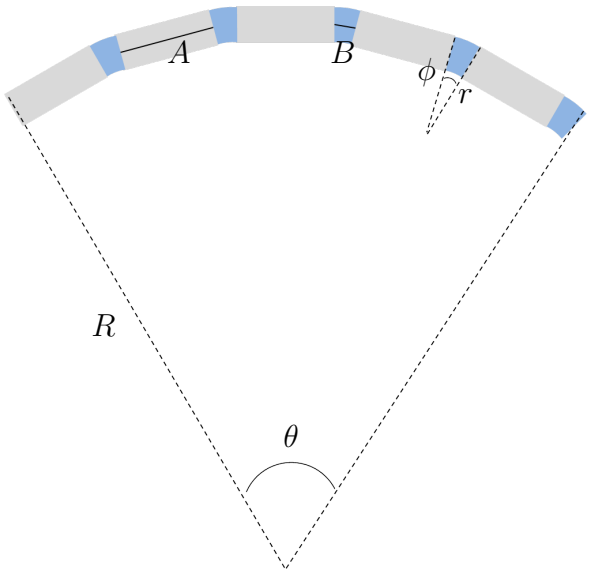

Figure 3.5: A model for a piecewise flexible structure consisting of rigid silicon parts of length A and flexible joints of length B, here shown for $N = 5$. The structure has a total length of $L = N(A+B)$. The structure is bend to a radius of curvature R which causes the individual joints to be bend to a radius of curvature r.

The maximum strain, both compressive and tensile, will be located at the edges of the materials. Using Equations 3.3 and 3.4, which define the distances from the neutral axis to the edges of the materials, the maximum strain for the polyimide and PDMS can be calculated, by inserting these equations in Equation 3.9:

$$\epsilon_{\text{polyimide,max}} = \frac{(E_1 H_1^2 + E_2 H_2^2 + 2E_2 H_1 H_2)}{2R(E_1 H_1 + E_2 H_2)} \left(1 + \frac{A}{B}\right) \tag{3.10}$$

$$\epsilon_{\text{PDMS,max}} = \frac{(E_1 H_1^2 + E_2 H_2^2 + 2E_1 H_1 H_2)}{2R(E_1 H_1 + E_2 H_2)} \left(1 + \frac{A}{B}\right) \tag{3.11}$$

where, in this case, H_1 and E_1 are the thickness and Young's modulus for the polyimide and H_2 and E_2 are the thickness and Young's modulus for the PDMS.

The maximum strain for the two materials are plotted in Figure 3.6 and 3.7 as a function of radius of curvature for the piecewise flexible structure and for different ratios of A and B. In all cases the thickness of the polyimide is 20 μm and the thickness of the PDMS is 350 μm. The thickness of the PDMS resembles the typical thickness of silicon wafers used for actual devices.

The maximum strain in the polyimide can be seen to be below 2 % for all designs, when $R \geq A/B$. Polyimides can take strains of up to 80-100 % depending

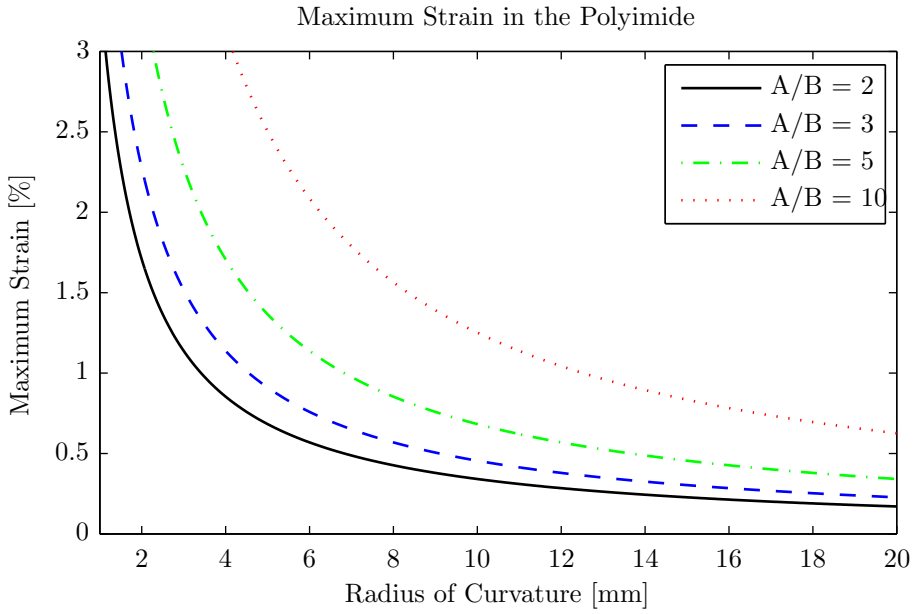

Figure 3.6: The maximum strain in the polyimide calculated for a flexible joint consisting of 20 μm thick polyimide and 350 μm thich PDMS. The maximum strain is plotted for several length ratios of the rigid silicon parts and the flexible joints. The maximum strain can be seen to be below 2 % for all designs, when $R \geq A/B$.

on the type and the curing process, which is far higher than needed. In the case with the PDMS the strain will under normal use of the silicon device platform be compressive. But if the device was bent in the opposite direction it will result in tensile strain. The strain in the PDMS is seen to be larger and will be below 30 % for all designs and $R \geq A/B$. A typical value of fracture strain for PDMS is 400 %, which again is larger than needed.

Regarding the placement of the electrical interconnects relative to the neutral axis a beam approximation consisting of three materials will be to complex as a model for the flexible joints. However, the metal used to form the electrical interconnects will only have a thickness of a few hundred nanometer, and although the Young's modulus for metals is much larger than for polyimide, the metal layer can, as an approximation, be ignored in the analysis. In [54] it was determined that free standing metal structures used in MEMS had a fracture strain of approximately 0.6-1.3 % depending of the ductility of the metal, with Au typically having values of 0.9-1.3 %. During fabrication the thickness of the polyimide cannot be completely controlled. Therefore, it must be expected that the electrical interconnects are not placed exactly at the neutral axis. A displacement of the electrical interconnects from the neutral axis should therefore not result in a strain larger than 0.5 % in order to ensure that they will not break.

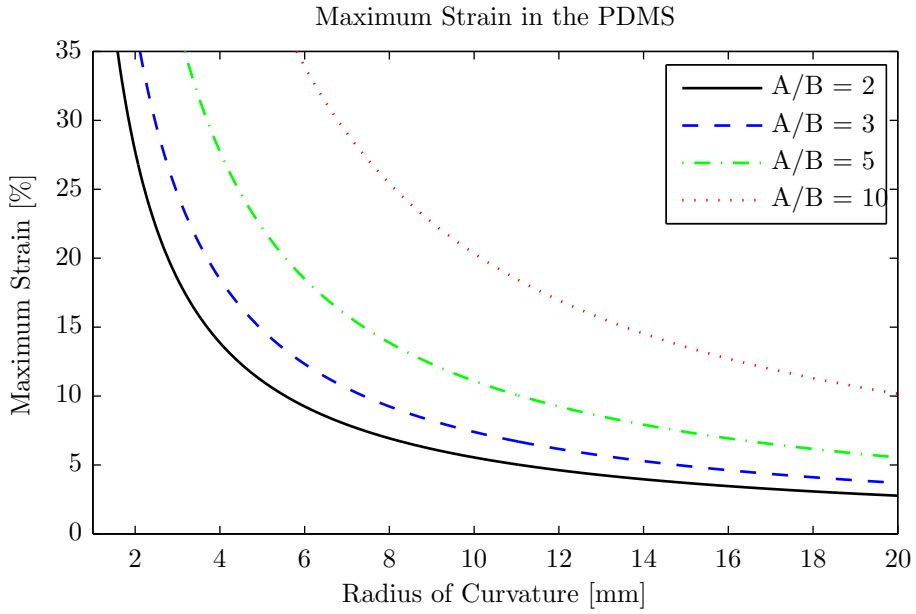

Figure 3.7: The maximum strain in the PDMS calculated for a flexible joint consisting of 20 μm polyimide and 350 μm PDMS. The maximum strain is plotted for several length ratios of the rigid silicon parts and the flexible joints. The maximum strain can be seen to be below 30 % for all designs, when $R \geq A/B$.

In the analysis presented above a flexible joint composed of 350 μm PDMS and 20 μm polyimide was investigated. This joint will have a neutral axis that is placed in the polyimide 8.9 μm from the interface between the PDMS and polyimide. If the electrical interconnects are placed halfway between the neutral axis and the top of the polyimide instead of directly at the neutral axis, this will place them at approximately 14.5 μm above the PDMS and polyimide interface and 5.5 μm above the neutral axis, they will experience a longitudinal strain when the piecewise flexible structure is bend. The strain, as function of radii of curvature, can be seen in Figure 3.8. In order not to exceed the 0.5 % strain level a piecewise flexible device should not be bent to a radius of curvature below 4 mm for an A/B value of 2 and not below a radius of curvature of 13 mm for an A/B value of 10. One design criteria for the flexible platform is that it can be bend to 90° over its full length, i.e. θ in Figure 3.5 should be 90°. The radius of curvature for a device with a flexible length of 25 mm bend to 90° will be 15.9 mm. For all combinations of A/B up to a value of 10 the electrical interconnect will not experience a strain larger than 0.5 %, even though they are displaced from the neutral axis by 5.5 μm.

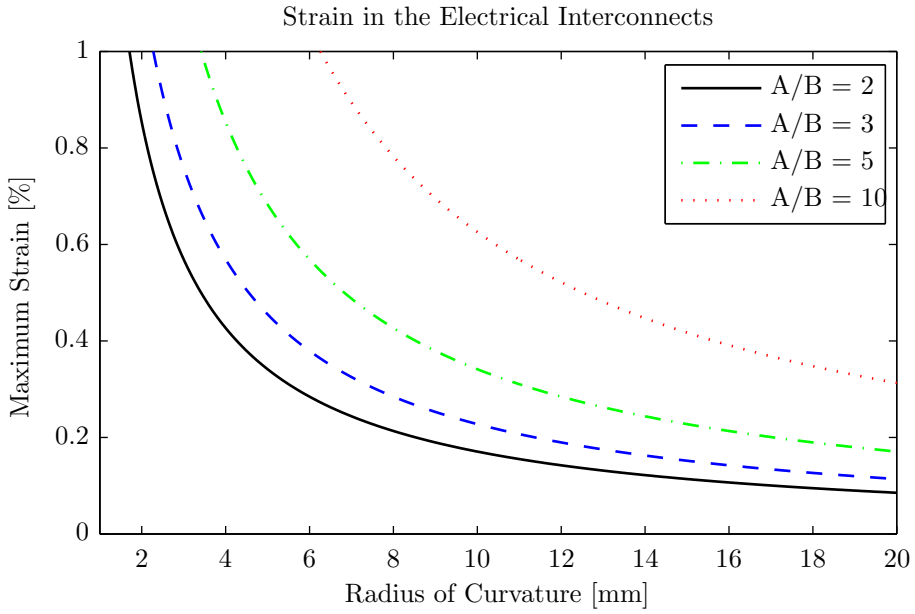

Figure 3.8: The strain in the electrical interconnects as a function of radius of curvature. The calculations are made from a piecewise flexible structure with flexible joints consisting of 350 μm PDMS and 20 μm polyimide. The electrical interconnects have been displaced from the neutral axis by 5.5 μm and are therefore subjected to tensile strain when the device is being bend.

3.3 Finite Element Analysis

The simplified model, where the flexible joints are treated as beams, can be used to give estimations regarding the thickness of polyimide needed to place the metal conductors in the neutral axis and how much the materials will be strained when the device is bend. However, the true design of the flexible joints are more complicated than a simple beam structure. The beam model does not take any edge effects into account and will therefore not show changes in the placement of the neutral axis near the silicon interface. Also, the real flexible design has a skin contact layer of PDMS beneath the silicon, which will effect the stress and strain in the joint when it is bend. In order to give a broader picture of the stress and strain for the flexible structure, the finite element method (FEM) analysis program COMSOL 4.3 has been used to model the design.

The model used for the FEM analysis is a 2D representation of a single flexible joint between two silicon blocks. The structure is similar to the one shown in Figure 3.2 and is composed of 350 μm thick silicon with a 100 μm thick PDMS layer on one side and a 20 μm thick polyimide layer on the other side. The thickness of the silicon resembles the typical thickness of silicon wafers used for actual devices. The width of the silicon blocks are 1 mm and the width of the PDMS in the flexible joint is 200 μm.

In order to model the bending of the structure, the bending is interpreted as a moment applied on each end of the silicon blocks. This is accomplished by forcing a rotation around the inward corners of both silicon domains, point B and C in Figure 3.9. Since the PDMS can contract, the two corners should be free to move in the

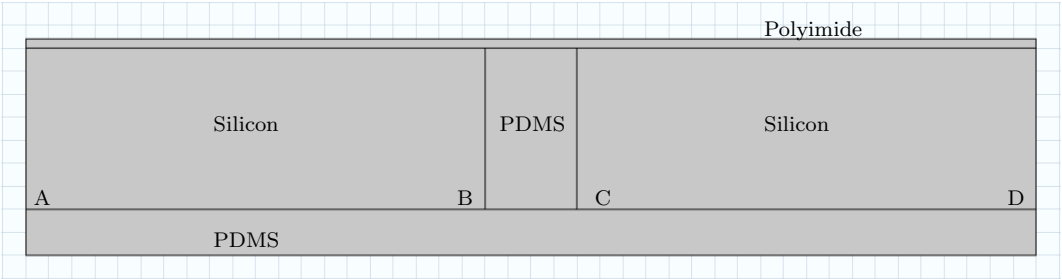

Figure 3.9: The 2D model of a single flexible joint used for COMSOL simulations. The model is made up of Silicon, PDMS and polyimide. The thin electrical interconnect is omitted because its influence on the structure would be insignificant. The dimension of the structures are 1 mm × 350 µm for the silicon blocks, 200 µm × 350 µm for the PDMS joint, 2.2 mm × 100 µm for the bottom PDMS layer and finally 2.2 mm × 20 µm for the polyimide. The points A, B, C and D are used to model a bending of the device as B and C are kept static in the y-direction, whereas A and D can move.

x-direction but fixed in the y-direction. In COMSOL, the prescribed displacement point function is used for semi-fixed points. At point B and C the displacement in the y-direction is set to zero. At point A and D the displacement in the y-direction is set to a negative value. This will bend the ends of the structure downwards. An example of simulated strain can be seen in Figure 3.10.

By varying the thickness of the polyimide layer for the COMSOL model and investigating where the strain in the polyimide is zero the neutral axis for this model can be determined as function of polyimide thickness. The result of the simulation can be seen in Figure 3.11. The figure also shows the analytical solution, from Equation 3.5, to the placement of the neutral axis for composite beams with 350 μm and 450 μm thick PDMS. The thickness of the PDMS, in the two analytical results, is chosen to resemble the thickness of PDMS between the silicon blocks and the total thickness of the flexible joint for the COMSOL model.

It can be seen that the results from the simulations using the COMSOL model differs from the analytical solutions of the two beams. The COMSOL simulation indicates that the neutral axis will be at the PDMS and polyimide interface for a thinner layer of polyimide than for the solutions from the analytical model. For a polyimide thickness between 10 μm and 30 μm the COMSOL simulation result is

Property	Silicon	PDMS	Polyimide
Density [kg/m^3]	2329	970	1300
Young's modulus [Pa]	170×10^9	1×10^6	2.2×10^9
Poisson's ratio	0.28	0.49	0.34

Table 3.1: The material parameters for the silicon, PDMS and polyimide, which are used in the COMSOL model. The PDMS and polyimide values are from the material data sheets for Sylgard 184 and HD-8820 respectively.

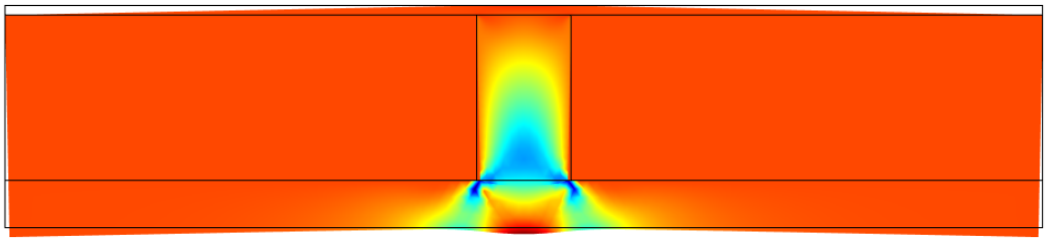

Figure 3.10: The model of the flexible joint design where the outer corners are displaced downwards. The color indicates the amount of strain the model is subjected to during bending. Red indicates expansion, yellow and blue indicates compression, and orange indicates no strain. It can be seen that the majority of the strain is confined to the soft PDMS near the flexible joint.

in better agreement with the analytical results. Regardless of how the placement of the neutral axis is modelled, placing the electrical interconnects between two layers of 10 μm of polyimide will reduce the longitudinal strain to a minimum.

Finally, the edge effects for the flexible joints are investigated by simulating the strain in the center line of the polyimide when the COMSOL model is bend to a radius of curvature of 7.5 mm. The center line for the 20 μm thick polyimide is of course located 10 μm from the PDMS and polyimide interface. The result can be seen in Figure 3.12. The flexible joint is located between 1 mm and 1.2 mm and the two silicon blocks are located outside this interval. The strain in the polyimide can be seen to be largest across the center part of the flexible joint with a value of 0.47 %. The reason why we see a strain is because the neutral axis is placed somewhat below the center line of the polyimide. Near the silicon edges the strain gradually decreases and eventually becomes insignificant about 100 μm into the silicon blocks. Since the strain will be largest at the center part of the flexible joint the maximum strain can be estimated by the analytical model presented in Section 3.2.3.

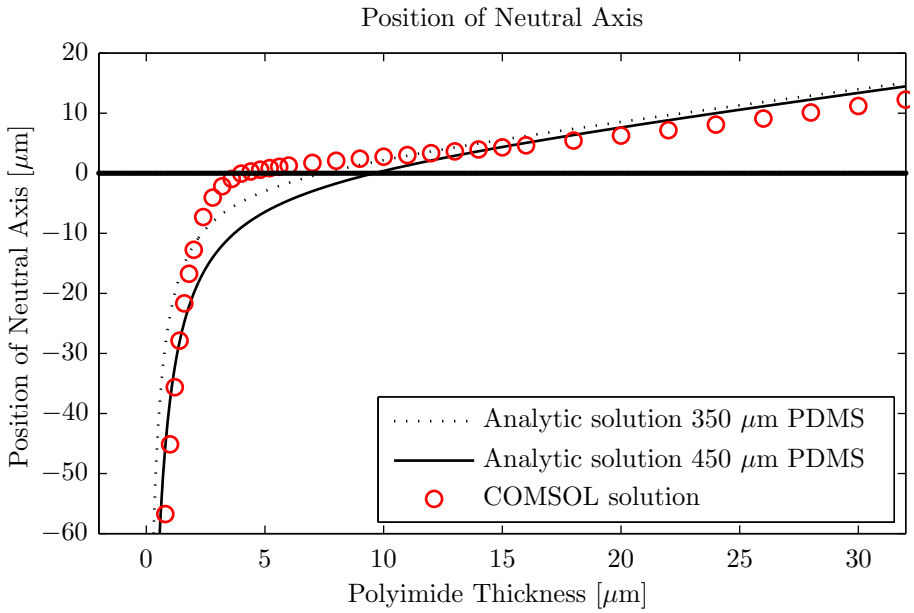

Figure 3.11: Comparison of the results from the analytical model for the neutral axis of a composite beam and the COMSOL simulations performed on the model shown in Figure 3.9. The neutral axis position is, for the COMSOL model, found at the centre of the flexible joint. For thin layers of polyimide the COMSOL model does not show the same results as the analytical solution of composite beams with 350 μm and 450 μm thick PDMS. However, for polyimide layer thicker than 10 μm the COMSOL model is in better agreement with the analytical composite beam model.

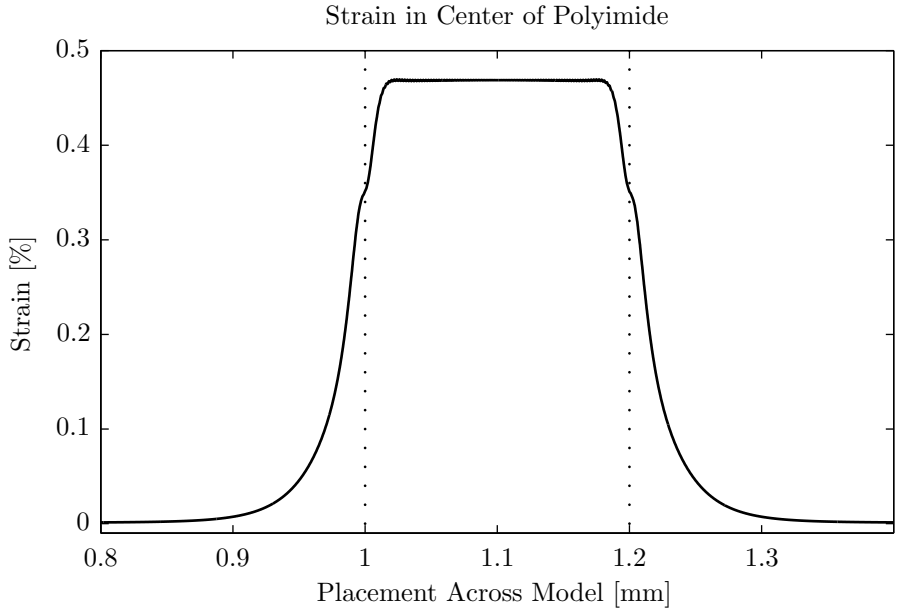

Figure 3.12: The longitudinal strain at the center line of the 20 µm polyimide as a function of distance across the model when it is bend. The edges between the flexible joint and the silicon blocks are located at 1 mm and 1.2 mm. The strain can be seen to be largest at the center part of the flexible joint and then gradually reducing in magnitude towards the silicon blocks, but still extent into the polyimide on the silicon blocks. In this simulation the model is bend to a radius of curvature of 7.5 mm.

3.4 Considerations for a 2D Square Matrix Flexible Silicon Platform

The 2D flexible silicon platform, which was shown i Figure 3.1b would essentially behave exactly as the linear array, if it was being bent in only one direction. Such a device could therefore also be fabricated, if it was only intended for use on a single curved surface. If the square array device was bent on a double curved surface, e.g. a spherical surface, the models for strain would no longer be applicable. If the device was bent on a spherical surface the square silicon parts would be displaced from each other relative to their neutral positions. This means that the materials in the flexible joints, including the electrical interconnect, would be subjected to both longitudinal, and transverse straining. Since the electrical interconnects can sustain some strain it is possible that a 2D device could be bent mainly in one direction and then partially in the other direction without destroying the electrical interconnects.

3.5 Discussion of the Models

Although the analytical models contain many details on how to describe the placement of the neutral axis or calculate the strain, they are still only approximations to the real problem. The models only describe the longitudinal strain as function of placement z. The model does not take the Poisson contraction into account, which might be of great importance, moreover, there is a large difference in the Poissons ratio for polyimide and PDMS. The model does not either consider any build-in stresses in the materials. Both polyimide and PDMS will have to be cured in order to be finalised and this process will introduce some stress into the materials. Finally, the composite beam model considers a beam made of two different materials that adhere perfectly to each other. In reality, polyimide and PDMS will adhere to each other, as can be seen from Chapter 6, but the adhesion is not strong.

The FEM model gives a better estimate of how the real flexible joints will perform, since it uses a flexible joint design that is closer to the real problem and takes the Poisson contraction into account. The FEM model, however, also suffers from some of the same simplicities as the analytical model because it to does not take build-in stresses and adhesion into account. The only way to get a complete understanding of the performance of the flexible silicon device platforms will be to test them when they are fabricated.

3.6 Summary

An outline for a flexible silicon device platform was presented. Beam mechanics were used to model how the neutral axis would be placed for a flexible joint consisting of PDMS and polyimide. An analytical model for a piecewise flexible structure was derived and used together with the beam mechanics. In this way the maximum strain in the different materials could be calculated when the devices are bend and the strain was found to be acceptable.

FEM simulations were used to model the strain and placement of the neutral axis for a complete model of the flexible joints. The analysis concluded that the proposed flexible platform design was feasible.

Chapter 4

Design of Infrared Detectors

The flexible platforms presented in Chapter 3 can easily be transformed into a light detection device by formation of pn-junction photo diodes in the silicon. However, the conclusion from the analysis of this design is that the electrical interconnects will all have to be placed at one side of the device in order to ensure that they follow the neutral axis and moreover avoid to obscure for the light. A pn-junction photo diode is typically contacted at both surfaces of the substrate with the depletion region formed close to the surface that the photons are incident upon. The absorption of the photons will then create electron-hole pairs, which for such a pn-junction photo diode, will happen close to or in the depletion region.

A backside pn-junction photo diode has all the electrical interconnects placed on the opposite surface upon which the light is incident. This causes the depletion region to be formed away from the main photon absorption volume and the electron-hole pairs are therefore generated in the bulk of the silicon. A schematic drawing of both types of photo diodes can be seen in Figure 4.1. In [55] backside photo diodes of high performance were successfully fabricated at the Danchip cleanroom facilities.

This chapter will present analytical analysis and simulations of the performance of backside photo diodes. The analysis about light in tissue, which was presented in Chapter 2, showed that the changes in diffuse reflected light, due to changes in cerebral oxygenation, were very small. In order to detect these small variations the photo diodes in the tissue oximetry device must be of high quality.

4.1 Backside Photo Diode

The pn-junction photo diode functions as a standard pn-junction. Thus, when it is exposed to light it can generate a current, which can be detected by an external circuit. An absorbed photon will generate an electron-hole pair. For a p-type substrate the electron will be the minority carrier and it will diffuse around in the

bulk of the silicon. If it does not recombine it may eventually reach the pn-junction near the back side. Here, it will be swept across the depletion region due to the electrical field and cause an increase in current known as the photo current. If the pn-junction is placed in reverse bias the total current, I, will be:

$$I = -I_P - I_R \tag{4.1}$$

where I_P is the photo current and I_R is the reverse bias current, also refereed to as the dark current. Since the photo current will carry the signal from the probed tissue it will have to be so significant that it can suppress any noise on the signal and also large enough to ensure that any change in photo current, caused by a change in tissue oxygenation, will be detectable when comparing it to the reverse bias current. The optimal design goal for making high quality photo detectors will therefore be to maximise the photo current and minimise the reverse bias current.

The reverse bias current will depend on a number of factors. An ideal pn-junction diode can be described by the Shockley equation [56]:

$$I = I_S \left[\exp\left(\frac{qV}{kT}\right) - 1 \right] \tag{4.2}$$

where I_S is the saturation current, q is the elementary charge, V is the applied voltage, k is the Boltzmann constant and T is the temperature. When the diode is put in reverse bias we will essentially just have: $I \approx -I_S$. However, the ideal diode is only possible in theory and a real pn-junction diode will have other current contributions, besides the saturation current, when put in reverse bias. The total

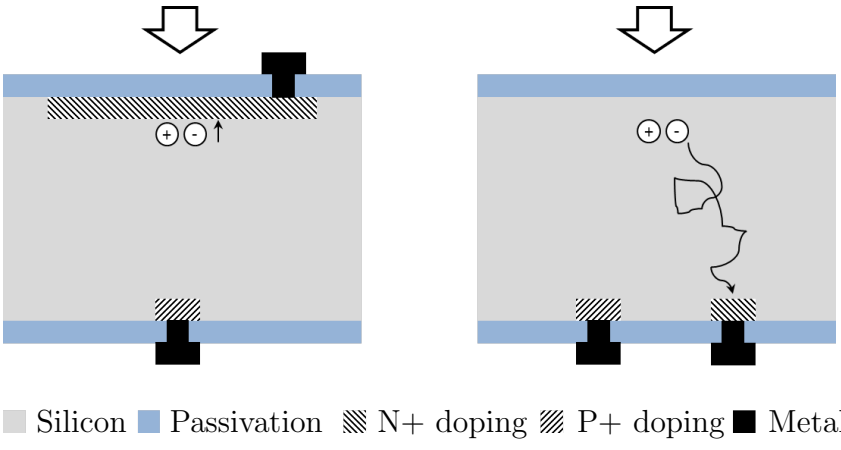

Figure 4.1: Schematic drawing of a normal photo diode (left), which has electrical contacts placed on both sides of the substrate and a backside photo diode (right), which has the electrical contacts on the same side of the substrate. The diodes are here shown for a p-type silicon substrate.

reverse bias current will be a sum of the saturation current and a generation current where the current is generated in the depletion region and by defects and surface effects [57]. The reverse bias current will, unlike, the saturation current not be almost constant but will increase slightly as function of the applied voltage until the diode reaches reverse bias breakdown. Using high quality silicon and surface passivation will be the best way to ensure a low reverse bias current.

What governs the ability of a photo diode to generate photo current can be described by the photo diode area, A, the photon flux, $\Phi(\lambda)$, and the quantum efficiency, $\eta(\lambda)$:

$$I_P = qA \int_{\lambda_1}^{\lambda_n} \Phi(\lambda)\eta(\lambda)d\lambda \tag{4.3}$$

where q is the elementary charge. In order to maximise the photo current the individual terms of Equation 4.3 should be maximised within the limits set up by the design. The detector area will be limited by the flexibility of the final devices as an increase in the size of the non-flexible silicon will decrease the flexibility of the piecewise flexible device, as described in Chapter 3. The incident photon rate is determined by the light source used to probe the tissue. The more photons that are injected into the tissue the more photons will be diffuse reflected and incident on the detector surface. This value is of course limited by the amount of power, which can safely be injected into the tissue. NIRS devices used on neonates will typically have LEDs or laser diodes emitting below 5 mW of power. The parameter that can be used to improve the photo current through design and fabrication is therefore the quantum efficiency.

4.2 Quantum Efficiency

The quantum efficiency simply defines the amount of incident photons that will contribute to the photo current and it is dependent on the wavelength of the light. It is also called the external quantum efficiency because it takes all incident photons into account. The internal quantum efficiency (IQE), η_{int}, defines the amount of photons that have entered the semiconductor and contributes to the photo current. The relation between the two definitions is given by [58]:

$$\eta(\lambda) = T(\lambda)\eta_{int}(\lambda) = [1 - R(\lambda)]\eta_{int}(\lambda) \tag{4.4}$$

Here, $T(\lambda)$ is the wavelength dependent transmittance and $R(\lambda)$ is the wavelength dependent reflectance. The external quantum efficiency can therefore be improved by increasing the transmittance (lowering the reflectance) and increasing the internal quantum efficiency of the semiconductor.

4.2.1 Internal Quantum Efficiency

There are many different models and assumptions that can be used when describing the internal quantum efficiency of a semiconductor. When looking at how light is absorbed in the silicon Beer-Lamberts law can be used as a first approximation. It simply states that the intensity of light passing through a medium will decrease exponentially as a function of the absorption coefficient and the thickness of the medium. By assuming that all absorbed light will contribute to the photo current the internal quantum efficiency can therefore be described as:

$$\eta_{int}(\lambda) = [1 - \exp(-\mu_a(\lambda)d)] \tag{4.5}$$

where d is the thickness of the medium. Estimation of the internal quantum efficiency can now be found as a function of device thickness using the absorption spectra for silicon. The absorption spectrum for silicon is plotted in Figure 4.2a and the device thickness needed to obtain a given internal quantum efficiency can be seen in Figure 4.2. It shows that the needed device thickness depends strongly on the wavelength of the light.

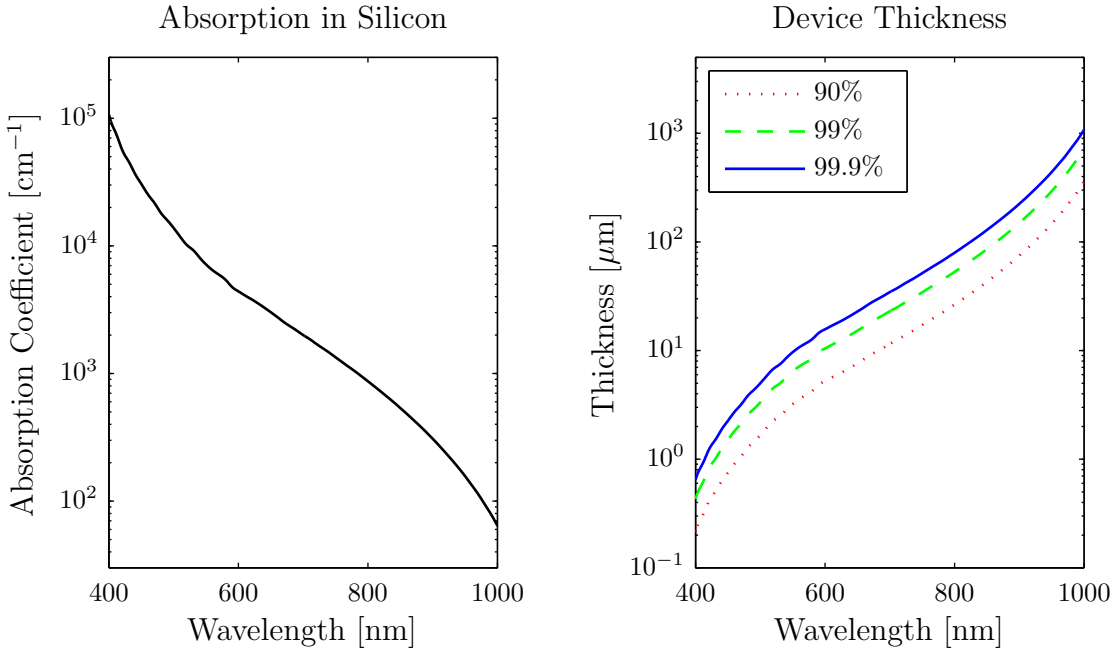

(a) *Absorption spectra for silicon [59]*

(b) *Absorption thickness*

Figure 4.2: The absorption behaviour of silicon as a function of wavelength. In (a) the absorption spectrum for silicon is shown. In (b) the thickness of silicon needed to absorb 90 %, 99 % and 99.9 % of the light is plotted as a function of wavelength of the light. It can be seen to be strongly dependent on the wavelength of the light.

LED wavelength [nm]	660	740	810	940
$QE_{90\%}$ Thickness [μm]	8.3	15.8	29.1	127
$QE_{99\%}$ Thickness [μm]	16.6	31.5	58.1	253
$QE_{99.9\%}$ Thickness [μm]	24.9	47.3	87.2	380

Table 4.1: The thickness of silicon needed to absorb 90 %, 99 % and 99.9 % of the light. The values are for typical wavelengths used by LEDs within the field of tissue oximetry. It can be seen that only 25 μm of silicon are needed to absorb 99.9 % of the red light from a 660 nm LED whereas more than 100 μm are needed to absorb only 90 % of the infrared light from a 940 nm LED.

The device thickness for some specific wavelengths, corresponding to LEDs typically used in tissue oximetry, are shown in Table 4.1. More than 250 μm of silicon is needed in order to absorb 99 % of the light with a wavelength of 940 nm. Thinning down the silicon to below 100 μm in thickness, as a method for achieving flexibility, is therefore not feasible.

For a backside photo diode the internal quantum efficiency can not be fully described using just Beer-Lamberts law. The generated electron-hole pairs will have to diffuse through the bulk of the detector before it reaches the depletion region and it is therefore possible that they will recombine due to different events. A model that takes this diffusion into account was derived in [60]. It is based on a one-dimensional slap of p-type silicon, which can be seen in Figure 4.3. The slap is made of bulk p-type silicon of length l_p with a minority carrier life time τ and diffusion coefficient D_n. The light enters at the front side ($x = 0$), which has a surface recombination velocity of S. Near the back side of the slap the n-type region of the pn-junction is located. It has a length of l_n and the resulting depletion region has a length of w. The diffusion length of the minority carrier electrons, in the p-type region, is given by $L_n = \sqrt{D_n \tau}$. The model is derived using the relation between current density, J, photon flux and internal quantum efficiency from Equation 4.3. This can be written as:

$$\eta_{int} = \frac{J}{q\Phi} \tag{4.6}$$

with the boundary conditions that at x = 0 the electrons will recombine with rate of the surface recombination velocity S and at x = l_p the excess carriers are extracted meaning that their concentration is zero. The final expression for η_{int} is (the full derivation is given in [60]):

$$\eta_{int} = \frac{\mu_a L^2}{\mu_a L^2 - 1} \cdot \frac{\mu_a D_n + S - e^{-\mu_a l_p}\left[\left(\frac{D_n}{L_n} + \mu_a S L_n\right)\sinh\left(\frac{l_p}{L_n}\right) + (\mu_a D_n + S)\cosh\left(\frac{l_p}{L_n}\right)\right]}{D_n \cosh\left(\frac{l_p}{L_n}\right) + S L_n \sinh\left(\frac{l_p}{L_n}\right)} \quad (4.7)$$

Even though Equation 4.7 is an approximation to the real physics behind the internal quantum efficiency it can still be used to derive important design considerations. The main parameters, which we have influence on, will be the diffusion length L_n, due to its dependence on the minority carrier lifetime τ, the p-type device thickness l_p and the surface recombination S. The internal quantum efficiency will also depend on the substrate doping level N_A because this level will affect the minority carrier lifetime and also the diffusion coefficient through the mobility. The results of modelling the internal quantum efficiency, using Equation 4.7, can be seen in the plots presented in Figure 4.4. When a parameter is varied the other parameters are kept constant at values considered to be the best achievable. This is $S = 100$ cm/s, $l_p = 350$ μm, $\tau = 500$ μs and $D_n = 32$ cm^2/s.

In the first case the surface recombination velocity is varied. In [61] it was possible to achieve surface recombination velocities as low as 10 cm/s using layers of Al_2O_3. For silicon passivated by thermal oxides values of down to 100 cm/s could be achieved and if the semiconductor was very poorly passivated it could have surface recombination velocities above 10,000 cm/s [62]. The plot in Figure 4.4a shows the internal quantum efficiency for surface recombination velocities of 100 cm/s, 1,000 cm/s and 10,000 cm/s. It can be seen that the internal quantum efficiency strongly depends on the surface recombination velocity as it on average will be ap-

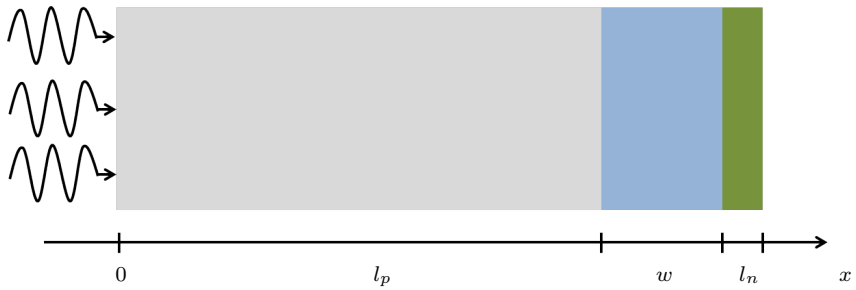

Figure 4.3: Schematic drawing of the 1-dimensional slap of silicon used to derive the model for the internal quantum efficiency. The light enters at $x = 0$ and is absorbed in the p-type bulk of length l_p. The carriers that reaches the depletion region after l_p, without recombining, will contribute to the internal quantum efficiency.

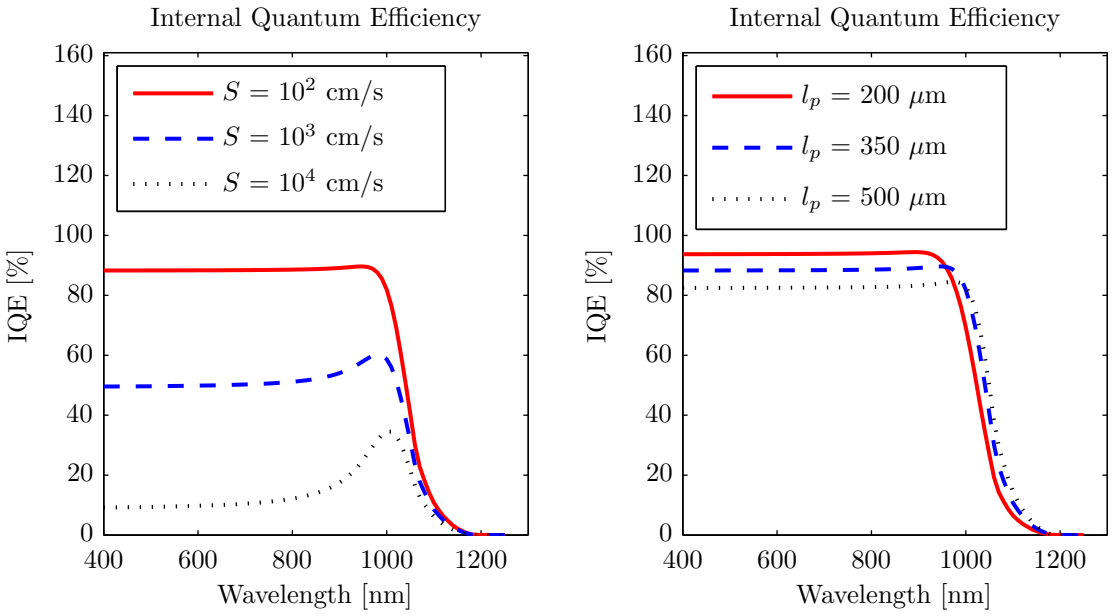

(a) *IQE for* S (b) *IQE for* l_p

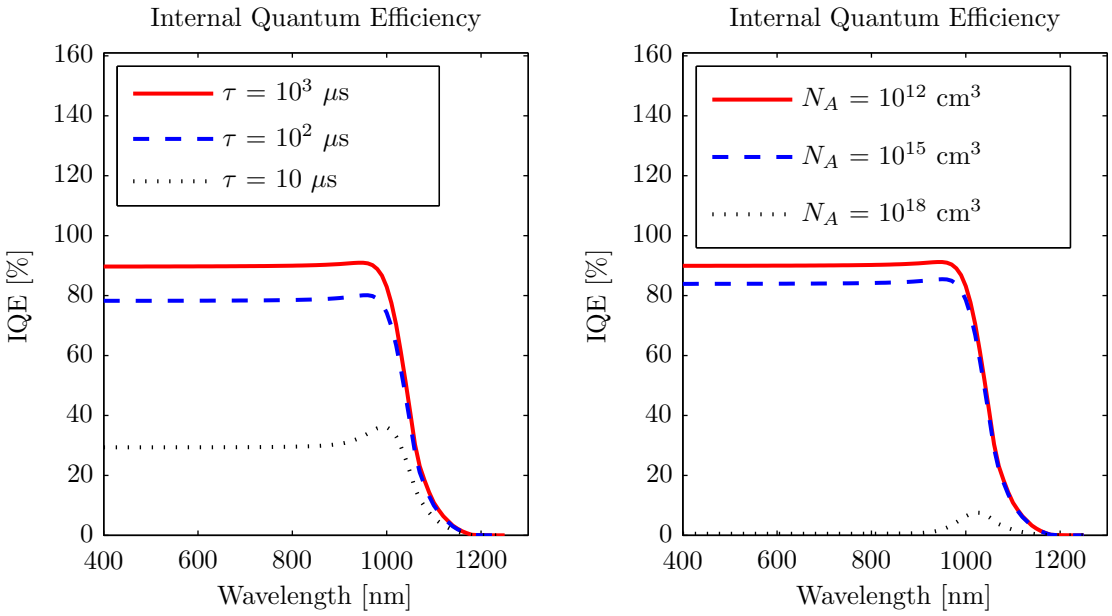

(c) *IQE for* τ (d) *IQE for* N_A

Figure 4.4: Plots of the internal quantum efficiency modelled from Equation 4.7. In (a) the surface recombination velocity is varied and it can be seen to have a strong impact. The device thickness is varied in (b) but it has almost no impact on the internal quantum efficiency. In (c) the minority carrier lifetime is varied and will produce acceptable results if kept above 100 μs. Finally, the wafer doping level is investigated in (d) and can be seen to have no effect for normal wafers.

proximately 90 %, 55 % and 20 % for the three surface recombination velocities and a wavelength range of 700-1000 nm. A well passivated front side surface will therefore be a top priority.

In Figure 4.4b the internal quantum efficiency is plotted for three values of the p-type silicon length. This will approximately be similar to the wafer thickness thus three typical 4" wafer thicknesses of 200 μm 350 μm and 500 μm have been chosen. It can be seen that the wafer thickness will not have any significant impact on the internal quantum efficiency, which will be in the order of 80-90 % for light with wavelengths of 700-1000 nm. Moreover, the plot shows that the internal quantum efficiency is larger for thinner wafers. This should be compared to the results from Figure 4.2b, which showed that a certain thickness was needed. Choosing 4" wafers with a standard thickness of 300-350 μm should be a suitable compromise.

The minority carrier life time is strongly dependent on the wafer quality and type but also on the device processing. Pristine float zone wafers can have minority carrier lifetimes of several milliseconds. However, when the wafers are processed τ will begin to decrease. It is in particular thermal processes that destroys the life time so the total thermal budget for the device process should be kept as low as possible. From Figure 4.4c it can be seen that a lower minority carrier life time will also result in a lower internal quantum efficiency. A life time of 100 μs will still result in a fairly high internal quantum efficiency of approximately 80 % compared to 90 % for a life time of 1 ms. However, if the life time is reduced again with a factor of 10 to only 10 μs, it will have a large negative impact on the internal quantum efficiency, which now only will be in the order of 30 %.

Finally, the internal quantum efficiency is plotted for the different wafer doping levels, as can be seen in Figure 4.4d. Silicon wafers will typically have doping levels of 10^{15} cm^{-3} but high resistive wafers with doping levels of 10^{12} cm^{-3} are also available. These doping levels do not have a large impact on the internal quantum efficiency, which will be approximately 85 % and 90 %, respectively. But using highly doped wafers will completely destroy the internal quantum efficiency due to the lowered carrier mobility and essentially cause the internal quantum efficiency to become 0 %.

4.2.2 Semiconductor Passivation

The typical method used to lower the surface recombination velocity for silicon is to use different kinds of thin films, e.g. thermally grown SiO_2. This will ensure that the surface recombination velocity becomes smaller than 100 cm/s.

Another approach is to ensure that the generated minority carriers will not diffuse to the front side of the device and potentially recombine. By diffusing acceptor atoms into the front side of p-type silicon a p+ doping area will be created, which

is called a front side field doping. This will cause a local bending of the conduction and valence band, which means that an electron diffusing towards the front side will now fell a potential barrier. The semiconductor simulation software PC1D has been used to simulate the effects of the front side field doping. The band diagram for a p-type piece of silicon with a doping of 10^{12} cm^{-3} and a diffused front side field doping with a peak concentration of 10^{19} cm^{-3}, can be seen in Figure 4.5a.

A potential problem with the field doping is that it will increase the Auger recombination, which will lower the internal quantum efficiency in the p+ region. More simulations regarding this problem have therefore been done, where diffusions with peak doping concentrations of 10^{17} cm^{-3}, 10^{19} cm^{-3} and 10^{21} cm^{-3} are compared to a device with no front side field doping. In all cases the front side surface recombination velocity is 10,000 cm/s, the minority carrier lifetime is 500 μs and the device is 350 μm thick. It can be seen from Figure 4.5b that all of the front side field doping levels will improve the internal quantum efficiency. However, the peak doping concentration should be kept below 10^{19} cm^{-3} in order not to have too high Auger recombination.

The photo detectors that are fabricated during this project will of course

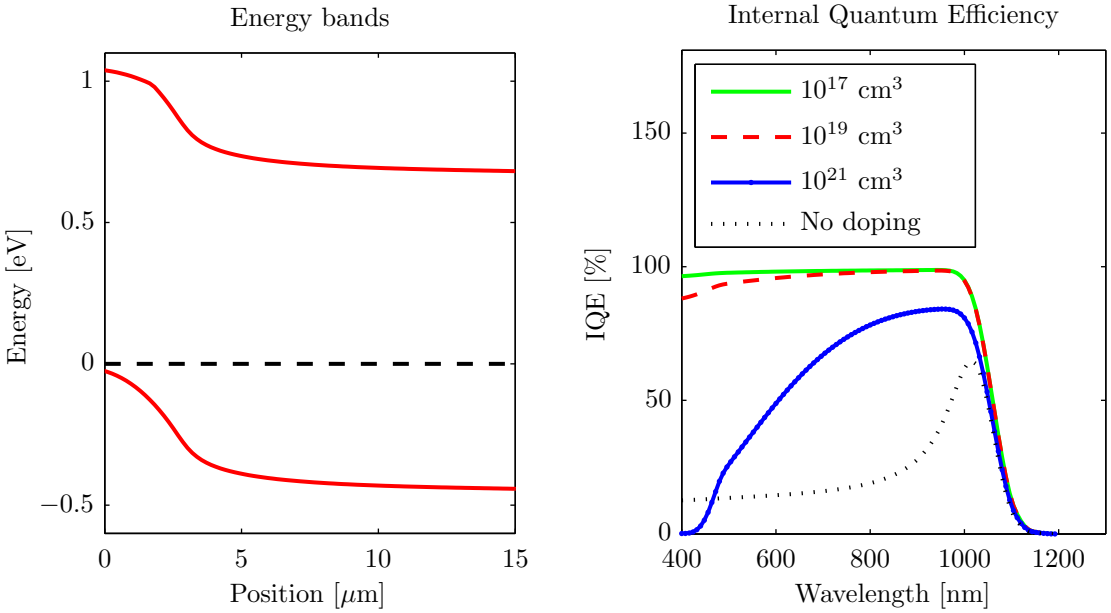

(a) *Band diagram* (b) *Internal quantum efficiency*

Figure 4.5: The results from the PC1D simulations. The band diagrams for a front side field doping is shown in (a). An electron diffusing toward the front side ($x = 0$) will now see a potential barrier causing it to change direction. The internal quantum efficiency is plotted in (b) for different peak doping concentrations of the front side field. The Auger recombination becomes too high for doping levels above 10^{19} cm^{-3}.

not be one dimensional. Both in the case of a 1D linear array and 2D square array, as described in Chapter 3, the detectors will have a relative small width and length compared to their thickness. This means that the unpassivated side walls will decrease the quantum efficiency of the detectors due to surface recombination. The light that enters the detector near its center will have a much greater chance of creating carriers that will diffuse to the depletion region rather than diffuse to one of the side walls. But carriers that are created in the detectors near the side walls will have a greater chance of recombining. This means that the detectors will have a quantum efficiency, which will change in the x and y direction across the surface of incidence.

This effect can be seen in Figure 4.6. Here, two detectors with the same thickness and length, but different widths, are shown. Since the volume effected by the surface recombination velocity at the edges are the same for the two detectors, the wide detector can be expected to exhibit a higher quantum efficiency than the narrow detector, due to fact that the wide detector has twice the volume of the narrow detector, but not much larger circumference. This will be a trade-off between good detectors and flexibility, because narrow detectors will result in a more flexible device, as described in Chapter 3. If the side walls are well passivated the detectors should have the same high quantum efficiency.

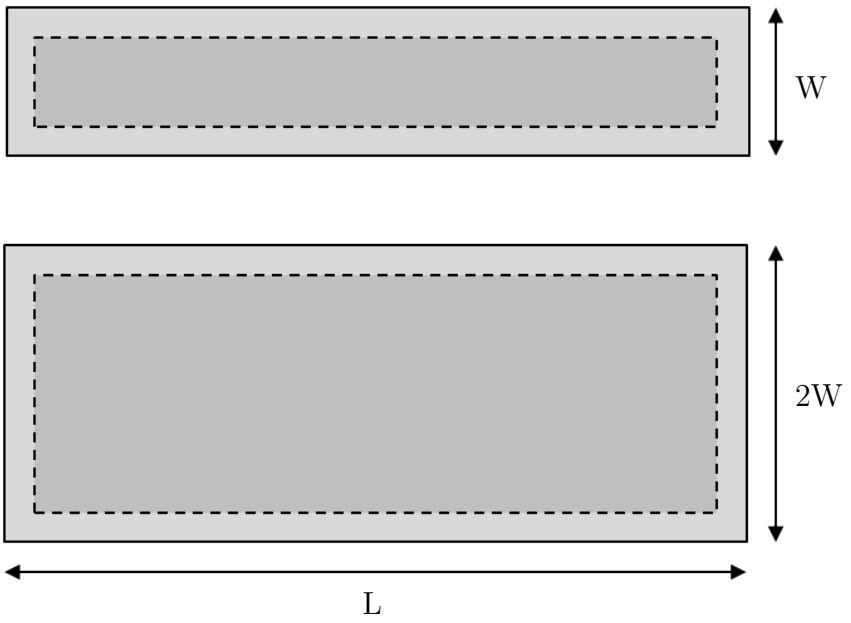

Figure 4.6: The effect from the unpassivated edges on the performance of two different detectors. The wider detector will have a higher quantum efficiency than the narrow detector, because it has a larger unaffected volume (dark grey) compared to the effected volume (light grey). The edge effect can potentially be removed by passivation e.g. using Al_2O_3

As will be described in Chapter 5 the side walls of the detectors can not readily be passivated because of cross contamination limitations in the DTU Danchip cleanroom facility and because the devices cannot be heated above 300 °C when they contain polyimide. However, during the spring of 2014 an atomic layer deposition (ALD) system became available at DTU Danchip, and this was used to test, if low temperature ($\leq$300 °C) depositions of Al_2O_3 were possible and would passivate the side walls.

4.2.3 Anti-reflection Layers

The quantum efficiency can also be improved, as can be seen from Equation 4.4, by ensuring that the light, which is incident upon the device will not be reflected by the device surface. Complex band pass filters, which only allow for certain wavelengths to pass, can be fabricated by multi layered structures of thin films or different organic coatings. However, the complexity behind the fabrication of these layers does not make it a feasible solution in this project. Instead simple layers of dielectric thin films can be applied to the device surface and act a high or low pass filters.

The optical simulation software Concise Macleod 8 has been used to estimate the reflectance from different thin film coatings of silicon dioxide and silicon nitride. The idea behind the usage of both oxide and nitride is that a thermally grown oxide will act as an excellent surface passivation layer for the photo diode [63] whereas silicon nitride have been proven to be a good barrier material for protection of the silicon from moisture and ions introduced by the environment [64]. The simulation results, using light incident normal to the surface, can be seen in Figure 4.7 where the reflectance is plotted as function of wavelength of the light.

The results from simulations of different thicknesses of the layers in the SiO_2/Si_3N_4 stack show that a stack of approximately 50 nm SiO_2 and 50 nm Si_3N_4 will lower the surface reflectance significantly compared to an un-coated silicon surface. The reflectance for an un-coated silicon wafer can be seen to be between 35-45 % for light with a wavelength between 400-1000 nm. The SiO_2/Si_3N_4 stack can be seen to lower the reflectance for the red and near infrared light and at the same time increase the reflectance for the blue and green light. The stack will therefore act as a high pass filter with respect to the wavelength of the light. It can also be seen that small changes in the thickness of the dielectric layers will change the filtering properties. It is therefore important that the film thicknesses are uniform across the entire surface of the wafer so each device will exhibit the same reflectance.

Concise models the light as incident from a medium with a refractive index of 1 for all wavelengths. This will not be the case for our design as the dielectric layers will be covered with a 150 μm thick layer of PDMS with a refractive index of

approximately 1.40-1.42 for light with a wavelength between 400-1000 nm. Moreover, the PDMS layer will cause absorption of the light. The true behaviour of the device reflectance have therefore been measured and is presented in Figure 6.2. It shows that the reflectance is still at a minimum for 700-1000 nm light, but now at a higher level of approximately 10 %. An advantage of the PDMS layer is that it has almost the same refractive index as the skin, and it will therefore minimise the Fresnel reflection at the device interface, when the devices are in skin contact.

4.2.4 Black Silicon Nanostructures

Low anti-reflection can also be achieved by other means than adding filters to the surface. Fabricating nanostructured surfaces can have a large effect on the surface reflectance. Black silicon is a general term for a number of nanostructured surfaces, which causes the silicon to appear black. These structures have been investigated during the past few decades and they were originally discovered as an unwanted effect of dry etching [65]. They can be fabricated using both dry and wet etching techniques and their true structure can be anything from holes, pyramids to tall nee-

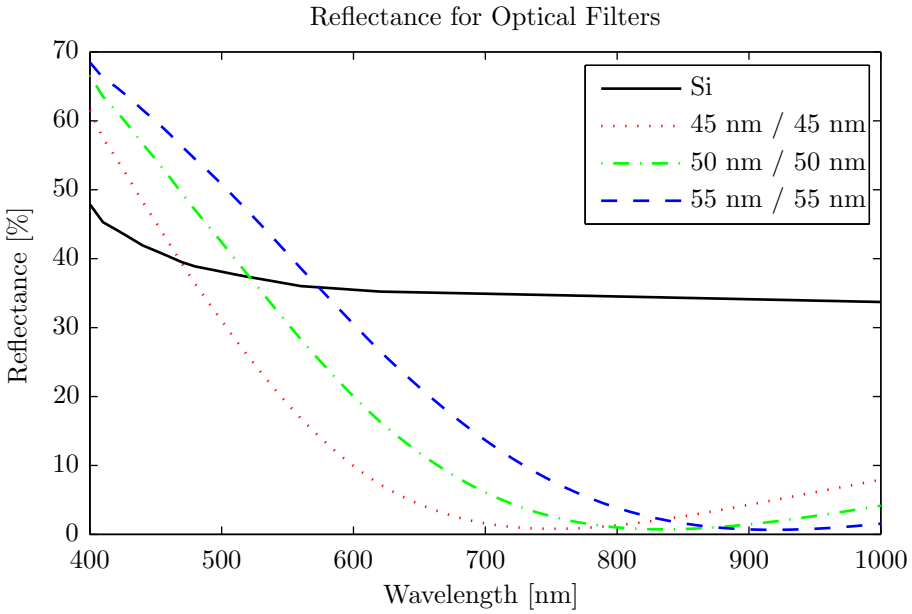

Figure 4.7: Results from Concise Macleod 8 simulations. The reflectance is plotted as function of the wavelength of the light. A pristine silicon surface with no coating can be seen to have a reflectance between 35-45 %. By applying the SiO_2/Si_3N_4 stack to the silicon the reflectance can be lowered to below 10 % for the wavelength of interest, i.e. 700-1000 nm. At the same time the reflectance of blue and green light is increased, thereby creating a high pass filter with respect to the wavelength of the light.

dle like structures. Their common quality is a randomised topology. Black silicon nano structures have been used in many different applications i.e. hydrophilic surfaces, Surface enhanced Raman spectroscopy (SERS) substrates and anti-reflection surfaces for solar cells.

The effectiveness of black silicon, as an anti-reflection surface, is because the structures form a continuous change in the refractive index, which lowers the Fresnel reflection. Furthermore, the randomised topology ensures that black silicon surfaces are much less dependent on the angle of incidence [66]. This would potentially be very useful for detectors used in tissue oximetry, since the diffuse reflected light will have scattered through so much tissue that it will be scattered completely isotropic, as described in Section 2.3, and therefore enter the surface of the detectors with many different angles of incidence. The reflectance of the dielectric filters shown in Figure 4.7 will change as a function of the angle of incidence and in general the reflectance will increase. Polymer filters used on commercial infrared detectors function extremely well as cut-off filters for visible light but they also suffer from being strongly dependent on the angle of incidence.

Different types of black silicon have successfully been fabricated at DTU Nanotech using dry etching techniques [67, 68]. Scanning electron microscope (SEM) images can be seen in Figure 4.8, where two different types of black silicon are fabricated using either reactive ion etching (RIE) or inductive coupled plasma (ICP) deep reactive ion etching. In this project we will investigate the possibility to include the dry etching process of black silicon nanostructures into the fabrication process of the tissue oximetry devices. The effectiveness of the black silicon as surface treatment, for capturing diffuse reflected light, will also be tested.

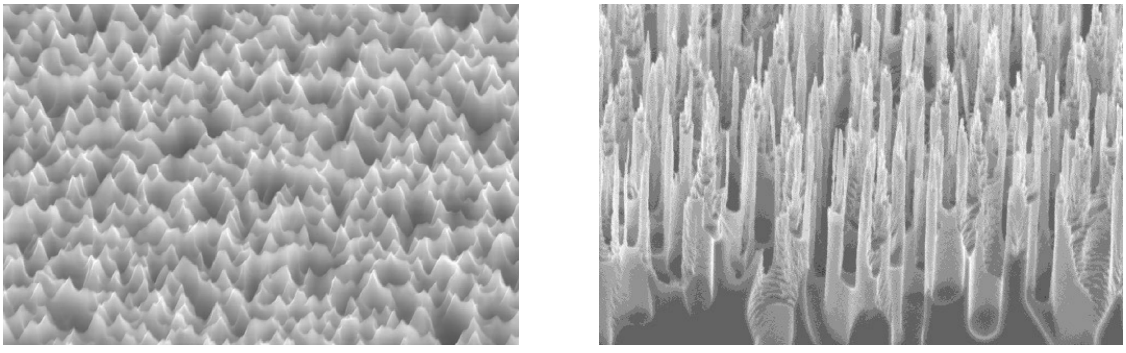

(a) *Black silicon etched usign RIE [67]* (b) *Black silicon etched using ICP [68]*

Figure 4.8: SEM images of two different types of black silicon both fabricated by dry etching using O_2 and SF_6 as gases. The pyramid like nanostructures shown in (a) are etched using low power RIE and are a few hundred nanometres in size. The nanostructures shown in (b) are etched by high power ICP and results in needle like structures, which are a few micrometres tall.

4.3 Summary

The concept of a back side diode and its use as a photo detector was explained. It is essential to design the diodes with a minimal reverse bias current and a maximum quantum efficiency. Calculations using a one dimensional analytical model showed that the internal quantum efficiency can be improved by using a low doped p-type substrate with a doping level of 10^{12} cm^{-3}, reducing the surface recombination velocity to approximately 100 cm/s on the surface of incidence and having a long minority carrier lifetime above 100 μs.

The detectors can be further optimised by adding a front side field doping to the surface of light incidence using an anti-reflection coating of 50 nm SiO_2 and 50 nm Si_3N_4 or black silicon nanostructures. The etched out side walls of the detectors can be passivated by ALD coating of aluminium oxide.

Chapter 5

Device Design and Fabrication

The previous chapters have presented the analysis of tissue oximetry, how flexible silicon devices can be realised and how high quality infrared detectors should be fabricated. As mentioned in the introduction several different devices have been fabricated and tested during this project. The fabrication process described in this chapter is the final result of many fabricated batches of devices and lengthy process optimisation. Although the devices appear different, due to their 1D or 2D layout, they can be fabricated using the same process sequence. The process development and optimisation, which have resulted in this final process sequence, are presented in chapter 6. This chapter gives an outline of the general device design as well as a presentation of the final optimised process flow for fabrication of the devices.

5.1 Device Designs

The devices that have been fabricated are designed as a combination of the flexible silicon device platforms described in Chapter 3 and the back side pn-junction photo diodes described in Chapter 4. A cross sectional drawing of a device is shown in Figure 5.1 and a top view drawing is shown in Figure 5.2. In order to realise this design by standard IC fabrication, four general groups of process steps will need to be carried out and there are some important considerations linked to each group:

- **High temperature processing** - All the high temperature process steps, i.e. oxide growth, Low pressure chemical vapour deposition (LPCVD), doping diffusions and annealing will have to be carried out as the first steps due to both contamination problems and because the introduction of metals and polyimide to the wafers will not make high temperature processing possible.
- **Deep etching** - The etch out of the individual photo detectors. This step will make the wafers fragile.

- **Polyimide and metallisation** - Formation of electrical contacts to the silicon and the flexible electrical interconnects, which are encapsulated in the polyimide. Wafers containing metals and/or polyimide will be restricted from some processes.

- **PDMS casting** - Casting and curing of the PDMS layer. Since this process is performed outside of the cleanroom facilities it should be carried out in the end of the process flow.

The devices are designed with electrical lead-outs that can fit into zero insertion force (ZIF) connectors. In this way a number of devices can be tested and characterised without the need for wire bonding.

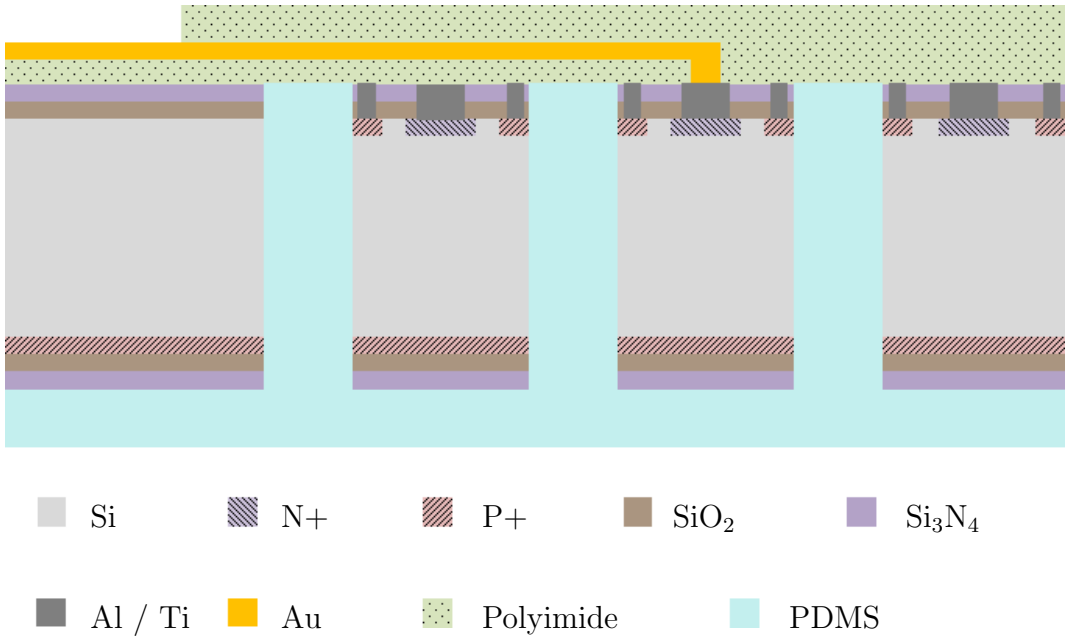

Figure 5.1: Schematic drawing showing the cross-sectional view of the devices. The front side of the device is the bottom part with the PDMS contact surface and the back side of the device is the top part with the electrical interconnects and polyimide. The devices are made from p-type silicon and have p+ diffusions made for substrate contacts near the back side and for front side field doping. In order to form the pn-junctions n+ diffusions are also made on the back side. SiO_2 and Si_3N_4 are used to form the passivation and optical filter. A Ti/Al metallisation is used to create contacts to the p+ and n+ areas. The back side of the device contains the Au electrical interconnects encapsulated in the polyimide. All n+ areas will have individual interconnects and all p+ areas will have a common interconnect. The front side of the device contains a PDMS layer, which also fills up the cavities that are etched out between the individual photo detectors.

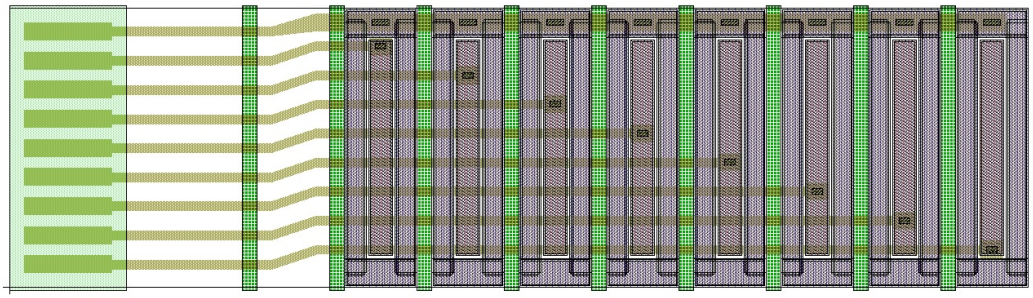

Figure 5.2: Computer aided design of a 1D linear array device. The device consists of an end piece with contact pads for a ZIF connector and nine silicon areas separated by nine flexible joints. Eight of the silicon areas contain back side pn-junction photo diodes as well as electrical interconnects.

The different devices that have been fabricated all have the same basic internal structure, as was shown in Figure 5.1, but they have different external designs. Different device designs have been used in this project as well as a number of test chips that resembles the individual detectors on the devices

- **Small linear arrays** - 5.3 mm × 29.0 mm devices used to test the linear area platform and the concept of back side pn-junction diodes. By making the devices small many could be fitted on a single 4" silicon wafer. These devices were made with varying widths of both the silicon areas: 1 mm or 2.75 mm and the flexible joints: 200 μm, 300 μm and 400 μm. They had two circular holes etched through the structure so they could be anchored during tests. A large number of batches were fabricated with this device design with a high yield of >90 %.

- **Large linear arrays** - The final generation of linear array devices being 13.6 mm × 55.0 mm. They were made large enough in order to measure at distances from 5 mm to 40 mm from the light source using eight measurement points. The silicon detectors are 2 mm wide and the flexible joints are 500 μm. The devices have a hole etched through the structure and contact pads so LEDs could be bonded to the device. Two batches with this design were fabricated but unfortunately they suffered from 0 % device yield, as will be described in Section 6.5.3.

- **2D square arrays** - Devices with 2 mm × 2 mm square silicon detectors surrounded by 500 μm joints. They measure 12 mm × 29 mm. These devices are still only supposed to be bend around a single curved surface, but offer a greater density of detectors. The devices consist of 36 individual elements.

- **Test chips** - A number of different test chips were fabricated using different designs. They were used to test the back side pn-junction diodes and if the different optimisation processes worked, i.e. the black silicon nanostructures and Al_2O_3 coatings.

5.2 Fabrication

The fabrication process is described in the following sections. The entire fabrication has been carried out at the DTU Danchip cleanroom facilities and at DTU Nanotech workshops. In order to fabricate the devices ten major process steps are needed. They all utilise nine different lithographic steps. A description of the lithographic mask set can been found in Table 5.1 and the complete detailed process flow is listed in Appendix B. A number of different materials are used to realise the design shown in Figure 5.1 The materials used in the fabrication of the devices are:

- **Silicon wafers** - The silicon wafers used are prime grade double side polished 4" (100) wafers from Topsil Semiconductor Materials A/S. They are p-type and doped with boron to a level of approximately 10^{12} cm^{-3} giving them a resistivity of >10,000 Ωcm. The wafers have a thickness of 300 ± 5 μm. They are fabricated using the float zone method and have a long carrier life time of >2 ms.

- **Polyimide** - The polyimide used is HD-8820 from HD MicroSystems. It is positive tone and can be developed in Tetramethylammonium hydroxide (TMAH) solutions. The polyimide should be cured at 250-300 °C in order to finalise it and will have final thicknesses in the order of 5-10 μm. When finalised it can be elongated up to 100 % and has a Youngs modulus of approximately 2 GPa.

- **Metals** - The metals used on the devices are all from Kurt J. Lesker Company. They are deposited using e-beam evaporation. They have a purity of: Al 99.999 %, Ti 99.995 % and Au 99.99 %.

- **PDMS** - Sylgard 184 from Dow Corning. A PDMS, which is transparent to infrared light and with fine biocompatibility. It is mixed from a two component solution and needs to be cured to be finalised. When finalised it can be elongated up to 400 % and has a Youngs modulus of approximately 1 MPa.

During the fabrication some general process steps are used. This includes: photo lithography, photo resist stripping, wafer cleaning and silicon oxide etching/stripping using buffered hydrofluoric acid (BHF). A description of these process steps are given below.

Mask name	Polarity	Description
Alignment	Pos.	Used to etch alignment marks into the silicon.
P+	Pos.	Used to make openings in a SiO_2 mask for a boron diffusion in order to form the P+ areas.
N+	Pos.	Used to make openings in a SiO_2 mask for a phosphorous diffusion in order to form the N+ areas.
Contacts	Pos.	Used to mask for a dry etch process, which etches contact openings in the dielectric layers.
Metal 1	Neg.	Used to create an image reversed resist mask on the wafers, which will then be used for lift-off metallisation of Ti/Al.
Deep etch	Pos.	Used to mask for a dry etching of an Al layer. The Al layer is then used as an etch mask for deep etching of the silicon.
Polyimide 1	Pos.	Used to define openings in the first polyimide layer so the electrical interconnects can make contact with the Ti/Al metallisation.
Metal 2	Pos.	Used to mask for a dry etch, which etches all the way through silicon wafers that are then used as shadow masks for the Au metallisation, which creates the electrical interconnects.
Polyimide 2	Pos.	Used to define openings in the second polyimide layer so the electrical interconnects can make contact to the out side world.

Table 5.1: A list of the nine lithographic masks used in the fabrication of the devices. The mask layouts are obviously different for the different devices, but all the masks serve the same purpose in the fabrication of the different devices.

- **Photo lithography** - A photo lithography step consists of: resist spinning, ultra violet (UV) exposure and development. The resist used is AZ 5214E from Clariant. The wafers are treated with hexamethyldisilazane (HMDS), which acts as an adhesion promoter. A 1.5 μm thick layer of resist is then spin coated onto the wafer and soft baked at 90 °C for 30 s. The resist is then exposed, using 1 to 1 UV lithography with a dose of 56 mJ/cm^2 (8 s of exposure time using the KS Aligner). The pattern is developed using AZ 351B developed, which is diluted 1:4 in deionised (DI) water, for 70 s.

- **Photo resist stripping** - The photo resist is stripped from the wafer using a plasma asher. The recipe uses: 400 sccm of O_2, 70 sccm of N_2, 1000 W of power and approximately 10 min.

- **RCA cleaning** - Before any thermal processing the wafers are cleaned using a so-called RCA clean. It consists of two cleaning steps with a short 30 s dip in 5 % HF after each step. Step 1 is 10 min in a 70 °C solution of NH_4OH, H_2O_2 and H_2O with a volume ratio of 1:1:5. Step 2 is 10 min in a 70 °C solution of HCl, H_2O_2 and H_2O also having a volume ratio of 1:1:5.

- **SiO_2 etching/stripping** - Silicon oxide layers are etched and stripped using a buffered hydrofluoric (BHF) solution, which is a mixture of NH_4F and HF in water. The etch rates are approximately 70 nm/min for thermal grown oxides and 150 nm/min for plasma enhanced chemical vapour deposition (PECVD) oxides.

5.2.1 Step 1: Alignment Marks

The first step is to etch alignment marks into the back side of the pristine silicon wafers. This ensures that all subsequent process steps can be aligned. The alignment marks are defined using photo lithography with mask: *"Alignment"*. They are then etched into the silicon by DRIE, to a depth of approximately 10 μm, and afterwards the resist is stripped.

5.2.2 Step 2: p+ Doping

In order to introduce the p+ doping, which will form the substrate contacts and front side field doping, the wafers are first RCA cleaned and then approximately 200 nm SiO_2 are grown using a wet thermal oxidation process at 1000 °C. The SiO_2 is patterned using photo lithography with mask: *"P+"* and BHF etching. This opens the oxide on the back side of the wafer for the substrate contacts and completely removes the oxide on the front side of the wafer for the front side field doping. After a resist strip and another RCA clean approximately 375 nm of boron doped silicon glass (BSG) is deposited on both sides of the wafers using PECVD. The process parameters are: flow of SiH_4: 17 sccm, flow of B_2H_6: 140 sccm, flow of N_2O: 1600 sccm, pressure: 400 mTorr, power: 380 W and time: 120 s. The boron is then driven into the silicon by an 85 min anneal at 1000 °C, which results in a peak concentration of 10^{20} cm^{-3}. Finally, the BSG and SiO_2 are stripped from the wafer using BHF.

5.2.3 Step 3: n+ Doping

A similar procedure is done for the n+ doping. After an RCA cleaning approximately 500 nm of SiO_2 are grown using a wet thermal oxidation process at 1000 °C. The

SiO_2 is patterned using photo lithography with mask: *"N+"* and BHF etching. However, this time the front side of the wafers is protected with a layer of resist so only openings for the n-doping are made in the oxide on the back side of the wafer. The resist is stripped and the wafers are RCA cleaned again. Phosphorous doping is now introduced into the silicon using gas phase diffusion of $POCl_3$ for 30 min at 1000 °C, which result in a peak concentration of 10^{21} cm^{-3}. Finally, the SiO_2 and phosphorous phase layer are stripped from the wafer using BHF.

5.2.4 Step 4: Optical Filter and Contact Openings

Immediately after the oxidation in the previous process step, the wafers are loaded into a furnace and 50 nm of oxide is grown using dry thermal oxidation at 1000 °C. This process step also finalises the phosphorous drive-in. Then, 50 nm of Si_3N_4 is deposited using LPCVD. Photo lithography is then performed with mask: *"Contacts"* in order to open contact holes to the n+ areas and p+ substrate contacts. The resist is used as an etch mask for two reactive ion etching (RIE) processes, which first etches through the silicon nitride and then trough the silicon oxide and stops on the silicon. The peak doping concentrations of the boron and phosphorous diffusions will after all the thermal processes measure 3.0×10^{19} cm^{-3} and 3.0×10^{20} cm^{-3} respectively.

5.2.5 Step 5: Metallisation

The first metallisation is realised using the lift-off technique. Here, the image reversal properties of the AZ 5214E is utilised. This is done by using a resist thickness of 2.2 μm, which is then exposed with the mask: *"Metal 1"* for 5 s, image reversal baked for 120 s at 120 °C and then flood exposed for 35 s. The development time is 80 s. Using e-beam evaporation 100 nm of Ti and 300 nm of Al are then evaporated onto the wafer and the lift-off is performed in acetone, which removes the metallisation from all unwanted places. Finally, the metal contacts are annealed in a N_2 atmosphere for 30 min at 425 °C. This ensures the formation of ohmic contacts with low contact resistance.

5.2.6 Step 6: Deep Etch

The deep etch process, which aim is to define the individual detectors, is split up in two parts. This was done due to challenges with the process yield, if the deep etch process was done in a single step, as will be explained in Chapter 6. The first step is to create an Al etch mask that can survive the subsequent process steps. This is done by depositing a 200 nm Al layer on the front side of the wafer. A resist mask is

then made using the photo lithography mask: *"Deep etch"* and used for a dry etch of the Al. The silicon deep etch is then performed using an advanced silicon etched, running the Bosch process, until approximately 50 μm of the 300 μm remains in the etched grooves.

5.2.7 Step 7: First Polyimide Layer

The polyimide encapsulation is applied in two steps. The first step aims at creating an approximately 9 μm thick layer of polyimide. This is done by first baking out the wafer in a 120 °C oven for 30 min. The HD-8820 is then spin coated on the back side of the wafer using a spin process with a 7 s spread spin at 500 rpm and a 60 s thinning spin at 1400 rpm. The polyimide is baked for 5 min at 120 °C and then exposed using mask: *"Polyimide 1"* and a dose of 630 mJ/cm^2 (90 s of exposure time using the KS Aligner). The polyimide is developed by immersion into MF-322 developer from Microposit for 90 s and then rinsed in DI water for 5 min. Finally, the polyimide is semi-cured by slowly heating the substrates to 300 °C in an N_2 atmosphere and keeping the substrates at 300 °C for 5 min before cool down. This ensures that the photo definable capabilities of the HD-8820 is destroyed without fully curing the film.

5.2.8 Step 8: Electrical Interconnects

The second metallisation creates the electrical interconnects, which will make connections to the individual detectors. They are created by e-beam evaporation through a shadow mask. The shadow masks are fabricated by etching patterns all the way through 525 μm thick 4" silicon wafers. First, photo lithography is performed on the wafers using mask: *"Metal 2"*. The wafers are then bonded to carrier wafers, using Crystalbond^{TM} 509 from Aremco, and the pattern is etched all the way through the wafer using DRIE. After the dry etching the shadow masks are separated from the carrier wafers and cleaned using plasma ashing.

The shadow masks can now be aligned to the device wafers using an optical microscope and clamped with semiconductor tape. 50 nm of Ti and 400 nm of Au are then evaporated onto the device wafers, through the shadow masks. Finally, the shadow masks can be carefully removed.

5.2.9 Step 9: Second Polyimide Layer

The second polyimide layer is applied in almost the same manner as the first layer. The difference being that it is spin coated using 1200 rpm and baked for 10 min. This will result in a final film thickness of approximately 11 μm, which should place

the electrical interconnects as close to the neutral axis as possible. The UV exposure is done using mask: *"Polyimide 2"* followed by the same development procedure as for the first layer. Finally, the curing is done by slowly heating the wafers to 300 °C in a N_2 atmosphere and keeping the substrates at 300 °C for 60 min before cool down. This process fully cures both layers of polyimide.

5.2.10 Step 10: Final etch and PDMS Casting

The final process step consists of two parts. First, the remaining silicon needs to be etched away so that the individual detectors will be completely released and electrically insulated from each other. Then, the PDMS needs to be cast in order to finalise the flexibility and biocompatibility of the devices.

The device wafers are bonded to carrier wafers, using Crystalbond™ 509, with the back side downwards. The last 50 μm of silicon is then etched away using the Bosch process from the advanced silicon etcher. This is done carefully in small steps, which consists of silicon etching and O_2 plasma cleans. This ensures that the wafers do not overheat and that the Bosch process does not create too much passivation.

After the silicon etch the 200 nm Al etch mask is removed in MF-322 and the device wafers are given a thorough clean in both DI water and O_2 plasma. The wafers can now be taken out of the cleanroom facility for PDMS spin casting. The Sylgard 184 is prepared by mixing 10:1 mass of elastomer and curing agent. The mixture is then left in a desiccator for 10 min in order to remove the majority of the air bobbles. The mixture is purred on the front side of the wafers and left again in a desiccator for 50 min. Finally, the wafer is spun at 300 rpm, for 60 s, which thins down the PDMS layer and the PDMS is cured in an oven for four hours at 65 °C.

The final devices can now be either diced out using a semiconductor dicing saw or cut out with a scalpel if the design has trails for that. As will be explained in Chapter 6 the larger devices, including both the final generation of 1D linear arrays and the 2D square matrix devices, exhibited very low fabrication yield when diced out. The yield was greatly improved by cutting these devices out with a scalpel. The devices can be released from the carrier wafer parts by melting the Crystalbond on a hot plate and cleaning the devices in DI water.

5.3 Finished Devices

Examples of finished devices are shown in Figure 5.3. 1D linear arrays are shown in 5.3a with a full detector array shown in the two top pictures and a test array shown in the bottom. The top picture shows the front side of the device with the individual

detectors and flexible joints clearly visible. The middle picture shows the back side of the device where all the electrical interconnects are located encapsulated in the polyimide layers. The bottom picture shows a test device with a single interconnect and contact pads set up for four wire measurements. Figure 5.3b shows 2D square matrices devices. The top device is a test device with two electrical interconnects set up for four wire measurements. The bottom device contains back side pn-junction diodes and has electrical interconnects to nine of the diodes.

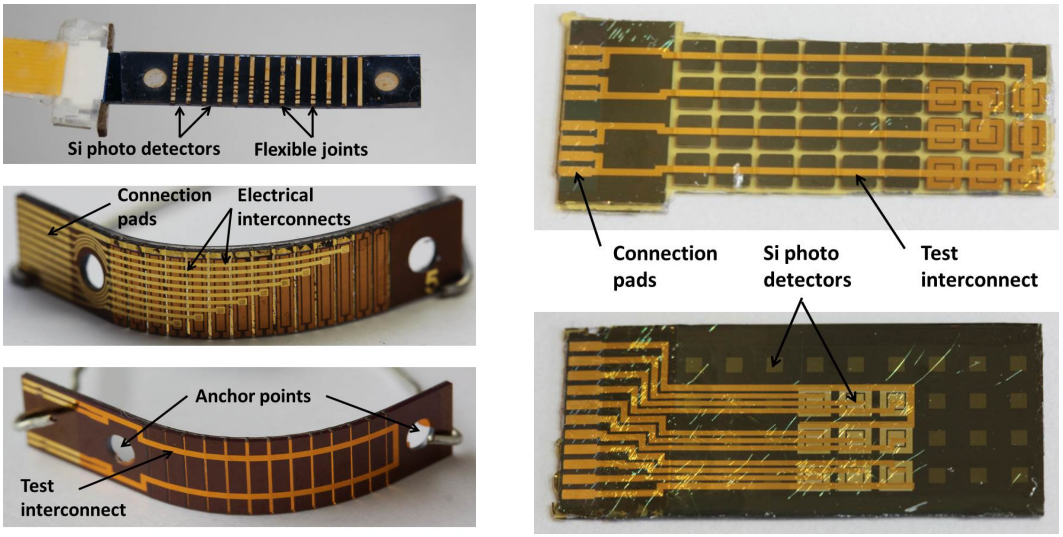

(a) 1D devices (b) 2D devices

Figure 5.3: Pictures showing some of the devices that have been fabricated during this project. The left column shows examples of 1D linear array devices and the right column shows examples of 2D square matrix devices.

5.4 Summary

A presentation of the device design was given and the different materials, lithography masks and general fabrication processes were explained. Three different device designs and a number of different test chips were fabricated during this project Finally, a detailed description of the final derived process flow is presented. The process flow consists of nine lithographic steps and ten major process steps.

Chapter 6

Process Development

The process sequence presented in the previous chapter is the end result of a lengthy development process, which has been ongoing during this entire project. The long development process is the result of both changing device generations and process problems, which occurred on process steps that had previously proven to be feasible, but seized to produce acceptable results.

This chapter presents the process development work and results, which were achieved during the development of the flexible silicon device platforms and the infrared detectors. The results are presented in four groups: thermal processing, polyimide and metallisation, deep etch and PDMS and finally black silicon and ALD coating.

6.1 Objectives and Challenges

The development challenges are linked to the two general project goals, which were listed in the introduction and included the development of flexible silicon device platforms and the integration of infrared detectors into these platforms. There is only very limited knowledge available about flexible devices, polyimide and the combination of silicon and PDMS at DTU Nanotech and DTU Danchip. All the required details for these process steps would have to be developed. During some previous projects the process steps for making back side pn-junction diodes have been developed, so these can be implemented [55,60,69]. The following sections will describe the development carried out in the three major process step groups as well as investigation into the optimisation of the photo detectors. The four parts are:

- **Thermal processing** - This includes the investigation of the p+ and n+ diffusions, how to mask for these and how to make the optical filter. Great results have already been achieved, in previous projects [55, 60], using drive-

in from a BSG for boron doping and gas phase diffusion for phosphorous. However, the same projects reported problems with the masking for these diffusion steps, which will have to be investigated.

- **Polyimide and metallisation** - The HD-8820 polyimide has not previous been used at DTU Danchip and it is also optimised for spray development, which is currently not available in our cleanroom facility. Therefore, we will investigate the general processing of the HD-8820 and ensure that we can run it in our cleanroom facility. The metallisation steps are standard process steps but should be compatible with the polyimide.

- **Deep etching and PDMS** - The deep etching processes are very well developed but a major challenge will be to combine the deep etch with the polyimide and metallisation. The same challenge will exist for the PDMS spin casting as its behaviour when combined with HD-8820 is unknown.

- **Black silicon and Al_2O_3** - Black silicon nanostructures are currently being researched at DTU nanotech as an anti-reflection surface for solar cells. It should therefore be investigated, if these structures can also be processed on the flexible devices and if they will thereby improve their performance. During the spring of 2014, an ALD system became available at the DTU Danchip cleanroom facility and this opened up the possibility of investigating if low temperature Al_2O_3 films were feasible.

6.2 Projects

In parallel to this Ph.D. project a number of bachelor and master projects were carried out within the research area of the Ph.D. project. Most of the students were partially supervised by this author as part of the three months teaching activities required by the Ph.D. programme. The results from these projects have contributed to the publications presented in this thesis as well as to the solving of the different problems related to the fabrication of the devices. The individual projects are presented in the following.

- The master project, by J. Clausen [70] was carried out from the fall of 2010 to the spring of 2011 and therefore predates the beginning of this Ph.D. project. It was the first attempt at DTU Nanotech to create a flexible silicon platform, which was biocompatible, had flexible electrical interconnects and could be used to create a device with an array of infrared detectors. The proposed solution was to deep etch all the way through the silicon wafers, spin cast a

layer of PDMS and finally deposit a thin layer of Au through a shadow mask, which would then form so called micro cracked layers of Au on the PDMS. This design was successful in making flexible devices but also identified a number of challenges that should be addressed.

- During the spring of 2012, a bachelor project, which investigated the properties of using polyimide and PDMS, was conducted by M. Engholm [71]. The goal of the project was to design, fabricate and characterise a flexible silicon platform, which could be bent in the longitudinal direction of the device so it could be fitted to a curved surface e.g. the head of an infant child. The project was still centred around the proposed design where polyimide and PDMS are used to create the flexible joints between the individual silicon areas. A different method for doing the deep etch of the silicon was also investigated and the devices were found to be exhibit excellent performance regarding flexibility and could be bent to small radii of curvature, i. e. the devices could be bent to more than 90° over their full lengths.

- The master project by A. Thyssen [72] was conducted between the fall of 2011 and the summer of 2012. The goal of the project was to use the developed flexible platform, utilising polyimide and PDMS, to fabricate and characterise an array of infrared detectors. The project showed that the proposed design was possible and could be fabricated by a process recipe containing nine lithography steps. The end result was a number of prototype chips, which served as prove of concept devices.

- J. D. Thomsen made a master project from the fall of 2013 to the spring of 2014 [73]. In this project the developed flexible design was spun off into a 2D flexible design, which concerned the fabrication and testing of 2D square matrix devices. In order to realise this new design a change to the process flow, regarding the deep etch of the individual detectors, had to be developed. The result was a well functioning device platform, which could be curved around a single curved surface. However, the photo detectors did not exhibit high quantum efficiency due to their small size and unpassivated side walls.

- Finally, a master project concerning the optimisation of photo detectors was carried out by L. Alcalá from the fall of 2013 to the summer of 2014 [74]. This project worked solely with test devices that resembles the individual photo detectors in the real devices. It identified the problem of having unpassivated side walls and its impact on the quantum efficiency and reverse bias current. Improvement to the devices was made by testing black silicon nanostructures and Al_2O_3 coating made by ALD.

6.3 Semiconductor Doping and High Temperature Processes

This section presents the results achieved during the development of the boron and phosphorous doping processes. This includes investigation of diffusion masking using wet thermal oxides or LPCVD oxides. The analysis of the optical filter is also presented.

6.3.1 Diffusion Masking

In order to introduce the boron and phosphorous into the silicon using diffusion a sufficiently efficient diffusion mask should be used. Thermal oxides have traditionally been used because they exhibit very low defect densities and excellent masking properties. However, thermal oxides will increase the thermal budget for the process sequence and lower the carrier lifetime. In [75] an investigation of the minimum required dry thermal oxide thickness for successful diffusion masking is given. The required mask thickness for boron is less than for phosphorous, but the masking also depends on the atmosphere in the furnace. For a 90 min process the minimum mask thickness for boron should be approximately 70 nm at 1000 °C and for a 60 min process, also at 1000 °C, it should be approximately 350 nm for phosphorous. Using wet thermal oxides as diffusion masking we chose thicknesses of 200 nm for boron masking and 500 nm for phosphorous masking, which take temperature ramping and other variables into account.

It was also investigated if LPCVD silicon oxides made from a tetraethyl orthosilicate (TEOS) process could be used as a diffusion mask. This process runs at only 725 °C, which should help minimising the reduction in carrier lifetime. However, when TEOS was used as a diffusion mask in [55] it proved insufficient for masking of the boron diffusion. This was also the result of a silicon oxide diffusion mask investigation presented in [76], which proved TEOS oxide as the poorest boron diffusion mask. An approximately 1 μm thick TEOS diffusion mask was tested for both phosphorous and boron diffusion, but the results were ambiguous. Test with secondary ion mass spectrometry (SIMS) showed no boron or phosphorous but the noise level of this method is around 10^{17} cm^{-3} and therefore much higher than the test substrate background doping level of 10^{15} cm^{-3}. Sheet resistance measurements showed a decrease in sheet resistance for both boron and phosphorus when the mask was removed and this could indicate that even 1 μm of TEOS is not sufficient for masking of the diffusions. Therefore, we chose to use the wet thermal oxide despite the fact that it will reduce the carrier lifetime.

6.3.2 P+ Boron doping

At the DTU danchip cleanroom facilities we have two possible methods for doing boron diffusion. The first method is to diffuse boron from source wafers places in between the device wafers. Thus, this method was found to degrade the lifetime of the wafers too much, since the boron source wafers contain unwanted impurities [69]. Furthermore, it was found to be very difficult to control the surface concentration in the diffused areas, which would then lead to a too high doping level for the front side field doping.

The second method is to deposit a BSG layer using PECVD deposition and then drive-in the boron in an annealing process. This process has previously been used and was found to work excellent. The goal was to have a single process, which could be used to make both the front side field doping and the substrates contacts. Though, for the front side field doping the peak surface concentration should not be much higher than 10^{19} cm^{-3} since this would increase the Auger recombination, but in order to create a good ohmic contact at the substrate contacts the peak surface concentration should not be much lower than 10^{20} cm^{-3} and definitely above 10^{19} cm^{-3} when having a Ti-Si contact [77]. We would therefore aim at developing a p-type doping process that would create p+ areas with a surface concentration of approximately 5×10^{19} cm^{-3} after all the thermal processes.

Although, recipes for making the BSG existed on the PECVD1 system, from previous projects, the system was decommissioned due to process issues and we therefore developed a new recipe on the PECVD2 system, which is a similar system from STS Ltd. The process was run by creating a silica glass using SiH_4 and N_2O and then adding B_2H_6 in order to introduce boron to the silica glass. The flow rate for the diborane was varied between 80-240 sccm and the best result was found for a flow of 140 sccm. This resulted in a peak concentration of 1.2×10^{20} cm^{-3} after the drive-in and 3×10^{19} cm^{-3} after all the thermal processes, which is an acceptable value. SIMS measurements showed that a lower flow would result in a too low surface concentration while higher flow rates increased the sheet resistance of the doped silicon, as can be seen in Table 6.1, possible due to the creation of boron precipitates at the silicon surface [73]. In [78] precipitates were observed for peak concentrations above 10^{20} cm^{-3}.

B_2H_6 flow rate [sccm]	80	120	130	140	160	240
Sheet resistance [Ω/sq]	2200	27	15	13	16	19

Table 6.1: Sheet resistance measurements performed on test wafers, which had been doped by BSG. The diborane flow rate was varied from 80-240 sccm.

6.3.3 N+ Phosphorous Doping

Phosphorous doping has been proven to act as a getter for interstitials that is created during the wet thermal oxidations [79]. We have therefore chosen to do the phosphorous doping after the boron doping since this might ensure a longer carrier lifetime. For doping with phosphorous there are also two possibilities either a gas phase doping with $POCl_3$ at 1000 °C or deposition of phosphorous silica glass. Previous work has shown that the doping with $POCl_3$ will result in both a well functioning n-type doping for the pn-junction and create a good ohmic contact. Since Auger recombination will not be a problem for the n+ layer near the depletion region we do not need to keep this doping level below a certain value. SIMS measurements for 30 min pre-deposition processes run at 850 °C, 900 °C, 950 °C and 1000 °C showed the best results for the highest temperature [72]. The peak surface concentration after 30 min pre-deposition and 20 min anneal was found to be 1.3×10^{21} cm^{-3} and 3×10^{20} cm^{-3} after all the thermal process steps.

Since the $POCl_3$ process contains oxygen it will create a phosphorous rich silicon oxide layer in the n+ diffusion areas. This layer is very difficult to remove, but 30 min in 5 % HF was found to remove it completely. However, it was observed that the surface of the n+ areas was hydrophilic whereas the undoped silicon was hydrophobic. After the dry thermal oxidation that creates the 50 nm oxide for the optical filter, the surfaces were now observed to be normal. It is therefore important that the n+ doping areas are oxidised after the pre-deposition even though the oxide is not used, i.e. if black silicon nanostructures are fabricated instead of the optical filter.

6.3.4 Passivation and Optical Filter

The surface passivation is fabricated as a dielectric stack of 50 nm SiO_2 and 50 nm Si_3N_4. It serves multiple purposes as both surface passivation layer, dielectric barrier, environmental barrier and optical filter. In order to fulfil all these objectives the stack should be of high quality, have a low amount of defects and a low thickness variation. The best quality for these two thin films is achieved by using dry thermal oxidation and LPCVD stoichiometric nitride deposition. First the 50 nm SiO_2 is grown using the phosphorous drive-in Furnace with dry atmosphere at 1000 °C for 1 hr. The wafers are then moved to the LPCVD nitride (6") furnace and processed using the 4nitdan recipe for 18 min.

The quality of the thin films was investigated by optical microscope and only a negligible amount of defects were observed, generally being as low as <1 cm^{-2}. The thickness uniformity was investigated on test wafers using the VASE ellipsometer. The dry thermal oxide was measured to be approximately 49 nm $\pm$ 1 nm and the

LPCVD nitride was measured to be 52 nm ± 2nm, when measuring on multiple test wafers. Two wafers were mapped using 225 points in order to determine how the thickness was varying across the wafer surface. The wafer with the silicon oxide had an average oxide thickness of 49.06 nm with a standard deviation of 0.219 nm. The wafer with the silicon nitride had an average nitride thickness of 52.15 nm and a standard deviation of 0.770 nm. These thickness variation values are acceptable when the thin films are used as optical filters. The complete thickness map, of the silicon oxide and silicon nitride, can be seen in Figure 6.1a and 6.1b, where the wafers are placed with the primary flat near the top of the image.

The anti-reflection properties of the thin film stack were determined using the Filmtek 4000 reflectrometer. The results for a silicon wafer with a 49 nm SiO_2 / 52 nm Si_3N_4 stack and a similar wafer which also have a 150 μm thick layer of PDMS, can be seen in Figure 6.2. The results are compared to a pristine silicon wafer as well as to the simulations from Concise Macleod 8. It can be seen that the optical filter lowers the reflectance significantly and that the reflectance will be below 10 % for near infrared wavelength used in this project. The PDMS layer can be seen to increase the reflection and absorption. Transmittance measurements performed on a slap of 150 μm thick PDMS showed a loss of approximately 5-10 % for visible light and 3-5 % for near infrared light due to specular reflectance and absorption. Furthermore, the reflectrometer is not designed to measure on thick films and it might therefore add uncertainties to the measurement.

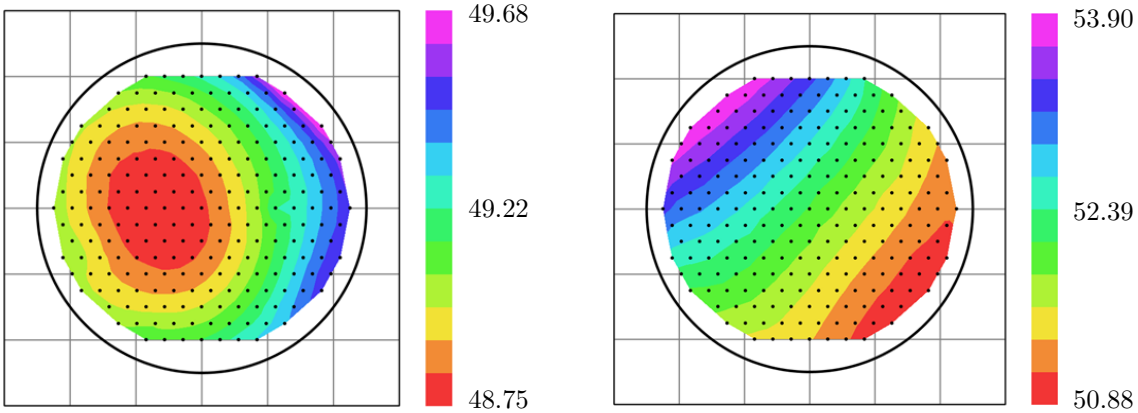

(a) *Thickness of SiO2* (b) *Thickness of Si_3N_4*

Figure 6.1: Ellipsometer measurements showing thin film thicknesses in nanometre on two 4" test wafers. The wafers are placed with the flats near the top. The thickness variation of a dry thermal SiO_2 is shown in (a). The average thickness is 49.06 nm and the standard deviation is 0.219 nm. The thickness variation of an LPCVD Si_3N_4 is shown in (b). The average thickness is 52.15 nm and the standard deviation is 0.770 nm.

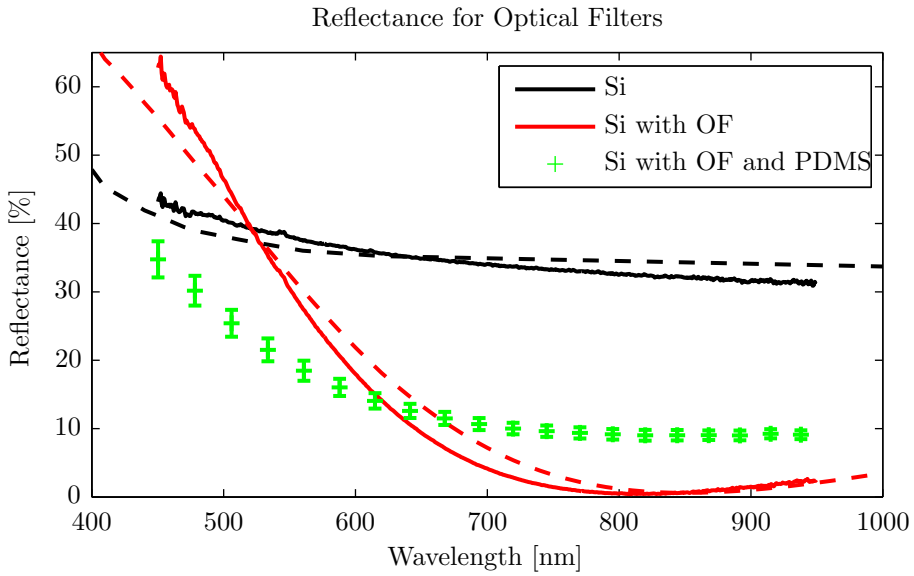

Figure 6.2: Reflectance measurements of a pristine silicon surface, a wafer with the optical filter and a finished device wafer with 150 µm PDMS, performed by a reflectrometer (full lines) and compared to the simulations from Concise Macleod 8 (dashed lines). All measurements are for light of normal incidence. The optical filter, consisting of 50 nm SiO_2 and 50 nm Si_3N_4 can be seen to drastically lower the reflectance for 700-1000 nm light. However, the reflectance and absorbance are increased when the PDMS layer is added.

6.4 Processing of Polyimide and Electrical Interconnects

The HD-8820 polyimide is a relatively new product from HD MicroSystems™ and only a few publications have been presented, which concern this specific product [80–83]. A process guide is supplied with the product but it contains limited information and only specifies the development process parameters when using spray development [84]. We have therefore put the processing of the HD-8820 through a detailed investigation. In general the processing with HD-8820 contains three parts: applying a layer using spin coating, expose and developing the layer and finally curing the layer in order to finalise its electrical and mechanical properties.

6.4.1 Spin Coating of HD-8820

The process guide states that the HD-8820 will adhere well to most semiconductors, ceramics and metals, but special adhesion promoters can be used as alternatives. Furthermore, the guide provides a spin curve for spinning on silicon wafers. We

have tested how adhesion can be improved without promoters and how the layer thickness will depend on spin speed for different surfaces.

The adhesion of HD-8820 was tested for pristine silicon wafers and silicon wafer with thermal silicon oxide, LPCVD silicon nitride or aluminium. Three different pre-treatments were tested and compared to wafers with no treatment: 10 min O_2 plasma cleaning of the wafers, HMDS mono layer treatment and bake out in a 120 °C oven for 30 min. For the pristine silicon wafers a short dip in HF, for native oxide removal, was also tested.

For the adhesion test a 10 μm thick layer was spin coated onto the wafers. The wafers were then baked on a hot plate for 5 min at 120 °C, exposed using a test mask and dose of 600 mJ/cm^2 and finally developed in MF-322 for 90 s. In all cases the adhesion was found to be poor if no pre-treatment was performed. This could be observed by optical microscope images, which showed that the HD-8820 layers had partially detached from the surface. Using an HF dip on the pristine wafers completely solved the detachment problem, making this an effective and fast pre-treatment method for cases where the HD-8820 should be coated onto silicon. The silicon oxide, nitride and aluminium layers showed the same behaviour to the pre-treatment processes. The oxygen plasma was found to have no effect on improving the adhesion, whereas both the HMDS treatment and bake out was successful at improving the adhesion. However, the HMDS treatment caused the HD-8820 to skip off the surface doing dispense resulting in an inhomogeneous film thickness. It was therefore concluded that the best pre-treatment for improving the adhesion was a 30 min, 120 °C bake out of the wafers. Examples of HD-8820 test patterns with poor and good adhesion, are illustrated in Figure 6.3.

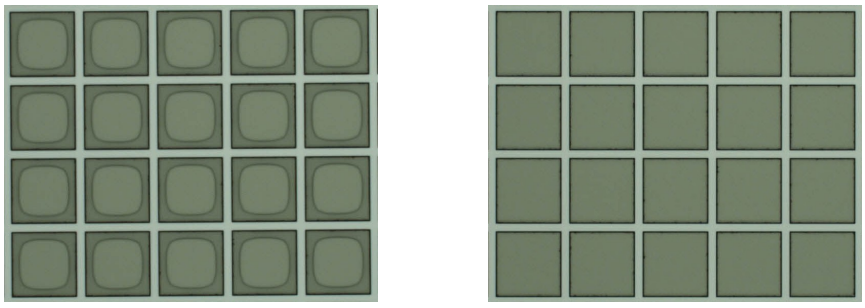

(a) *Poor adhesion* (b) *Good adhesion*

Figure 6.3: Optical microscope images showing test patterns of HD-8820 on a wafer with a silicon oxide surface. The pattern consists of 1 mm × 1 mm squares with 100 µm spacing. In (a) the HD-8820 layer is spin coated on a wafer with no pre-treatment and as a result the layer can be seen to detach, near the centre of the squares, after development. In (b) the wafers have been pre-treated with a bake out and no detachment was observed.

The spin coating tests were performed to both generate spin curves for the HD-8820 for different steps in the process and for different wafer surfaces. The spin speeds were generally kept between 1000 rpm and 3000 rpm. Faster speeds were possible but resulted in film thicknesses that were too thin for our applications and slower speed resulted in inhomogeneous films, which would crack during the curing process.

The first test involved spinning on silicon surfaces and then measuring the film thickness using a profilometer. The measurements were performed on films after the spin and pre-exposure bake, after the exposure and development and finally after the curing. The wafers were in all cases pre-treated with an HF dip and the spinning process was done by dispensing 3 ml HD-8820 on the wafers and then performing a two step spin process. The two steps were a spread spin using 500 rpm for 7 s and then a thinning spin using the desired spin speed for 60 s. The spread spin was introduced because it produced layers with better thickness homogeneity and a smaller edge beak. For both spin steps the acceleration was 500 rpm/s. After the spin the wafers were pre-exposure baked at a hot plate for 5 min at 120 °C. When spinning a layer of HD-8820 on top of another HD-8820 layer, the post spin baking time was increased to 10 min as this would reduce the formation of bobbles in the top layer.

The exposure was done using a dose of 630 mJ/cm^2 and the development

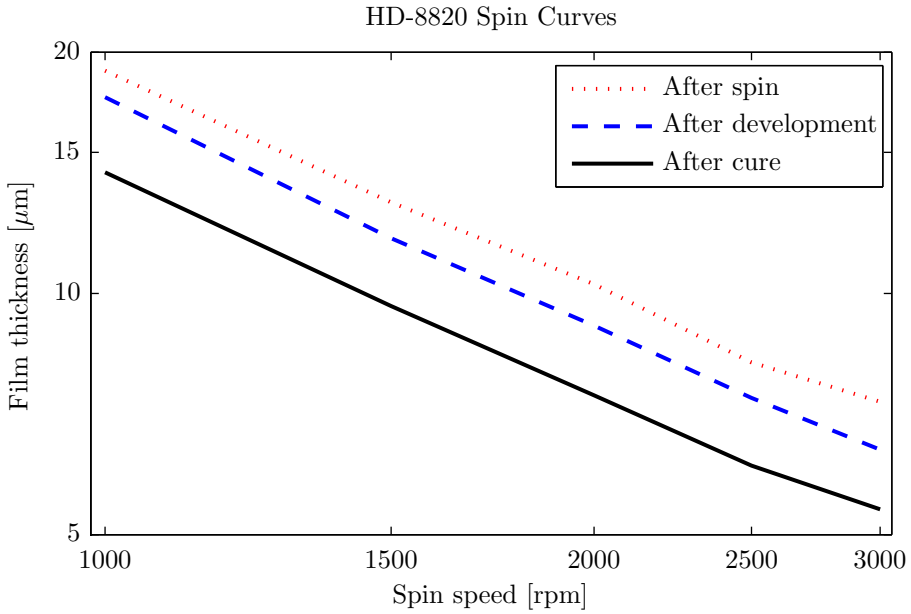

Figure 6.4: Spin curves for HD-8820 on a silicon surface. The resulting average thickness of the HD-8820 is measured after the spinning, after the development and after the curing. It can be seen that the thickness of the HD-8820 will decrease during the processing.

was done by immersion in MF-322 for 90 s. Finally, the curing was done in a nitrogen atmosphere using a slow ramp to 300 °C and keeping the substrate at 300 °C for 1 hour. The resulting spin curves can be seen in Figure 6.4. It can be seen that the spin curves are almost completely straight lines in a double logarithmic plot indicating that the HD-8820 acts as a non-volatile Newtonian liquid [85], as is expected. Furthermore, it can be seen that the thickness of the HD-8820 decreases during the process, but that final thicknesses in the order of 5-15 μm are achievable.

When the devices are fabricated the first layer of HD-8820 is spun onto an LPCVD silicon nitride surface and the second layer is spun onto the first polyimide layer. It is therefore of great importance to know how the final thicknesses of these layer will be, as function of spin speed, in order to fabricate them with a thickness of approximately 9 μm for the first layer and 11 μm for the second layer. These thicknesses should place the electrical interconnects as close to the neutral axis as possible. The spin tests were performed for spin speeds between 900 rpm and 1400 rpm and for the same spin parameters as listed in the first spin test. The result can be seen in Figure 6.5. The spin curves does not show the same straight lines, in the double logarithmic plot, as the previous spin test, but the tendency is still observed. It can be seen that the thickness when spinning the polyimide on polyimide is similar to a spin on silicon but that spinning the polyimide on LPCVD silicon nitride results in a thinner layer. In order to achieve the best placement for the electrical interconnects relative to the neutral axis, the first layer should be spin coated using 1400 rpm and the second layer using 1200 rpm.

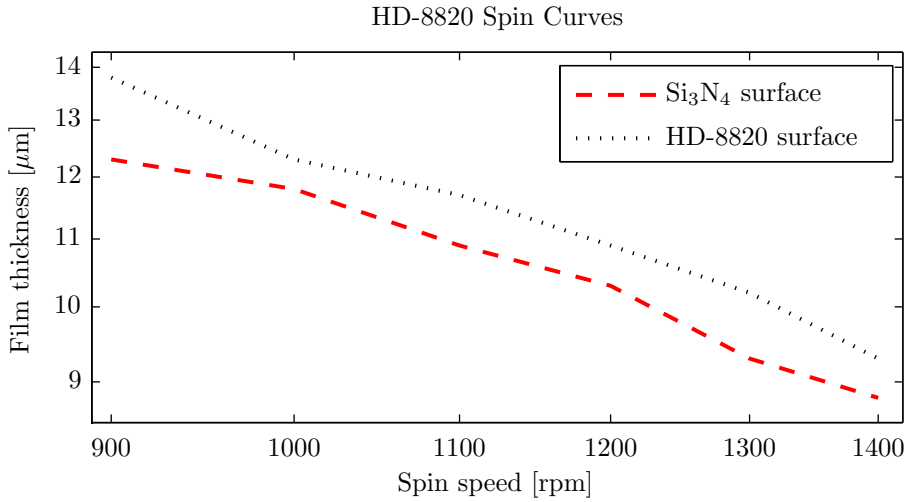

Figure 6.5: Spin curves for HD-8820 on a silicon nitride surface and a semi-cured HD-8820 surface. The resulting average thickness of the HD-8820 is measured by profilometer after the complete process of spin, exposure, development and curing.

6.4.2 HD-8820 Exposure and Development

The HD-8820 is designed for spray development, which will result in resist features with almost vertical side walls. For our application of the HD-8820 we would like the side walls to be sloped in order to make it easier to route the thin electrical interconnects from the top of the thick polyimide to the substrate contacts. This can be achieved using a simple trick where the polyimide is over-exposed, which causes the diffraction near the mask corners to be so significant that it exposes the resist with a high enough dose. Furthermore, we did not have access to spin developing with MF-322, until the very end of this project, which is why we investigated how immersion development could be used instead.

According to the process guide, the minimum exposure level for the HD-8820 is 280 mJ/cm^2 and the development should be done in two steps each using 37 s puddle time. We tested a number of different exposure doses in the range of 420-840 mJ/cm^2 and immersion development times between 60-120 s. The resist patterns were then investigated using scanning electron microscopy (SEM) optical microscopes and a profilometer. As regard the dose no consistent effect was observed on the side wall angle as all the doses and development time resulted in angles of 55-65° after development. Angles in this range would be suitable for our electrical interconnect routing compared to the 80-90° side wall angle that result when using a dose of 280 mJ/cm^2, as can be seen from Figure 6.6. The development time did not have a significant impact on the side wall angle, but times below 90 s were found to be too low for some doses and was consequently not used. The longer times would etch more of the unexposed HD-8820, which is undesirables, so the final chosen

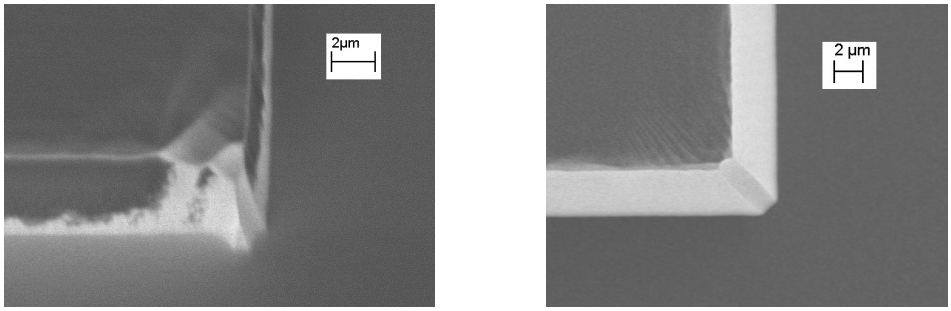

(a) *SEM image of low dose exposure*

(b) *SEM image of high dose exposure*

Figure 6.6: Low vacuum SEM images showing the edges of the developed HD-8820 patterns. The pattern in (a) is exposed using a dose of 280 mJ/cm^2 and developed for 90 s. It has a side wall angle of approximate 80° with respect to the substrate. The pattern in (b) is exposed using a dose of 630 mJ/cm^2 and developed for 90 s. It shows a much lower side wall angle, with respect to the substrate, of approximately 60°.

parameters were a dose of 620 mJ/cm^2 and a development time of 90 s. After development the wafers were rinsed in DI wafer for 5 min. The side wall profile will also change when the polyimide is cured due to shrinkage of the film. This shrinkage would remove the sharp corners still existing between the top surface and the side walls of the polyimide and thus creating an even better profile for routing the thin electrical interconnects. An example of the final profile, which is ideal for routing of electrical interconnects, can be seen in Figure 6.7.

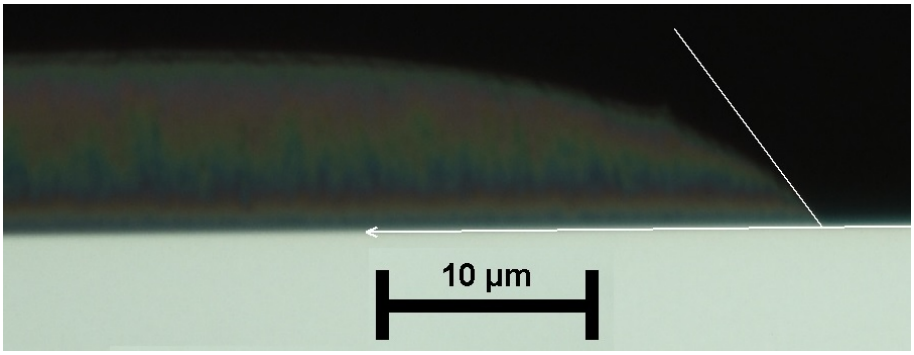

Figure 6.7: Optical microscope image of a cleaved test sample with a finalised layer of HD-8820. It can be seen that the shrinkage of the film, which occurs during the curing process, has removed the sharp corner and instead created an edge, which slowly decreases in thickness across 20-25 µm. The contact angle between the HD-8820 layer and the substrate is approximately 55°.

6.4.3 Curing of HD-8820

In order to finalise the polyimide it has to be cured at a temperature of 250-300 °C for 1-4 hours according to the process guide. However, when multiple layers of HD-8820 should be build on top of each other the first layers will have to be semi-cured and the entire final stack fully cured. The semi-curing process should destroy the photo sensitivity of the polyimide, but not cause the film to cure completely as this would create mismatch in the interface of the layers due to shrinkage. The final quality of the finished films also depends on how the curing is performed. According to the process guide the films should be mechanically superior if the curing is done at higher temperature and shorter times than films cured for longer times at lower temperatures. Furthermore, the HD-8820 film can crack due to stress if heated or cooled too fast, which is why temperature ramping should be investigated.

The curing process for the HD-8820 was tested using two different ovens. The first oven was running at 250 °C with normal air atmosphere and did not have any temperature ramping capabilities. The curing time was 4 hours. The second oven (BCB curing oven) had programmable temperature ramp up to 450 °C and can use

a nitrogen atmosphere. Here the curing was performed at 300 °C for 1 hour but different temperature ramp cycles were tested.

If the wafers were cured in the first oven the HD-8820 films would contain a large amount of cracks covering the entire surface but with a higher concentration near the wafer edge. Secondly, the film would exhibit a distinct colour change from greenish to copper, as seen from Figure 6.8b. This could indicate that the film reacts with oxygen during the high temperature cure. When working with membranes of the cured film it appeared to be brittle and would easily break. When curing films in the second oven, using at temperature ramp of 20 °C/min the film would still

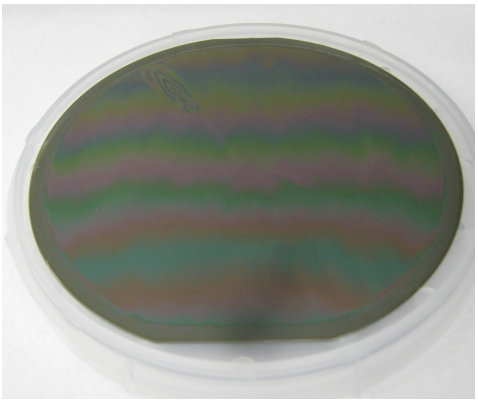

(a) *Cured in N_2 atmosphere*

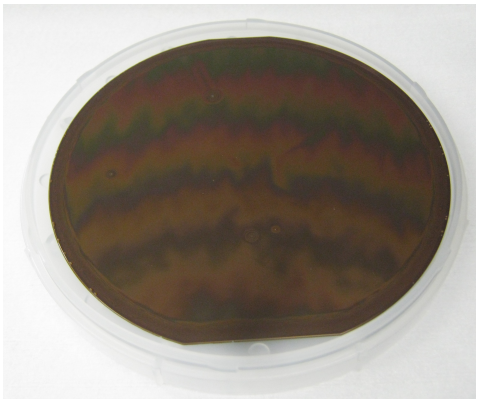

(b) *Cured in air*

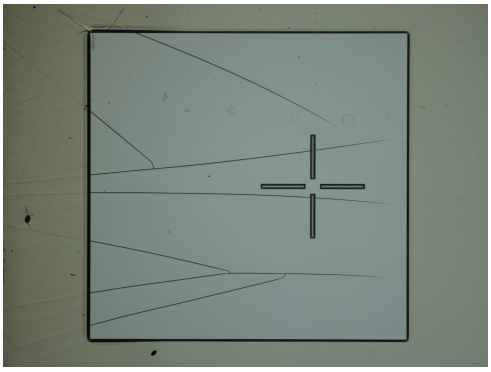

(c) *Cured using fast temperature ramping*

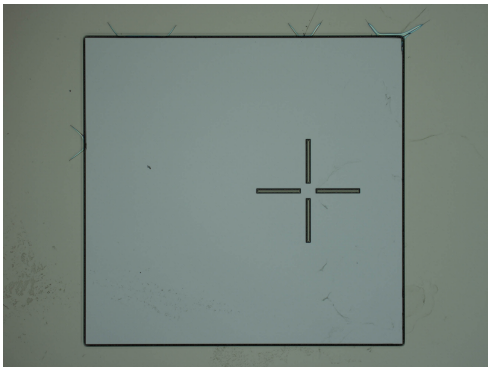

(d) *Cured using slow two step temperature ramping*

Figure 6.8: Investigations of the cured HD-8820 polyimide. When cured in a N_2 atmosphere the film does not show any colour change (a) but a colour change is observed when curing in air (b). The amount of cracks formed in the film during the curing process can be reduced significantly by ramping the temperature. If the ramp is fast many cracks will form in both layers as seen in (c). Using a two step slow temperature ramp, as done in (d), the cracks are few and small in size.

contain a similar amount of cracks but no colour chance was observed, as seen from Figure 6.8a. Film membranes now appeared more elastic. If the curing was performed on a wafer with two layers of HD-8820 the cracking would be even worse and occur in both layers. The amount of cracks was severely reduced by ramping the temperature in two steps during heat up, as can be seen in Figure 6.8c and 6.8d. This was observed for both single and multi layered films. The two steps in the temperature ramp is first a fast heating step from room temperature to 150 °C in 30 min and the a slow heating step from 150 °C to 300 °C in 90 min.

A semi-cure process that destroys the photo sensitivity of the wafers was also developed. At first it was investigated if this step could be performed by simply baking the wafers on a hot plate at 120 °C for longer periods of time. But even at 30 min bake would only lower the photo sensitivity but not destroy it. Instead a ramping process, which is completely similar to the curing process was investigated but in this process the wafers where only held at 300 °C for 5 min and not 1 hour. This resulted in films that were not fully cured, showed no photo sensitivity and could not be etched by the MF-322 developed.

The ability of the HD-8820 films to withstand different process steps were also tested. The process steps included immersion into acetone and MF-322 as well as O_2 plasma using a plasma asher, with 400 sccm O_2, 70 sccm N_2 and a power of 1000 W. The resulting etch rates for the process steps can be seen in Table 6.2.

	Acetone	MF-322	O_2 Plasma
Un-cured	>10,000 nm/min	740 nm/min	260 nm/min
Semi-cured	30 nm/min	∼0 nm/min	80 nm/min
Fully cured	∼0 nm/min	∼0 nm/min	60 nm/min

Table 6.2: Average etch rates in HD-8820 films that are un-cured, semi-cured at 300 °C for 5 min and fully cured at 300 °C for 1 hour. The etch rates were tested in acetone, MF-322 and an O_2 plasma in a plasma asher.

6.4.4 Metallisation

As mentioned in Chapter 5 the metallisation is a two step process. First the substrate contacts are made by a Ti/Al lift-off process and the metal contacts are then annealed to ensure low contact resistance. This is a standard process at DTU Nanotech and was therefore chosen for the first metallisation [86]. Furthermore, HD-8820 was found to adhere well to aluminium if the wafers were treated with a bake out before the spin coating.

The second metallisation should form the electrical interconnects and are made using gold due to its high ductility. The first fabrication attempt was to

use lift-off since this would ensure very precise alignment between the two metallisations. Tests showed that it was possible to make image reversal patterns of AZ 5214E, on top of HD-8820 films, and use these patterns for lift-off of gold. The gold was found to partially detach from the polyimide surface during the lift-off but this could be solved by evaporating a 20 nm Ti adhesion layer. However, the lift-off method was found to cause problems for the metallisation. First, the immersion in acetone caused the formation of cracks in the bottom layer of the polyimide, as can be seen in Figure 6.9a. In the most severe cases the cracks would sever the electrical interconnects but a number of devices were found to maintain conductivity in the interconnects despite the formation of cracks. However, electrical characterisation of the devices showed that none of the diodes had working connections. Investigation by SEM identified the cause to be horizontal cracks in the gold that appeared at the top corner of the HD-8820 layer, as seen in Figure 6.9b. Tests showed that the HD-8820 would absorb acetone, during the lift-off process, causing the layers to swell and forming the cracks in the polyimide and gold.

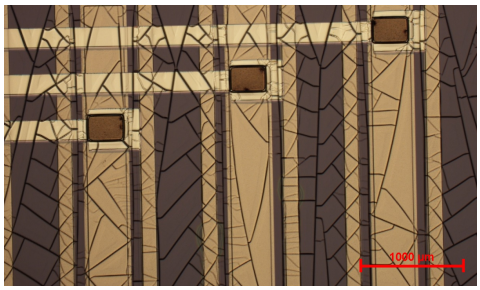

(a) *Cracks in bottom polyimide layer*

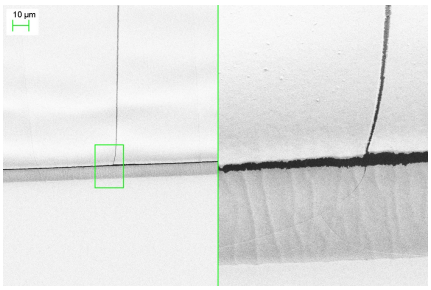

(b) *SEM image of cracks in the gold*

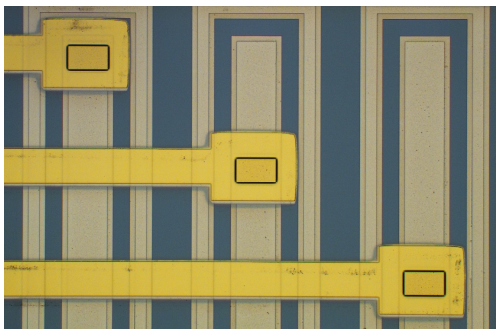

(c) *Electrical interconnects fabricated using deposition through shadow mask*

Figure 6.9: Images of the gold electrical interconnects. The lift-off results are shown in (a) and (b). The process caused the formation of cracks in both the polyimide and gold. The problem was solved by depositing the metals for the electrical interconnects through a shadow mask, as seen in (c).

A feasible solution was to evaporate the Ti and Au through a shadow mask. The shadow masks were made from 525 μm thick wafers with the pattern etched all the way through the wafer. The shadow masks were clamped to the device wafers using semiconductor tape and could be aligned with fairly good precision of ± 50 μm in the x and y directions, as shown in Figure 6.9c.

6.4.5 Multi Layered Electrical Interconnects

A final test was performed, which investigated the possibility of fabricating multiple layered electrical interconnects. All the devices fabricated during this project consist of only a single metallisation encapsulated between two polyimide layers. But if 2D square array devices were to be fabricated consisting of many functioning detectors, the electrical interconnects would have crossed each other and thus be routed in two metallisation layers encapsulated in three polyimide layers.

Wafers with two layers of test electrodes and three layers of 10 μm thick HD-8820 were fabricated. First a layer of HD-8820 was spin coated on a wafer and semi-cured. The first metallisation step was then evaporated through a shadow mask. The second polyimide layer was spin coated, exposed, developed and semi-cured before the final metallisation was deposited. Finally, the third HD-8820 layer was spin coated, exposed, developed and the wafer was fully cured. The two lithography steps had removed the HD-8820 at contact pads so the cross, 400 μm wide, metallisations could be probed. The final result can be seen in Figure 6.10b.

The impedance of two 400 μm wide interconnects, which crosses each other orthogonally, was measured using an Agilent 4294A impedance analyser. The fre-

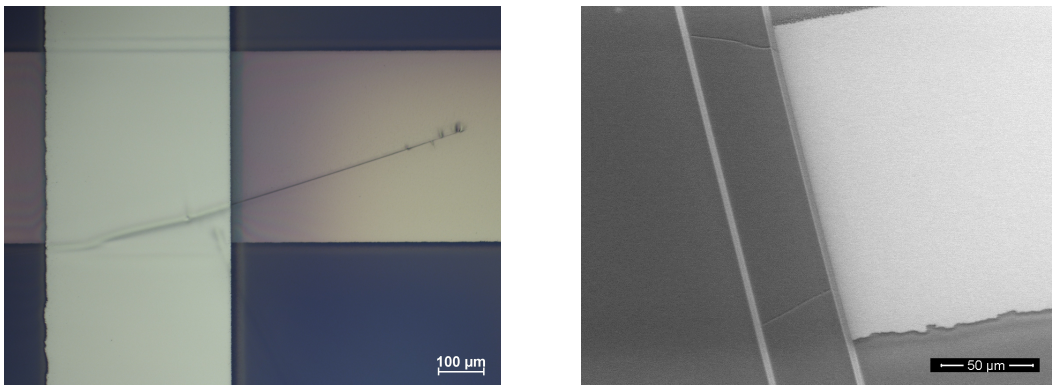

(a) *Two electrodes crossing each other* (b) *Double opening of HD-8820*

Figure 6.10: The fabricated test wafers with two metallisation layers and three HD-8820 layers. An optical microscope picture of two electrical interconnects crossing each other with a 10 μm thick layer of polyimide in between, is shown in (a). The SEM image in (b) shows the opening of the top and middle layer of HD-8820 down to the bottom interconnect.

quency was swept from 100 Hz to 10 MHz and the resulting impedance can be seen in Figure 6.11. It can be seen that the impedance will be mega-ohm for lower frequencies, which indicates that the 10 μm thick layer of HD-8820 has excellent dielectric properties. For NIRS tissue oximetry the devices will typically run at a few Hertz, but if the flexible device platform should be used for other application, e.g. CMUTs, the operating frequency will be a few mega-Hertz. At this frequency the impedance drops to kilo-ohm, which might not be adequate. This could be solved by spinning multiple layers of HD-8820 between the crossing interconnects thus increasing the dielectric strength of the film.

The final consideration would be how to route the electrical interconnects, so they would all be placed near the neutral axis at the flexible joints. One possible solution may be to only make the interconnects cross each other on the silicon areas and then keep all interconnects in the same plane and clamped between two layers of polyimide at the joints.

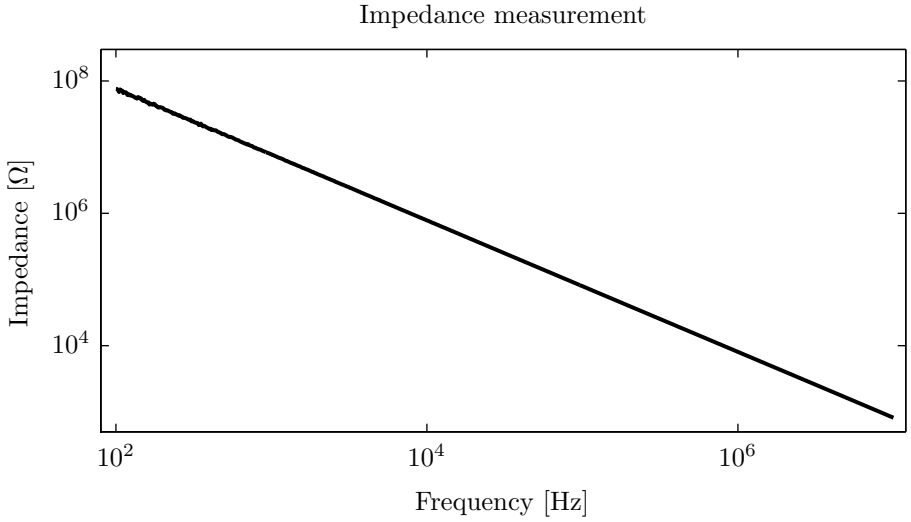

Figure 6.11: Impedance measurement performed on two 400 μm electrical interconnects that crosses each other orthogonally. The interconnects are separated by a 10 μm thick layer of HD-8820. The straight decreasing line in the double logarithmic plot shows that the interconnect crossing behaves as a capacitor as expected. The impedance will be in mega-ohm for low frequencies and kilo-ohm for high frequencies.

6.5 Silicon Deep Etching and PDMS Casting

The deep etch process serves two purposes for the devices. It defines the individual detectors and creates the trenches, which will become the flexible joints. It is a very critical process step because wafers might become damaged or unrecoverable

if something goes wrong during the etch. The final steps concerning PDMS spin coating and device release are also critical because of the difficulties in removing unwanted PDMS and damage inflicted upon the devices if they are diced out by a semiconductor saw.

6.5.1 Deep Etching of Devices

Two different approaches for doing the deep etch, on the majority of the wafers, were carried out in this project. A third method was also tested on a few wafers but it was not found to be feasible. All deep etching in this project is performed using the Bosch process. The reason that two different methods were used on the majority of the wafers is due to the fact that the first implemented method suddenly ceased to function and instead damaged the devices to an extent where they could not be recovered. The two different methods are depicted in Figure 6.12.

The first method was conceived as the simplest idea for doing the deep etch. In this method all the high temperature processes were first carried out and then the back side metallisation and polyimide were applied. Finally, the deep etch was performed by etching through the front side of the wafer, using photo resist as an etch mask and stopping on the polyimide. During the deep etch the device wafer was bonded to a carrier wafer using Crystalbond^{TM} 509. This etch was performed on DTU Danchips DRIE machine a Pegasus from SPTS. Most of the devices fabricated during this project were etched by this method with an acceptable yield. From time to time the etch would locally punch through the photo resist and damage the devices by etching away the optical filter and creating holes into the device surface. No explanation could be found as to why the process would occasionally fail, but insufficient cooling of the back side provided by helium, might be the cause.

After using this etch method for the first half of the project the method suddenly failed completely when fabricating a batch of devices. There were two reasons for the failure of the etch method. Firstly, the selectivity between the photo resist and the silicon decreased, which meant that even relatively thick layers of photo resist were inadequate at masking the 300 μm deep etch. The resist appeared to be over heated and turned grey as illustrated in Figure 6.13a. Secondly, it was observed that the polyimide was damaged by heating and would appear burned and locally detach from the wafer surface, as seen in Figure 6.13b. The exact reason of this problem is still not known, but the characteristics indicate a problem with insufficient cooling. The insufficient cooling can be caused by the fact that the heating is generated on the front side of the device wafer during the etch and that the cooling is delivered to the back side of the carrier wafer. The heat will have to drain through the device wafer, through the polyimide stack, through the crystal

bond and then finally through the carrier wafer. A simple cooling test with crystal bonded dummy wafers showed that the heat conductance of the HD-8820 layer was poor, so the problem is most likely caused by overheating of the device wafer.

In order to solve the problem the second etch method was derived. The etching process was done by using the advanced silicon etcher from SPTS, which is available in the DTU Danchip cleanroom. This deep etching tool is older than the Pegasus and therefore etches slower with lower selectivity between silicon and photo resist, however, it also generate less heat. The deep etch process was tested on a batch of dummy wafer and the following conclusions could be made: the deep etch process did not damage the polyimide layers as was seen on the Pegasus. It was not feasible

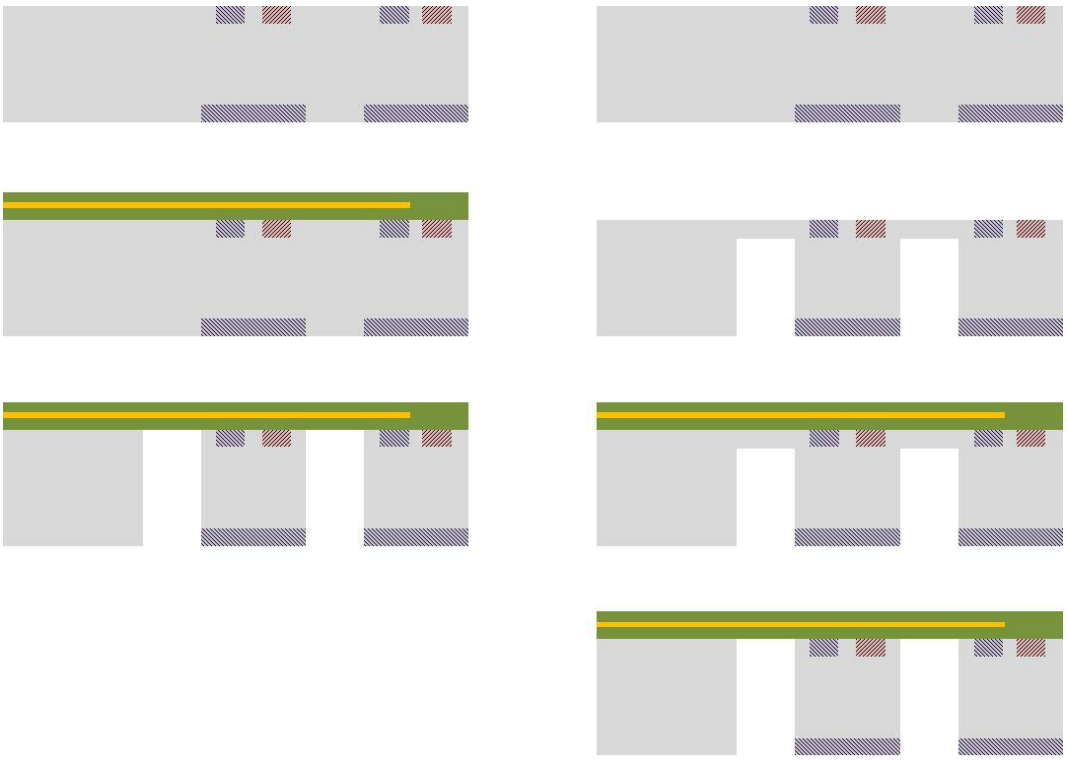

Figure 6.12: Schematic drawing showing the cross section of the devices during the processing with the two different etch methods. The initial method is shown as the three drawings to the left and the new method is shown as the four drawings to the right. In both cases all the high temperature process steps are performed as the first steps. In the initial method this was followed by the creation of the metallisation and polyimide on the back side and then followed by deep etch through the front side. In the new method the deep etch was partially performed until an approximately 50 µm membrane of silicon was left. The metallisation and polyimide were then created and finally the remaining silicon membranes were etched away in the trenches. The deep etch masking for the first etch method was done using photo resist and for the second process aluminium was used.

to use photo resist for the deep etch process due to the low selectivity. If polyimide layers were present on the back side of the wafer it would cause the deep etch Bosch process to over passivate so the process would only etch approximately 100-150 μm into the silicon. This problem was again most likely due to overheating of the device wafer. Finally, if no polyimide layers were available on the back side of the device wafer the deep etch process worked without any problems.

With these observations in mind we developed the deep etch method shown in Figure 6.12 using a 200 nm thick aluminium layer as etch mask instead of photo resist. The deep etch process was then spilt up in two parts: first etching until approximately 50 μm of silicon were left, then building up the back side layers and finally etching the remaining 50 μm of silicon. The deep etch process could etch away the 50 μm of silicon without having problems with over passivation. Another advantage of using aluminium as etch mask is that this mask would survive the numerous process steps that are located in between the two deep etch steps. The MF-322 polyimide developer would etch the aluminium, but only with approximately 25-30 nm during the 90 s development steps.

As mentioned a third method for doing the deep etch was tried. It was only tested while the deep etch process on the DRIE Pegasus was still working. The idea behind this method was to create a spring like structure in the polyimide at the flexible joints. Hopefully, this could potentially increase the flexibility of the devices in a similar manner to conductors formed on pre-stretched elastomer substrates [87]. The process was performed by first creating and then semi-curing the bottom layer of HD-8820. The deep etch was then performed and the metallisation and top layer

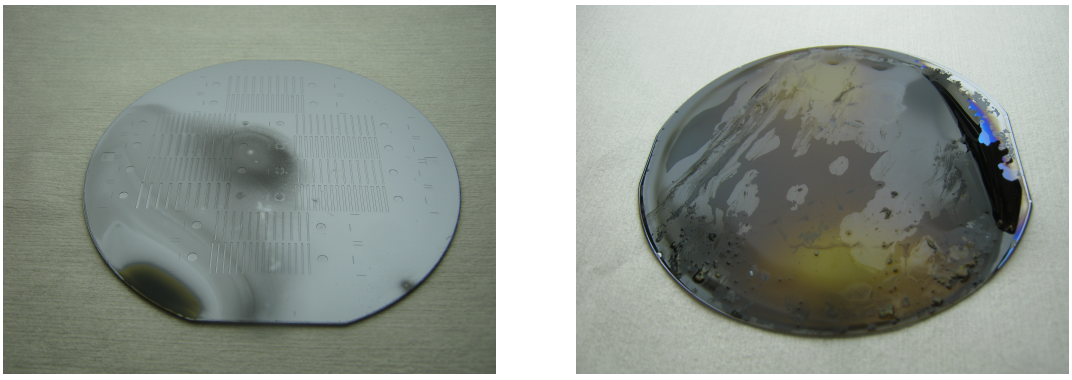

(a) *Damaged photo resist* (b) *Damaged polyimide*

Figure 6.13: Images of a device wafer that has been damaged during the deep etch. The front side of the wafer is shown in (a). Only a very thin layer of resist is left on the wafer after etching 50 μm into the silicon. The back side of the wafer can be seen in (b). It has a 20 μm thick "dummy" layer og HD-8820. The layer can be seen to be burned due to its colour change and at some parts of the wafer it has detached from the surface.

of HD-8820 was created before the final curing. The process succeeded in creating bulging in the gold interconnects and polyimide at the flexible joints, as can be seen from Figure 6.14a. However, the process would occasionally fail due to cracks on the metallisation and the polyimide membranes that were created after the deep etch, would not always survive the subsequent process steps, as seen in Figure 6.14b. But testing of the devices showed an improvement when the test devices where stretched longitudinally as will be presented in Section 7.1.

6.5.2 PDMS Spin Casting

PDMS spin casting is a relative standard process at DTU Nanotech. It is performed out side of the cleanroom and consists of mixing the PDMS, removing air bobbles from the PDMS in a desiccator, thinning down the PDMS by spinning and finally curing the PDMS. Before the work carried out with the PDMS, the wafers were given a short O_2 clean in a plasma asher, since this would remove the remaining passivation from the deep etch process and improve the adhesion of the PDMS to the silicon. During the spin coating the device wafer is still bonded to the carrier wafer used during the deep etch. This ensures that the back side of the device wafer is not contaminated with PDMS.

Two different types of PDMS were tested: Sylgard 184 and MDX4-4210 both from Dow Corning. The PDMS was mixed according to its standard amounts from the data sheets. The mixture was left in the desiccator for 1 hour and then thinned down by spinning. A microscopic analysis showed that 30 min or 45 min in the

(a) *Bulging polyimide membrane* (b) *Cracks in polyimide membrane*

Figure 6.14: Optical microscope images of the polyimide membranes from the third etch method. In (a) a finished electrical interconnect is shown crossing the trench where the silicon has been etched away. It can be seen that the polyimide will bulge at the areas where the silicon has been removed. Problems occurring during this process were amongst other cracks in the bottom polyimide layer as shown by the back lit image in (b).

desiccator were not enough to remove all air bobbles although the PDMS appeared fine by the naked eye. The curing was performed at 65 °C for 2 hours. A curing time of 1 hour should be enough at 65 °C, but it was observed that the PDMS would not always be cured near the polyimide interface, but this was solved by simply extending the curing time to 2 hours. The optimal PDMS thickness was approximately 150 μm. The resulting thickness, as function of spin speed, can be seen in Figure 6.15.

When the Sylgaard 184 was thinned down it was observed that the thinning process would not always result in a layer with a homogeneous thickness. The problem occurred at the flexible joints where the PDMS would be thinner. The problem was a function of both spin speed, as it occurred less frequently for lower speeds, and the width of the flexible joints, as wider joints made the problem more likely to occur. Examples of homogeneous and inhomogeneous thicknesses can be seen in Figure 6.16. If the spinning speed was kept low, i.e. at 500 rpm, the resulting film had a homogeneous thickness for trench widths up to 500 μm.

6.5.3 Device Releasing

All the devices were designed with the purpose of being diced out using a semiconductor saw. The 1D devices were still framed to the silicon wafer after the deep etch and were not released until diced out. The 2D devices are, however, fully released from the silicon wafer after the deep etch, so only the PDMS and polyimide are fixating them to the wafer. It is therefore essential that they are still bonded to

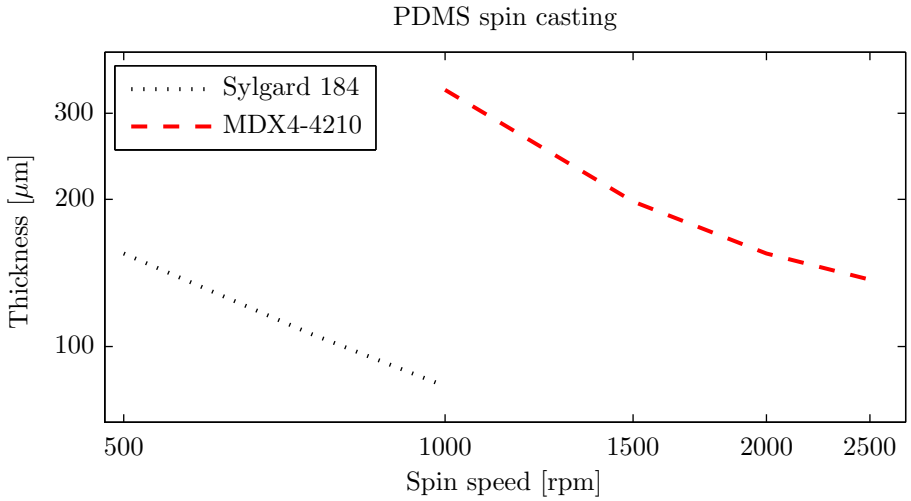

Figure 6.15: Spin curves of Sylgard 184 and MDX4-4210, showing the average thickness. It can be seen that in order to achieve a thickness of approximately 150 μm the Sylgard should be spin coated with 500 rpm and the MDX4-4210 with 2000 rpm.

the carrier wafers in order to avoid any out of plane displacement of the individual detectors, which could potentially damage the electrical interconnects.

All the "smaller" 1D devices, see Section 5.1, were diced out using the saw with a resulting high yield. The best method for dicing the devices was to cut all the way through the device wafer and half way into the carrier wafer. The devices could then be broken out while still being attached to the carrier wafer. The devices were then separated from the carrier pieces in warm DI water.

However, when the 2D devices were diced out using the same method it resulted in a low device yield due to damaged electrical interconnects. The devices were still firmly attached to the carrier pieces after the dicing so the cause of damage is most likely due to mechanical vibrations. This problem could be solved by using a scalpel to instead cut the devices out manually.

The same problem occurred for the final generation of "larger" 1D devices. These devices could unfortunately only be released by dicing since they were still attached to the wafer after the deep etch. For all the tested devices the electrical interconnects were only intact for a few but not all of the individual detectors, meaning a device yield of 0 %. The cause of the failure was traced by measuring if the electrical interconnects would maintain their conducting ability during the final process steps. It showed that the damage to the interconnects only occurred during the dicing process. Unfortunately, the final batch of devices was not ready until the end of this project so there was not enough time to test possible solutions. It is also not known why the "smaller" 1D devices could be diced out without any

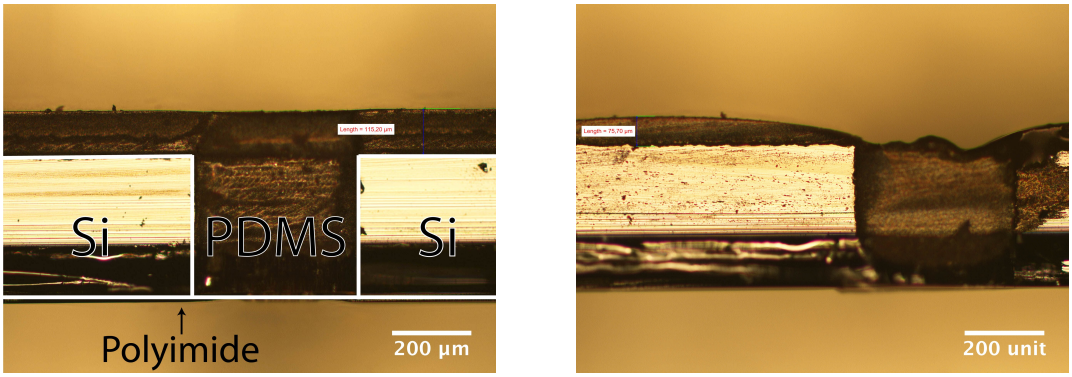

(a) *Cleaved test sample showing a homogeneous layer of PDMS*

(b) *Cleaved test sample showing an inhomogeneous layer of PDMS*

Figure 6.16: Optical microscope images showing the profile of cleaved devices with a flexible joint width of 400 µm. In (a) The Sylgard 184 is spin coated using 500 rpm and it is seen that this will result in a homogeneous layer of PDMS on the front side of the device. In (b) the spin speed is increased 750 rpm and as a result the thickness of the PDMS layer become inhomogeneous at the flexible joint.

problems while the "larger" 1D devices would fail. The only design difference of the two devices are their widths and therefore the lengths of the etched trenches that forms the flexible joints.

One possible solution could be to either add a frame around the devices when the deep etch is performed, so the devices can be cut out by scalpel. However, this might make the wafer too fragile if too many devices should be fabricated on each wafer. Alternatively, the thickness of the polyimide layers could be increased. As was shown with the investigation of the multi layered electrical interconnects the HD-8820 layers can easily be build on top of each other, so instead of using two 10 μm thick layers for encapsulation, several of such layers could be applied.

6.6 Black Silicon and Al_2O_3 Coating

As mentioned in Chapter 4 it was investigated if the performance of the infrared detectors could be improved by using black silicon nanostructures as an anti-reflection surface, which would lower the reflectance for light of all angles of incidence. Moreover, depositing aluminium oxide as surface passivation layer could potentially reduce the reverse bias current and also improve the quantum efficiency. Both of these processes were tested on batches consisting of test chips.

Regarding the black silicon we tested two different fabrication methods, which resulted in two different types of nanostructures. Both fabrication methods were dry etching processes and developed by R. S. Davidsen as part of his Ph.D. project concerning the optimisation of solar cells [88]. The first method used a RIE machine with low power and the second method used an ICP DRIE machine with high power. Both processes used O_2 and SF_6 as gasses. The RIE etch was performed for 10 min and etched approximately 1.1 μm into the silicon surface. The result was pyramid shaped nanostructures with a height of 100-300 nm. The second process ran for 16 min and etched 3.8 μm into the surface. The result was here needle like structures with a height of approximately 1.5 μm. SEM images of the two types of black silicon nanostructures can be seen in Figure 6.17a and 6.17b. Both types of structures have a random topology.

The Aluminium oxide layers, tested in this project, were deposited using a Picosun R200 ALD. The layers will normally be deposited at temperatures above 300 °C, but we wanted to test if layers of sufficient quality could be deposited at lower temperatures, due to the fact that the HD-8820 layers would be present on the device wafer during this process step. Low temperature deposition has been proven to function [89]. In order to achive very low surface recombination velocities the aluminium oxide will have to be annealed after deposition at temperatures of around 400 °C [90]. This is again not possible due to the polyimide present on the

wafer so we will test how well the un-annealed layers work.

Layers were deposited using a 250 °C process and 294 cycles, which produced a thickness of approximately 30 nm. The deposition was tested in etched trenches and the result can be seen in Figure 6.17c. The ALD process can be seen to have deposited a layer of aluminium oxide on the side walls and it is therefore a feasible method for adding surface passivation to the etched out detectors. The black silicon nanostructures were also investigated using SEM after the deposition, and it was observed that the roughness of the RIE etched nanostructures would be reduced by the 30 nm thick layer of Al_2O_3. This could potentially nullify the anti-reflection effect of the nanostructures but then thinner layers of aluminium oxide could be deposited.

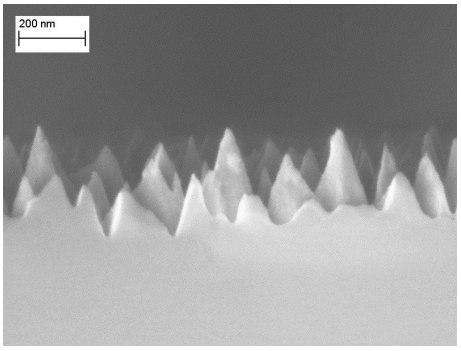

(a) *Black silicon nanotructures fabricated by RIE*

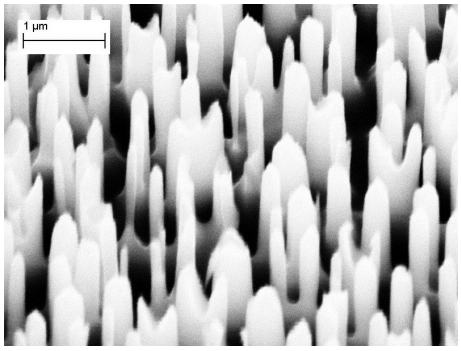

(b) *Black silicon nanotructures fabricated by ICP DRIE*

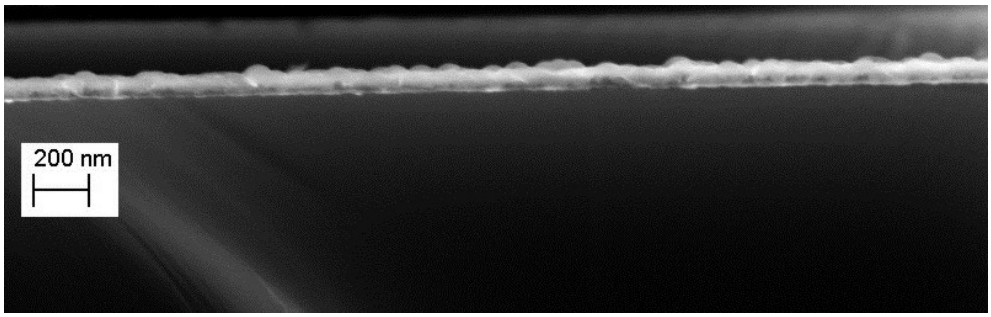

(c) *Al_2O_3 layer deposited using ALD*

Figure 6.17: SEM images of the two different types of black silicon nanostructures and a cleaved test sample with 30 nm Al_2O_3 deposited by ALD. The structures shown in (a) are made by RIE. They resembles pyramids and have a height of 100-300 nm. The structures shown in (b) resembles needles and have a height of approximately 1.5 µm. They are fabricated using ICP DRIE. Both types of structures have a random topology. A SEM image, of a cleaved test sample, showing the aluminium oxide layer that has been deposited on the side wall of the etched trenched can be seen in (c).

6.7 Summary

This chapter presented an overview of the process development that has been carried out in order to optimise the fabrication process flow. The development process has been split into four major parts. The first part considered the thermal processes in which a diffusion from BSG was used for p-type doping with boron to a final peak concentration of 5×10^{19} cm^{-3} and $POCl_3$ was used for an n-type doping with phosphorous to a final peak concentration of 3×10^{20} cm^{-3}. Both doping processes were masked by wet thermal oxide. It was also investigated that the optical filter could be made with sufficient uniformity across the entire wafer.

The process investigation regarding the HD-8820 polyimide identified methods for improving adhesion and minimising the formation of cracks during the curing process. An exposure and development method for creating low angle side walls was also developed. Multi layers of HD-8820 and metallisation can successfully be fabricated.

The deep etching of the individual detectors was found to be difficult but a secondary process flow solved the problem, albeit at the expense of a more complicated fabrication process. The devices could be finalised with a problem less spin casting of PDMS but the device release process was found to be problematic for the final generation of 1D linear array devices and the 2D square matrix devices. Finally, the processing of black silicon nanostructures and ALD coated aluminium oxide were investigated as improvements for the photo detectors.

Chapter 7

Test and Characterisation of Devices

The quality of the different device types will have to be investigated in order to determine, if the device designs are feasible solutions. The devices have been tested and analysed mechanically and electrically and these results and discussions of the results are presented in this chapter.

The 1D linear array and the 2D square matrix device platforms have been tested mechanically using both qualitative and quantitative methods. The qualitative test showed the behaviour of the devices when being handled and the quantitative test defined the limits of the mechanical performance of the devices.

The electrical analysis of the devices is composed of I-V measurements and quantum efficiency measurements. The I-V measurements will then determine if the etched out devices can perform acceptably and if the ALD coatings will improve this performance. The measurements of the quantum efficiency can determine if the detectors are of high enough quality and if the ALD coating and black silicon nanostructures offer improvement.

7.1 Mechanical tests of the Flexible Device Platforms

Both the 1D linear array and the 2D square matrix device platforms were tested in order to evaluate their performance. Firstly, this was done qualitatively by simply observing if the devices could be handled in a manner that would be expected of them. It was observed that the devices could be handled with the fingers, be bent around the forearm, be bent around the index finger, be stretched slightly by being pulled between the fingers and being bent for days without any indication of

damage to the device or electrical interconnects. However it was also observed that the devices could not withstand vertical displacement between the joints, as this would sever the electrical interconnects. Another qualitative observation was that devices with narrow silicon areas and wide flexible joints, i.e. a small A/B value as defined in Chapter 3, would feel much more flexible and would easier confine to curved surfaces compared to devices with relatively large silicon area widths or large A/B values. The 2D square matrix devices were observed to confine better to most surfaces. This is most likely due to the fact that they can be bend in the longitudinal direction while still being bent slightly in the transverse direction.

If the devices were deliberately destroyed by pulling them apart it was observed that the electrical interconnects would be severed first and then the polyimide would break before the PDMS would detach from the silicon as would be expected. Measurements that showed the behaviour of the electrical interconnects when the devices were bent, stretched and twisted were performed in order to give a more precise definition of the device limitations.

7.1.1 Bending Tests

The bending tests were performed by bending the devices, in the longitudinal direction, across discs with a varying radius of curvature, as shown in Figure C.1, in Appendix C. At the same time the resistance of the electrical interconnects was measured using a four-wire measurement method and a Keithley 2700 multimeter. The devices were kept at constant room temperature and the resistance was averaged over 60 s and 300 samples. The results for the 1D linear arrays are presented in Figure 7.1, which shows the relative change in resistance as function of curvature. The curvature is given as the reciprocal value of the radius of curvature. The devices used for this test all had silicon areas that were 1 mm wide, i.e. $A = 1$ mm and flexible joints, i.e. B values, which were 100 μm, 200 μm or 400 μm wide. The initial resistance was, on average, measured to be: 26.61 Ω, 26.26 Ω and 27.32 Ω for the test sensors with the 100 μm, 200 μm and 400 μm wide joints, respectively. These resistances correspond to an average sheet resistance of 65 mΩ/sq for the electrical interconnects, which is close to the theoretical value of 61 mΩ/sq. It can be seen that the relative change in resistance is almost negligible for all three designs even for relative large curvatures. One design criteria was that the devices should be able to be bent to 90° over their full length. Bending the entire flexible area of the linear array to 90° corresponds to a curvature of approximately 107 m^{-1}, which can be seen to have no effect on the electrical interconnects. Furthermore, it can be seen that maximum curvature corresponds to almost a bending of 180° over the full length of the devices, and even at this level the electrical interconnects still function

as expected.

Similar tests were performed on the 2D square matrix devices. The relative change in resistance was in the same order as for the 1D devices, i.e. approximately 0.2 % for a curvature of 100 m^{-1}.

The durability of the devices, when being bent, were also tested. This was done using an automated setup build from LEGO® mindstorms. The devices were fixed in one end and a lever was used to push the opposite end so the device would bent to 90° over its full length, as shown in Figure C.2. The lever then moved back thus relaxing the device. This process was repeated in cycles of approximately 4 s using 2 s to bend the device and 2 s to relax the device. An example of a resistance measurement is shown in Figure 7.2a. After 10,000 cycles no change in resistance and no wear were observed in the electrical interconnects when examined by optical microscopy. This test was also performed on the 2D square matrix devices and the result was the same with no change in resistance observed after 24,000 bending cycles.

The 2D devices were also bent by transverse twisting. The devices contained both an outer and an inner electrical interconnect for testing, as was shown in Figure 5.3b. The non-flexible end of the chip, with the connection pads, was fixed at

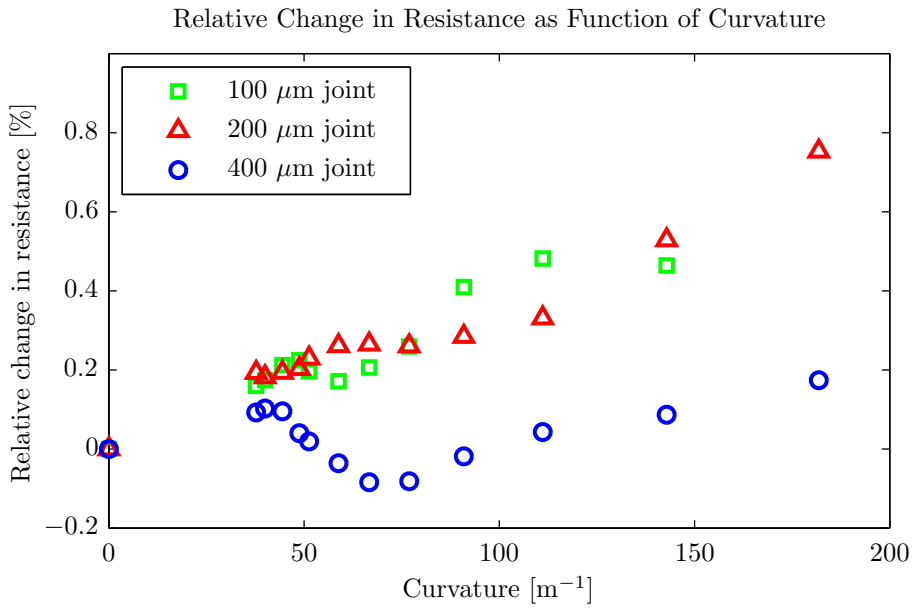

Figure 7.1: Plot of the relative change in resistance as function of curvature. The figure shows the average measurement from three different device designs all using 1 mm wide silicon areas and 100 μm, 200 μm or 400 μm wide flexible joints. In all cases the relative change in resistance is negligible and the devices can be bend to more than 90° over their full length.

a stationary position while the other end was fixed at a twisting arm. The twisting arm was set to move up and down by ±20° while the resistance in the two electrical interconnects was measured. Each twist cycle lasted approximately 1 s. The outer electrical interconnects were seen to break immediately. The inner electrical interconnects would not break immediately but instead the resistance was seen to slowly increase due to wear. After approximately 4.5 hours the inner interconnects would also break, as can be seen in Figure 7.2b.

7.1.2 Stretching Tests

The devices are not designed to withstand stretching. This would change the pitch between the detectors and result in inaccurate spatially measurements. However, they should still be able to withstand being handled, which could potentially mean that they are stretched longitudinally. As mentioned the qualitative test showed that the electrical interconnects did not break when the device was handled carefully but also that the interconnects could be broken by simply stretching the devices using the fingers.

The amount of strain that the devices could withstand was measured by an-

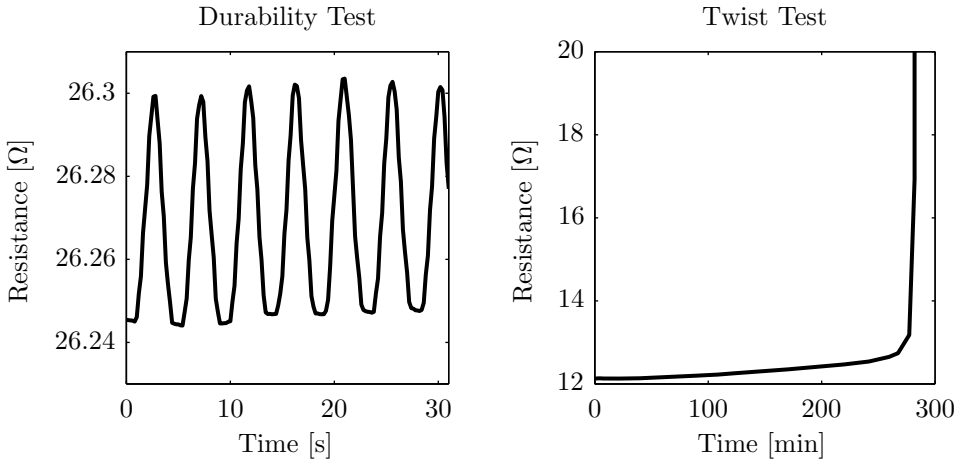

(a) *Bending test of 1D device over time* (b) *Twisting test of 2D device over time*

Figure 7.2: Resistance measurements over time when the devices are bend or twisted. The bending test is shown in (a) where no change in resistance was seen after 10,000 bends. The graph shows how the resistance of the interconnect increases when the device is bend and returns to the initial value when the device is released. The result from a twisting test is shown in (b). The outer interconnect, which is subjected to the largest amplitude of the twist, broke immediately. The resistance of the inner interconnect is seen to slowly increase until the interconnect finally fails after 4.5 hours.

choring the devices to a holder, which could be displaced using a micrometer screw. The devices were then placed in their neutral position and then stretched by 10 μm steps while measuring the resistance of the electrical interconnects. The measurement setup can be seen in Figure C.4 in Appendix C.

The measurements were performed on both 1D array and 2D matrix devices but also the 1D devices fabricated using the special technique, which resulted in bulging polyimide and interconnects across the flexible joints, as shown in Section 6.5.1. For both the 1D and 2D devices the resistance was seen to increase immediately after the strain was applied. The devices could typically withstand a strain of up to approximately 3 %, in their flexible joints before the interconnects would break. A measurement example is presented in Figure 7.3, which shows a relative increase in resistance of 0.75 % before the electrical interconnect breaks. A measurement of a similar straining of two devices fabricated using the alternative deep etch method, with resulting bulging, is presented in Figure 7.4. It can be seen that the relative change in resistance only increases slowly as a function of strain up to approximately 5.5 % strain for a device with 200 μm wide joints and 6 % strain for a device with 400 μm wide joints. After this point the resistance will increase abruptly and finally the interconnects will break.

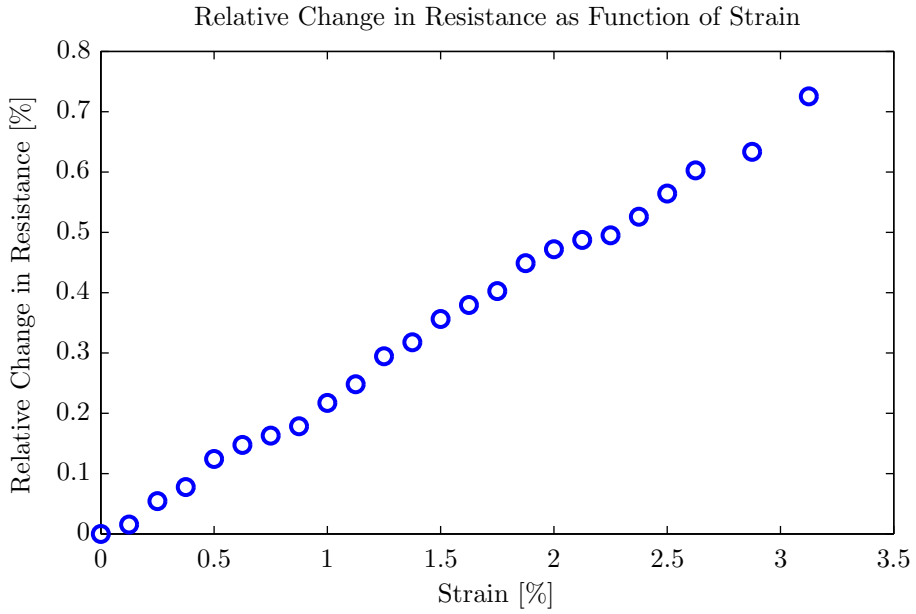

Figure 7.3: Relative change in resistance measured as function of strain in the flexible joints when the device is stretched longitudinally. The resistance change can be seen to be linear as a function of straining. Above 3 % strain the electrical interconnects will break with a maximum relative change in resistance of approximetely 0.75 %.

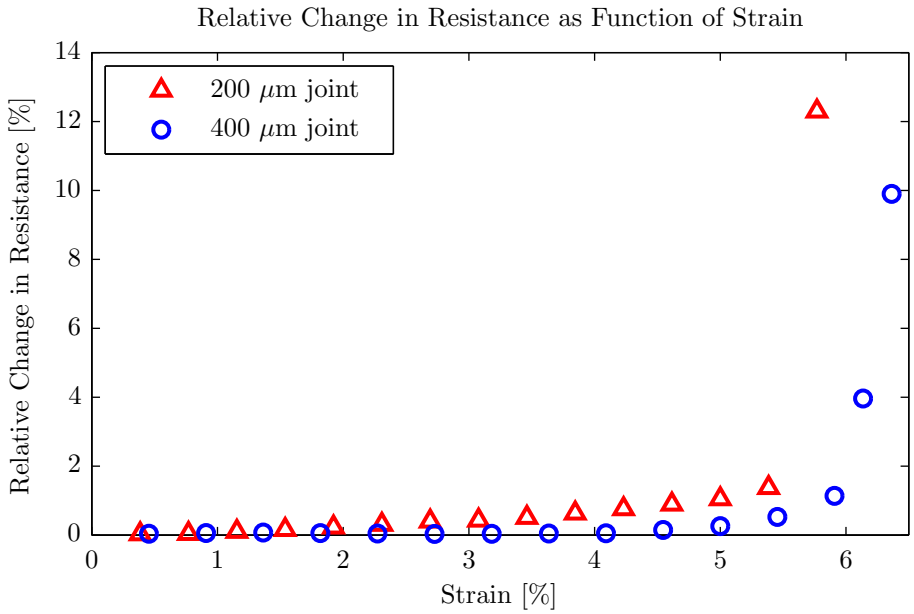

Figure 7.4: Relative change in resistance measured as function of strain in the flexible joints when the devices, with bulging interconnects across the flexible joints, are stretched longitudinally. The measurements are performed on devices with both 200 μm and 400 μm wide joints. The resistance only increases slowly until a strain of approximately 5 % where the resistance increases abruptly and finally the interconnects breaks.

7.1.3 Discussion

When analysing the results from the bending tests it is evident that the platform for this sensor is both durable and capable of introducing flexibility to the array or matrix of silicon detectors. Although, a variation of approximately 0.5 % in the measured electrical interconnect resistance from sensor to sensor occurs, the relative change in resistance is seen to be negligible when the sensor arrays are bend up to 90°. This bending ability is, however, still outperformed by other presented devices i.e. [91]. If the idea with the neutral axis design worked perfectly there should be no change in resistance when the devices are bend. But these measurements indicate that the concept does not truly apply. This could be both due to the fact that the interconnects are not placed exactly at the neutral axis or because the composite beam model, used in Chapter 3, is too simple. Since the sensor platforms can be bend thousands of times, without indications of fatigue in the electrical interconnects, they show adequate durability for clinical use.

The stretching test showed that the sensor array can be stretched to an amount which correlates to a strain of approximately 3 % in the flexible joints while having only a small resistance increase in the electrical interconnects. The strain, which

causes fracture in the bulging electrical interconnects is in the order of 6 %. It has been reported in [54] that free standing metal thin films will fracture at a strain of typically 1 %, so placing the metallisation in a sandwich structure of polyimide ensures increased durability to longitudinal strain for the sensor array. The higher strain for the bulging devices indicates that the bulging interconnects are first straightened out and then strained. It could be an advantage to have twice as large fracture strain for the electrical interconnects but as mentioned in Chapter 6 the fabrication process is no longer possible and when it worked it did show some problems that lowered the yield. The 6 % fracture stain is not as high as for electrical interconnects fabricated directly for the purpose of being stretchable. In [92] fracture strain of up to 32 % is reported, when fabricating micro-cracked gold thin film on PDMS substrates. However, it is also reported that delamination between gold and PDMS substrate is a problem. This is not a problem that is observed for our design where the gold is completely encapsulated.

The relation between the relative change in resistance and the strain is called the gauge factor G and is given by:

$$G = \frac{\Delta R}{R\epsilon} = \frac{\Delta R}{R}\frac{L}{\Delta L} \tag{7.1}$$

where R and L are the initial resistance and length respectively and ΔR and ΔL are the change in resistance and length respective. Linear fitting to the stretching measurements, like the one shown in Figure 7.3 can be used to find the gauge factor however since part of the interconnects are located on the silicon and will not be strained the initial length should be the entire lengths of the interconnect. This results in gauge factors between 1.2-1.5. The gauge factor for thin gold films were determined in [93] to be approximately 2. The lower gauge factor that we are observing could indicate that even the interconnects fabricated using the normal methods do have some spring effect.

Besides being bendable and somewhat stretchable the advantage of the flexible platforms is a relatively simple fabrication process, which results in electrical interconnects with low resistivity. The sheet resistance of the 400 nm thick gold interconnects was measured to be 65 mΩ/sq. This sheet resistance is much lower than the reported values for other flexible gold conductors e.g. 1 Ω/sq in [92]. Here, the larger sheet resistance is a consequence of the very thin layers of gold, which is needed to form micro cracked metal films. If our electrical interconnects are compared to other approaches of making flexible conductors the same picture is seen. In [94] silver particles are introduced into PDMS to form flexible and stretchable conductors. This results in a resistivity of 3.33×10^{-5} Ωm, which corresponds to a sheet resistance of approximately 80 Ω/sq, for a conductor which has the same thickness as the gold interconnects used in our project.

7.2 I-V Measurements

The I-V measurements have been performed using an HP 4145B semiconductor parameter analyser. All measurements were performed in complete darkness and shielded by a metal cage. Many types of devices were tested and also at different steps in the fabrication process, including diodes still on the wafer. The majority of the devices were fabricated with detectors that had unpassivated side walls but the effect of Al_2O_3 coatings were tested in the last part of the project.

7.2.1 Unpassivated Detectors

The pn-junction diodes will operate in reverse bias when used as detectors. However, the diodes can still show some interesting properties concerning their performance when operated in forward mode. Figure 7.5 shows the average I-V measurements performed on the eight detectors in a 1D linear array device with at detector size of 9.5 mm × 3.0 mm. The measurements are performed at different stages in the fabrication: firstly, when the device is still on the wafer and no deep etching has been performed. Then after the deep etching process, which now generate unpassivated side walls and finally after the device has been diced out and the measurement is performed through the electrical interconnects. The detectors are compared to an Osram BP-104-FAS pin-diode [95]. In the forward direction the diodes behave similarly except for the final flexible devices, which exhibit a larger series resistance due to the resistance in the electrical interconnects and the contact resistance between the substrate metallisation of the interconnects. In reverse bias the effect of etching out the devices can clearly be seen as it increases the reverse bias current. The photo detectors are clearly outperformed by the commercial Osram pin-diode in reverse bias.

A more detailed investigation of the forward bias behaviour is presented in Figure 7.6. It is evident that the detectors do not follow the behaviour of an ideal diode described by Equation 4.2, where the ideality factor $n = 1$:

$$I = I_S \left[\exp\left(\frac{qV}{nkT}\right) - 1 \right] \tag{7.2}$$

Instead the fit to the measurement is made using a high injection diode equation [96]:

$$I = I_S \frac{\exp\left(\frac{qV}{nkT}\right) - 1}{\frac{1}{2} + \frac{1}{2}\sqrt{1 + k_h\left(\exp\left(\frac{qV}{nkT}\right) - 1\right)}} \tag{7.3}$$

where k_h is the high injection parameter. The fitted values are: $I_S = 3.75 \times 10^{-10}$ A, $n = 1.088$ and $k_h = 6.90 \times 10^{-5}$. The series resistance of the device can also be ex-

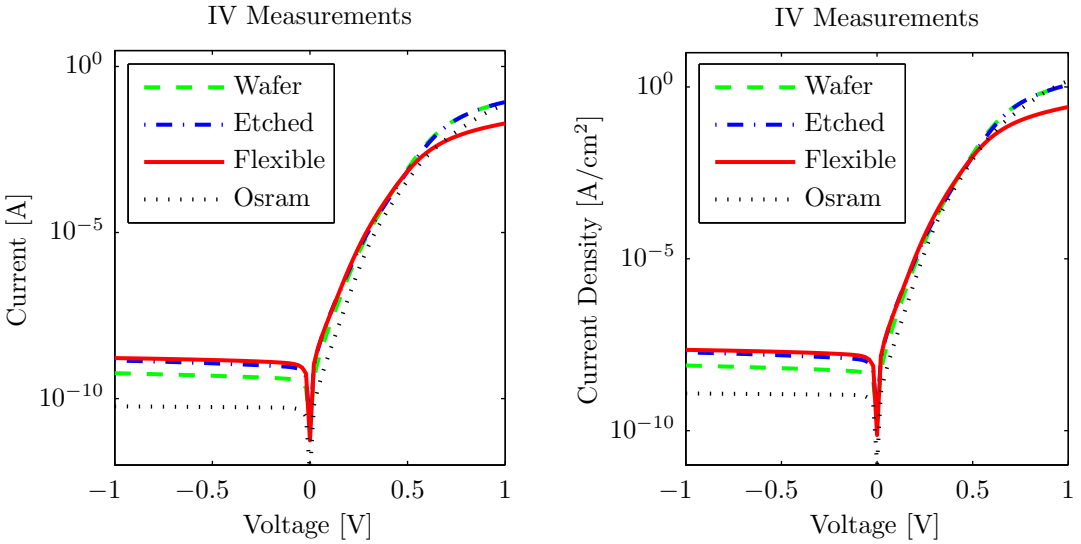

(a) *I-V measurements of current* (b) *I-V measurements of current density*

Figure 7.5: I-V measurements performed on an array of eight 9.5 mm × 3.0 mm photo detectors. The measurements are performed at different points in the fabrication process: on the wafer, etched out, full flexible device and finally compared to a commercial available infrared detector. The measurements are performed from -1 V to 1 V and the resulting current is plotted in (a) while the current density is plotted in (b).

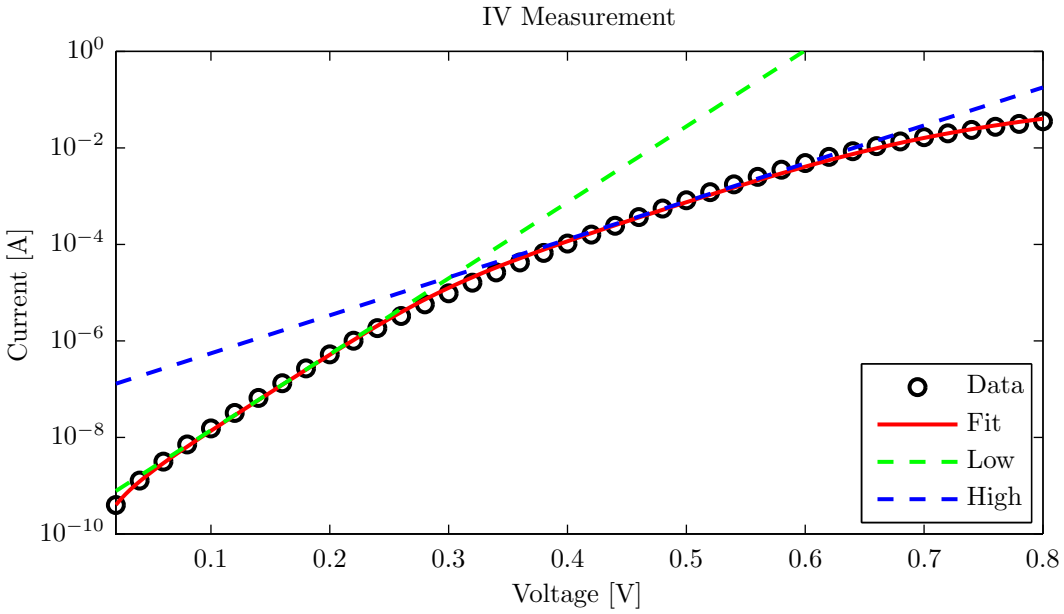

Figure 7.6: I-V measurement performed on a 9.5 × 3.0 mm pn-diode from 0-0.8 V. Equation 7.3 has been used to generate the fit. The diode can be seen not to follow the ideal diode equation, with n = 1, for voltages higher than 0.3 V. Here, it enters high injection state where n = 2. finally, above 0.65 V the series resistance begins to dominate.

tracted using:

$$V = V_a - R_S I \Leftrightarrow R_S = \frac{V_a - V}{I} \tag{7.4}$$

where V_a is the applied voltage from the outside (V is the junction voltage from Equation 7.3) and R_S is the series resistance. For the above fit the series resistance is found to be 2.0 Ω. Also plotted in Figure 7.6 are the fits for low and high injection where Equation 7.2 has been using with $n = 1$ and $n = 2$, respectively. The diode can be seen to be in low injection up to 0.3 V, then enter high injection up to 0.65 V where the series resistance then begins to dominate.

The reverse bias properties of the devices were also investigated on "wide" detectors: 9.50 mm × 3.00 mm with a junction area of 7.40×10^{-2} cm^2 and "narrow" detectors: 9.50 mm × 1.25 mm with a junction area of 3.33×10^{-2} cm^2. The current density when sweeping the bias from -1 V to -10 V is presented in Figure 7.7 together with the measurement of the Osram BP-104-FAS pin-diode. There are eight measurements of both the "narrow" and "wide" detectors. These measurements have been performed on detectors from different wafers from two production batches. It can be seen that there is fair homogeneity for the devices. At -5 V the average current density and standard deviation for the narrow and wide detectors are: 67.6 ± 14.4 nA/cm^2 and 34.6 ± 5.44 nA/cm^2. This is, however, a significantly higher current density than for the Osram diode, which has: 1.45 nA/cm^2.

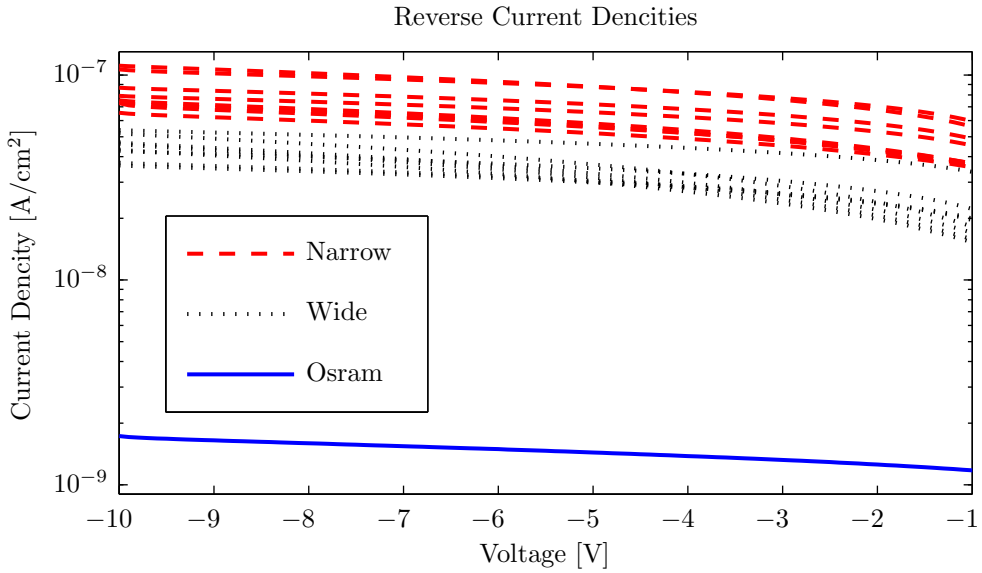

Figure 7.7: Reverse bias measurements performed on eight "narrow" detectors and eight "wide" detectors. The detectors are compared to the Osram BP-104-FAS pin-diode. At a reverse bias of 5 V the "narrow" and "wide" devices have a current density of: 67.6 ± 14.4 nA/cm^2 and 34.6 ± 5.44 nA/cm^2, respectively.

7.2.2 Detectors Passivated with Al_2O_3

In order to test the effect of covering the etched out side walls with Al_2O_3 some test chips were fabricated. The test chips were all 10 mm long and for this test either 10 mm or 1.5 mm wide. The 10 mm wide diodes had a distance between the pn-junction and the side walls of 2 mm whereas this distance was only 400 μm for the 1.5 mm wide diodes. Essentially, this would mean that ALD coating would not have any effect on the 10 mm wide diodes but might lower the reverse bias current for the 1.5 mm wide devices.

The measurements were performed on three 10 mm and three 1.5 mm wide devices, both before and after the ALD coating. The average current density is plotted in Figure 7.8. It can be seen that the current densities for the 10 mm wide diode are approximately the same before and after the ALD coating (it actually increases slightly after the coating). For the 1.5 mm wide diode a decrease is observed as expected. However, the decrease is only from an average of 26.5 nA/cm^2 to 18.7 nA/cm^2, corresponding to approximately 8 nA/cm^2 or a 30 % decrease, and it is still a much higher value than for the Osram BP-104-FAS pin-diode.

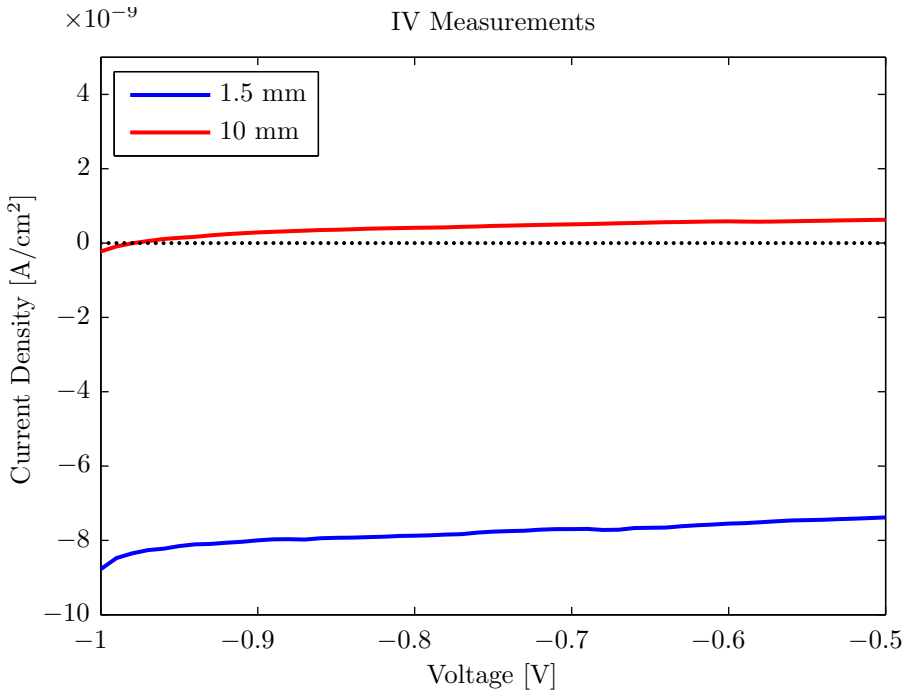

Figure 7.8: The average difference in reverse bias current density for 1.5 mm and 10 mm wide diodes, before and after ALD coating. Positive values indicate an increase and negative value a decrease after the coating. It can be seen that there is no change for the 10 mm wide diodes, which is expected. The 1.5 mm wide diodes exhibits an average decrease of approximately 8 nA/cm^2. However, this decrease is only 30 % from the initial value.

7.2.3 Discussion

It is clear from Figure 7.5 that the performance of the detectors are lowered when they are etched out. When the detectors are etched out in one direction and latter diced out in the other direction the resulting unpassivated surfaces cause an increase in reverse bias current and thus a larger dark current. This effect can also be seen from Figure 7.7 where all the measured detectors have reverse bias current densities that are much higher than the Osram BP-104-FAS pin-diode. Commercial photo diodes with even lower reverse bias currents exist, e.g. the S1133-01 from Hamamutsu [97], which has a reverse bias current density well below 1 nA/cm^2. Adding a 30 nm thick layer of Al_2O_3, using a 250 °C ALD process, was seen to lower the reverse bias current for the narrow detectors. However, the decrease was only 30 % and the ALD coated narrow detectors were still outperformed by both the wider uncoated detectors and the commercial diodes.

If the reverse bias of the detectors is compared to other back side photo diodes fabricated at the DTU Danchip cleanroom facility, during the past years, it reveals fairly good values of down to 12 nA/cm^2, as can be seen in Table 7.1.

The analysis of the diode in forward bias indicated well functioning devices. The diodes would exhibit ideal behaviour for low voltages and then move into high injection mode for higher voltages. It can be seen from Figure 7.6 that Equation 7.3, although relatively simple, can be used to generate precise fits. The low series resistance indicates that the p+ substrate doping, although kept at a moderate surface concentration, would function well for the formation of an ohmic contact.

	A	B	C	D	E	F	G	H
V_R [V]	-0.5	-0.5	-0.5	-0.5	-5.0	-0.5	-0.5	-1.0
A_J [mm^2]	7.4	33.64	6.51	1.0	N/A	0.4	4.84	6.16
J_R [nA/cm^2]	12	5.3	39	30	280	100	1.1	0.14
Flexible	Yes	No	Yes	Yes	No	No	No	No

Table 7.1: Comparison of the reverse bias current density from several devices marked as A to H. The listed device parameters are: V_R, the reverse bias at which the measurement is performed, A_J, the junction area and finally J_R, the reverse bias current density. (A) the best unpassivated 9.5 mm × 3.0 mm detector, from a finished 1D linear array. (B) The lowest measured reverse bias current, which was measured during this project. It was measured on a 10 mm × 10 mm test diode that had been ALD coated. (C) The best 5.3 mm × 2.75 mm n-type detector fabricated in 2012 by A. Thyssen [72]. (D) the best 2D diode fabricated by J. D. Thomsen [73]. (E) the best p-type detector fabricated in 2008 by S. Duun [55]. (F) Best device fabricated by A. M. Jorgensen in 2002 [60]. (G) The Osram BP-104-FAS pin-diode [95]. (H) The Hamamatsu S1133-01 diode [97].

7.3 Quantum Efficiency Measurements

The quantum efficiency of the detectors was measured using a Jobin-Yvon H-20 monochromator setup with a wavelength step of 10 nm. The setup was calibrated by using an 818-UV reference photo detector from Newport. For each wavelength step, a light beam from the monochromator was directed through a collimator lens, a beam restrictor with a 1 mm pinhole and finally focused onto the detector by an objective. When infrared light was used a filter was placed in front of the monochromator in order to remove 2nd order effects. The diameter of the focused spot was measured to be approximately 300 μm. The generated photo currents were then measured by using a Keithley 6485 picoammeter. The measurements were performed in complete darkness so only the light beam from the monochromator excited carriers in the photo detectors. Due to noise and the limited precision of the monochromator, tests on commercial diodes showed that the measured quantum efficiency will have an uncertainty of ± 3 %. Images of the quantum efficiency measurement setup can be seen in Figure C.5 and C.6 in Appendix C.

The quantum efficiency for the detectors can be calculated by using the relation between the measured current for the detectors and the current for the reference detector, if the two detectors are illuminated by the same light beam:

$$\eta = \frac{I}{I_{\text{ref}}}\eta_{\text{ref}} \tag{7.5}$$

where η_{ref} is the quantum efficiency of the reference detector and I_{ref} is the measured current in the reference detector. Since the quantum efficiency of the reference detector is known, the current for the reference detector and the detector, which is to be investigated, should be measured.

7.3.1 Detector Size

During the many measurements of the quantum efficiency it became evident that the detector size would influence the quantum efficiency as is described by Figure 4.6. The focused spot was directed at the centre of the detectors, which would mean that large detectors would suffer very little from the recombination centres located at the unpassivated side wall, whereas small detectors would experience a decrease in quantum efficiency due to recombination. This effect was investigated on a number of test detectors that were fabricated in the same manner as the real detectors. All the test detectors were 10 mm long but were varying between 1.5 mm and 10 mm in width.

The average internal quantum efficiency for light with a wavelength of 700-1000 nm was measured and the result is presented in Figure 7.9. It can be seen

that the internal quantum efficiency is approximately constant for devices with a width between 4 and 10 mm. For widths of 3 mm and below the internal quantum efficiency can be seen to decrease. Since, the measurements are performed by focusing the beam spot at the centres of the detectors, the resulting internal quantum efficiencies show the very best performance of the detectors. If the light beam was scanned across the detector surface, the result would be an average internal quantum efficiency, which would be lower than the values presented in Figure 7.9.

7.3.2 Devices with Optical Filter

The quantum efficiency of the many prototype devices, as well as the final generation of 1D linear array device, were measured. All of these devices utilised the optical filter and were covered with a 150 μm layer of PDMS, giving then an approximate reflectance as shown in Figure 6.2. The measured detectors are from the following devices: (A) the final generation of p-type 1D linear array arrays with 2.50 mm $\times$ 9.50 mm detectors; (B) n-type prototype 1D linear array with 2.75 mm $\times$ 5.30 mm detectors; (C) similar as (B) but with 1.00 mm $\times$ 5.30 mm detectors;

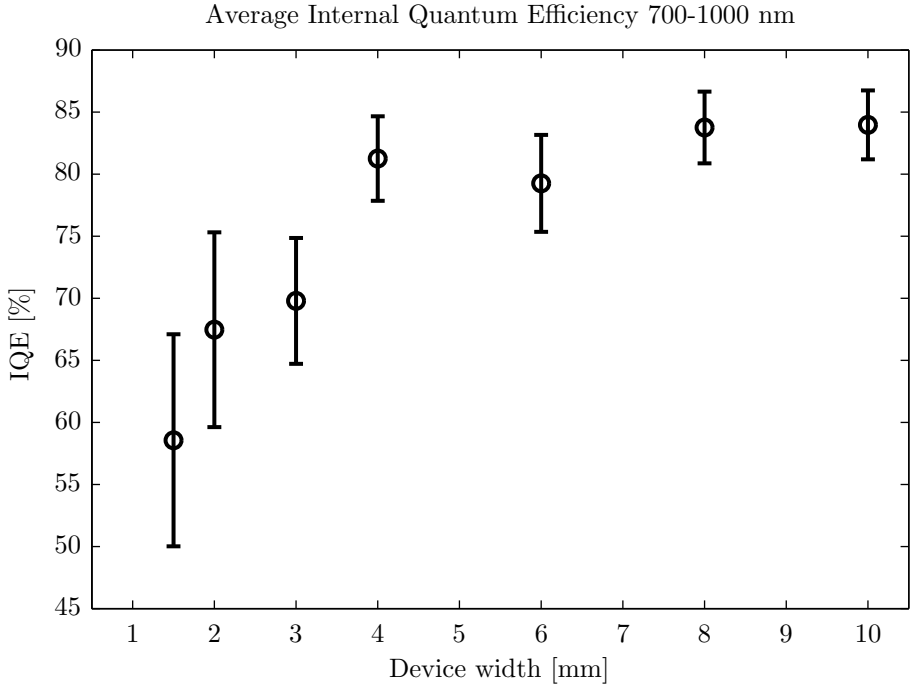

Figure 7.9: Measurements of the internal quantum efficiency for a number of devices with a varying width but constant length of 10 mm. The internal quantum efficiency will approximately be constant for devices with a width between 4 and 10 mm but will decrease for device widths below 4 mm.

(D) 2D square matrix device with p-type 2.00 mm × 2.00 mm detectors. The measurements are presented in Figure 7.10. It can be seen that the wider detectors are outperforming the narrow detectors as expected. The different devices exhibit a similar behaviour by having increasing but low quantum efficiencies for 400-700 nm light and larger more constant quantum efficiencies for the near infrared light (700-1000 nm). However, the final generation of detectors (A) show a sharp increase in quantum efficiency between 900-1000 nm.

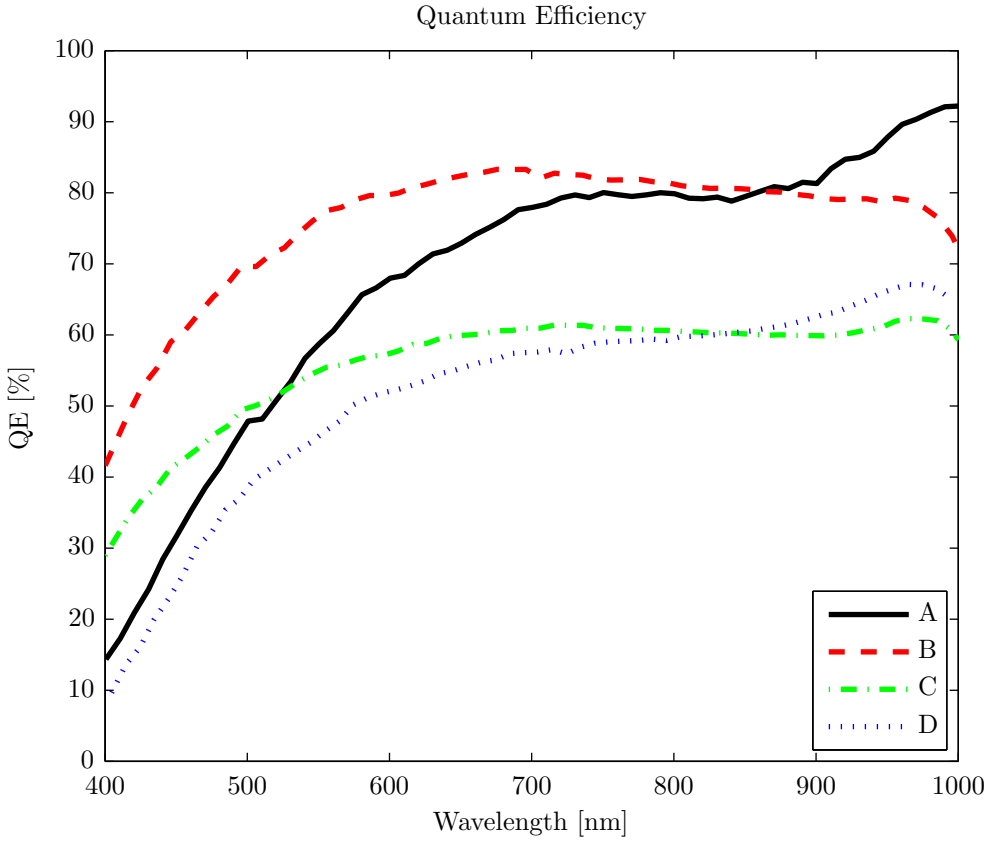

Figure 7.10: Average quantum efficiency for four different detectors that have been fabricated during this project. All the detectors have the optical filter and are covered with a layer of PDMS. (A) is the 2.50 mm × 9.50 mm detectors that are located on the final generation of 1D flexible array devices. They are fabricated using 300 µm thick p-type substrates. (B) and (C) are two types of detectors from 1D flexible array prototypes. They are both fabricated using 350 µm thick n-type substrates. They have the same length of 5.30 mm but different widths, with 2.75 mm for (B) and 1.00 mm for (A). It is clear that the narrow detectors exhibits a lower quantum efficiency. Finally, the quantum efficiency of the 2 mm × 2 mm detectors from the 2D square matrix devices is shown in (D). They are fabricated using the same substrates as (A) but their small size and four etched out side walls reduce the quantum efficiency.

The average quantum efficiencies with the detector to detector variation are also plotted in Figure 7.11, for wavelengths between 700-950 nm. Light sources for NIRS tissue oximetry will typically utilise this wavelength interval. It can be seen that there is no significant difference between the p-type and n-type detectors. The detectors from the 2D square matrix device exhibit a larger variation when compared to the detectors from the 1D linear arrays.

7.3.3 Devices with Black Silicon Nanostructures and Al_2O_3

The major goal of the black silicon nanostructures was to act as an anti-reflection surface for light incident at many angles. This was tested by comparing the reflectance of silicon wafers, which had surfaces with either the SiO_2 / Si_3N_4 optical filter or the black silicon nanostructures. The reflection for the optical filter was measured at different angles using an ellipsometer, which offers a good inspection of the reflectance due to the specular reflecting properties of the thin dielectric films. However, a similar measurement of the black silicon surfaces will not result in a true description of the reflecting properties because the nanostructures will cause

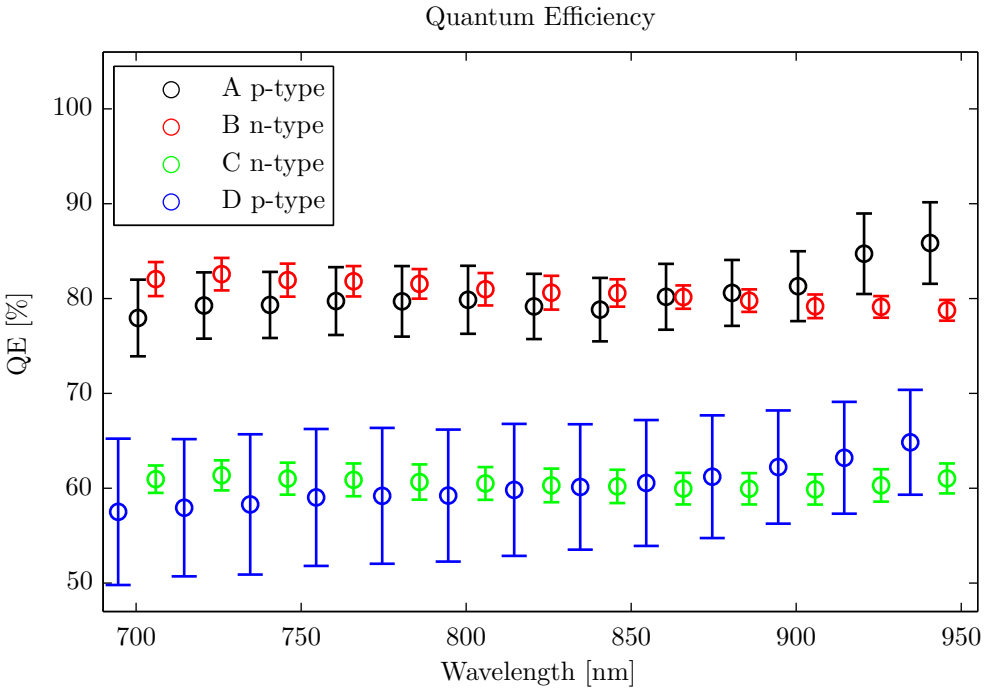

Figure 7.11: The average quantum efficiency for detectors A to D, here shown with the detector to detector variation. The plot is made for 700-950 nm, which is a typical working regime for NIRS tissue oximetry. It can be seen that there is no noticeable difference in quantum efficiency between n-type and p-type detectors of the approximately same size.

the reflecting light to be scattered in all directions. Using an ellipsometer would therefore make the black silicon surfaces appear more anti-reflective than they truly are. The reflectance of the black silicon surfaces have therefore been measured using an integrating sphere. The reflectance of the two surfaces are presented in Figure 7.12 and it can be seen that the black silicon surface have lower reflectance for all angles of incidence, when using light with a wavelength of 700-1000 nm.

Quantum efficiency measurements were also performed on devices with black silicon nanostructures. It became clear that devices, which had the tall needle like black silicon, etched by the ICP DRIE, would exhibit very poor quantum efficiencies. The quantum efficiencies would be below 10 % for the major part of the investigated spectrum finally increasing to approximately 30 % near 1000 nm. This was caused by complete removal of the front side field doping during the black silicon etch, which resulted in a very high surface recombination velocity. The pyramid structures, etched using RIE, did not remove all of the front side field doping and these detectors were compared to detectors with the optical filter. In the comparison test light of normal incidence and light of 38° from normal incidence were shone onto the detectors. The 38° tilt was the maximum possible angle for the quantum efficiency measurement setup. The decrease in quantum efficiency, when tilting the detectors 38°, can be seen in Figure 7.13. It can be seen that the detectors with the black silicon nanostructures performed better then detectors with the optical filter. The average decrease for light with a wavelength of 700-950 nm is 5.2 % and 9.1 % for the detectors with the black silicon nanostructures and the optical filter, respectively.

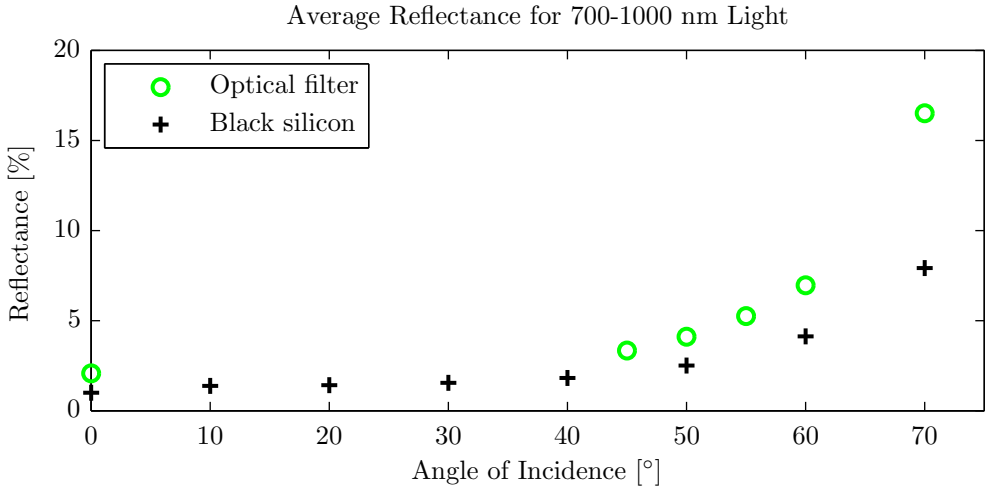

Figure 7.12: Average reflectance for light with a wavelength of 700-1000 nm. The reflectance is measured using an ellipsometer for the optical filter and an integrating sphere for the black silicon surface. The reflectance can be seen to be lower for the black silicon surface for all angles of incidence.

Finally, the effect of the ALD coating on the quantum efficiency was investigated. This was done by measuring on the same 10 mm and 1.5 mm wide devices, which were also used in the ALD IV-measurements. The result of the measurements are plotted in Figure 7.14, as the average internal quantum efficiency. It would be expected that the 10 mm wide detectors would exhibit the same quantum efficiency before and after coating, but also that the narrow 1.5 mm detectors would profit from the coating and show an increased quantum efficiency. However, both detector types show a fluctuating difference, which cannot truly be distinguished from the ±3 % uncertainty that the quantum efficiency measurements have.

7.3.4 Discussion

The investigations of the quantum efficiencies indicate a clear dependence on the device size, as predicted in Section 4.2.2. For the series of test detectors the decrease in quantum efficiency was observed for widths of 3 mm and below. However, for the real devices detectors with widths of 2.75 mm and 2.5 mm still exhibited high quantum efficiencies. The decrease in the quantum efficiency was here observed for 1 mm wide detectors and the 2 mm × 2 mm detectors from the 2D square matrix

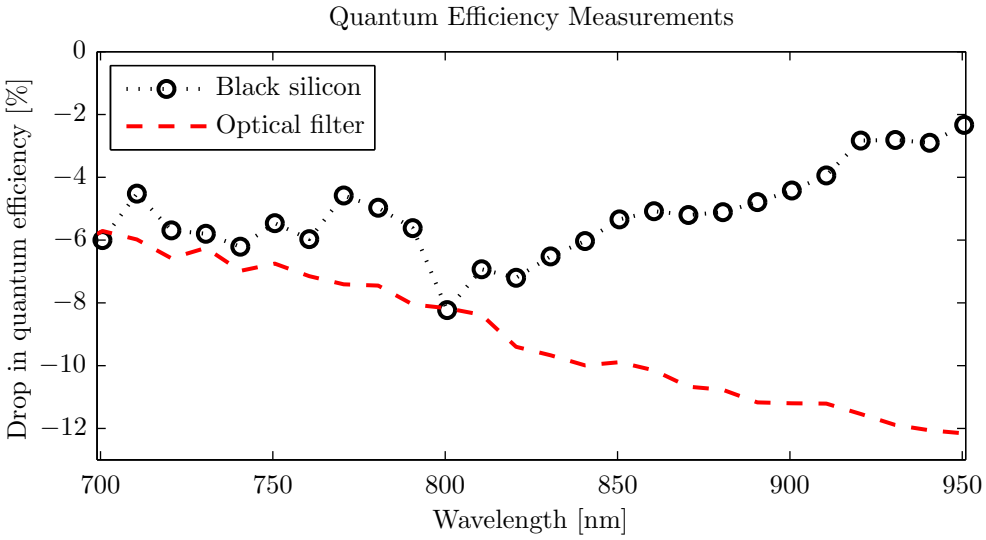

Figure 7.13: The decrease in quantum efficiency for 10 mm wide detectors, with either the optical filter or the black silicon nanostructured surface, when they are tilted 38° degrees from normal. The quantum efficiency for the optical filter can be seen to decrease further with increasing wavelength, which is as expected. The black silicon nanostructures exhibit a more wavelength independent decrease. The average decrease, for 700-950 nm light, is 5.2 % for the black silicon nanostructured detectors and 9.1 % for the detectors with the optical filter.

devices. This indicates that fairly small and narrow detectors can be made and still have high quantum efficiencies. Although, as previously mentioned the measurement method by focussing the spot at the centre of the detectors will show only the best performance of the detectors.

The final devices show quantum efficiencies of approximately 80-85 % for light with wavelengths of 700-950 nm. These values are similar to the reference diode used for the measurement as well as for other commercial silicon diodes that have been tested during this project including the Osram BP-104-FAS pin-diode. Photo diodes fabricated using very specific processes have been reported to achieve close to 100 % internal quantum efficiency [98]. In [55] detectors with quantum efficiencies up to 92 % were fabricated but these were not covered with a layer of PDMS, which absorbs part of the light. The detectors fabricated during this project are therefore of similar high quality as commercial detectors and possible around the highest possible quality which can be achieved at the Danchip cleanroom facility.

The tests where black silicon nanostructures were used as anti reflection coating proved feasible. Reflectance measurements showed that the reflectance would be lowered for all angles between 0-70°. This effect was seen to minimise the drop in quantum efficiency when the angle of incidence was changed to 38° from normal. The average measured drop in quantum efficiency was 5.2 % for the black silicon and 9.1 % for the optical filter. Commercial detectors coated with polymeric infrared

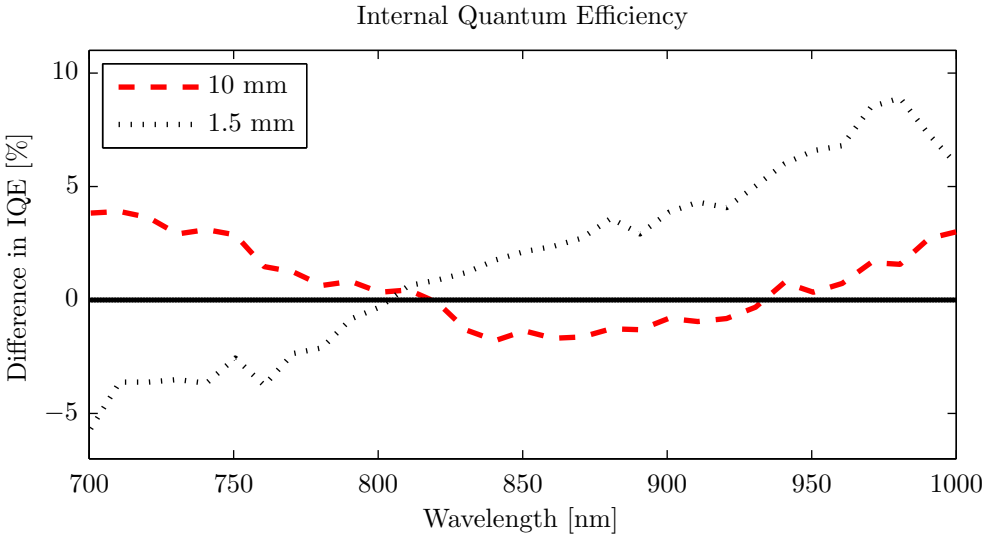

Figure 7.14: The average difference in internal quantum efficiency for 1.5 mm and 10 mm wide diodes, before and after ALD coating. Positive values indicate an increase and negative value a decrease after the coating. No consistent result can be deduced from the measurements, although there might be a slight tendency for improvement of the 1.5 mm wide diodes for 900-1000 nm.

filters will typically exhibit a drop in the order of 20-25 % at the same angle of incidence [95]. This improvement would be less for light incident with a lower angle than 38° but more for larger incident angles according to Figure 7.12.

As presented earlier the test with ALD coated aluminium oxide showed a slight reduction in reverse bias current, but it was not possible to conclude that it would improve the quantum efficiency of small or narrow detectors. Even though low temperature ALD coated aluminium oxide has been reported in literature, it must be concluded that the annealing process is essential to the formation of high quality passivation, which will reduce the surface recombination velocity of the deep etched side walls. One possibility could be to use rapid thermal annealing as this would only bring the polyimide above the 300 °C threshold for a short period of time.

7.4 Summary

The device characterisation was split into a mechanical and an electrical part. The mechanical tests showed that general handling of the devices was feasible without any damage to the structures or the fragile electrical interconnects. However, the devices could be damaged if intended. Both the 1D linear array and 2D square matrix device platforms could be bent around a single curved surface to more than 90° over their full lengths. During this the electrical interconnects only showed negligible increases in resistance. The devices could be strained longitudinally up to approximately 3 % before the interconnects broke.

The electrical analysis showed reverse bias current densities, which were low compared to previous devices fabricated at DTU Nanotech yet still higher than commercial available photo diodes. The deviation in the reverse bias current density from device to device was found to be acceptable. Quantum efficiency measurements showed that wider detectors were less affected by the unpassivated side walls compared to narrow or smaller detectors. Wide detectors showed quantum efficiencies of approximately 80 % for near infrared light of 700-1000 nm, whereas the smaller detectors only showed approximately 60 %. The best detectors had internal quantum efficiencies comparable to commercial photo diodes. The testing of black silicon nanostructures proved feasible as an anti-reflection surface. The ALD coated Al_2O_3 was found to lower the reverse bias current for narrow devices but did not show any improvement in quantum efficiency.

Chapter 8

Conclusion and Outlook

This project consisted of two goals: firstly, to develop flexible device platforms where the flexibility and biocompatibility are integrated into the silicon and secondly, to use these platforms for fabrication of infrared detector arrays. In order to achieve these goals we investigated the designs of commercial tissue oximeter devices and research devices reported in literature. This resulted in our proposed design where both polyimide and PDMS are combined with silicon in order to form the flexible and biocompatible arrays. The proposed design, where the flexibility and biocompatibility are integrated into the silicon using polyimide and PDMS, was found to be feasible. We developed the final fabrication process from a thorough investigation of the individual process steps. We can conclude that this fabrication process resulted in device yield of 90 %, when using manual dicing.

A derived analytical expression for the strain in the flexible joints was derived. The mechanical tests of the devices proved that it correctly predicted that only negligible strain would be present in the joints when the devices were bent. Mechanical testing of the 1D linear array and 2D square matrix device platforms showed that they could be manually handled as intended and that they were capable of being bent to far more than 90° over their full lengths without any damage to the electrical interconnects and with only negligible increase in resistance of below 1 %. The maximum longitudinal strain was found to be approximately 3 %, which was a larger value than found in free standing metallisations used in MEMS. It can therefore be concluded that the device platforms will be useful for bendable applications.

Regarding the design of the back side photo diodes, both analytical models and numerical simulation were used to predict the best design parameters. The electrical characterisation of the devices showed that the fabrication method, where the individual detectors are defined by deep etching, increases the reverse bias current. The reverse bias current densities, for the different detectors, were however, still acceptable with values as low as 12 nA/cm^2. The detectors fabricated in this project

did in general exhibit lower reverse bias current densities than previously fabricated detectors but still not as low as commercial devices. The tests using ALD coatings of aluminium oxide did show a slight improvement for the "narrow" detectors, by a reduction in reverse bias current of 30 %.

Quantum efficiency measurements showed a dependence on the detector widths. Detectors, which were narrower than approximately 2.5 mm, did exhibit a lower quantum efficiency and in this case it was not possible to improve the detector performance with the ALD coatings. However, the detectors that were wider than 2.5 mm were found to exhibit high quantum efficiencies of 80-85 %. The angular dependence of the quantum efficiency was found to be improved using black silicon nanostructures as an anti-reflection surface. It was found to lower the reflection for all angles between 0-70°, when compared to the optical filter. The effect on the quantum efficiency was also investigated for normal incident light and light incident at 38° from normal. This showed a drop in quantum efficiency of only 5.2 % for the black silicon compared to 9.1 % for the optical filter and approximately 20-25 % for polymeric filters. We can conclude that the 1D linear array device design can produce detectors with sufficient high quantum efficiency and that the black silicon nanostructures can be used to improve the detectors performance when measuring on isotropic scattered light.

8.1 Outlook

The sensors that have been developed during this project will only be the tip of the iceberg regarding SRS tissue oximetry. A complete SRS tissue oximetry system would also require: light sources, shielded wiring, electronics for control and amplification and software containing algorithms for calculation of the TOI. All of this, which have been beyond the scope of this project, would have to be investigated.

As mentioned the last generation of 1D array devices failed during the dicing process. These devices were designed with both the real dimensions and with the possibility of mounting multi core LEDs on contact pads, so the LEDs could inject light into the tissue through etched holes in the devices. It was planed that these devices should have been tested on optical phantoms and if possible on the lower arms of adult test subjects in a collaboration study with the University Hospital of Copenhagen. It would therefore be essential for future work that the final devices were completed, e.g. using either thicker polyimide for encapsulation or manual dicing methods. In this way the feasibility of the developed devices, as tissue oximeters, could be determined. Finally, it would be interesting to investigate if other medical sensors or transducers e.g. CMUTs could be integrated into the flexible platforms.

Bibliography

[1] F. Althabe *et al.* Born to soon. Technical report, World Health Orginazation, 2012.

[2] R. M. Ward and J. C. Beachy. Neonatal complications following preterm birth. *BJOG*, 110:8–16, 2003.

[3] A. F. Korner, D. K. Stevenson, T. Forrest J. C. Constantinou, S. Dimiceli, and B. W. Brown. Preterm medical complications differentially affect neurobehavioral functions: Results from a new neonatal medical index. *Infant behavior and development*, 17:37–43, 1994.

[4] J. C. Fenik and K. Rais-Bahrami. Neonatal cerebral oximetry monitoring during ecmo cannulation. *Journal of Perinatology*, pages 1–6, 2009.

[5] W. A. Carlo *et al.* Target ranges of oxygen saturation in extremely preterm infants. *The New England journal of medicine*, 362(21):1959–1969, 2010.

[6] N. Finer and T. Leone. Oxygen saturation monitoring for the preterm infant: The evidence basis for current practice. *Pediatric Research*, 65:375–380, 2009.

[7] W. Tin and S. Gupta. Optimum oxygen therapy in preterm babies. *Arch Dis Child Fetal Neonatal*, 92:143–147, 2007.

[8] C. Gilbert. Retinopathy of prematurity: A global perspective of the epidemics, population of babies at risk and implications for control. *Early Human Development*, 84:77–82, 2008.

[9] E. S. Potharst, A. G. van Wassenaer, B. A. Houtzagar, J. W. P. van Hus, B. F. Last, and J. H. Kok. High incidence of multi-domain disabilities in very preterm children at five years of age. *Arch Dis Child Fetal Neonatal*, 159(1):79–85, 2011.

[10] N. Marlow, D. Wolke, M. A. Bracewell, and M. Samara. Neurologic and developmental disability at six years of age after extremely preterm birth. *The New England journal of medicine*, 352(1):9–19, 2005.

[11] L. P. Madsen, M. K. Rasmussen, L. L. Bjerregaard, S. B. Nøhr, and F. Ebbesen. Impact of blood sampling in very preterm infants. *Scandinavian Journal of Clinical & Laboratory Investigation*, 60:125–132, 2000.

[12] G. Greisen, T. Leung, and M. Wolf. Has the time come to use near-infrared spectroscopy as a routine clinical tool in preterm infants undergoing intensive care? *Philosofical transactions of the royal society A*, 369(1955):4440–4451, 2011.

[13] J. M. Murkin and M. Arango. Near-infrared spectroscopy as an index of brain and tissue oxygenation. *British Journal of Anaesthesia*, 113:3–13, 2009.

[14] G. Naulaers, G. Morren, S. van Huffel, P. Casaer, and H. Devlieger. Cerebral tissue oxygenation index in very premature infants. *Arch Dis Child Fetal Neonatal*, 87:89–92, 2002.

[15] L. C. Sorensen and G. Greisen. Precision of measurement of cerebral tissue oxygenation index using near-infrared spectroscopy in preterm neonates. *Journal of Biomedical Optics*, 11(5):054005–1–5, 2006.

[16] R. Bay-Hansen, B. Elfving, and G. Greisen. Use of near infrared spectroscopy for estimation of peripheral venous saturation in newborns: Comparison with co-oximetry of central venous blood. *Biology of the neonate*, 82:1–8, 2002.

[17] S. Hyttel-Sorensen, L. C. Sorensen, J. Riera, and G. Greisen. Tissue oximetry: a comparison of mean values of regional tissue saturation, reproducibility and dynamic range of four nirs-instruments on the human forearm. *Biomedical optics express*, 2(11):3047–3057, 2011.

[18] M. Firbank, C. E. Elwell, C. E. Cooper, and D. T. Delphy. Experimental and theoretical comparison of nir spectroscopy measurements of cerebral hemoglobin changes. *Journal of applied physiology*, 85(5):1915–1921, 1998.

[19] T. Aoyagi, M. Kishi, K. Yamaguchi, and S. Watanabe. Improvement of an earpiece oximeter. *13th Annual Meeting of the Japan Society of Medical Electronics and Biological Engineering*, pages 90–91, 1974.

[20] T. Aoyagi. Pulse oximetry: its invention, theory, and future. *Journal of Anesthesia*, 17:259–266, 2003.

[21] A. Vogel and V. Venugopalan. Mechanisms of pulsed laser ablation of biological tissues. *Chemical reviews*, 103(2):577–644, 2003.

[22] Optical Apsorption of Hemoglobin. `http://www.cia.gov/cia/publications/factbook/index.html`. Internet, 2013.

[23] R. G. Haahr, S. Duun, E. V. Thomsen, K. Hoppe, and J. Branebjerg. A wearable "electronic patch" for wireless continuous monitoring of chronically diseased patients. *Proceedings of the 5th International Workshop on Wearable and Implantable Body Sensor Networks*, pages 66–70, 2008.

[24] Rasmus Haahr. *Wearable Health Monitoring Technologies*. PhD thesis, DTU Nanotech, February 2010.

[25] Nonin Medical Inc. `www.nonin.com`. Internet, 2014.

[26] Rigshospitalet. `http://www.rigshospitalet.dk/menu/afdelinger/Juliane+Marie+Centret/Klinikker/Neonatalklinikken/Forskningihovedmenu/SafeboosC`. Internet, 2014.

[27] Covidien. `www.covidien.com`. Internet, 2014.

[28] Neuroscience center Zurich. `http://www.neuroscience.ethz.ch/research/biomedical_technology/wolf`. Internet, 2014.

[29] D. M. Heuber, S. Fantini, A. E. Cerussi, and B. Barbieri. New optical probe design for absolute (self-calibrating) nir tissue hemoglobin measurements. *Proc. SPIE, Optical Tomography and Spectroscopy of Tissue III*, 3597:618–631, 1999.

[30] S. Suzuki, S. Takasaki, T. Ozaki, and Y. Kobayashi. A tissue oxygenation monitor using NIR spatially resolved spectroscopy. SPIE *Conference on optical tomography and spectroscopy*, 3597:582–592, 1999.

[31] J. C. Hebden, M. Varela, S. Magasov, N. Everdell, A. Gibson, J. Meek, and T. Austin. Diffuse optical imaging of the newborn infant brain. *IEEE Biomedical Imaging*, pages 503–505, 2012.

[32] T. M. Baran, J. D. Wilson, S. Mitra, J. L. Yao, E. M. Messing, D. L. Waldmann, and T. H. Foster. Optical property measurements establish the feasibility of photodynamic therapy as a minimally invasive intervention for tumors of the kidney. *Journal of biomedical optics*, 17(9):098002–1–8, 2012.

[33] F. K. Jiang, Y. C. Tai, K. Walsh, T. Tsao, G. B. Lee, and C. M. Ho. A flexible mems technology and its first application to shear stress sensor skin. *IEEE intanational workshop MEMS*, pages 465–470, 1997.

[34] X. Zhuang, D-S. Lin, O. Oralkan, and B. T. Khuri-Yakub. Fabrication of flexible trunsducer arrays with through-wafer electrical interconnects based on trench refilling with pdms. *Journal of microelectromechanical systems*, 17(2):446–452, 2008.

[35] S. P. Lacour, S. Wagner, Z. Huang, and Z. Suo. Stretchable gold conductors on elastomeric substrates. *Applied physics letters*, 82(15), 2003.

[36] X. Niu, S. Peng, L. Liu, W. Wen, and P. Sheng. Characterizing and patterning of pdms-based conducting composites. *Advanced materials*, 19:2682–2686, 2007.

[37] D-H. Kim, Y-S. Kim, J. Wu, Z. Liu, J. Song, H-S. Kim, Y. Y. Huang, K-C. Hwang, and J. A. Rogers. Ultrathin silicon circuits with strain-isolation layers and mesh layouts for high-performance electronics on fabric, vinyl, leather, and paper. *Advanced Materials*, 21:3703–3707, 2009.

[38] V. Tuchin. *Tissue Optics*. SPIE Press, 2 edition, 2007.

[39] F. Martelli, S. D. Bianco, A. Ismaelli, and G. Zaccanti. *Light Propagation through Biological Tissue*. SPIE Press, 1 edition, 2010.

[40] L. V. Wang and H. Wu. *Biomedical Optics*. Wiley, 1 edition, 2007.

[41] T. J. Farrell, B. C. Wilson, and M. S. Patterson. The use of a neural network to determine tissue optical properties from spatislly resolved diffuse reflectance measurements. *Physics in Medicine and Biology*, 37(12):2281–2286, 1992.

[42] J. S. Dam, P. E. Andersen, T. Dalgaard, and P. E. Fabricius. Determination of tissue optical properties from diffuse reflectance profiles by multivariate calibration. *Applied Optics*, 37(4):772–778, 1998.

[43] M. S. Patterson, E. Schwartz, and B. C. Wilson. Quantitative reflectance spectrophotometry for the noninvasive measurement of photosensitizer concentration in tissue during photodynamic therapy. SPIE P*hotodynamic* T*herapy: M*e*chanisms*, 1065:115–122, 1989.

[44] S. J. Matcher, P. Kirkpatrick, K. Nahid, M. Cope, and D. T. Delphy. Absolute quantification methods in tissue near infrared spectroscopy. SPIE *Conference on optical tomography and spectroscopy*, 2389:486–495, 1995.

[45] L. Wang, S. L. Jacques, and L. Zheng. MCML - monte carlo modeling of light transport in multi-layered tissue. *Computer Methods and programs in biomedicine*, 47:131–146, 1995.

[46] S-H. Tseng, P. Bargo, A. Durkin, and N. Kollias. Chromophore concentrations, absorption and scattering properties of human skin in-vivo. *Optics Express*, 17(17):14599–14617, 2009.

[47] H. Ding, J. Q. Lu, W. A. Wooden, P. J. Kragel, and X-H. Hu. Refractive indices of human skin tissues at eight wavelengths and estimated dispersion relations between 300 and 1600 nm. *Physics in Medicine and Biology*, 51(6):1479–1489, 2006.

[48] M. Firbank, M. Hiraoka, M. Essenpreis, and D. T. Delpy. Measurement of the optical properties of the skull in the wavelength range 650-950 nm. *Physics in Medicine and Biology*, 38:503–510, 1993.

[49] Y. Fukui, Y. Ajichi, and E. Okada. Monte carlo prediction of near-infrared light propagation in realistic adult and neonatal head models. *Applied Optics*, 42(16):2881–2887, 2003.

[50] A. N. Yaroslavsky, P. C. Schulze, I. V. Yaroslavsky, R. Schober, F. Ulrich, and H-J. Schwarzmaier. Optical properties of selected native and coagulated human brain tissues in vitro in the visible and near infrared spectral range. *Physics in Medicine and Biology*, 47(12):2059–2073, 2002.

[51] T. R. Fenton. A new growth chart for preterm babies: Babson and benda's chart updated with recent data and a new format. *BMC Pediatrics*, 3(13), 2003.

[52] S. D. Senturia. *Microsystem Design*. Springer, 2001.

[53] J. M. Gere. *Mechanics of Materials*. Thomson, 6 edition, 2006.

[54] H. Huang and F. Spaepen. Tensile testing of free-standing cu, ag and al thin films and ag/cu multilayers. *Acta materialia*, 48:3261–3269, 2000.

[55] Sune Duun. *The Electronic Patch*. PhD thesis, DTU Nanotech, April 2010.

[56] D. A. Neamen. *Semiconductor Physics and Devices*. McGraw - Hill, 3 edition, 2003.

[57] S. M. Sze and K. K. Ng. *Physics of Semiconductor Devices*. Wiley, 3 edition, 2007.

[58] B. E. A. Saleh and M. C. Teich. *Fundamentals of Photonics*. John Wiley and Sons, 1991.

[59] E. D. Palik. *Handbook of optical constants of solids*. Academic Press, 1998.

[60] Anders Michael Jorgensen. *Optical Detection in Bio/Chemical Microsystems*. PhD thesis, DTU Nanotech, November 2002.

[61] P. Saint-Cast, D. Kania, M. Hofmann, J. Benick, J. Rentsch, and R. Preu. Very low surface recombination velocity on p-type c-si by high-rate plasma-deposited aluminum oxide. *Applied physics letters*, 95:151502–1–3, 2009.

[62] D. Baek, S. Rouvimov, B. Kim, T-C. Jo, and D. K. Schroder. Surface recombination velocity of silicon wafers by photoluminescence. *Applied physics letters*, 86:112110–1–3, 2006.

[63] Y. Larionova, V. Mertens, N-P. Harder, and R. Brendel. Surface passivation of n-type czochralski silicon substrates by thermal-sio_2/plasma-enhanced chemical vapor deposition sin stacks. *Applied physics letters*, 96:03215, 2010.

[64] A. Hyldgård, K. Birkelund, J. Janting, and E.V. Thomsen. Direct exposure of MEMS multi-sensor systems using a potted-tube packaging concept. *Sensors and actuator A*, 142:398–404, 2008.

[65] H. Jansen, M. Boer, R. Legtenberg, and M. Elwenspoek. The black silicon method: a universal method for determining the parameter setting of a fluorine-based reactive ion etcher in deep silicon trench etching with profile control. *J. Micromech. Microeng.*, 5:115–120, 1995.

[66] R. S. Davidsen, M. S. Schmidt, A. Boisen, and O. Hansen. Plasma etching on large-area mono-, multi- and quasi-mono crystalline silicon. *Proceedings of the 39th International Conference on Micro and Nano Engineering*, 2013.

[67] S. D. Petersen and A. Thaulow. Black silicon nanostructures, June 2004.

[68] R. S. Davidsen. Nanostructured silicon surfaces for photovoltaic applications, December 2009.

[69] M. F. Laursen. Design, fabrication and characterisation of photodiodes for a pulse oximetry sensor embedded in an electronic patch. Master's thesis, DTU Nanotech, October 2008.

[70] J. Clausen. Flexible photodetectors for an electronic patch. Master's thesis, DTU Nanotech, April 2011.

[71] M. Engholm. Flexible sensor platform, June 2012.

[72] A. Thyssen. Design fabrication and characterisation of flexible photodiodes for tissue oximetry. Master's thesis, DTU Nanotech, June 2012.

[73] J. D. Thomsen. Fabrication of 2d flexible photodetector arrays. Master's thesis, DTU Nanotech, February 2014.

[74] L. Alcalá. Optimization, design, fabrication and characterization of photodetectors for tissue oximetry. Master's thesis, DTU Nanotech, August 2014.

[75] S. K. Ghandhi. *The theory and practice of microelectronics*. Wiley, 1986.

[76] K. V. Anand, H. D. McKell, and D. C. Northrop. The properties of silicon dioxide films on silicon as diffusion masks for boron. *J.Phys.D: Appl.Phys.*, 4:1722–1730, 1971.

[77] K. K. Ng and R. Lui. On the calculation of specific contact resistivity on $< 100 >$ si. *IEEE transactions on electron devices*, 32(6):1535–1537, 1990.

[78] P. S. Dobson and J. D. Filby. Pricipitation of boron in silicon. *Journal of crystal growth*, 3(4):209–213, 1968.

[79] R. Lagos, A. Moehlecke, J. Alonso, I. Tobias, and A. Luque. Contamination and gettering evaluation by lifetime measurements during single crystal cell prossesing. *First world conference on photovoltaic energy conversion*, pages 1629–1632, 1994.

[80] A. A. Carreno, D. Conchouso, and I. G. Foulds. Optimized cantilever-to-anchor configuration of buckled cantilever plate structures for transducer applications. *Proceedings of the 2012 COMSOL Conference*, 2012.

[81] J. H. Lake, S. D. Cambron, K. M. Walsh, and S. McNamara. Maskless grayscale lithography using a positive-tone photodefinable polyimide for mems applications. *Journal of microelectromechanical systems*, 20(6):1483–1488, 2011.

[82] M. Fredenberg, P. Möller, and M. Töpper. Novel multi-layer wiring build-up using electrochemical pattern replication (ecpr). *Electronic Components and Technology Conference*, pages 585–590, 2009.

[83] X. Chen, D. S. Espinoza, E. F. Dudley, Z. Li, M. Mohamed, Y. Cui, W. Park, L. Shang, and A. R. Mickelson. Polymer-clad silicon on insulator slot modulator. *Signal Processing in Photonic Communications*, 2011.

[84] HD MicroSystems™. `http://hdmicrosystems.com/HDMicroSystems/en_US/products/photodefineable/HD-8800_positive_aqueous.html`. Internet, 2014.

[85] S. Middleman and A. K. Hochberg. *Process engineering analysis in semiconductor device fabrication.* McGraw Hill, 1993.

[86] S. D. Petersen and A. Greve. Piezoresistance of strained silicon germanium. Technical report, DTU Nanotech, 2005.

[87] P. Görnn, W. Cao, and S. Wagner. Isotropically stretchable gold conductors on elastomeric substrates. *Soft Matter*, 7:7177–7180, 2011.

[88] R. S. Davidsen, Ø. Nordseth, A. Boisen, M. S. Schmidt, and O. Hansen. Plasma texturing on large-area industrial grade cz silicon solar cells. *Proceedings of the 28th European PV Solar Energy Conference and Exhibition*, 2013.

[89] M. D. Groner, F. H. Fabreguette, J. W. Elam, and S. M. George. Low temperature al_2o_3 atomic layer deposition. *Chemistry of Materials*, 16:639–645, 2004.

[90] B. Hoex, S. B. S. Heil, E. Langereis, M. C. M. van de Sanden, and W. M. M. Kessels. Ultralow surface recombination of c-si substrates passivated by plasma-assisted atomic layer deposited al_2o_3. *Applied physics letters*, 89:042112–1–3, 2006.

[91] D-H. Kim, Z. Liu, Y-S. Kim, J. Wu, J. Song, H-S. Kim, Y. Huang, K-C. Hwang, Y. Zhang, and J. A. Rogers. Optimized structural designs for stretchable silicon integrated circuits. *Small*, 5(24):2841–2847, 2009.

[92] S. P. Lacour, D. Chan, S. Wagner, T. Li, and Z. Suo. Mechanisms of reversible stretchability of thin metal films on elastomeric substrates. *Applied physics letters*, 88:204103–1–3, 2006.

[93] R. L. Parker and A. Krinsky. Electrical resistance-strain characteristics of thin evaporated metal films. *Journal of applied physics*, 34(9):2700–2708, 1963.

[94] X. Niu, S. Peng, L. Liu, W. Wen, and P. Sheng. Characterizing and patterning of pdms-based conducting composites. *Advanched materials*, 19:2682–2686, 2007.

[95] Osram. `http://docs-europe.electrocomponents.com/webdocs/08b4/0900766b808b4435.pdf`. Internet, 2014.

[96] E. V. Thomsen. The diode equation at high injection. Technical report, DTU Nanotech, 2012.

[97] Hamamatsu. `http://www.hamamatsu.com/resources/pdf/ssd/s1087_etc_kspd1039e03.pdf`. Internet, 2014.

[98] E. F. Zalewski and C. R. Duda. Silicon photodiode device with 100 % external quantum efficiency. *Applied optics*, 22(18):2867–2873, 1983.

Appendix A

List of Publications

Publications:

- S. D. Petersen, A. Thyssen, M. Engholm and E. V. Thomsen, "A Flexible Infrared Sensor for Tissue Oximetry", Micro and Nano Engineering, 2012.
- S. D. Petersen, A. Thyssen, M. Engholm and E. V. Thomsen, "A Flexible Infrared Sensor for Tissue Oximetry", Microelectronic Engineering 111 (2013) 130-136.
- S. D. Petersen, R. S. Davidsen, L. R. Alcalá, M. S. Schmidt, A. Boisen, O. Hansen and E. V. Thomsen, "Improvement of Infrared Detectors for Tissue Oximetry using Black Silicon Nanostructures", Eurosensors, 2014.
- S. D. Petersen, J. D. Thomsen and E. V. Thomsen, "A Flexible Matrix Sensor for Spatially Resolved Spectroscopy Oximetry Measurements on Prematurely Born Children", (Submitted) Sensors and Actuators A, 2015.

Patent:

- S. D. Petersen, R. S. Davidsen, O. Hansen, A. Boisen, M. S. Schmidt and E. V. Thomsen, "A Photodetector for use in Spatially Resolved Spectroscopy Applications", Application number: PA 2014 70546, 2014.

A Flexible Infrared Sensor for Tissue Oximetry

Søren Dahl Petersen [a], Anders Thyssen [a], Mathias Engholm [a], and Erik Vilain Thomsen [a]

[a] DTU Nanotech, Kongens Lyngby, DK-2800, Denmark
e-mail: sdpet@nanotech.dtu.dk

Keywords: Flexible sensor, PDMS, polyimide, photo detectors, tissue oximetry, NIRS

Sensors, actuators and integrated circuits have traditionally been fabricated as solid silicon chips. However, over the past few years effort have been put into incorporation of flexibility in the chips. Within the field of displays, solar cells and medical sensors, process steps that add flexibility, have been integrated into standard IC fabrication [1].

We present a sensor system consisting of multiple silicon photo detectors for use in near infrared spectroscopy (NIRS). The goal of the detector system is to work as a sensor for oximetry of brain tissue, specifically to measure the oxygenation of brain tissue in prematurely born infants. Such a sensor system should be flexible so it can easily follow the curvature of an infant childs head. The multiple detectors enables the sensor to perform spatially resolved spectroscopy.

The flexibility is achieved by combining silicon with PDMS [2] and polyimide [3], using simple process steps. The soft PDMS makes up the backbone of the sensor and ensures flexibility. The harder polyimide encloses the electrical conductors and places the neutral axis very close to the center line of the conductors, so they will not experience any longitudinal stresses or strains when bended. The grooves with PDMS are varied in the design so they are: 100 µm, 200 µm and 400 µm wide, respectively. The silicon photo detectors are 1 mm or 2.75 mm wide and made as backside pn-junctions [4].

The complete process sequence can be seen in Fig.1. First pn-junctions are made in the silicon substrate to form back side photo diodes. Then, the back side contacts are made as a “sandwich” structure of 10 µm thick polyimide layers and 400 nm thick gold. The individual photo diodes are defined by DRIE and the cavities are filled with PDMS using a spin coating process, that also creates a thin layer of PDMS on the front side of the sensor. Finally the wafer is diced out thus releasing the individual finished chips, which can be seen in Fig. 2.

In order to investigate the performance of the chips, test chips were also produced which could be used to measure the resistance of the electrical interconnects, when the chips are bended or strained. In a bending test the chips were bended around different circles with decreasing radii of curvature. When the curvature of the chips increased an increase in resistance was also measured, however, it was relatively small, as can be seen from Fig. 3. For a curvature that corresponds to a 90° bend of the sensor, the relative increase in resistance was: 0.35%, 0.27% and 0.06%, for the sensors with the 100 µm, 200 µm and 400 µm wide PDMS trenches, respectively. The test chips were strained by pulling them in the longitudinal direction and the resistance was measured for chips with 200 µm and 400 µm wide PDMS trenches. The relative change in resistance can be seen in Fig. 4. It is neglectable for strains up to 4%. Above 4.5% strain the chip with the narrow 200 µm PDMS trenches experiences an increase in resistance and above 6% strain the gold connectors break. For the chip with the wider 400 µm PDMS trenches the increase in resistance happens at 5.5% and the break in the connectors happens above 7% strain. Finally the quantum efficiency of the sensor was measured, on a chip with six individual photo diodes. For the wavelengths of interest, i.e. 700-1000 nm, the quantum efficency was found to be in the order of 70-80%.

In conclusion, we have presented a process sequence for adding flexibility to MEMS sensors by incorporating simple process steps using polyimide and PDMS. The process is added to the fabrication of photo diodes, and we can maintain electrical contact throughout the sensor, even when the sensor is bended and strained. The photo diodes were tested and found to have high quantum efficiency for the wavelengths of interest.

[1] Dae-Hyeong Kim, Zhuangjian Liu, Yun-Soung Kim, Jian Wu, Jizhou Song, Hoon-Sik Kim, Yonggang Huang, Keh-chih Hwang, Yongwei Zhang, and John A. Rogers, Science, 320 (2008) 507-511.
[2] Sylgard 184, Dow corning, www.dowcorning.com
[3] HD-8820, HD MicroSystems, www.hdmicrosystems.com
[4] Sune Bro Duun, Rasmus G. Haahr, Karen Birkelund, and Erik V. Thomsen, IEEE Sensors Journal, Vol. 10 (2010) 261-268.

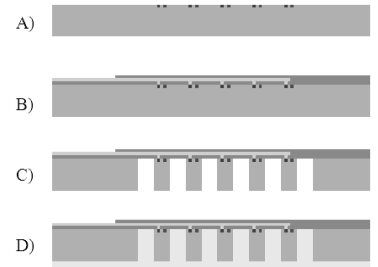

Figure 1. Process flow: A) pn-junctions, B) electrical interconnects in polyimide, C) DRIE to create the individual photo diodes, and D) PDMS spin coating and dicing of chips.

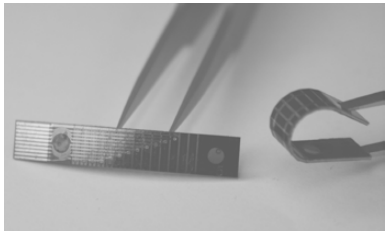

Figure 2. Two finished chips. A real infrared sensor chip to the left with nine individual silicon photo diodes and a resistance test chip to the right.

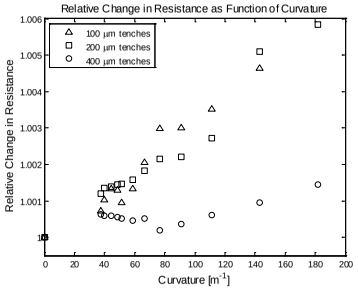

Figure 3. Relative change in resistance as a function of sensor curvature. Three different sensors were tested, having 100 µm, 200 µm and 400 µm wide PDMS trenches and 1 mm detectors.

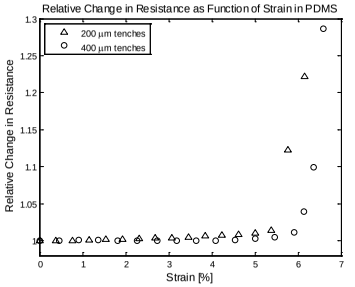

Figure 4. Relative change in resistance as function of the strain in the PDMS parts of the sensor. Sensors with 200 µm and 400 µm wide PDMS trenches were tested.

Microelectronic Engineering 111 (2013) 130–136

Contents lists available at SciVerse ScienceDirect

Microelectronic Engineering

journal homepage: www.elsevier.com/locate/mee

A flexible infrared sensor for tissue oximetry

Søren Dahl Petersen *, Anders Thyssen, Mathias Engholm, Erik Vilain Thomsen

DTU Nanotech, Technical University of Denmark, Kongens Lyngby, Denmark

ARTICLE INFO

Article history:
Available online 27 March 2013

Keywords:
Tissue oximetry
Infrared photo detector
Flexible sensor
PDMS
Polyimide

ABSTRACT

We present a flexible infrared sensor for use in tissue oximetry with the aim of treating prematurely born infants. The sensor will detect the oxygen saturation in brain tissue through near infrared spectroscopy. The sensor itself consists of several individual silicon photo detectors fully integrated in a flexible array. The flexibility is achieved by combining silicon with Polydimethylsiloxane and polyimide using standard IC manufacturing. This ensures that the electrical interconnects on the sensor can withstand being bent in order for the sensor to confine to the curved surface of the head of a neonatal. The sensor platform has been tested and is found to be very durable and capable of being both bent to small radii of curvature and strained in the longitudinal direction. The electrical interconnects on the sensor only experience a relative small increase in resistance when the sensor is bent up to 90° and they can withstand a longitudinal strain of up to 5% without being damaged. A durability test has shown no fatigue or change in resistance for the electrical interconnects when the sensor had been bent 10,000 times. Two different sizes of photo detectors have been characterized. The smaller detectors have quantum efficiencies in the near infrared region between 50% and 60%, whereas the larger detectors can achieve quantum efficiencies of 75–85%.

1. Introduction

According to the 2012 report, from the World Health Organization, 15 million children are born prematurely every year [1]. Infant children, who have been born prematurely, are in a state where they can easily suffer from complications, when recovering in their incubators [2,3]. It is therefore essential to their survival that their vital signs are monitored. One of the most important parameters to monitor is the oxygen saturation in the brain tissue [4]. The neonates have difficulties in regulating the oxygen saturation in their bodies, so they often receive oxygen from an artificial supply. This oxygenation has to be monitored by drawing blood samples from the veins, since a too low concentration can lead to brain damage and having a too high concentration can cause blindness [5]. However, the constant need for blood samples is stressful for the neonates [6].

During the past few years, hospitals have started using different sensor systems that utilizes near infrared spectroscopy (NIRS) in order to measure the cerebral oxygen saturation non-invasively [7]. Many studies have been conducted and they show the feasibility of NIRS sensor systems, when used for tissue oximetry monitoring, but also the limitations of the systems developed so far [8–11]. In order to ensure better medical treatment of neonatals sensor systems which offer higher precision in determining the cerebral oxygen saturation must be invented.

The NIRS tissue oximetry systems use infrared light of different wavelengths which are injected into the brain where it undergoes scattering and absorption. The diffuse reflected signal is measured by a number of detectors placed at different distances from the light source. This specific method is called spatially resolved spectroscopy (SRS) [12]. Near infrared light, with a wavelength in the order of 700–1000 nm, has the advantage that it can penetrate deep into most kinds of tissue and has low absorption from water, melanin and proteins [13]. Furthermore it can be detected using silicon based detectors. However, the absorption from haemoglobin strongly depends on whether the haemoglobin is oxygenated (HbO) or de-oxygenated (Hb). The absorption of HbO and Hb also depends on the wavelength of the light. Adding more light sources of different wavelengths and detectors to the sensor will increase the resolution of the measurements. By plotting the normalized detector signal as function of detector distance from light source, the Boltzmann transport equation can be used to compute the absorption and scattering coefficients of the tissue for the given wavelength [14]. Finally, algorithms can be used to determine the oxygen saturation from all the signals received by the detectors.

Besides consisting of several detectors the sensor system also has to be flexible in order to follow the curvature of the neonates head. Furthermore, the contact surface between the sensor and the skin has to be soft and biocompatible. This is typically achieved for medical sensors by integrating discrete sensors into a silicone

* Corresponding author. Address: DTU Nanotech, Ørsteds Plads 345B, Kongens Lyngby DK-2800, Denmark. Tel.: +45 45255692; fax: +45 45887762.
E-mail address: sdpet@nanotech.dtu.dk (S.D. Petersen).

0167-9317/$ - see front matter © 2013 Elsevier B.V. All rights reserved.
http://dx.doi.org/10.1016/j.mee.2013.03.035

support structure or a medical patch [15–17]. However, these systems often only rely on few detectors so they have limited resolution on the spatially component of the measurement and they suffer from being sensitive to invisible artefacts in the skin. A sensor system, for diffuse optical imaging, which works using many detectors, has also been investigated [18] but it is based on time resolved spectroscopy. A solution, which can improve the resolution for sensors using the spatially resolved method, is therefore to integrate the flexibility and the functionality of a "patch" directly into the silicon and consequently make an entire array of detectors.

Integrating flexibility directly into the silicon has over the past few years been the new trend for medical sensors and actuators. Typically, polydimethylsiloxane (PDMS) [19–21] or polyimide [22–25] are used directly in the silicon processing. These materials can create flexible areas in the silicon or serve as flexible substrates for the sensors. In this paper we will present a sensor platform which uses both PDMS and polyimide to achieve flexible areas in the silicon. These areas will serve as joints between the individual photo detectors in the sensor array. As will be described in Section 3, a combination of PDMS and polyimide can be used to ensure minimal stress in the electrical interconnects, when the sensor array is bent, by positioning the electrical interconnects near the neutral axis of the structure. The PDMS will also be a biocompatible surface for contact with the skin. Protection of the sensor array against the environment is also very important to take into consideration. Specific types of polyimide offer excellent protection against moisture and metal ions and are therefore an obvious choice as protection for flexible electrical interconnects. Silicon nitride will be used as a barrier material for protection of the silicon against moisture and ions, since this has already been proven as a successful packaging concept [26].

2. Materials and methods

2.1. Sensor design

As described in the introduction the NIRS sensors should be flexible, biocompatible and consist of multiple individual infrared detectors. A schematic cross-sectional drawing of the sensor design showing silicon, polyimide, gold interconnects and PDMS is shown in Fig. 1A. This design will implement: Flexibility, biocompatibility and infrared sensing in the following manner: pn-junction diodes will be made in the silicon and will function as the infrared detectors. The individual detectors will be defined in the silicon by lithography and dry etching. The PDMS will function as the flexible backbone of the sensor array and for the biocompatible patch structure on the front side of the sensor, which will be in contact with the skin. The electrical interconnects will be placed on the back side of the sensor and will be encapsulated between two layers of polyimide, which will offer protection against moisture and ions from the environment. This encapsulation will also minimize the longitudinal strain when the sensor array is bent. Pictures of a fabricated flexible sensor array can be seen in Fig. 1B and C.

For an SRS NIRS sensor the distance between the individual detectors does not need to have any particular value. However, in order to improve the resolution of the measurements they will have to be placed relatively close to each other. The flexible PDMS joints are therefore varied in the design so they are: 100 μm, 200 μm and 400 μm wide, respectively. The width of the individual silicon photo detectors are chosen to be 1 mm or 2.75 mm. By fabricating both small and large detectors we can make two different types of arrays; one which can easily be confined to a curved surface, but might have lower infrared sensitivity and one which is less deformable but should have detectors with high sensitivity. There are nine individual detectors on the sensor arrays with the

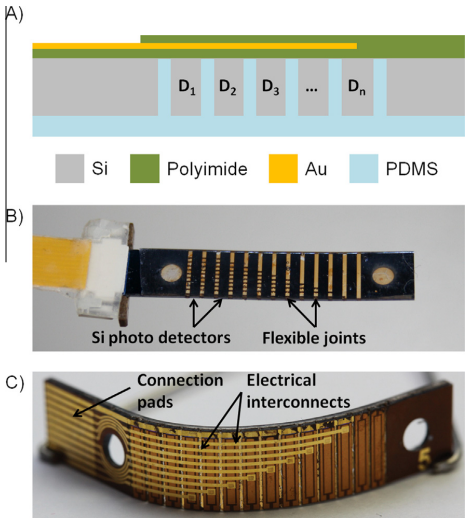

Fig. 1. The flexible sensor array. (A) A simple schematic cross-sectional drawing of the flexible sensor array design consisting of individual silicon photo detectors (D_1–D_n), polyimide, gold conductors and PDMS. (B) Picture of the front side of the sensor showing the individual silicon detectors and the flexible PDMS joints between the detectors. The front side also contains the PDMS surface for the skin contact. (C) Picture of the back side of the sensor showing the encapsulated electrical interconnects and ZIF connection pads.

1 mm wide detectors, and 5 or 6 individual detectors on the sensor arrays with the 2.75 mm wide detectors. The sensors are 29 mm long and 5.4 mm wide and are designed to fit into a 10 pin zero insertion force (ZIF) connector. Test sensors, which do not contain pn-junctions but only the electrical interconnects have also been fabricated in order to test the electrical interconnects' response to stress.

In order to minimize light reflection at the PDMS/silicon interface, the silicon detector surface is coated with an anti-reflection coating (see Section 2.2). The reflection simulation software Concise Macleod 8.12 was used to simulate reflectance from different dielectric layers and it was found that a simple structure of 50 nm SiO_2 and 50 nm SiN would lower the reflectance of the interface. For angles of incidence between 0 and 70° this double layer will lower the reflectance from 25–35% to 5–20% with the highest reflectance occurring for the highest angles of incident. Moreover, the SiN will act as a barrier material for protection of the silicon against moisture and ions.

2.2. Sensor fabrication

The fabrication of the infrared sensor arrays is mainly done by using standard cleanroom processes. A schematic drawing of the process sequence is shown in Fig. 2. Boron doped, (1 0 0) silicon wafers with a resistivity of approximately 10,000 Ω cm are being used in the start phase. First, patterns are being made in a 400 nm wet thermal oxide on the wafers by using ultra violet (UV) lithography and hydrofluoric acid (HF) wet etching. Hereafter, 375 nm of borosilicate glass is deposited on each side of the wafers in a Plasma enhanced chemical vapour deposition (PECVD) process. The wafers are annealed at 1000 °C for 85 min in order to drive the boron into the silicon both on the open front side, to create a field doping, and the patterned back side to create p+ contact areas.

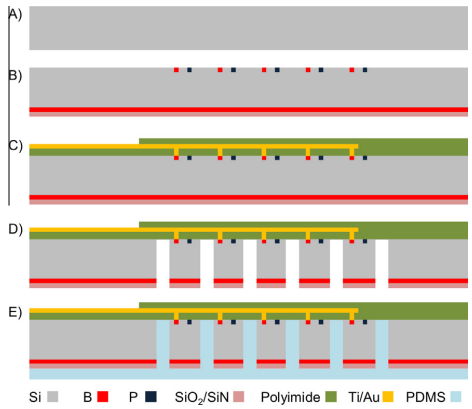

Fig. 2. A schematic drawing of the process flow. (A) High resistivity p-type silicon wafers. (B) Phosphorus and boron are introduced using diffusion and a SiO_2/SiN anti-reflection coating is formed. (C) The electrical interconnects are fabricated as a sandwich structure of gold and polyimide (showing only the electrical interconnects to the p-type areas on this drawing). (D) The individual detectors are defined by using DRIE. (E) PDMS is spin coated finalizing the detector array.

The borosilicate glass and the masking oxide are removed and a 1 μm thick oxide mask for phosphorus doping, is deposited using Tetraethyl orthosilicate (TEOS). The n-type junctions are then formed in the patterned TEOS using gaseous pre-deposition from $POCl_3$, at 1000 °C for 30 min. Again the oxide mask is stripped in HF and the wafers are placed in an oxidation furnace, which creates a 50 nm thick oxide, using a dry oxidation process at 1000 °C, and drives in the dopants.

A 50 nm thick silicon nitride is then deposited on the oxide using low pressure chemical vapour deposition (LPCVD). This creates the anti-reflection layer. The back side electrical interconnects are then formed in a double layer of HD-8820 polyimide, which functions as a positive photoresist and can be patterned using standard UV lithography. First a contact metallization layer, consisting of 100 nm Ti and 500 nm Al, is deposited on the silicon using e-beam evaporation through a shadow mask. The Al/Ti contacts are annealed at 425 °C for 30 min in order to ensure the formation of an ohmic contact to the silicon.

The wafers are then placed in a 250 °C oven in order to remove moisture from the surface and thereby improve the adhesion between the silicon surface and the polyimide. The HD-8820 is then spin coated on the wafer surface using 1500 rpm for 60 s followed by a 5 min baking on a 120 °C hotplate giving a thickness of 10 μm. Hereafter, the HD-8820 is exposed using 540 mJ/cm^2 and developed in a tetramethylammonium hydroxide (TMAH) solution (MF-322) for 60 s. This ensures the formation of sloped sidewalls in the HD-8820, which enables easier routing of the metallization onto the silicon (see Section 4.1). Afterwards, the polyimide is semi-cured for 30 min in a 250 °C oven.

The electrical interconnects are formed by e-beam evaporation of 20 nm Ti and 400 nm Au through a shadow mask. The final layer of HD-8820 is spin coated on the wafer and this layer is also patterned by UV lithography and developed. After that the polyimide layers are fully cured for 4 h at 250 °C. The individual photo detectors are defined by a deep reactive ion etching (DRIE) step, which etches completely through the silicon and stops on the polyimide.

The wafers are given a final clean in an oxygen plasma which improves the adhesion between the silicon and the PDMS. Hereafter, Sylgard 184 PDMS is prepared by mixing and degassing in a vacuum chamber. The PDMS is poured over the wafer and thinned down by spinning the wafer at 500 rpm for 30 s. The wafer is then placed in a vacuum chamber for 30 min in order to remove the remaining air from the PDMS and the PDMS is cured at 120 °C for 3 h. Finally, the sensors are diced out from the wafer, thus releasing the individual flexible sensor arrays.

2.3. Measurement setups

The sensors were tested mechanically and electrically in order to investigate if they can withstand "daily use" at a hospital. Moreover, it was tested whether the sensing properties are sufficient or not. Regarding the mechanical test it is important that the sensors can be bent to at least 90° over the full length of the array, while still maintaining electrical conduction. The sensors should also be able to be stretched in the longitudinal direction without breaking the electrical conductors, since this might occur during the usage. *IV* characterizations and quantum efficiency measurements have been performed in order to investigate the infrared sensing capability of the sensors.

2.4. Bending measurements

In order to measure how the resistance of the electrical interconnects behaves when the sensors are bent the fabricated test chips were fixed in the ZIF connector and bent around wooden discs with different radii of curvature. For each of the 12 discs used, the resistance of the test chips were measured using a Keithley 2700 multimeter with four-wire sensing by taking 300 samples over a 60 s period. The largest disc had a radius of 26.5 mm and the smallest disc a radius of 7.0 mm. The durability was tested by repeatedly bending a test sensor from its neutral position to a 90° bent. This was done by fixating one end of the test sensor and pushing the non-fixated end with a motor driven lever and recording the resistance using the Keithley 2700 multimeter. Each bending cycle took approximately 4 s divided into a 2 s bending step and a 2 s release step.

2.4.1. Stretching measurements

The functionality of the sensor does not include stretching; however, the sensor can most likely be stretched when handled and should consequently be able to be strained slightly without loss off electrical conductivity. The test sensors were therefore stretched in the longitudinal direction in order to see how the resistance behaves as a function of strain in the PDMS joints. The sensors were mounted on a stage that could be moved by a micrometer screw. As the two parts of the stage were separated, the resistance in the gold conductors on the sensors was measured, using a Keithley 2700 multimeter, again by the four-wire method. The sensor straining was performed by increasing the stage separation in steps of 10 μm. Each 10 μm increment step took approximately 1 s followed by a resistance measuring period of 30 s where the resistance was averaged from 150 samples.

2.4.2. Electrical characterization

The *IV* characterization of the pn-junctions was made by using a HP 4145B semiconductor parameter analyser. The parameters of interest were extracted by fitting the measurements to the ideal diode equation:

$$I = I_s\left(\exp\left(\frac{V - IR}{nkT}\right)\right) \quad (1)$$

Here I is the current, I_S is the saturation current, V is the voltage, R is the series resistance, n is the ideality factor, k is the Boltzmann constant and T is the temperature. The sensors were kept in complete darkness during the *IV* measurements.

2.4.3. Quantum efficiency measurements

The quantum efficiency was measured on the silicon sensor arrays, using a Jobin–Yvon H-20 monochromator set-up with a wavelength step of 10 nm. The setup was calibrated by using an 818-UV reference photo detector from Newport. For each wavelength step, a light beam from the monochromator was directed through a 1 mm pinhole and focused onto the detector by a lens. The generated photocurrents were then measured by using a Keithley 6485 picoammeter. The measurements were performed in complete darkness so only the light beam from the monochromator excited carriers in the photo detectors.

3. Theory

It is important that the flexible sensor array can be bent without breaking the electrical interconnects. When the sensor array is bent, the flexible regions in between the silicon will undergo both tensile and compressive stress. If the flexible regions are approximated as beams, an estimation can be given for the optimal placement of the electrical interconnects. When a beam is bent, there will be a line through the material where no stress occurs i.e. the neutral axis. For a composite beam made up of two materials the position of the neutral axis depends on the Young's modulus as well as the thicknesses of the two materials. From [27] the position of the neutral axis from the edge of material 1, h_1, can be calculated for a beam of two materials:

$$h_1 = \frac{1}{2}\frac{E_1H_1^2 + E_2H_2^2 + 2E_2H_1H_2}{E_1H_1 + E_2H_2} \tag{2}$$

Here H_1 and H_2 are the thicknesses of the two materials, and E_1 and E_2 are the Young's modulus for the two materials. The distance of the neutral axis from the interface of the two materials, h_{NA}, can then be determined by subtracting h_1 from H_1:

$$h_{NA} = H_1 - h_1 = \frac{1}{2}\frac{E_1H_1^2 - E_2H_2^2}{E_1H_1 + E_2H_2} \tag{3}$$

One can now determine how the choice of materials as well as their thicknesses can influence the position of the neutral axis for the flexible joints between the silicon detectors. As described in Section 2.2 the flexible joints are made of PDMS which has a Young's modulus of 1 MPa and polyimide with a Young's modulus of 2.2 GPa. The thickness of the PDMS is set to that of the silicon wafer, which is 350 μm. Using these values one can plot the position of the neutral axis as a function of polyimide thickness, as shown in Fig. 3. It is evident that the much stiffer polyimide draws the position of the neutral towards the part of the flexible region where the electrical interconnects will be located. When the polyimide has a thickness of just 7.5 μm, the neutral axis can be seen to position itself in the interface between the PDMS and the polyimide. Even thicker layers of polyimide (>20 μm) will draw the neutral axis close to the centre line of the polyimide layer and the electrical interconnects, which are placed in the middle of the polyimide, should consequently experience minimal stress when the sensor array is bent.

The flexible joints for the final sensor design will be more complicated than just a beam of two materials. To ensure the patch like structure of the sensor array, the front side of the array, which will be in contact with the skin, has a layer of PDMS covering the silicon detectors. In order to further investigate the stress and strain relations for the sensor system it has been analysed using the finite element system COMSOL 4.2. Here the proposed design shows very promising results when the sensor is bent. The analysis shows that the strain is in general confined to the softer PDMS and only very little strain, 0.4% for a 90° bend of the sensor array, is seen in the stiffer polyimide on the back side of the sensor.

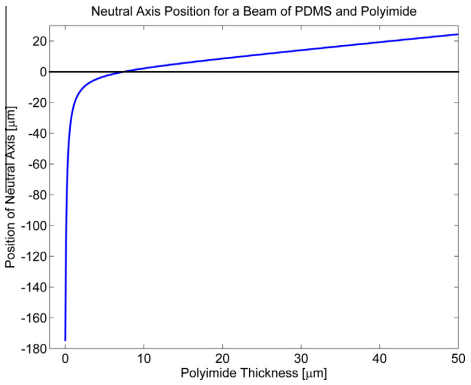

Fig. 3. Position of the neutral axis. Plot of the neutral axis in the PDMS and polyimide composite beam as a function of polyimide thickness. Negative values place the neutral axis in the thick PDMS and positive values place the neutral axis in the thin polyimide.

4. Results

4.1. Pattern optimization of HD-8820 polyimide

The HD-8820 polyimide is optimized for spray development and should produce patterns with vertical sidewalls when exposed and developed according to the specifications from HD MicroSystems. However, we would like to develop the polyimide by using conventional immersion in development bath. Moreover, we would also like to have non-vertical sidewalls in the polyimide pattern. If the pattern sidewalls form a low angle with respect to the substrate, it will ease the routing of the electrical interconnects from the 10 μm thick layer of polyimide and onto the contact point with the silicon. However, there are no reports in literature on the development process and results when immersion development is used. Exposure and development tests were therefore performed. The first tests of exposure and development were done using doses of: 280, 320 and 360 mJ/cm^2 and a development time of 30, 60, 90 and 120 s, where the wafers were simply dipped in TMAH (MF-322) and rinsed in DI water. All three different doses using development times of both 60 s and 90 s resulted in complete development of all patterns without removing more than 10% of the unexposed polyimide. The patterns were investigated by SEM and the sidewalls were found to be vertical having angles in the order of 84–90° with respect to the substrate surface. Additional tests were carried out where the patterns were overexposed using doses of: 420, 630 and 840 mJ/cm^2 and development times were 60, 90 and 120 s. The patterns were again investigated by SEM and the sidewalls were now observed to have lower angles with respect to the substrate. In all cases the patterns had been completely developed. The sidewall angles were measured to be 53–58° and there was a tendency that shorter development times produced the lowest angles for all exposure doses. For the sensor fabrication a dose of 540 mJ/cm^2 and a development time of 60 s were chosen.

4.2. Bending tests

The durability test, performed on five different test sensors with both 100 μm, 200 μm and 400 μm wide PDMS joints, showed that the sensors could be bent more than 10,000 times without the electrical interconnects showing any sign of increased resistance. The flexible structure was investigated by optical microscope and no sign of fatigue or delamination were observed.

Bending tests were performed on nine test sensors with 1 mm wide silicon detectors and 100 μm, 200 μm and 400 μm wide PDMS joints. The relative change in resistance can be seen in Fig. 4. In general, the resistance is seen to increase when the curvature of the sensors are increased. However, it is only a relatively small change for all design types. The initial resistance was, on average, measured to be: 26.61 Ω, 26.26 Ω and 27.32 Ω for the test sensors with the 100 μm, 200 μm and 400 μm wide PDMS joints, respectively. These resistances correspond to an average sheet resistance of 65 mΩ/sq for the electrical interconnects. For a curvature that corresponds to a 90° bend of the entire sensor array, the relative increase in resistance was on average: 0.48%, 0.33% and 0.04%, for the sensors with the 100 μm, 200 μm and 400 μm wide PDMS joints, respectively. The sensors could be bent to even smaller radii of curvature and still maintain the electrical conductivity of the gold conductors. When the sensors were returned to their neutral state, the resistance was also seen to return to the initial value.

4.3. Stretching tests

Stretching tests were performed on five test sensors. The relative change in resistance as function of strain in the flexible PDMS joints can be seen in Fig. 5, where it was measured for sensors with 100 μm, 200 μm and 400 μm wide PDMS joints. The relative change in resistance is seen to increase with strain. For the test sensors with 100 μm wide PDMS joints the resistance is seen to increase linearly op to about 6.5% strain. Above 7% strain the resistance increases to mega ohm, which indicates failure of the electrical interconnects. The resistance is seen to increase more rapidly for the test sensors with 200 μm wide PDMS joints. At 6% strain the resistance increases with 12% indicating necking of the gold interconnects. Further straining causes the electrical interconnects to break. For the test sensors with 400 μm wide PDMS joints the relative change in resistance is neglectable for up to 4% strain. Between 4% and 6% strain the resistance increases and above 6.5% strain the resistance measurements indicates that the electrical interconnects begin to neck and then break.

4.4. IV characterization

Five small 1 mm wide detectors and four large 2.75 mm wide detectors were analyzed. The small detectors were found to have an ideality factor of 1.7, a saturation current density of 312.1 nA/cm^2 and a series resistance of 85.7 Ω. The large detectors have an ideality factor of 1.6, a saturation current density of 67.7 nA/cm^2 and a series resistance of 5.15 Ω.

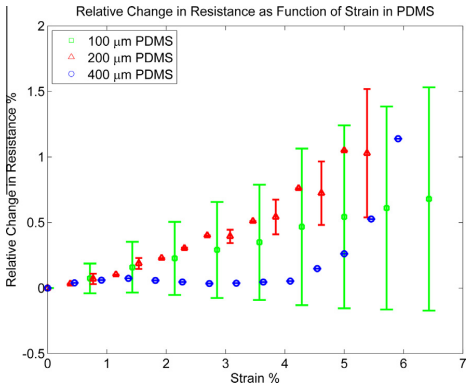

Fig. 5. Stretching of the flexible sensor arrays. The relative change in resistance as a function of strain in the PDMS joints, measured for test sensors with 100 μm, 200 μm and 400 μm wide flexible joints. The error bars show the sensor-to-sensor standard deviation.

4.5. Quantum efficiency

The external quantum efficiency was measured for five small 1 mm wide detectors and four large 2.75 mm wide detectors. For a sensor array with the smaller 1 mm detectors the quantum efficiency was in the order of 50–60% for the wavelengths of interest, i.e. 700–1000 nm (see Fig. 6). For a sensor array with the larger 2.75 mm individual photo sensors the quantum efficiency was found to be in the order of 75–85%. The quantum efficiency is also seen to be relatively constant in this interval for both detectors, and the deviations between the individual photo detectors are acceptable. When compared to a state-of-the-art commercial infrared photo sensor the sensor array with the larger detectors shows almost the same performance.

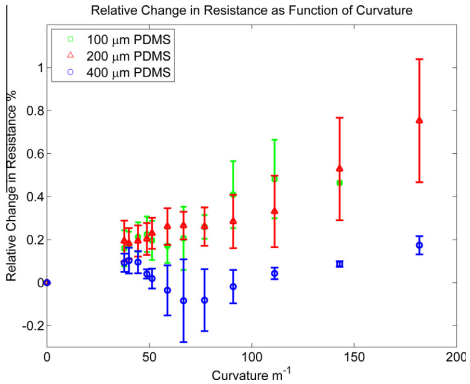

Fig. 4. Bending of the test sensors. The change in resistance as a function of curvature for three different widths of the PDMS joints. The change in resistance is seen to be low for all three designs. The error bars show the sensor-to-sensor standard deviation.

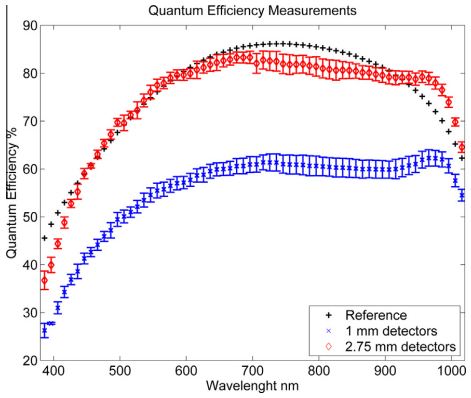

Fig. 6. Quantum efficiency measurements. The quantum efficiency measurements for the reference detector and for both sensors with the 1 mm and 2.75 mm wide detectors. The error bars show the detector-to-detector standard deviation.

5. Discussion

The characterization and testing of the sensor arrays were performed in order to investigate if the proposed design, where flexibility and patch properties are integrated directly into the silicon processing, was feasible. The feasibility investigation had a twofold purpose; firstly the functionality and durability of the flexible sensor platform itself and secondly the introduction of photo detectors for a NIRS sensor to the flexible platform.

When analyzing the results from the bending tests it is evident that the platform for this sensor is both durable and capable of introducing flexibility to the array of silicon detectors. Although, a variation in the measured electrical interconnect resistance from sensor to sensor occurs, the relative change in resistance is seen to be neglectable when the sensor arrays are bent up to 90°. Since the sensor platform can be bent up to 10,000 times without indications of fatigue in the electrical interconnects the system shows adequate durability for clinical use.

The stretching test showed that the sensor array can be stretched to an amount which correlates to a strain of 5% in the flexible joints having only a small resistance increase in the electrical interconnects. The strain which causes fracture in the electrical interconnects is in the order of 6–7%. It has been reported in [28] that free standing metal thin films will fracture at a strain of typically 1–2%, so placing the metallization in a sandwich structure of polyimide ensures increased durability to longitudinal strain for the sensor array. The 6–7% fracture stain is not as high as for electrical interconnects fabricated directly for the purpose of being stretchable. In [29] fracture strain of up to 32% is reported, when fabricating micro-cracked gold thin film on PDMS substrates. However, it is also reported that delamination between gold and PDMS substrate is a problem. This is not a problem that is observed for our design where the gold is completely encapsulated. Since it is not a design parameter for the flexible sensor array to be stretchable the 6–7% fracture strain is acceptable.

Besides being flexible and stretchable the advantage of the flexible platform is a relatively simple fabrication process which results in electrical interconnects with low resistivity. The sheet resistance of the gold interconnects was measured to be 65 mΩ/sq, which is close to the theoretical value of 61 mΩ/sq. This sheet resistance is much lower than the reported values for other flexible gold conductors i.e. 1 Ω/sq in [29]. Here the larger sheet resistance is a consequence of the very thin layers of gold, which is needed to form micro cracked metal films. If our electrical interconnects are compared to other approaches of making flexible conductors the same picture is seen. In [30] silver particles are introduced into PDMS to form flexible and stretchable conductors. However, the best achieved resistivity is 3.33×10^{-5} Ωm, which corresponds to a sheet resistance of approximately 80 Ω/sq, for a conductor which has the same thickness as the gold interconnects used in the present study.

The quantum efficiency measurements showed a strong dependence on the size of the silicon detectors. For the larger detectors, which are 2.75 mm wide, the quantum efficiency was 75–85% for the wavelengths of interest. These values are comparable to commercial available detectors. The sensor arrays with the smaller 1 mm wide detectors only had a quantum efficiency of 50–60% in the 700–1000 nm regime. It is expected that the lower quantum efficiency is caused by higher recombination rates because the surface area is now larger compared to the volume of the detector. The best performance is therefore achieved by making the detectors significantly wider than the thickness of the silicon wafer. This will ensure that the surface recombination is kept at a minimum. Another solution, which can improve the quantum efficiency, could be to introduce a field doping at the DRIE etched surfaces of the 1 mm detectors. This will repel the carriers from the surfaces where the recombination rate is higher. The detector-to-detector standard deviation of the quantum efficiency measurements is in the order of 1–2% for wavelengths of 700–1000 nm, which is acceptable.

In order to fully evaluate the NIRS functionality of the flexible sensor array tests on tissue phantoms or clinical studies must be made. However, the advantages and disadvantages of the presented sensor can still be analysed by comparison to other published sensor systems and commercially available systems. The NIRS systems which are presented in literature and the commercial systems are in general fabricated from discrete detectors which are embedded into a silicone patch. This limits the number of detectors as well as the detector size. By integrating the flexibility and the patch functionality into the silicon the photo detector size and the number of individual detectors in the array are only limited by lithography. Using our design a large amount of individual detectors can be fabricated in a flexible array with very high spatial precision. The comparison study performed in [10] evaluates the performance of three commercial NIRS sensors and one experimental sensor. The study showed that the sensors did not perform equally and as a result of this the measured oxygen saturation differed from sensor to sensor. The sensors were also very sensitive to positioning during the measurements. In all cases the sensors had a maximum of two individual detectors. Adding many individual photo detectors to the sensor will increase both the spatial resolution and make the sensor less affected by tissue artefacts than systems with only two individual photo detectors. However, our flexible sensor array is also limited by its small size, since it will only give a local measurement of the cerebral tissue oxygenation. The sensor system presented in [17] offers global diffuse optical imaging of the neonates' brain, albeit at lower spatial resolution.

6. Conclusion

We have designed and fabricated a flexible infrared sensor system for use in tissue oximetry. The system is intended to be used on neonates to detect the oxygen saturation in their brain tissue. The sensor system has several individual infrared detectors and integrated flexibility in order to follow the curvature of the head of an infant child. The calculations and simulations of the design using PDMS and polyimide in combination with silicon, show promising results regarding to the mechanical stability of the sensor and the electrical interconnects on the array, when it is bent. The fabricated sensors have been tested and are capable both of being bent to 90° and stretched to 5–6% strain without loss of conductivity in the electrical interconnects on the sensor. The introduced flexible design is simple, biocompatible and offers electrical interconnects with low sheet resistance of 65 mΩ/sq. This enables the possibility of using the sensor platform for other devices where flexibility should be introduced into silicon. The individual silicon detectors also perform well, when compared to a commercial infrared detector, if they are made with a width that is sufficiently larger than the thickness of the silicon substrate a quantum efficiency of 75–85% can be achieved for near infrared wavelengths. The sensor system thus shows promising results as an array of silicon photo detectors with integrated flexibility. By combining this detector array with light sources, a finalized NIRS system for spatially resolved spectroscopy is ready for clinical testing.

References

[1] F. Althabe et al., Born too Soon, WHO, 2012.
[2] R.M. Ward, J.C. Beachy, BJOG 110 (Suppl. 20) (2003) 8–16.

[3] M.A. Morgan, R.L. Goldenberg, J. Schulkin, J. Matern. Fetal Neonatal Med. 21 (2) (2008) 115–121.
[4] J.C. Fenik, K. Rais-Bahrami, Neonatal cerebral oximetry monitoring during ECMO Cannulation, J. of Perinatology (2009) 1–6.
[5] C. Gilbert, Early Hum. Dev. 84 (2008) 77–82.
[6] L.P. Madsen, M.K. Rasmussen, L.L. Bjerregaard, S.B. Nøhr, F. Ebbesen, Scand J. Clin. Lab Invest. 60 (2000) 125–132.
[7] G. Greisen, T. Leung, M. Wolf, Phil. Trans. R Soc. A 369 (2011) 4440–4451.
[8] L.C. Sorensen, G. Greisen, J. Biomed. Opt. 11 (5) (2006) 054005.
[9] R. Bay-Hansen, B. Elfving, G. Greisen, Biol. Neonate 82 (2002) 1–8.
[10] S. Hyttel-Sorensen, L.C. Sorensen, J. Riera, G. Greisen, Biomed. Opt. Exp. 2 (11) (2011) 3047–3057.
[11] M. Firbank, C.E. Elwell, C.E. Cooper, D.T. Delpy, J. Appl. Physiol. 85 (5) (1998) 1915–1921.
[12] A. Pellicer, M.C. Bravo, Semin. Fetal Neonatal Med. 16 (2011) 42–49.
[13] W.G. Zijlstra, A. Buursma, W.P. Meeuwsen-van der Roest, Chemistry 37 (9) (1991) 1633–1638.
[14] E.L. Hull, T.H. Foster, J. Opt. Soc. Am. 18 (3) (2001) 584–599.
[15] S. Suzuki, S. Takasaki, T. Ozaki, Y. Kobayasi, SPIE 3597 (1999) 582–592.
[16] S.B. Duun, R.G. Haahr, K. Birkelund, E.V. Thomsen, IEEE Sensor J. 10 (2) (2010) 261–268.
[17] T. Shiga, K. Tanabe, Y. Nakase, T. Shida, B. Chance, Med. Biol. Eng. Comput. 33 (1995) 622–626.
[18] J.C. Hebden, M. Varela, S. Magazov, N. Everdell, A. Gibson, J. Meek, T. Austin, IEEE ISBI (2012) 503–505.
[19] X. Zhuang, D.S. Lin, Ö. Oralkan, B.T. Khuri-Yakub, J. Microelectr. Sys. 17 (2) (2008) 446–452.
[20] P. Peng, R. Rajamani, A.G. Erdman, J. Microelectr. Sys. 18 (6) (2009) 1226–1233.
[21] S.H. Song, G.T. Gillies, M.R. Begley, M. Utz, W.C. Broaddus, J. Med. Eng. Technol. 36 (3) (2012) 156–162.
[22] P. Alpuim, V. Correia, E.S. Marins, J.G. Rocha, I.G. Trindade, S. Lanceros-Mendez, Thin Solid Films 519 (2011) 4574–4577.
[23] Y. Moser, M.A.M. Gijs, J. Microelectr. Sys. 16 (6) (2007) 1349–1354.
[24] E. Hofer, F. Keplinger, T. Thurner, T. Wiener, D. Sanchez-Quintana, V. Climent, G. Plank, Biosens. Bioelectr. 21 (2006) 2232–2239.
[25] S. Kisban, D. Moser, B. Rubehn, T. Stieglitz, O. Paul, P. Ruther, IFMBE Proc. 22 (2008) 1594–1597.
[26] A. Hyldgård, K. Birkelund, J. Janting, E.V. Thomsen, Sens. Actuators A 142 (2008) 398–404.
[27] J.M. Gere, Mechanics of Materials, sixth ed., Thomson, 2006.
[28] H. Huang, F. Spaepen, Acta Mater. 48 (2000) 3261–3269.
[29] S.P. Lacour, S. Wagner, Z. Huang, Z. Suo, Appl. Phys. L 85 (15) (2003) 2404–2406.
[30] X. Niu, S. Peng, L. Liu, W. Wen, P. Sheng, Adv. Mater. 19 (2007) 2682–2686.

Available online at www.sciencedirect.com

ScienceDirect

Procedia Engineering 00 (2014) 000–000

Procedia Engineering

www.elsevier.com/locate/procedia

EUROSENSORS 2014, the XXVIII edition of the conference series

Improvement of Infrared Detectors for Tissue Oximetry using Black Silicon Nanostructures

S. D. Petersen[a]*, R. S. Davidsen[a], L. R. Alcalá[a], M. S. Schmidt[a], A. Boisen[a], O. Hansen[a], E.V. Thomsen[a]

[a]*DTU Nanotech, Technical University of Denmark, Kongens Lyngby, DK-2800, Denmark*

Abstract

We present a nanostructured surface, made of dry etched black silicon, which lowers the reflectance for light incident at all angles. This surface is fabricated on infrared detectors used for tissue oximetry, where the detection of weak diffuse light signals is important. Monte Carlo simulations performed on a model of a neonatal head shows that approximately 60% of the injected light will be diffuse reflected. However, the change in diffuse reflected light due to the change in cerebral oxygenation is very low and the light will be completely isotropic scattered. The reflectance of the black silicon surface was measured for different angels of incident and was fund to be below 10% for angles of incident up to 70°. The quantum efficiency of detectors with the black silicon nanostructures was measured and compared to detectors with a simple anti-reflection coating. The result was an improvement in quantum efficiency for both normal incident light and light incident at 38°.

Peer-review under responsibility of the scientific committee of Eurosensors 2014.

Keywords: Tissue oximetry; infrared detectors; black silicon; quantum efficiency; diffuse reflected light

1. Introduction

Near infrared tissue oximetry, as a medical diagnostic method, is next in line to continue in the successful footsteps of pulse oximetry, which today is widely used at hospitals. Tissue oximetry is of special interest within

* Corresponding author. Tel.: +45-45255692; fax: +45-45887762.
E-mail address: sdpet@nanotech.dtu.dk

Peer-review under responsibility of the scientific committee of Eurosensors 2014.

neonatology where it is used to non-invasively monitor the oxygenation of brain tissue on prematurely born infants [1]. The most widely used measurement method is spatially resolved spectroscopy (SRS) where light of different wavelengths is injected into the tissue and the diffuse reflected light is measured as a function of distance to the light source, generally done using distances of several centimeters, see Fig. 1a. We have previously presented a device for SRS measurements on neonates, consisting of nine individual detectors, made from silicon polyimide and PDMS and optimized for detection of light with a wavelength of 700-1000 nm, which can be seen in Fig. 1b [2].

Although a majority of the light is diffuse reflected from most tissue types the changes in signal due to changes in cerebral oxygenation are typically small. In order to maximize the detected signal the reflectance from the surface of the detectors should be as low as possible. A typical solution is to apply anti-reflection (AR) coatings to the detector surface, but such coatings are very dependent on the incident angle of light and the diffuse reflected light will be incident on the detectors at all angles (0-90°). We present a solution to this problem by using black silicon nanostructures, which are dry etched into the silicon surface of the detectors. Black silicon has already proven to be a very effective anti-reflection surface for solar cells because it offers low reflectance for a wide range of wavelengths as well as for a wide range of incident angles [3].

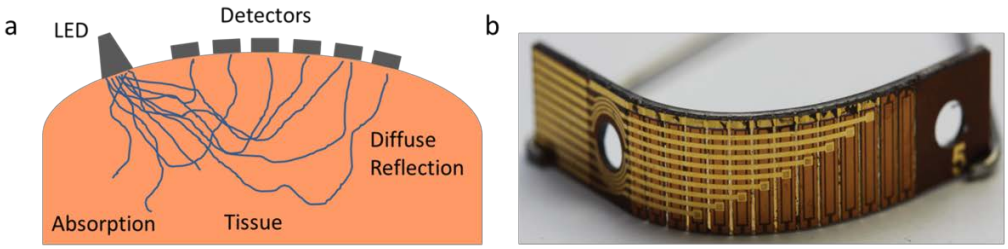

Fig. 1. (a) The principle behind spatially resolved spectroscopy. (b) A flexible array of infrared detectors used for tissue oximetry.

2. Results and discussion

2.1. Monte Carlo simulations

In order to investigate how the diffuse reflected light will behave as a function of cerebral oxygenation for a neonate we have used Monte Carlo simulation on a model of a neonatal head [4]. The model consists of four different layers corresponding to the skin, the skull, the cerebrospinal fluid and the cerebral tissue into which a pencil beam of light is injected. When the cerebral oxygenation changes it will lead to a change in the ratio between oxygenated hemoglobin and deoxygenated hemoglobin. This will in turn change the absorption coefficient of the cerebral tissue. Using data of the absorption coefficient for the two different types of hemoglobin the change in diffuse reflected light can be simulated as function of the cerebral oxygenation (StO2) for different wavelengths [5]. The results can be seen in Fig. 2a, which shows the diffuse reflected light as function of cerebral oxygenation for three different wavelengths. It can be seen that approximately 60% of the injected light will be diffuse reflected. However, the change in diffuse reflected light due to the change in cerebral oxygenation is very small, which indicates that the infrared detectors need to be of very high quality. Furthermore, the distance which the light has to travel before being completely isotropic scattered can be described as being greater than the inverse of the reduced scattering coefficient, which for the tissues in a neonatal head will be approximately 20 cm^{-1}. This means that the light will be isotropic scattered after travelling >0.5 mm into the tissue. The diffuse reflected light will therefore be both very weakly changing as function of cerebral oxygenation and arrive at the detectors from all angles between 0-90°.

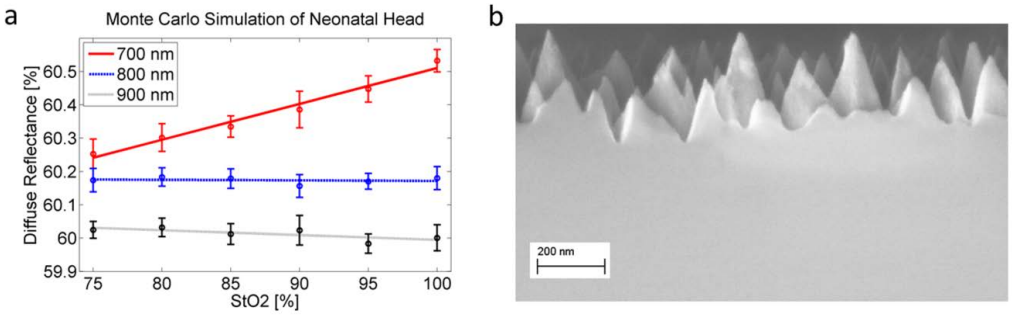

Fig. 2. (a) Results from Monte Carlo simulations. (b) SEM image of the black silicon nanostructures.

2.2. Device fabrication

The infrared detectors are fabricated on high quality (001) p-type silicon wafers with a resistivity of 10,000 Ω/cm. The detectors are fabricated as back side pn-junction diodes, using boron and phosphorous diffusions, where the junction is located on the opposite side of the light incident surface. This ensures that the electrical interconnects will not obscure for the incident light. A p-type front side field doping is also made by diffusion, in order to ensure that the generated minority carrier electrons will not diffuse towards the front side surface where the recombination velocity will be very high. The back side electrical interconnects are made by aluminum metallization and finally the black silicon nanostructures are etched into the front side using RIE with an SF_6/O_2 plasma. The black silicon nanostructures have a random topology and a height of 100-300 nm, as can be seen from Fig. 2b. Other devices where fabricated with a 50 nm SiO_2 / 50 nm SiN anti-reflection coating instead of the black silicon nanostructured surface. This ensured that the performance of the black silicon surface could be compared to a more standard AR coating.

The dry etching process for making the black silicon nanostructures has the advantage that it is compatible with polymers and metals that are on the silicon wafers when the etching process is performed. This is essential for many medical devices made from a silicon wafer platform, where a wet etch used for fabrication of the black silicon is not possible [6].

2.3. Reflectance and quantum efficiency measurements

The reflectance of the black silicon and the SiO_2/SiN AR coating were measured for light with a wavelength of 700-1000 nm using an integrating sphere and an ellipsometer, respectively. The result can be seen in Fig. 3a. For all the measured angles the black silicon can be seen to have a lower reflectance when compared to the AR coating. The quantum efficiency where measured, as a function of wavelength, for finished devices with both the black silicon nanostructures and the AR coating. The measurements were performed using a monochromator with 10 nm steps and a calibration photodiode with a known responsively and were done for normal incident light and light incident at 38° (the largest possible angle for our setup). The results can be seen in Fig. 3b. The devices with the black silicon nanostructures can be seen to have larger quantum efficiency for almost the entire wavelength span. For the entire spectrum (700-1000 nm) the devices with the black silicon nanostructures have an average quantum efficiency of 83.7% and 79.1% for light incident at 0° and 38° respectively. Whereas the devices with the AR coating have an average quantum efficiency of 74.1% and 61.6% for light incident at 0° and 38° respectively.

The anti-reflection properties of the black silicon nanostructures are seen to outperform the SiO_2/SiN AR coating both in terms of dependence on wavelength and angle. The quantum efficiency is higher for the devices with the black silicon nanostructures in the entire spectrum (700-1000nm). Furthermore, the quantum efficiency is only decreasing with 5.4% for the devices with the black silicon nanostructures when the incident angle is increased to 38°. For the devices with the AR coating the decrease is 16.9%. For many commercial infrared detectors for medical

use an IR transparent plastic coating is used, which acts as a cut-off filter for wavelengths below 700 nm. These commercial devices exhibit the same high quantum efficiency as the black silicon devices presented in this paper, but they still suffer from a strong angular dependence for the reflectance. For a typical commercial IR photodiode, coated with such a filter, a quantum efficiency reduction of approximately 25% at a light incident angle of 40° is normal [7].

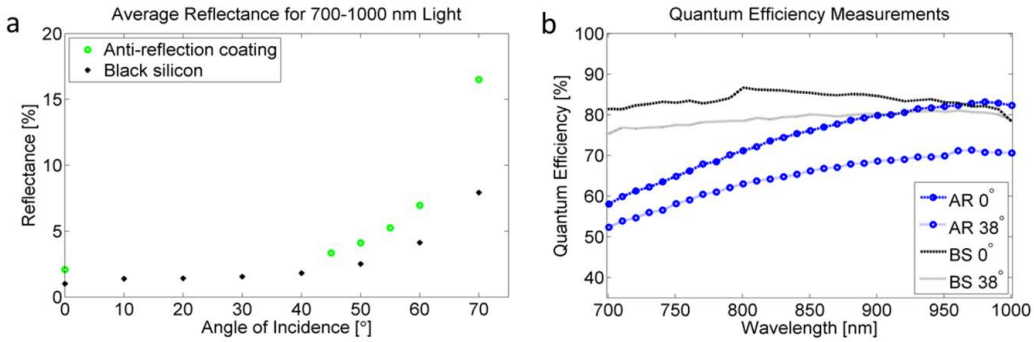

Fig. 3. (a) Reflectance measurements of AR coating and black silicon nanostructures. (b) Quantum efficiency measurements.

3. Conclusion

We have presented a black silicon nanostructured surface, which have been used to improve the anti-reflection capabilities for infrared detectors for tissue oximetry. The importance of the detector improvement has been proven by Monte Carlo simulations that showed how the diffuse reflected light would only be weakly dependent on the cerebral oxygenation and be completely isotropic scattered. The black silicon nanostructures are fabricated using a dry etch RIE process, which is compatible with wafers containing polymers and metals making it useful for various applications. Investigations of the black silicon nanostructured surfaces showed a decrease in reflectance for angles from 0-70° when comparing with a standard AR coating. Furthermore, the anti-reflection effect of the black silicon nanostructures was tested on infrared detectors. This showed higher quantum efficiencies for devices with the black silicon nanostructures at two angles when comparing them to devices with an anti-reflection coating and thus an improvement for the devices ability to detect weak diffuse scattered light.

References

[1] G. Greisen, T. Leung and M. Wolf, Has the time come to use near-infrared spectroscopy as a routine clinical tool in preterm infants undergoing intensive care, Phil. Trans. R Soc. A, 369 (2011) 4440–4451.
[2] S. D. Petersen, A. Thyssen, M. Engholm and E. V. Thomsen, A Flexible Infrared Sensor for Tissue Oximetry, Microelectronic Engineering, 111 (2013) 130-136.
[3] R. S. Davidsen, M. S. Schmidt, A. Boisen and O. Hansen, Plasma Etching on Large-area Mono-, Multi- and Quasi-mono Crystalline Silicon, Proceedings of the 39th International Conference on Micro and Nano Engineering, 2013.
[4] L. Wang, S. L. Jacques and L. Zheng, MCML - Monte Carlo Modeling of Light Transport in Multi-layered Tissue, Computer Methods and Programs in Biomedicine, 47 (1995) 131-146.
[5] B. L. Horecker, The Absorption Spectra of Hemoglobin and its Derivatives in the Visible and Near Infra-red Regions, J. Biol. Chem., 148 (1943) 173-183.
[6] Y. Su, S. Li, G. Zhao, Z. Wu, Y. Yang, W. Li and Y. Jiang, Optical Properties of Black Silicon Prepared by Wet Etching, J. Mat. Sci: Mater Electron, 23 (2012) 1558-1561.
[7] http://docs-europe.electrocomponents.com/webdocs/0655/0900766b806557c0.pdf

A Flexible Matrix Sensor for Spatially Resolved Spectroscopy Oximetry Measurements on Prematurely Born Children

Søren Dahl Petersen*[a], Joachim Dahl Thomsen[a], Erik Vilain Thomsen[a]

[a]*DTU Nanotech, Technical University of Denmark, Kongens Lyngby, Denmark*

We present a flexible matrix infrared sensor for use in tissue oximetry with the aim of treating prematurely born infants. The sensor will detect the oxygen saturation in brain tissue through near infrared spectroscopy. The sensor itself consists of several individual silicon photo detectors fully integrated in a flexible matrix. The flexibility is achieved by combining silicon with Polydimethylsiloxane and polyimide using standard IC manufacturing. This ensures that the electrical interconnects on the sensor can withstand being bent in one direction in order for the sensor to confine to the curved surface of the head of a neonatal. The sensor platform has been tested and is found to be very durable and capable of being both bent to small radii of curvature and strained in the longitudinal direction. The electrical interconnects on the sensor only experience a relative small increase in resistance when the sensor is bent up to 90° and they can withstand a longitudinal strain of up to 3 % without being damaged. A durability test has shown no fatigue or change in resistance for the electrical interconnects when the sensor had been bent 18,000 times. The average dark current density was found to be 2.32 nA/cm^2 and quantum efficiencies in the near infrared region was measured to be 55-65 %.

Keywords: Tissue oximetry, Infrared photo detector, flexible sensor, PDMS, polyimide

1. Introduction

The World Health Organisation has released a report, which determines that 15 million children are born prematurely every year [1]. Prematurely born children can easily suffer from complications when recovering in their incubators [2, 3] thus it is essential to their survival that their vital signs are monitored. One of the most important vital parameter to monitor is the oxygen saturation in the cerebral tissue [4-7]. This is due to the fact that the prematurely born neonates have difficulties in regulating the oxygen saturation in their bodies and they will therefore often receive oxygen from an artificial supply through a nasal cannula. However, this oxygenation has to be monitored since a too low concentration can lead to brain damage and a too high concentration can cause blindness as well as other disabilities [8-10]. Being able to precisely monitor and regulate the cerebral oxygenation are very crucial for the future medical treatment of neonates.

A typical method used for analysing the cerebral oxygenation is by drawing blood samples and investigating the parameters using a blood gas analyser. However, this method is invasive and can be stressful for the neonates, due to the inflicted pain, as well as removing relatively large volumes of blood, which can result in the need for blood transfusions [11]. Furthermore, a blood gas analysing is not an on-line method for cerebral oxygenation measurement and a certain delay is therefore expected between sampling and result.

During the past few years, hospitals have started using different sensor systems that utilise near infrared spectroscopy (NIRS) in order to measure the cerebral oxygen saturation non-invasively [12-14]. Many studies have been conducted and they show the feasibility of NIRS sensor systems, when used for tissue oximetry monitoring, but also the limitations of the systems developed so far [15-18]. Today, we are left with three decades of research within tissue oximetry systems as well as with some commercial systems that have recently entered the marked. However, in order to ensure better medical treatment of prematurely born neonates sensor systems, which offer higher precision in determining the cerebral oxygen saturation must be invented.

The NIRS tissue oximetry systems utilise infrared light of different wavelengths which are injected into the brain where it undergoes scattering and absorption. The diffuse reflected signal is then measured by a number of detectors placed at different distances from the light source. This specific method is called spatially resolved spectroscopy (SRS) [19]. Near infrared light can penetrate deep into most kinds of tissue, has low absorption from water, melanin and proteins [20] and can easily be detected using silicon based detectors. Moreover, the absorption from haemoglobin strongly depends on whether the haemoglobin is oxygenated (HbO) or de-oxygenated (Hb) and exhibit varying spectra as function of wavelengths. Adding more light sources of different wavelengths and more detectors to the sensor will increase the resolution of the measurements, as reported in [21]. By plotting the normalized detector signal as function of detector distance from the light source, the radiative transport equation can be used to calculate the absorption and scattering coefficients of the tissue for the given wavelength [22]. Finally, algorithms can be used to determine the oxygen saturation from all the signals received by the detectors.

The tissue oximetry devices do not only have to consist of several detectors they also have to be flexible in order to follow the curvature of the heads of the neonates. Furthermore, the contact surface between the sensor and the skin has to be soft and biocompatible. Typically, this is achieved by integrating discrete sensors into a silicone support structure or a medical patch [23-25]. Both commercial systems and devices presented in literature often only rely on two detectors so they have limited resolution on the spatially component of the measurement and they suffer from being sensitive to invisible artefacts in the skin. One possible solution, using the spatially resolved method, is to integrate the flexibility and the functionality of a "patch" directly into the silicon and consequently make entire arrays of detectors. Integrating biocompatibility and flexibility directly into the silicon has over the past few years been the new trend for medical sensors and actuators. Typically, polydimethylsiloxane (PDMS) [26-28] or polyimide [29-32] are used as these materials can create flexible areas in the silicon or serve as flexible substrates for the sensors.

We have previously presented such devices, which combined both polyimide and PDMS with silicon in order to achieve flexibility and biocompatibility [33]. The device

author's email: sdpet@nanotech.dtu.dk

platform proved feasible but was designed as a linear array of detectors. This meant that only a limited number of detectors could be placed on a device and that only on detector was available for each measurement distance. By designing the device as a matrix of detectors instead of an array both the detector density and amount of measurement points can be increased for a device with a given size, as can be seen in Fig. 1. Moreover, such a flexible matrix platform could be used for other medical devices that use 2D arrays of detectors e.g. capacitive micro machined ultrasonic transducers (CMUTs) [26].

In this paper we will present a flexible matrix sensor platform, which uses both PDMS and polyimide to achieve flexible areas in the silicon. These areas will serve as joints between the individual photo detectors in the sensor matrix. As will be described in section 3, a combination of PDMS and polyimide can be used to ensure minimal stress in the electrical interconnects, when the sensor array is being bent, by positioning the electrical interconnects near the neutral axis of the flexible joints. The device is designed so it can follow the curvature of a head of a neonate, which means that it will basically only be bend in the longitudinal direction. The PDMS will be a biocompatible surface for contact with the skin and the polyimide will offer excellent protection against moisture and metal ions by encapsulating the flexible electrical interconnects.

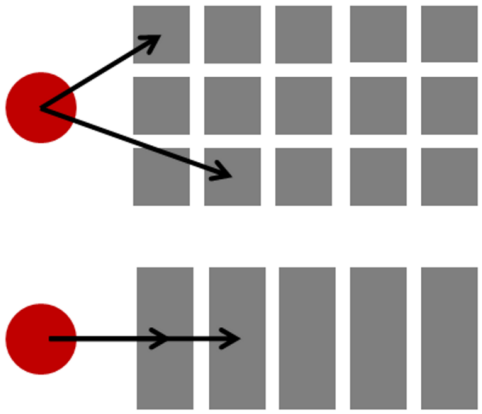

Figure 1: Schematic drawings of a 1D sensor array (bottom) and a 2D sensor matrix (top). The two devices measure the diffuse reflected light, which has scattered from the point of incident (red dot), using individual silicon detectors (grey). The matrix sensor offers a larger density of individual detectors and can thus provide better spatial resolution.

2. Materials and Methods

2.1 Sensor Design.

The NIRS device should be flexible, biocompatible and consist of multiple individual infrared detectors. This is achieved in the following manner: pn-junctions will be fabricated in the silicon in order to form photo diodes and the individual detectors will be defined using lithography and dry etching. Polyimide will be used to encapsulate the electrical interconnects and make them flexible. Finally, PDMS will act as a biocompatible contact surface and the flexible backbone of the entire device. The photo diodes are all fabricated as back side diodes where all the connections to both the n-type and p-type areas are placed at the opposite surface to which the light is incident upon. A schematic drawing of the device cross section can be seen in Fig 2a and a finished device can be seen in Fig. 2b. The device consists of 36 individual detectors that are arranged in a 4 × 9 matrix. Each detector is 2 mm × 2 mm and the flexible joints are 500 µm wide. The entire device is 28.9 mm long and 9.5 mm wide. The connector end is designed to fit into a 10 pin zero insertion force (ZIF) connector with electrical interconnects made to nine of the 36 detectors. Test device were also fabricated in order to test the performance of the electrical interconnects when the device is being bent, stretched and twisted. These test devices did not have pn-junctions but "inner" and "outer" electrical interconnects, which can be seen in Fig. 2c.

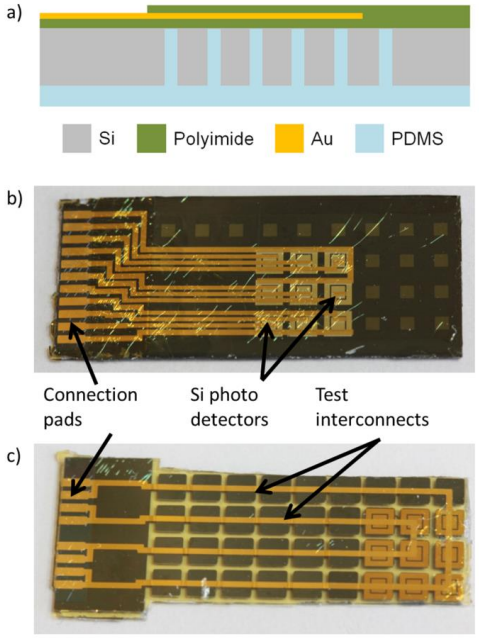

Figure 2: The 2D flexible matrix devices. A schematic cross sectional drawing of the devices is shown in a). A finished device with electrical interconnects leading to 9 individual detectors is shown in b). Finally, c) shows a test device with an "inner" and "outer" interconnect used for testing.

In order to improve the performance of the detectors the light incident surface will be doped, a so called front side field doping, with the same dopant used in the substrate. This will create a bending in the energy band near the surface and any minority carrier generated by the incident light will see this as a potential barrier and thus not diffuse to the surface where the recombination velocity is higher than in the bulk. Light reflection at the PDMS/silicon interface is minimised by coating the silicon detector surface with an anti-reflection coating made from dielectric layers (see section 2.2). The reflection simulation software Concise Macleod 8.12 was used to simulate reflectance from different dielectric layers and it was found that a simple structure of 50 nm SiO_2 and 50 nm SiN would lower the reflectance of the interface for light with a wavelength of 700-950 nm. For angles of incidence between 0-70° this double layer will lower the reflectance from 25-35% to 5-20% with the highest reflectance occurring for the highest

author's email: sdpet@nanotech.dtu.dk

angles of incident. Moreover, the dielectric layers will act as a passivation for the silicon surface.

2.2 Sensor Fabrication

Standard cleanroom processes are used for the major part of the device fabrication, which requires nine lithography steps. A schematic drawing of the process sequence is shown in Fig. 3. The devices are made from boron doped, (100) silicon wafers with a resistivity of 10,000 Ωcm and a thickness of 300 µm. First, alignment marks are etched into the silicon by reactive ion etching using patterned AZ 5412E photoresist as an etch mask. 400 nm of silicon oxide is then grown using wet thermal oxidation and this oxide is patterned using lithography and wet etching in hydrofluoric acid (HF). The thermal oxide is used as a masking material for boron diffusion. This is done by depositing 400 nm of borosilicate glass (BSG) using a plasma enhanced chemical vapour deposition process. The boron is driven into the silicon by an annealing process in nitrogen atmosphere running for 85 min at 1000 °C. The doped areas will have a final peak surface concentration of 3×10^{19} cm^{-3} after all thermal processes are completed. This boron diffusion will form the p+ substrate contacts for all of the detectors as well as the front side field doping.

The BSG and oxide mask is then stripped in HF and a new 500 nm thick wet thermal oxide is grown. This oxide is patterned in the same manner in order to create openings for n-gaseous pre-deposition from $POCl_3$, at 1000 °C for 30 min, which will result in a final peak surface concentration of 3×10^{20} cm^{-3}. The oxide mask is stripped in HF and a 50 nm dry thermal oxide is grown, which will form the first half of the anti-reflection coating and act as a surface passivation layer. A 50 nm thick silicon nitride is then deposited on the oxide using low pressure chemical vapour deposition, thus finalising the anti-reflection coating. A contact metallisation for the n-type and p-type areas, made of 100 nm Ti and 400 nm Al, is realised using lift-off. All of the above mentioned steps are performed on what will become the back side of the devices.

The flexibility is now added to the devices by deep reactive ion etching (DRIE), which is split into two parts in order to form the flexible electrical interconnects encapsulated in the polyimide. The DRIE steps are performed on the wafer surface that will become the front side of the devices, which will be the side facing towards the skin during measurements. The DRIE process is masked by a 200 nm thick layer of Al, which is evaporated onto the wafer surface using e-beam evaporation. The Al etch mask is then patterned using dry etching with Cl_2 and the first DRIE step is performed, which etches approximately 250 µm deep grooves into the wafers.

After the first DRIE step the flexible back side is realised using two layers of HD-8820 polyimide and one layer of metallisation. The wafers are placed in a 250 °C oven in order to remove moisture from the surface and thereby improve the adhesion between the silicon surface and the polyimide.

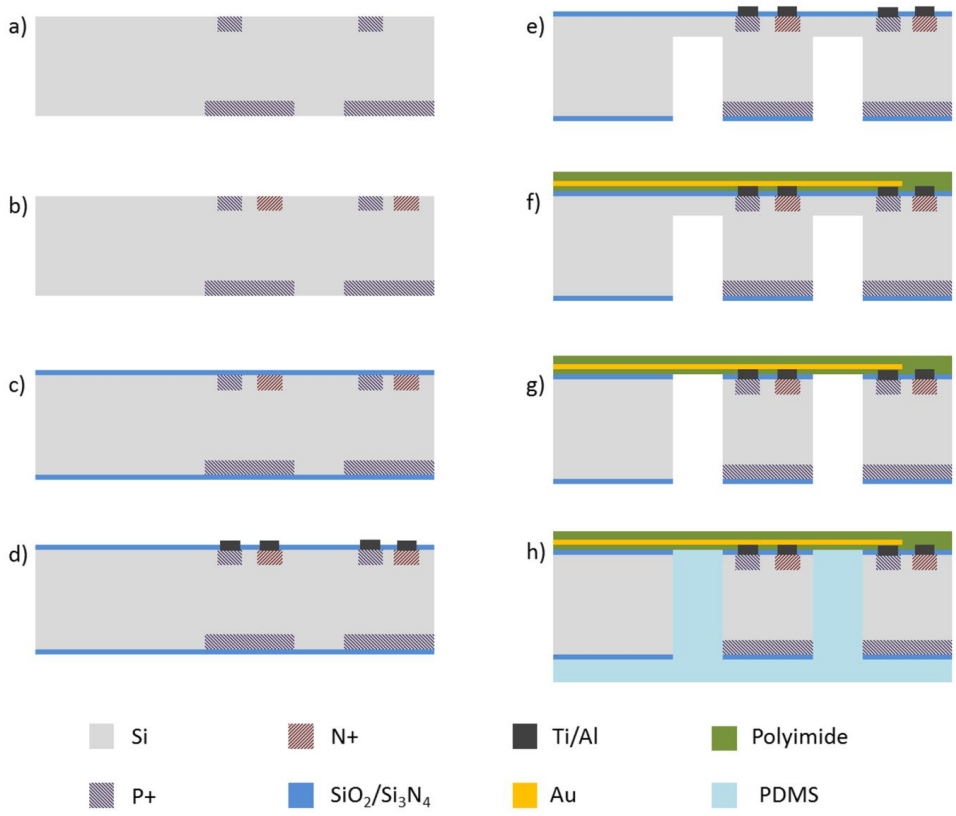

Figure 3: Schematic drawing of the process flow. a) p+ doping with boron. b) n+ doping with phosphorous. c) anti-reflection coating. d) Contact opening and first metallisation. e) Partial deep etch. f) Build-up of flexible back side using Au and polyimide. g) Final deep etch step. h) spin casting of PDMS.

author's email: sdpet@nanotech.dtu.dk

1500 rpm for 60 s followed by a 5 min baking on a 120 °C hotplate giving a thickness of approximately 10 µm. Hereafter, the HD-8820 is exposed using 540 mJ/cm^2 and developed in a tetramethylammonium hydroxide (TMAH) solution (MF-322) for 90 s. This ensures the formation of sloped sidewalls in the HD-8820 openings, which enables easier routing of the metallization onto the contact metallisation. The 200 nm thick Al etch mask is etched slightly by the TMAH developer, but will survive the process steps. Finally, the polyimide layer is semi-cured in order to destroy its photo sensitive capabilities. This is done in an N_2 atmosphere oven, where the temperature is slowly increased to 300 °C over 120 min and then decreased back to room temperature over 10 min.

The electrical interconnects are then formed by e-beam evaporation through shadow masks, which are aligned to the wafers. The electrical interconnects are made from 20 nm Ti and 400 nm Au. This ensures adhesion to the polyimide layer and ductile interconnects with low resistance. The second layer of polyimide is processed in the same manner as the first layer, but the post spin bake time is increased to 10 min in order to minimise the formation of bobbles. The layer is opened, using exposure and development, at the contact pad areas. The polyimide layers are now fully cured in the same N_2 oven, but are this time kept at 300 °C for 60 min, after the ramp up in temperature, in order to finalise the curing process.

The second deep etch step is then performed, which carefully removes the remaining 50 µm silicon from the etched grooves and stops on the polyimide layer. In order to process the wafers when they have the polyimide layers on the back side, they are bonded to carrier wafers using crystal bond 509 from Aremco Products Inc. The deep etch process does not use O_2, which reduces the etch rate in the polyimide to zero, so all the grooves can be etched to completion without damaging the polyimide layers. The Al etch mask is stripped from the wafers using MF-322 and the wafers are given a short O_2 clean in a plasma asher.

Finally, the biocompatible PDMS contact surface layer is formed using Sylgard 184 from Dow corning. The PDMS is prepared by mixing and degassing in a vacuum chamber for 15 min. It is then poured over the wafer and degassed a second time in order to remove any air bubbles left before being thinned down by spinning the wafers at 500 rpm for 30 s and cured at 120 °C for 3 hr. Finally, the individual devices are diced out from the wafer using a scalpel and separated from the carrier wafer, thus releasing the individual flexible sensor matrices.

2.3 Measurement Setups

The flexible matrix test devices were tested mechanically and electrically in order to investigate if they can withstand "daily use". Moreover, it was tested whether the infrared sensing properties, on the real devices, are sufficient or not. Simple qualitative tests, where the test devices were handled between fingers, bent around an arm and folded to small radii of curvature proved that the device concept was feasible. Quantitative tests were also performed in order to determine the limitations of the device platform. It is important that the devices can be bent to at least 90° over the full length of the device, while still maintaining electrical conduction. The sensors should also be able to be stretched slightly in the longitudinal direction without breaking the electrical conductors, since this might occur during the usage. A twisting test was also performed. Finally, IV characterizations and quantum efficiency measurements have been performed in order to determine the electrical properties of the diodes and their infrared sensing capability.

author's email: sdpet@nanotech.dtu.dk

2.3.1 Bending Measurements

In order to measure how the resistance of the electrical interconnects behaves when the sensors are bent the fabricated test chips were fixed in the ZIF connector and bent around wooden discs with different radii of curvature. The measurements were performed in an oven at 35 °C to ensure constant temperature. For each of the discs used, the resistance of the test chips were measured using a Keithley 2700 multimeter with four-wire sensing by taking 300 samples over a 60 s period. The largest disc had a radius of 65 mm and the smallest disc had a radius of 10 mm.

The device durability was tested by repeatedly bending a test sensor from its neutral position to a 90° bent. This was done by fixating one end of the test sensor and pushing the non-fixated end with a motor driven lever and recording the resistance using the Keithley 2700 multimeter. Each bending cycle took approximately 2 s divided into a 1 s bending step and a 1 s release step.

2.3.2 Stretching Measurements

The functionality of the sensor does not include stretching; however, the sensor can most likely be stretched when handled and should consequently be able to be strained slightly without loss off electrical conductivity. The test sensors were therefore stretched in the longitudinal direction in order to see how the resistance behaves as a function of strain in the joints. The sensors were fixed on a stage that could be moved by a micrometre screw. As the two parts of the stage were separated, the resistance in the gold conductors on the test sensors was measured, using a Keithley 2700 multimeter, again by the four-wire method. The sensor straining was performed by increasing the stage separation in steps of 10 µm.

2.3.3 Twisting Measurements

The electrical interconnects capability to withstand strain when the device is twisted was investigated by fixating the connector end of the device while twisting the opposite device end, in a corkscrew manner, using an electrical motor. The twist was set to ±20° from the normal plane with a full twisting cycle lasting approximately 1 s. Again, the resistance in the gold conductors on the test sensors was measured, using a Keithley 2700 multimeter.

2.3.4 Electrical Characterization

The IV characterization of the pn-junctions was made by using a HP 4145B semiconductor parameter analyser. The sensors were kept in complete darkness during the IV measurements. The parameters of interest were extracted by fitting the measurements to a modified version of the ideal diode equation [34]. This equation also takes high injection into account:

$$I = I_S \frac{\exp\left(\frac{qV}{nkT}\right)-1}{\frac{1}{2}+\frac{1}{2}\sqrt{1+k_H\left(\exp\left(\frac{qV}{nkT}\right)-1\right)}} \quad (1)$$

Here, I is the current, I_S is the saturation current, q is the elementary charge, V is the voltage, n is the diode ideality factor, k is the Boltzmann constant, T is the temperature and K_H is the high injection parameter.

2.3.5 Quantum Efficiency Measurements

The quantum efficiency was measured for the individual detectors, using a Jobin-Yvon H-20 monochromator

set-up with a wavelength step of 10 nm. The setup was calibrated by using an 818-UV reference photo detector from Newport. For each wavelength step, a light beam from the monochromator was directed through a 1 mm pinhole and focused onto the detector by a lens. The generated photocurrents were then measured by using a Keithley 6485 picoammeter. The measurements were performed in complete darkness so only the light beam from the monochromator excited carriers in the photo detectors.

3. Theory

It is important that the flexible sensor can be bent without breaking the electrical interconnects. When the device is bent, the flexible regions in between the silicon will undergo both tensile and compressive stress. If the flexible regions are approximated as beams, an estimation can be given for the optimal placement of the electrical interconnects. When a beam is bent, there will be a line through the material where no stress occurs i.e. the neutral axis. The longitudinal strain in the beam, ε_x, is given by:

$$\varepsilon_x = \frac{z}{r} \tag{2}$$

where z is the distance from the neutral axis and r is the radius of curvature for the bent beam. For a composite beam made up of two materials the position of the neutral axis depends on the Young's modulus as well as the thicknesses of the two materials. From [35] the position of the neutral axis from the edge of material 1, h_1, can be calculated for a beam of two materials:

$$h_1 = \frac{1}{2}\frac{E_1H_1^2 + E_2H_2^2 + 2E_2H_1H_2}{E_1H_1 + E_2H_2} \tag{3}$$

here H_1 and H_2 are the thicknesses of the two materials, and E_1 and E_2 are the Young's moduli for the two materials. The distance of the neutral axis from the interface of the two materials, h_{NA}, can then be determined by subtracting h_1 from H_1:

$$h_{NA} = H_1 - h_1 = \frac{1}{2}\frac{E_1H_1^2 - E_2H_2^2}{E_1H_1 + E_2H_2} \tag{4}$$

One can now determine how the choice of materials as well as their thicknesses can influence the position of the neutral axis for the flexible joints between the silicon detectors and thereby determine the optimal placement of the electrical interconnects.

However, when the device is being bent on a cured surface, with a certain radius of curvature, only the flexible joints and not the rigid silicon parts can bend. This means that the resulting bend in the flexible joints will depend on the width of the joints and the silicon detectors. A model for the strain in the flexible joints for such a piecewise flexible system can be derived using some simplifying assumptions. The model of such a device with length L is depicted in Fig. 4. It consists of N ridged silicon elements of length A with a flexible joint of length B. The device is curved circularly with a radius of curvature R thus forming an ach spanning an angle, θ, given by:

$$\theta = \frac{L}{R} = \frac{N(A+B)}{R} \tag{5}$$

Assuming that the device is bend uniformly in the N sections each joint will span an angle, ϕ, of:

$$\phi = \frac{\theta}{N} \tag{6}$$

author's email: sdpet@nanotech.dtu.dk

Each of the joints will be bent to a radius of curvature, r, given by:

$$r = \frac{B}{\phi} = \frac{BN}{\theta} = \frac{RB}{A+B} \tag{7}$$

By inserting this value of the radius of curvature into Eq. 2 the strain in the flexible joints can be defined:

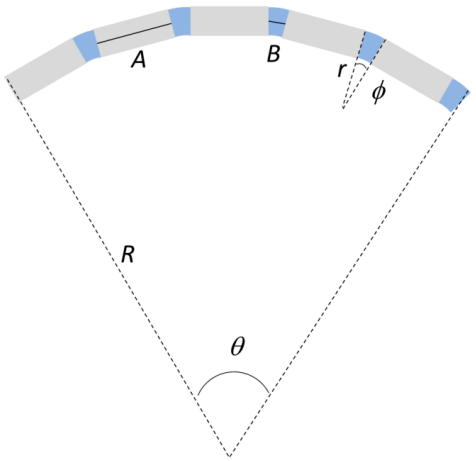

Figure 4: Schematic drawing showing the model for a piecewise flexible structure. The ridged silicon (gray) has length A and the flexible joints (blue) has length B. The entire device is bent with a radius of curvature R causing the joints to be bent with a radius of curvature of r.

$$\varepsilon_x = \frac{z}{r} = \frac{z(A+B)}{RB} = \frac{z}{R}\left(1 + \frac{A}{B}\right) \tag{8}$$

This equation will of course not make sense for all values of R. Due to the piecewise flexibility of the device the length of the rigid silicon parts will define how small a radius of curvature the device can be conformed to while still making the model valid. The model will therefore only be considered for $A \leq 5$ mm and $R \geq A/B$.

By inserting Eq. 3 into Eq. 8 the maximum strain in the polyimide can be found for different values of A and B and as a function of radius of curvature for the device. The material parameters for the composite beam joints are H_1 = 20 µm, E_1 = 2.2 GPa, H_2 = 350 µm and E_2 = 1.0 MPa. The resulting maximum strain in the polyimide can be calculated to be below 2 % even for radii of curvatures down to 2 mm. This is far lower than the fracture strain for the HD-8820 polyimide, which is approximately 100 %. Much more critical is the strain that will occur in the fragile electrical interconnects if they are not placed exactly at the position of the neutral axis. The limitations of the planar processing techniques, used to spin coat the polyimide makes it impossible to ensure this, so a misalignment of the electrical interconnects with respect to the neutral axis must be expected. If the electrical interconnects are severely misplaced upwards by 5 µm, from the neutral axis, they will be subjected to strain when the device is being bent. The amount of strain can be calculated from Eq. 8, by assuming that the electrical interconnects do not influence the placement of the neutral axis due to their extremely small thickness. The resulting strain for several design values of A/B

is plotted in Fig. 5 as a function of radius of curvature for the device. It can be seen that the strain for a given radius of curvature is much higher in devices with wider silicon areas and narrow flexible joints.

In [36] it was determined that free standing metal structures used in micro technology had a fracture strain in the order of 1-2 %. In order not to exceed more than 0.5 % strain in the misplaced electrical interconnects, a device with an *A*/*B* value of 2 can still be bent to a radius of curvature of 4 mm and a device with an *A*/*B* value of 10 should not be bend below a radius of curvature of 13 mm. The chosen design, for the presented device, with a silicon area width of 2 mm and a flexible joint width of 0.5 mm, corresponding to an *A*/*B* value of 4, can withstand a bend to a radius of curvature of down to 6 mm. This is a far smaller radius of curvature than needed in order to fulfil the design parameter of bending the device to a 90° arc over its full length, which requires a radius of curvature of 9.2 mm.

4. Results

4.1 Bending Tests

The durability test, performed on two different test sensors showed that the sensors could be bent more than 18,000 times without the electrical interconnects showing any sign of increased resistance. During the bend the resistance would increase by approximately 0.3 % from the initial value of 12 Ω and then return to the initial value when the device was relaxed. The flexible structure was investigated and no sign of fatigue or delamination were observed.

Bending tests were performed, while measuring on both the inner and outer electrical interconnects. The resistances were observed to increase when the curvature of the bend was increased, as can be seen from Fig. 5. The maximum increase was 0.16 % for the inner interconnects and 0.23 % for the outer interconnects.

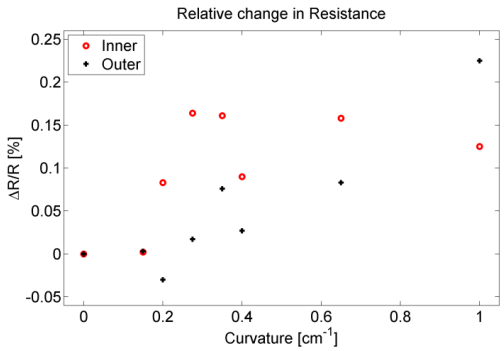

Figure 5: Plot showing the relative change in resistance for the "inner" and "outer" electrical interconnects as function of curvature for the device.

4.2 Stretching Tests

Stretching tests were performed on test devices and the electrical interconnects could withstand an average of 3 % strain before they began to neck and then break. The resistance increased with up to 0.8 % before the breaking occurred. The relation between strain and resistance increase was found to be linear as is expected from a strain gauge. The gauge factor for the devices was on average 1.47. A plot from a strain test can be seen in Fig. 6.

author's email: sdpet@nanotech.dtu.dk

4.3 Twisting Tests

The twisting test was performed while measuring on both the inner and outer electrical interconnects. It was observed that the outer interconnect, which is subjected to the largest displacement, broke immediately. The inner interconnect was, however, observed to be conducting with its resistance increasing when the device was twisted to either side and returning to the initial value when the twist was at 0°. After approximately 45 min (>2500 twists) the base resistance began to increase and this continued until approximately 4.5 hr when the inner interconnect broke. The resistance as function of time is plotted in Fig. 7.

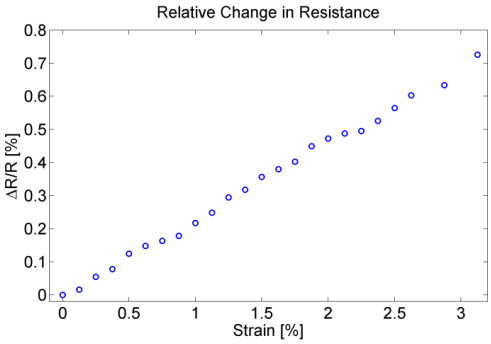

Figure 6: Plot showing the relative change in resistance for the "outer" electrical interconnect as function of strain when the device is being stretched.

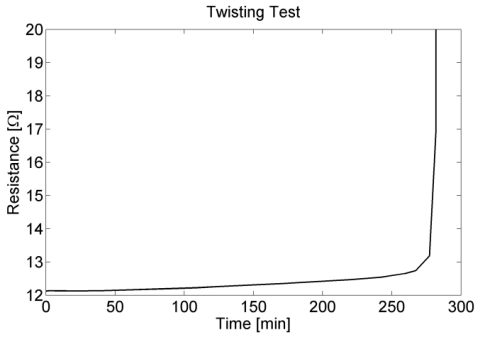

Figure 7: Plot showing the resistance of the "inner" electrical interconnect as function of time when the device is being twisted. The "outer" interconnect broke immediately.

4.4 IV Characterization

IV measurements were performed on 18 individual detectors by direct probing. Fitting Eq. 1 to the measurement data for the detectors showed an average ideality factor of 1.02, a series resistance of 2.00 Ω and an average high injection factor of 1.79×10^{-4}. The average reverse bias current density at -1 V was found to be 2.32 nA/cm^2. When put in forward bias the diode would exhibit normal behaviour up to 0.35 V but from 0.35 V to 0.75 V they would exhibit high injection behaviour. For even larger voltages the series resistance would dominate. When performing IV measurements by contacting the flexible electrical interconnects, the detectors were found to

exhibit similar parameters except for the series resistances, which were now increase to 6-23 Ω depending on the length of the interconnects.

4.5 Quantum Efficiency

The external quantum efficiency was measured was measured on five detectors and the average quantum efficiency and standard deviation is plotted in Fig. 8 from 400-1100 nm. It can be seen that the detectors exhibit the largest quantum efficiency of approximately 55-65 % in the desired wavelength interval of 700-1000 nm. The standard deviation in the same wavelength interval is 2 %, which is in the order of the measurement uncertainty of the quantum efficiency measurement setup.

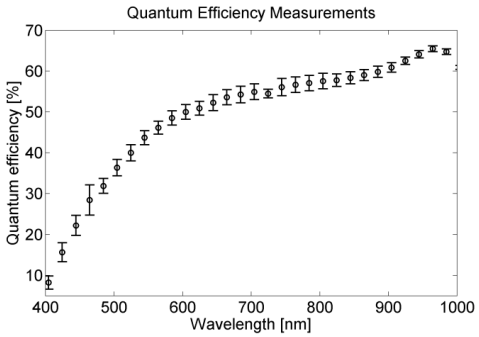

Figure 8: Plot showing the average quantum efficiency as a function of wavelength for five detectors.

5. Discussion

The testing and characterization of the devices were performed in order to investigate if the proposed design, where flexibility and patch properties are integrated directly into the silicon processing, was feasible. The feasibility investigation had a twofold purpose: the functionality and durability of the flexible matrix platform itself and the introduction of photo detectors for a NIRS sensor to the flexible platform.

The first qualitative analysis proved that the platform design could be handled and utilized as a medical sensor without damage to the device structure and the electrical interconnects. The results from the quantitative bending tests also show that the platform for this sensor is both durable and capable of introducing flexibility. Although, a variation in the measured electrical interconnect resistance from sensor to sensor occurs, the relative change in resistance is seen to be neglectable when the sensor arrays are bent up to 90°. Since the sensor platform can be bent more than 18,000 times without indications of fatigue in the electrical interconnects the flexible matrix platform shows adequate durability for clinical use.

The stretching test showed that the electrical interconnects can be stretched while exhibiting only a small resistance increase in the electrical interconnects. The strain which causes fracture in the electrical interconnects is approximately 3-3.5 %. It has been reported in [36] that free standing metal thin films will fracture at a strain of typically 1-2 %, so placing the metallization in a sandwich structure of polyimide ensures increased durability to longitudinal strain for the sensor array. This can also be seen by the gauge factor, which as determined to be 2 for all metal thin films in [37]. The measured average gauge factor of 1.47 indicated that the resistance change is lower for a given increase in strain. This could be caused by build in stress in the polyimide, which creates a spring like structure for the electrical interconnects at the flexible joints.

The 3-3.5 % fracture stain is not as high as for electrical interconnects fabricated directly for the purpose of being stretchable. In [38] fracture strain of up to 32 % is reported, when fabricating micro-cracked gold thin film on PDMS substrates. However, it is also reported that delamination between gold and PDMS substrate is a problem. This is not a problem that is observed for our design where the gold is completely encapsulated.

A limitation to the flexible matrix platform was determined by the twisting tests. This test clearly proved that although the platform itself can withstand being twisted the electrical interconnects cannot. The electrical interconnects will either break immediately if the amplitude of the twist is large or be slowly damaged by wear if the amplitude is small. However, since they can withstand the twisting that will occur doing manual handling of the devices it will not impose a problem for the specified use of the devices.

An advantage of the flexible matrix platform is a relatively simple fabrication process, which results in electrical interconnects with low resistivity. The sheet resistance of the 400 nm thick gold interconnects was measured to be 65 mΩ/sq, which is close to the theoretical value of 61 mΩ/sq. This sheet resistance is much lower than the reported values for other flexible gold conductors i.e. 1 Ω/sq in [38]. Here the larger sheet resistance is a consequence of the very thin layers of gold, which is needed to form micro cracked metal films. If our electrical interconnects are compared to other approaches of making flexible conductors the same picture is seen. In [39] silver particles are introduced into PDMS to form flexible and stretchable conductors. However, the best achieved resistivity is 3.33×10^{-5} Ωm, which corresponds to a sheet resistance of approximately 80 Ω/sq, for a conductor which has the same thickness as the gold interconnects used in the present study.

The quantum efficiency measurements showed a quantum efficiency of 55-65 % for the wavelengths of interest. These values are low when compared to commercial available detectors, which can reach up to 90 % for near infrared light and also when compared to the previously presented detectors from the linear detector array, which showed 75-85 %. The lower quantum efficiency is most likely caused by the relatively small detector size combined with the un-passivated sidewalls that are created when the individual detectors are etched out. Generated carriers that diffuse to the sidewalls will most likely recombine and thus not contribute to the photo current. A possible solution to this problem could be to coat the etched out sidewalls with surface passivation layer e.g. aluminium oxide deposited using atomic layer deposition. This layer could also reduce the dark current of the devices, which would make the detectors even more sensitive. The measured dark current at -1 V is at an acceptable level, but not close to commercial available detectors, which can reach down to pico amps per square centimetre. The detector-to-detector standard deviation of the quantum efficiency measurements is in the order of 2 % for wavelengths of 700-1000 nm, which is acceptable.

The NIRS systems, which are presented in literature and the commercial available systems are in general fabricated from discrete detectors which are embedded into a silicone patch, which limits the number of individual detectors. By integrating the flexibility and the patch functionality into the silicon the photo detector size and the number of individual detectors in the flexible matrix platform are only limited by lithography. Using our design a large amount of individual detectors can be fabricated in a flexible matrix with very high

author's email: sdpet@nanotech.dtu.dk

spatial precision. Adding many individual photo detectors to the sensor will increase both the spatial resolution and make the sensor less affected by tissue artefacts than systems with only two individual photo detectors. Furthermore, the platform could potentially be used for other medical transducers, e.g. CMUT arrays. However, in order to fully investigate the potential of the flexible matrix NIRS device, tests on tissue phantoms using IR light sources, will have to be carried out.

6. Conclusion

We present a flexible 2D matrix infrared sensor system for use in tissue oximetry. The system is intended to be used on neonates to detect the oxygen saturation in their brain tissue. The sensor system has several individual infrared detectors and integrated flexibility in order to follow the curvature of the head of an infant child. We present a design and process flow for realising such a device.

The design of the device has been investigated using a derived analytical model for a piecewise flexible structure. The analytical model proves that only insignificant strain should be present in the electrical interconnects when the device is being bent even if the interconnects cannot be placed exactly at the position of the neutral axis.

The fabricated sensors have been tested and are capable both of being repeatedly bent to 90° and strained 3 % without loss of conductivity in the electrical interconnects on the sensor. The introduced flexible design is simple, biocompatible and offers electrical interconnects with low sheet resistance of 65 mΩ/sq. This enables the possibility of using the sensor platform for other devices where flexibility should be introduced into silicon.

The individual silicon detectors also perform acceptable exhibiting reverse bias current densities in the order of a few nano amps per square centimetre and quantum efficiencies of 55-65 % for near infrared wavelengths. The sensor system thus shows promising results as a matrix of silicon photo detectors with integrated flexibility. By combining this detector array with light sources, a finalized NIRS system for spatially resolved spectroscopy is ready for clinical testing.

References

[1] F. Althabe et al, Born too Soon, WHO, 2012.
[2] R.M. Ward, J.C. Beachy, Neonatal Complications following Preterm Births, BJOG, Vol. 110 Suppl. 20 (2003) 8–16.
[3] A.F. Korner, D.K. Stevenson, T. Forrest, J.C. Constantinou, S. Dimiceli, B. W. Brown, Preterm medical complications differentially affect neurobehavioral functions: Results from a new neonatal medical index, Infant behavior and development 17 (1994) 37-43.
[4] J.C. Fenik, K. Rais-Bahrami, Neonatal cerebral oximetry monitoring during ECMO Cannulation, J. of Perinatology (2009) 1–6.
[5] W.A. Carlo et al, Target ranges of oxygen saturation in extremely preterm infants, The New Engl. J. of med, 362(21) (2010) 1959-1969.
[6] N. Finer, T. Leone, Oxygen saturation monitoring for the preterm infant: The evidence basis for current practice, pediatric res. 65 (2009) 375-380.
[7] W. Tin, S. Gupta, optimum oxygen therapy in preterm babies, Arch dis child fetal neonatal 92 (2007) 143-147.
[8] C. Gilbert, Retinopathy of prematurity: A global perspective of the epidemics, population of babies at risk and implications for control, Early Human Development 84 (2008) 77–82.
[9] E.S. Potharst, A.G. von Wassennaer, B.A. Houtzagar, J.W.P. van Hus, B.F. Last, J.H. Kok, High incidence of multi-domain disabilities in very preterm children at five years of age, Arch dis child fetal neonatal 159(1) (2011) 79-85.
[10] N. Marlow, D. Wolke, M.A. Bracewell, M. Samara, Neurologic and developmental disability at six years of age after extremely preterm birth, The New Engl. J. of med, 352(1) (2005) 9-19.
[11] L.P. Madsen, M.K. Rasmussen, L.L. Bjerregaard, S.B. Nøhr, F. Ebbesen, Impact of Blood Sampling in very Preterm Infants, Scand J. Clin. Lab Invest. 60 (2000) 125-132.
[12] G. Greisen, T. Leung, M. Wolf, Has the time come to use near-infrared spectroscopy as a routine clinical tool in preterm infants undergoing intensive care, Phil. Trans. R. Soc. A 369 (2011) 4440–4451.
[13] J.M. Murkin, M. Arango, Near-infrared spectroscopy as an index of brain and tissue oxygenation, British j. of anaesthesia 113 (2009) 3-13.
[14] G. Naulaers, G. Morren, S. van Huel, P. Casaer, H. Devlieger, Cerebral tissue oxygenation index in very premature infants, Arch dis child fetal neonatal 87 (2002) 89-92.
[15] L.C. Sorensen, G. Greisen, Precision of measurement of cerebral tissue oxygenation index using near-infrared spectroscopy in preterm neonates, J. Biomedi. Optics 11(5) (2006) 054005.
[16] R. Bay-Hansen, B. Elfving, G. Greisen, Use of Near Infrared Spectroscopy for Estimation of peripheral Venous Saturation in Newborns: Comparison with Co-Oximetry of Central Venous Blood, Biol Neonate 82 (2002) 1–8.
[17] S. Hyttel-Sorensen, L.C. Sorensen, J. Riera, G. Greisen, Tissue oximetry: a comparison of mean values of regional tissue saturation, reproducibility and dynamic range of four NIRS-instruments on the human forearm, Biomedi. optics exp. Vol. 2 11 (2011) 3047-3057.
[18] M. Firbank, C. E. Elwell, C. E. Cooper, D. T. Delpy, Experimental and theoretical comparison of NIR spectroscopy measurements of cerebral hemoglobin changes, J. Appl. Physiol. 85(5) (1998) 1915-1921.
[19] A. Pellicer, M. C. Bravo, Near-infrared spectroscopy: A methodology-focused review, Sem. in fetal neonat. med. 16 (2011) 42-49.
[20] W.G. Zijlstra, A. Buursma, W.P. Meeuwsen-van der Roest, Absorption spectra of human fetal and adult oxyhemoglobin, de-oxyhemoglobin, carboxyhemoglobin and methemoglobin, clin. Chem. 37(9) (1991) 1633-1638.
[21] T.M. Baran, J.D. Wilson, S. Mitra, J.L. Yao, E.M. Messing, D.L.Waldmann, T.H. Foster, Optical property measurements establish the feasibility of photodynamic therapy as a minimally invasive intervention for tumors of the kidney, J. of biomedical optics, 17(9) (2012) 098002-1-8.
[22] E. L. Hull, T. H. Foster, Steady-state reflectance spectroscopy in the P3 approximation, J. Opt. Soc. Am. Vol. 18(3) (2001) 584-599.
[23] S. Suzuki, S. Takasaki, T. Ozaki, Y. Kobayasi, A tissue oxygenation monitor using NIR spatially resolved spectroscopy, SPIE vol. 3597 (1999) 582-592.
[24] S.B. Duun, R.G. Haahr, K. Birkelund, E.V. Thomsen, A Ring-Shaped Photodiode Designed for use in a Reflectance Pulse Oximetry Sensor in Wireless Health Monitoring Applications, IEEE sensor J. vol. 10(2) (2010) 261-268.
[25] T. Shiga, K. Tanabe, Y. Nakase, T. Shida, B. Chance, Development of a portable tissue oximeter using near infra-red spectroscopy, Med. & Biol. Eng. & Comput. 33 (1995) 622-626.
[26] X. Zhuang, D.S. Lin, Ö. Oralkan, B.T. Khuri-Yakub, Fabrication of Flexible Transducer Arrays with Through-Wafer Electrical Interconnects Based on Trench Refilling With PDMS, J. Microelec. Sys. Vol. 17(2) (2008) 446-452.
[27] P. Peng, R. Rajamani, A.G. Erdman, Flexible Tactile Sensor for Tissue Elasticity Measurements, J. Microelec. Sys. Vol. 18(6) (2009) 1226-1233.
[28] S.H. Song, G.T. Gillies, M.R. Begley, M. Utz, W.C. Broaddus, Inductively coupled microfluidic pressure meter for in vivo monitoring of cerebrospinal fluid shunt function, J. Medical Eng. Tech. 36(3) (2012) 156–162.
[29] P. Alpuim, V. Correia, E.S. Marins, J.G. Rocha, I.G. Trindade, S. Lanceros-Mendez, Piezoresistive silicon thin film sensor array for biomedical applications, Thin Solid Films 519 (2011) 4574–4577.
[30] Y. Moser, M.A.M. Gijs, Miniaturized Flexible Temperature Sensor, J. Microelec. Sys. Vol. 16(6) (2007) 1349-1354.
[31] E. Hofer, F. Keplinger, T. Thurner, T. Wiener, D. Sanchez-Quintana, V. Climent, G. Plank, A new floating sensor array to detect electric near fields of beating heart preparations, Biosens. Bioelect. 21 (2006) 2232–2239.
[32] S. Kisban, D. Moser, B. Rubehn, T. Stieglitz, O. Paul and P. Ruther, Fatigue Testing of Polyimide-Based Micro Implants, IFMBE Pro. Vol. 22 (2008) 1594–1597.

author's email: sdpet@nanotech.dtu.dk

[33] S.D. Petersen, A. Thyssen, M. Engholm, E.V. Thomsen, A Flexible Infrared Sensor for Tissue Oximetry, Microelectronic engineering 111 (2013) 130-136.
[34] S. Duun, The Electronic Patch, Ph.D. Thesis, DTU Nanotech 2010.
[35] J.M. Gere, Mechanics of materials, sixth ed., Thomson, 2006.
[36] H. Huang, F. Spaepen, Tensile testing of free-standing, Cu, Ag and Al thin films and Ag/Cu multilayers, Acta mater. 48 (2000) 3261-3269.
[37] R.L. Parker, A. Krinsky, Electrical resistance-strain characterisestics of thin evaporated metal films, J. applied physics, 34 (1963) 2700-2708.
[38] S.P. Lacour, S. Wagner, Z. Huang, Z. Suo, Stretchable gold conductors on elastomeric substrates, Appl. Phys. L. Vol 85(15) (2003) 2404-2406.
[39] X. Niu, S. Peng, L. Liu, W. Wen, P. Sheng, Characterizing and Patterning of PDMS-Based Conducting Composites, Adv. Mater. 19 (2007) 2682-2686.

author's email: sdpet@nanotech.dtu.dk

Appendix B

Process Recipe

Step 1. Alignment Marks

Step	Process	Machine	Parameters	Comments
1.1	New wafers			Double side polished P-type 525 um thick
1.2	HMDS	HMDS oven (1.006)	Recipe: 4	Process takes ~35 min.
1.3	AZ resist spinning (Top-side)	SSE Spinner (1.028)	Resist: AZ5214E Thickness: 1.5 um Recipe: 1.5 um 4inch	Top side of wafer
1.4	Photolithography	KS Aligner (1.003)	Hard contact Exposure: 7s Mask: **Alignment**	First print (activate back side microscope)
1.5	Development	Developer-1 (1.007) or Developer-2 (1.008)	Developer: AZ351 Time: 60s Rinse 3 min in DI water	
1.6	Descum	Plasma Asher 2 (1.031)	Recipe: Manual Parameters: O2: 200 sccm, N2: 50 sccm, power: 500W, time: 2 min	
1.7	DRIE	DRIE-Pegasus (3.027)	Recipe: Process A Chuck temp: 20C Etch time: 5 cycles	Use cassette loader 1 min etch time should give ~10 um etch depth.
1.8	Acetone resist strip	Rough Strip (1.012) and Fine Strip (1.013)	Rough time: 2 min Fine time: 3 min Rinse in DI water: 5 min	
1.9	7-up Cleaning	7-up 6” (4.008)	Time: 10 min Rinse in DI water 5 min	Step added due to some resist still on the wafers. Even on the back side.

Step 2. Boron Diffusion Doping

Step	Process	Machine	Parameters	Comments
2.1	RCA Cleaning	RCA (4",6") (4.014)		Takes 1-1.5 hr.
2.2	Wet thermal oxidation	Furnace: Boron Drive-in and Pre-dep (A1) (5.004)	Temp: 1000C Process: Wet Time: 30 min + 20 min anneal.	Thickness: ~200 nm Measure real thickness using Filmtek (8.018)
2.3	HMDS	HMDS oven (1.006)	Recipe: 4	Process takes ~35 min.
2.4	AZ resist spinning (Top-side)	SSE Spinner (1.028)	Resist: AZ5214E Thickness: 1.5 um Recipe: 1.5 um 4inch	Top side of wafer
2.5	Photolithography	KS Aligner (1.003)	Hard contact Exposure: 7s Mask: **Boron diffusion**	Alignment
2.6	Development	Developer-1 (1.007) or Developer-2 (1.008)	Developer: AZ351 Time: 60s Rinse 3 min in DI water	
2.7	BHF	Buffered HF – Clean (3.007)	Time: ~8 min Rinse 5 min in DI water	Set time according to the thickness measured in step 2.2 Etch rate: ~70 nm/min
2.8	Acetone resist strip	Rough Strip (1.012) and Fine Strip (1.013)	Rough time: 2 min Fine time: 3 min Rinse in DI water: 5 min	
2.9	RCA Cleaning	RCA (4",6") (4.014)	**NO HF-dips!!!**	Takes 1-1.5 hr.
2.10	PECVD BSG	PECVD2 (2.008)	Recipe: sdp_bsg Time: 2 min	Thickness: ~375 nm Front side Use dedicated holder
2.11	PECVD BSG	PECVD2 (2.008)	Recipe: sdp_bsg Time: 2 min	Thickness: ~375 nm Back side Use dedicated holder
2.12	Drive-in	Furnace: Anneal-oxide (C1) (5.006)	Temp: 1000C Time: 85 min	Anneal in N2
2.13	Oxide strip	Buffered HF – Clean (3.007)	Time: 60 min Rinse 5 min in DI water	

Step 3. Phosphorus Diffusion Doping

Step	Process	Machine	Parameters	Comments
3.1	RCA Cleaning	RCA (4",6") (4.014)		Takes 1-1.5 hr.
3.2	Wet thermal oxidation	Furnace: Anneal-oxide (C1) (5.006)	Temp: 1000C Process: Wet Time: 120 min + 20 min anneal.	Thickness: ~500 nm Measure real thickness using Filmtek (8.018)
3.3	HMDS	HMDS oven (1.006)	Recipe: 4	Process takes ~35 min.
3.4	AZ resist spinning (Back-side)	SSE Spinner (1.028)	Resist: AZ4562 Thickness: 6.2 um Recipe: AZ4562_4inch_6.2um	Back side of wafer It takes around 10 min in total per wafer(just this side)
3.5	AZ resist spinning (Top-side)	SSE Spinner (1.028)	Resist: AZ5214E Thickness: 1.5 um Recipe: 1.5um 4inch	Top side of wafer No bake!
3.6	Resist bake	Oven 90C (1.016)	Time: 30 min	
3.7	Photolithography	KS Aligner (1.003)	Hard contact Exposure: 7s Mask: **Phosphorus diffusion**	Alignment
3.8	Development	Developer-1 (1.007) or Developer-2 (1.008)	Developer: AZ351 Time: 60s Rinse 3 min in DI water	
3.9	BHF	Buffered HF – Clean (3.007)	Time: ~8 min Rinse 5 min in DI water	Set time according to the thickness measured in step 3.2 Etch rate: ~70 nm/min
3.10	Acetone resist strip	Rough Strip (1.012) and Fine Strip (1.013)	Rough time: 2 min Fine time: 3 min Rinse in DI water: 5 min	
3.11	RCA Cleaning	RCA (4",6") (4.014)	**NO HF-dips!!!**	Takes 1-1.5 hr.
3.12	Phosphorus pre-deposition	Furnace: Phosphorus Predep (A4) (5.001)	Recipe: POCL1000 Temp: 1000C Time: 30 min + 20 min anneal	
3.13	Oxide strip	Buffered HF – Predep (4.016)	Time: 60 min	Located at RCA bench

Step 4. Optical filter and Contact Openings

Step	Process	Machine	Parameters	Comments
4.1	Dry thermal oxidation + phosphorus drive-in	Furnace: Anneal-oxide (C1) (5.006)	Temp: 1100C Process: Dry Time: 20 min + 20 min anneal.	RCA clean wafers if not directly from step 3.13. Thickness: ~50 nm Measure real thickness using Ellipsometer VASE
4.2	LPCVD Nitride	Furnace: LPCVD Nitride (6") (E3) (2.015)	Recipe: 4nitdan1 Time: 18 min.	Thickness: ~50 nm Measure real thickness using Ellipsometer VASE (8.045)
4.3	HMDS	HMDS oven (1.006)	Recipe: 4	Process takes ~35 min.
4.4	AZ resist spinning (Top-side)	SSE Spinner (1.028)	Resist: AZ5214E Thickness: 1.5 um Recipe: 1.5um 4inch	Top side of wafer
4.5	Photolithography	KS Aligner (1.003)	Hard contact Exposure: 7s Mask: **Contact openings**	Alignment
4.6	Development	Developer-1 (1.007) or Developer-2 (1.008)	Developer: AZ351 Time: 60s Rinse 3 min in DI water	
4.7	Descum	Plasma asher (1.005) or Plasma Asher 2 (1.031)	Recipe: Manual Parameters: O2: 200 sccm, N2: 50 sccm, power: 500W, time: 2 min	
4.8	Nitride dry etch	RIE2 (3.004)	Recipe: BGE-NITR Time: ~3 min	Set time according to the thickness measured in step 4.1 Etch rate: ~40 nm/min
4.9	Oxide dry etch	RIE2 (3.004)	Recipe: 1SiO2mre Time: ~4 min	Set time according to the thickness measured in step 4.2 Etch rate: ~30 nm/min
4.10	Acetone resist strip	Rough Strip (1.012) and Fine Strip (1.013)	Rough time: 2 min Fine time: 3 min Rinse in DI water: 5 min	
4.11	7-up Cleaning	7-up 6" (4.008)	Time: 10 min Rinse in DI water 5 min	

Step 5. Metallization

Step	Process	Machine	Parameters	Comments
5.1	HMDS	HMDS oven (1.006)	Recipe: 4	Process takes ~35 min.
5.2	AZ resist spinning (Top-side)	SSE Spinner (1.028)	Resist: AZ5214E Thickness: 2.2 um Recipe: 2.2um 4inch	Top side of wafer
5.3	Photolithography (Image reversal)	KS Aligner (1.003)	Hard contact Exposure: 5s Mask: **Metal 1** Bake on hotplate: 110C for 2 min. Flood exposure: 30s	Alignment image reversal process
5.4	Development	Developer-1 (1.007) or Developer-2 (1.008)	Developer: AZ351 Time: 70s Rinse 3 min in DI water	
5.5	Metal deposition	Wordentec (2.013)	100 nm Ti / 400 nm Al	
5.6	Lift-off	Lift-off wet bench (1.009)	1 min without US then 120 min with US.	Increase US time if lift-off is incomplete
5.7	Al contact anneal	Furnace: Al-Anneal (C4) (5.005)	Temp: 425C Time: 30 min	

Step 6. Partial Deep Etch

Step	Process	Machine	Parameters	Comments
6.1	Al Deposition	Alcatel (2.002)	Al: 200 nm	Deposit as 2 x 100 nm. (Back side wafer)
6.2	AZ resist spinning (Back-side)	SSE Spinner (1.028)	Resist: AZ5214E Thickness: 1.5 um Recipe: 1.5um 4inch	Back side of wafer Pre-bake wafer at 150C for 5 min (two by two better)
6.3	Photolithography	KS Aligner (1.003)	Hard contact Exposure: 7s Mask: **Deep etch**	Alignment
6.4	Development	Developer-1 (1.007) or Developer-2 (1.008)	Developer: AZ351 Time: 60s Rinse 3 min in DI water	Remember to write: "Al on wafers" in logbook
6.5	Bond of device wafer to 6" carrier wafer	Hotplate next to Manual Spinner (Polymers) (1.033)	Temp: 70C	Bond with crytalbond
6.6	Al dry etching	ICP Metal Etch (3.028)	Recipe: Al etch Chuck temp: 20C Etch time: ~120 s	Abort when etch has over etched for ~10s (end point detection, ask to use program) After etch separate device wafer from 6" carrier and clean device wafer in DI water to remove crystal bond.
6.7	Silicon dry etching	ASE (3.002)	Recipe: residual Time: 2 min Followed by Recipe: sdp_deep Cycles: 120 Temp: 20C	Measure depth using dektak. The etch depth for a 525 um wafer should be ~450 nm
6.8	Descum	Plasma Asher (1.005)	Recipe: Manual Parameters: O2: 200 sccm, N2: 50 sccm, power: 500W, time: 2 min	

Step 7. Polyimide 1

Step	Process	Machine	Parameters	Comments
7.1	Bake out	Oven 250C (1.018)	10 min	
7.2	Polyimide spinning	KS Spinner (1.002)	Resist: HD-8820 Thickness: ~9 um Recipe: 1500 rpm for 60 s, bake 120C for 5 min.	Use the "non-vacuum" chuck (book also manual spinner to use hotplate)
7.3	Photolithography	KS Aligner (1.003)	Soft contact Exposure: 90s Mask: **Polyimide 1**	Alignment
7.4	Development	Fumehood (Bases) (3.021)	Developer: MF-322 Time: 90s Rinse 3 min in DI water	
7.5	Curing	BCB curring oven (5.015)	Recipe: SDP_PI1	Semi curing (process takes 3 hr)

Step 8. Metallization 2

Step	Process	Machine	Parameters	Comments
8.1A	New wafers			Single side polished P-type 525 um thick
8.2A	HMDS	HMDS oven (1.006)	Recipe: 4	Process takes ~35 min.
8.3A	AZ resist spinning (Front-side)	SSE Spinner (1.028)	Resist: AZ5214E Thickness: 4.2 um Recipe: 4.2um 4inch	Front side of wafer
8.4A	Photolithography	KS Aligner (1.003)	Soft contact Exposure: 20s Mask: **Metal 2**	First print
8.5A	Development	Developer-1 (1.007) or Developer-2 (1.008)	Developer: AZ351 Time: 180s Rinse 3 min in DI water	
8.6A	Bond of device wafer to carrier wafer	Hotplate next to Manual Spinner (Polymers) (1.033)	Temp: 70C	
8.7A	DRIE	DRIE-Pegasus (3.027)	Recipe: Shadow mask Chuck temp: 10C Etch time: ~30 min	Use load lock to manually load wafers. Etch wafers for 30 cycles at a time, then switch to other wafer. Check each trough using 200 cycles on a test wafer.
8.8A	Resist strip	Plasma asher (1.005)	Recipe: Manual Parameters: O2: 400 sccm, N2: 70 sccm, power: 1000W, time: 20 min	
8.1B	Align shadow masks	Nikon eclipse L200 (8.025)		Fixate shadow mask to wafer using blue film.
8.2B	Metal deposition	Wordentec (2.013)	Deposition of either: 50 nm Ti / 400 nm Au	

Step 9. Polyimide 2

Step	Process	Machine	Parameters	Comments
9.1	Bake out	Oven 250C (1.018)	5 min	
9.2	Polyimide spinning	KS Spinner (1.002)	Resist: HD-8820 Thickness: ~11 um Recipe: 1200 rpm for 60 s, bake 120C for 10 min.	Use the "non-vacuum" chuck (book also manual spinner to use hotplate)
9.3	Photolithography	KS Aligner (1.003)	Soft contact Exposure: 90s Mask: **Polyimide 2**	Alignment
9.4	Development	Fumehood (Bases) (3.021)	Developer: MF-322 Time: 90s Rinse 3 min in DI water	
9.5	Curing	BCB curring oven (5.015)	Recipe: SDP_PI2	Semi curing (process takes 4 hr)

Step 10. Full Deep Etch and PDMS

Step	Process	Machine	Parameters	Comments
10.1	Bond of device wafer to 4" carrier wafer	Hotplate next to Manual Spinner (Polymers) (1.033)	Temp: 70C	
10.2	Silicon dry etching	ASE (3.002)	Recipe: residual Time: 2 min Followed by Recipe: sdp_deep Cycles: 30 Finally: Recipe: sdp_iso Cycles: 10 Temp: -10C	When the polyimide becomes visible switch to sdp_iso (it doesn´t have O2).
10.3	Al strip	Fumehood (1.036)	Stripper: MF-322 Etch time: ~15min	Strip all Al(doesn´t etch through polyimide and nitride, it etches trough Si 1nm/min)
10.4	Plasma cleaning	Plasma asher (1.005)	Recipe: Manual Parameters: O2: 200 sccm, N2: 50 sccm, power: 400W, time: 10 x 20 s	Use quartz boat for wafers with metal
10.5	PDMS spin casting	PDMS spinner	Rpm: 300 Time: 60s	Mix PDMS resin and curing agent 10:1 (20g) Leave mixture in desiccator for 10 min Pour mixture on wafer and leave in desiccator for 50 min. Spin wafer and cure in oven at 65C for 4 hr. Clean the outer part of wafers covered with PDMS before curring.
10.6	Chip releasing			Separate device wafer from carrier on hotplate. Cut out chips with scalpel.

Appendix C

Measurement Setup Images

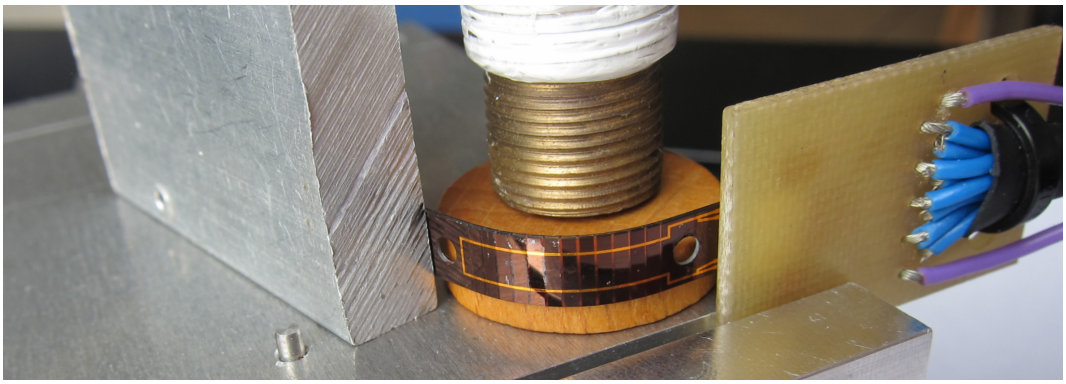

Figure C.1: Measurement setup for investigation of how the electrical interconnects behave when the device is bend. The device is fixed to the right by the ZIF connector and to the left by a metal plate. The device can now be bend around objects with a known radius of curvature and the change in resistance, in the electrical interconnects, can be measured.

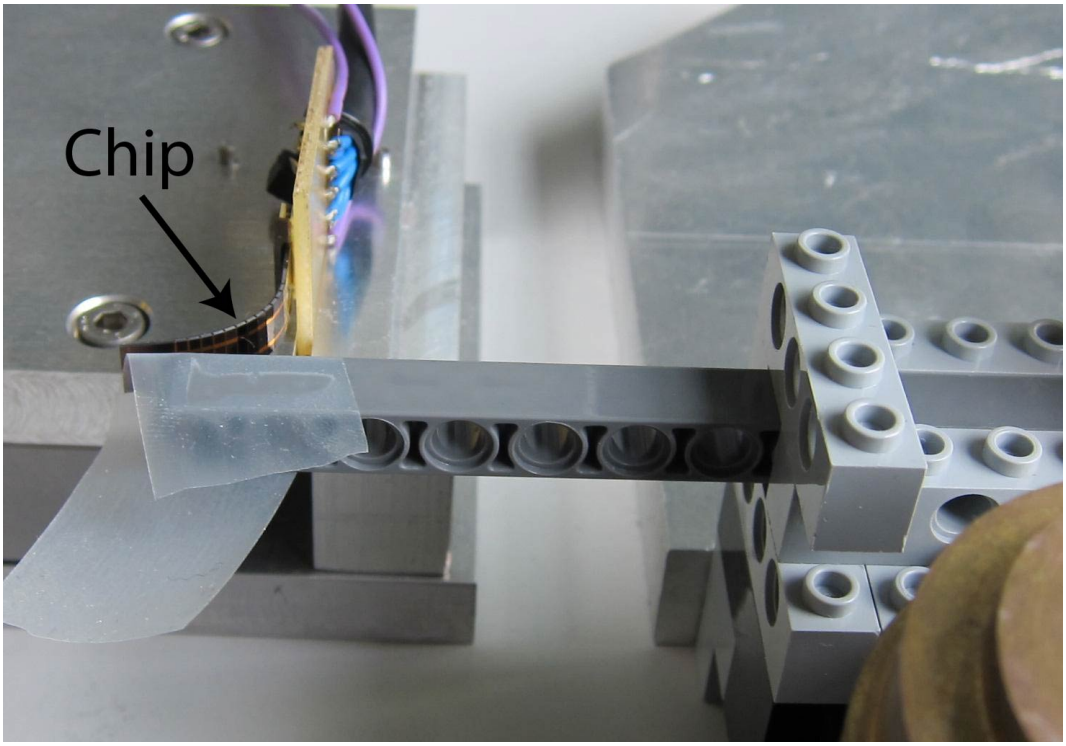

Figure C.2: Setup for testing the durability of the devices when being bent. The device is fixed in the ZIF connector and then repeatedly bend to 90° by a lever, which can move left to right. The bending and release cycle takes approximately 4 s.

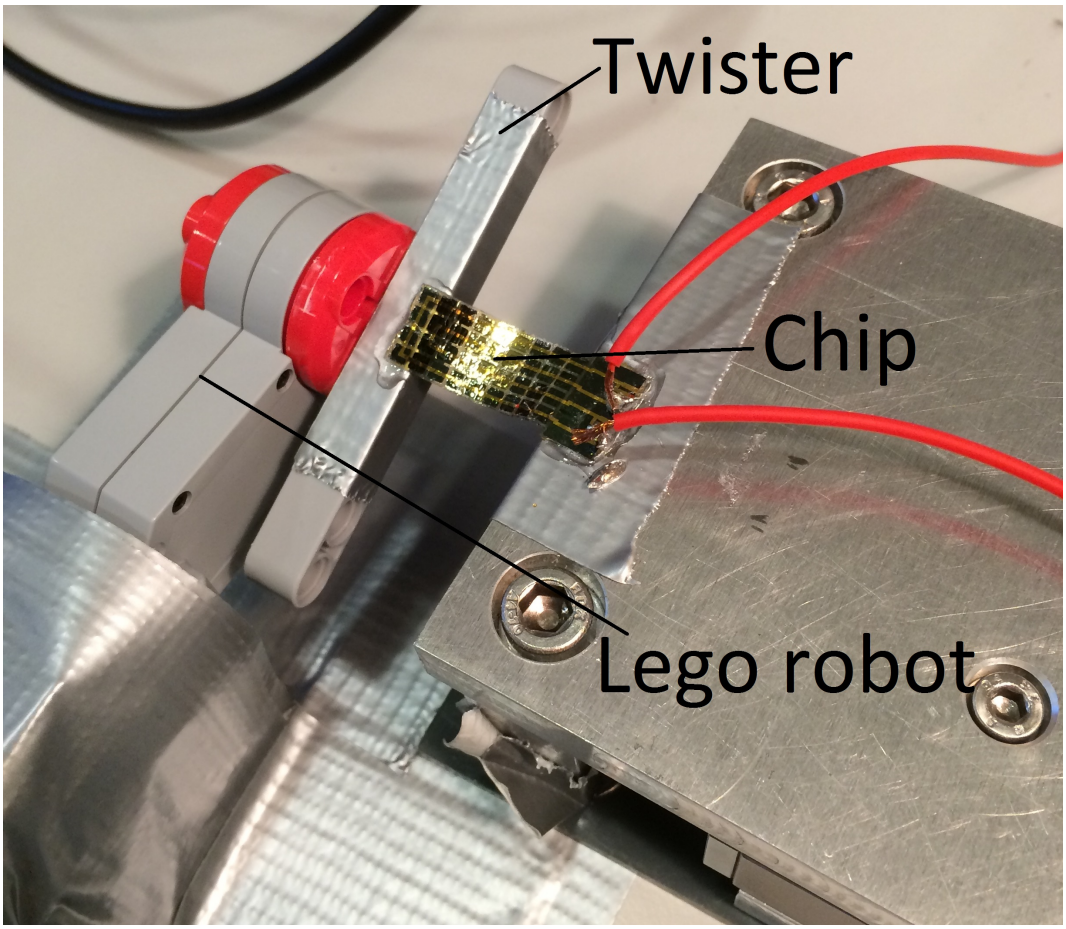

Figure C.3: Picture of the setup used to twist the 2D square matrix devices. The non-flexible end of the chip, with the connection pads, is fixed at a stationary position while the other end is fixed at the twisting arm. The twisting arm is set to move up and down by ±20° while the resistance in the two electrical interconnects is measured.

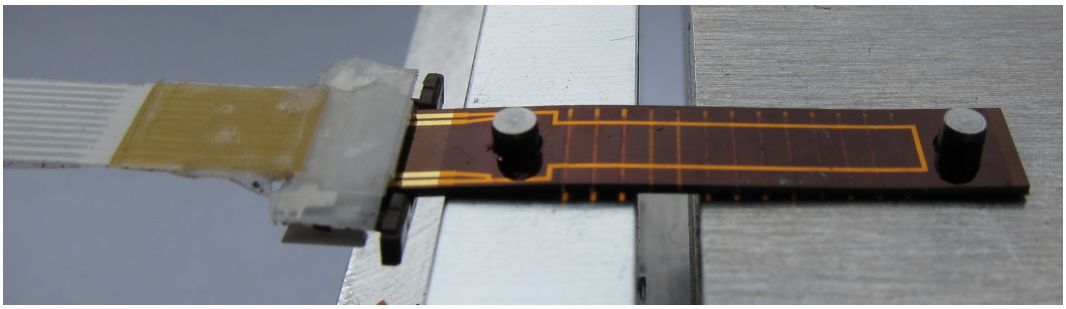

Figure C.4: A 1D test device anchored to the pins on the stretching setup. The two schor ponits can be moved using a micrometer screw. When the test was perfomed on the 2D devices, which did not hav holes for achoring, the devices were instead fixed using metal clamps and epoxy glue.

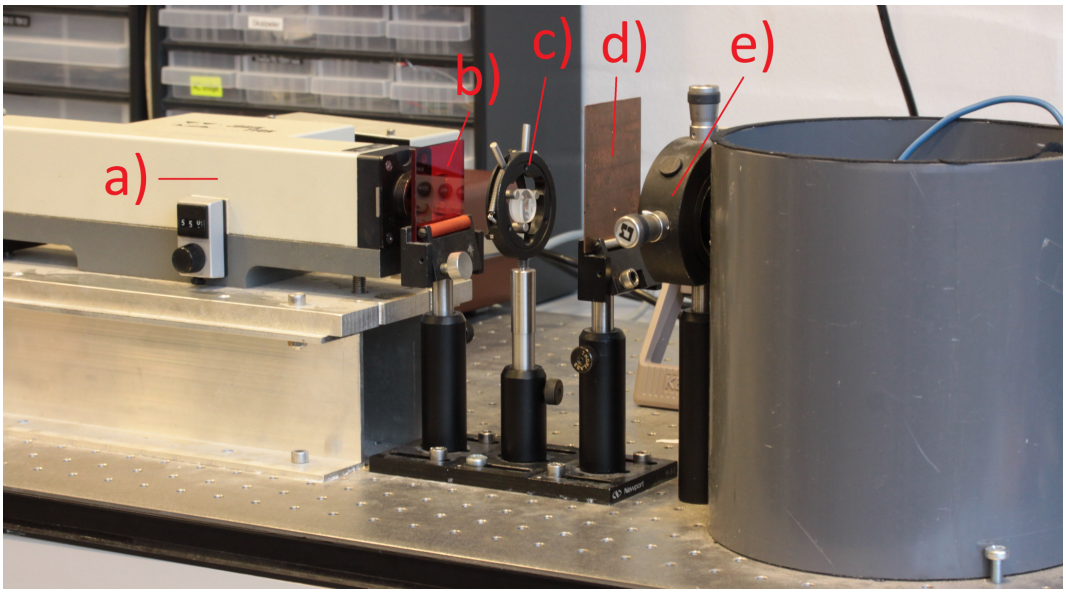

Figure C.5: The quantum efficiency setup consisting of: (a) monochromator, (b) infrared filter, (c) collimator lens, (d) aperture and (e) focussing lens. The sample is placed inside the grey cylinder, which can be covered to create darkness.

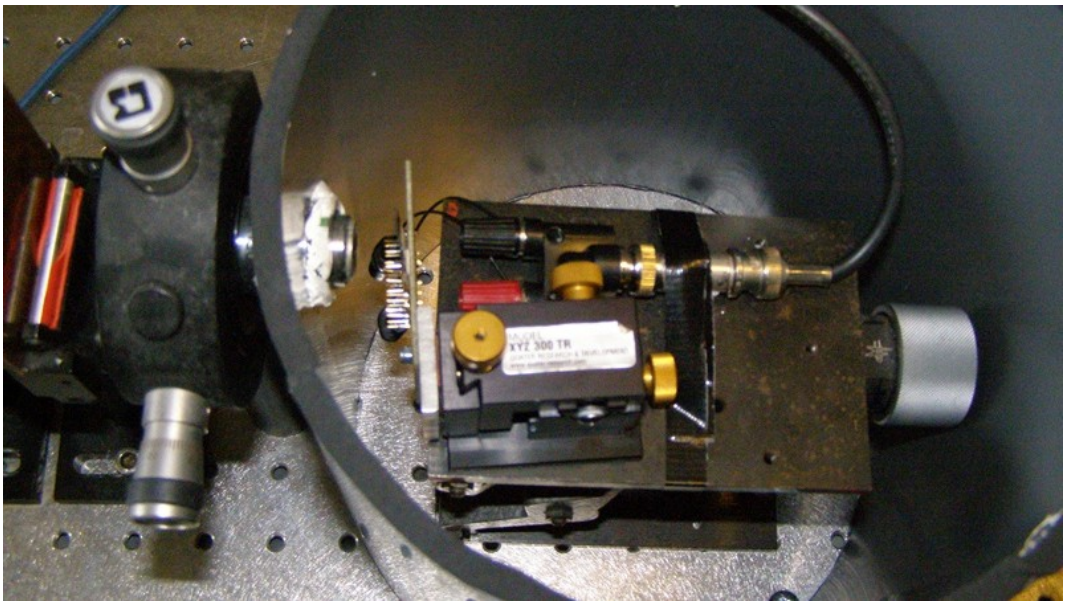

Figure C.6: The sample can be positioned exactly at the focal point of the beam by using an xyz-stage. The reference detectors is so large that it can be positioned correctly without the need of the stage.

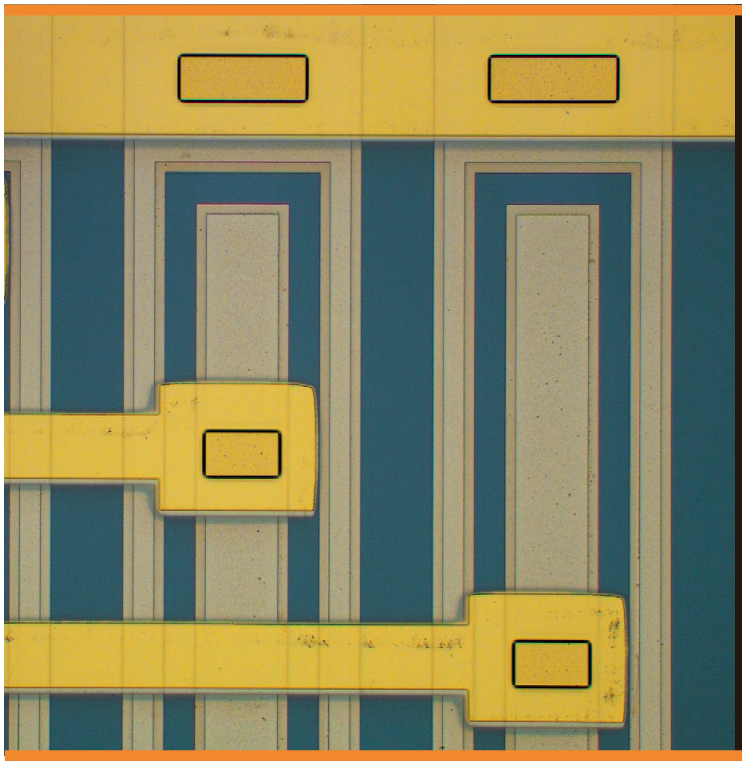

Published by:
DTU Nanotech
Department of Micro- and Nanotechnology
Technical University of Denmark
Ørsteds Plads, building 345B
DK-2800 Kgs. Lyngby